

University of Nottingham
UK | CHINA | MALAYSIA

Scalar-Tensor Fifth Forces in Galactic Environments

Thesis submitted to the University of Nottingham for the degree of **Doctor of Philosophy, September 2025.**

Bradley March

14315727

Supervised by

Prof. Clare Burrage

Signature _____

Date _____ / _____ / _____

Summary

Scalar-tensor theories of gravity have emerged as compelling alternatives to General Relativity, offering potential explanations for cosmic acceleration and the nature of dark matter. These theories introduce additional scalar fields that couple to matter, leading to modifications of gravitational interactions through fifth forces. However, such modifications must be carefully constructed to evade stringent local tests of gravity, necessitating the development of screening mechanisms that suppress scalar effects in well-tested high-density environments like the Solar System, while preserving phenomena in low-density galactic outskirts. Understanding these screening mechanisms and scalar fifth forces on galactic scales forms the central focus of this thesis.

In chapter 1, we detail the historical background of modern cosmology and galactic physics, as well as the theoretical framework of scalar-tensor theories, with particular focus on chameleon and symmetron models. The numerical and statistical methodologies required to implement these theories in realistic galactic environments are outlined in chapter 2, including a mock-galaxy generation pipeline that transforms observable galactic properties into detailed density profiles, and the numerical solver we utilise to compute accurate scalar field configurations.

The core investigations of this thesis examine the validity of approximations and assumptions commonly adopted in scalar field studies. Chapter 3 rigorously tests frequently used methods for estimating screening radii — the boundaries of screened regions within galaxies. Through precise

numerical solutions, and novel methods to calculate the screening radii, we reveal significant discrepancies between approximate and true screening radii. We find that the widely used binary screening condition, based on the galaxies virial potential, drastically underestimates the parameter space where galactic discs are screened, leading to erroneously tight constraints. While more sophisticated partial screening approximations perform better, they still exhibit systematic errors when Compton wavelengths become comparable to galactic scales, suggesting that many existing observational constraints may be overstated.

Building on these methods, chapter 4 examines the validity of assuming continuous stellar density profiles in $f(R)$ theories. When Compton wavelengths approach typical stellar separation — as we find to be the case in screened galactic regions — the discrete nature of stars significantly alters scalar field behaviour. We posit that the field profile becomes highly heterogeneous in this regime: relaxing to values determined solely by smooth dark matter in the interstellar medium while becoming strongly screened near individual stars. This shifts screening radii toward galactic centres, potentially exposing previously screened regions to scalar modifications.

Chapter 5 develops a novel framework to measure scalar theories through weak gravitational lensing observations, with an application focused on the radial acceleration relation in galaxies. We test our framework for several symmetron-based models that introduce small photon masses, enabling photons to couple to scalar fields and exhibit fifth-force-like lensing enhancements. This work opens new observational pathways for constraining modified gravity theories.

The key findings and broader implications of this research are presented in chapter 6.

Acknowledgements

First and foremost, I would like to thank my supervisor, Clare Burrage. This is undoubtedly the most important acknowledgement of all, as without your support and guidance, this thesis would not exist. Words cannot fully express my gratitude towards you and my immense fortune in being one of your students. Your supervisory style is one I aspire to emulate, and I hope to one day support and guide any understudy I take on as brilliantly as you have done for me. Beyond the invaluable academic support week in and week out, I am especially grateful for the personal support you have given me through difficult times and for your unwavering belief in my abilities. Your humility, kindness, and compassion do not go unnoticed, and unquestionably reflect the true character of the person you are. Thank you for everything.

I also owe an enormous debt of gratitude to my long-term collaborator and mentor, Aneesh Naik. Without your help and support in the early days of my PhD, I would not have reached where I am today. I learned a tremendous amount of technical skills from you that have been invaluable to my research and will undoubtedly prove essential in my future career. Your patience and willingness to help me has been deeply appreciated. Thank you for being an exceptional mentor and friend.

I would also like to thank Ed Copeland — if I could bottle your enthusiasm for physics and life in general, I would be extraordinarily wealthy. As a bright-eyed youngster, I was hugely influenced by watching your Sixty Symbols videos, and it remains somewhat surreal to think that I have had the privilege of working with you.

This PhD was not the beginning of my academic journey, and I would be remiss not to express thanks towards Tasos Avgoustidis for the support and guidance as my undergraduate and master's project supervisor. The advanced topics you introduced me to and the skills you taught me along

the way have proved invaluable in kickstarting my research career.

Nottingham has been an outstanding place to work, and this is no coincidence. The department is filled with exceptional people, who work hard to make it so, and I would like to thank all the academic staff for their contributions over the years. In particular, I would like to thank Omar Almaini for your enthusiasm as head of postgraduate studies and for always taking the time to listen to myself and the other postgraduate representatives. I would also like to thank Tony Padilla, for the inside scoop on LFC news and the visits to Anfield, YNWA. The university is not complete without its support staff, including the God of IT, Phil Parry; the admin staff who have been invaluable in navigating the bureaucratic maze of academia; and the university landscapers, for maintaining such a picturesque campus.

During my time at the department, I have been fortunate to befriend many wonderful people. In an attempt to keep this reasonably brief, I will divide them into overlapping categories without mentioning specific names. The footballers, Italian or otherwise; the bouldering crew; the lunchtime crossworders; the usual pub crew; the DA gang of old; the astronomers; the particle theorists; and especially my many officemates, past and present, for the helpful discussions and welcomed distractions. As mentioned, no names are to be specified; however, I contend that nicknames don't count, so special shout outs to Lawn Gawn, Swaghetti Mishballs, the Kezzy Dubler, and my amigo Serkhio. Thank you all, for the laughs and wonderful times we have shared.

Outside the department, I would like to thank the NCC gang for the late nights and obscene portions of chicken wings; my undergraduate housemates for the endless kitchen conversations about topics that barely qualify as physics; Sanjay for the adventures around Nottingham and beyond; and my oldest and dearest friend, Will, for always being there and serving as the voice of reason (sometimes), less than three.

Finally, I would like to thank my extended family for always being supportive and proud of me. To my sisters, for being hilarious — don't let it go to your heads, you learned from the best. To Nana, for your unconditional love and support and for being a remarkable role model of compassion. To my parents, for your unwavering support and encouragement throughout my life. You knew exactly how much freedom and direction to provide, and you always believed in me, even when I doubted myself. Thank you for your countless sacrifices — without your support, I would not be where I am, or who I am today.

Declaration

I declare that this thesis is my own work, except where otherwise acknowledged. No part of this thesis has been submitted in any form for another degree or professional qualification. This thesis contains work from the following published papers:

1. Burrage, C., March, B., and Naik, A. P. (2024). Accurate computation of the screening of scalar fifth forces in galaxies. *JCAP*, 2024(4):004

2. March, B., Burrage, C., and Naik, A. P. (2024). Galactic Compton wavelengths in f(R) screening theories. *JCAP*, 2024(12):027

The work in chapters 2 and 3 is based on Burrage et al. (2024). The work in chapter 4 is based on March et al. (2024). The work in chapter 5 is currently under preparation for submission to a peer-reviewed journal.

Contents

Summary i

Acknowledgements iii

Declaration v

List of Figures xii

Abbreviations xx

Conventions xx

Chapter 1 Introduction 1

1.1 Cosmological Model 1

1.1.1 General Relativity 1

Newtonian Gravity 1

Steps Towards General Relativity 2

How Geometry Tells Matter to Move 3

How Matter Tells Spacetime to Curve 5

Action Formulation of General Relativity 6

1.1.2 The Standard Model of Cosmology 7

The Expanding Universe 7

Dynamics of the Universe 11

The Hot Big Bang 14

Dark Matter 16

Structure Formation in ΛCDM 16

1.1.3 Beyond ΛCDM 19

1.2 Galaxies 22

1.2.1 Historical Development of Galactic Studies 22

1.2.2 Modern Galactic Astronomy 24

1.2.3 Galactic Density Models 27

Dark Matter Component 28
Stellar Disc Component 32
Other Galactic Components 33
1.3 Screened Modified Gravity Theories 35
1.3.1 General Scalar-Tensor Model 35
1.3.2 Solving the General Scalar Field Equation of Motion 37
Fully Screened Solution 38
Fully Unscreened Solution 38
Partially Screened Solution 42
1.3.3 Approximations for the Screening Radius 43
1.3.4 Screening Mechanisms 44
1.3.5 Chameleon 47
1.3.6 $f(R)$ Gravity 48
Hu-Sawicki $f(R)$ 50
1.3.7 Symmetron 52
1.3.8 Tests of Gravity 55
Laboratory Tests 56
Solar System Tests 58
Astrophysical Tests 59
1.4 Weak Lensing 61
Chapter 2 Methodology 65
2.1 Galactic Parameter Pipeline 65
2.1.1 Galactic Parameter Relations 68
Mass Relations 68
NFW Parameters 69
Galactic Disc Parameters 70
2.1.2 Galactic Parameter Generation 72
Aside: Bayesian Statistics and MCMC Methods . . . 74
Galactic Parameter MCMC Sampling 77
Bayesian Inference for Modified Gravity Parameters . 80
2.2 Numerical Methods 81

2.2.1 Numerical Solver 82

Chapter 3 Accurate Computation of the Screening of Scalar Fifth Forces in Galaxies 88

3.1 Summary 88

3.2 Introduction 89

3.3 Theory 91

3.3.1 Scalar-Tensor Gravity 91

3.3.2 Astrophysical Screening Approximations 92

3.3.3 Chameleon $f(R)$ 94

3.3.4 Symmetron 95

3.4 Numerical Screening Solutions 97

3.4.1 Galactic Model 98

3.4.2 Numerical Solver 101

3.4.3 Screening Conditions 102

3.5 The Screening of Galaxies 106

3.5.1 Position and Shape of Screening Surfaces 106

3.5.2 Amounts of Galactic Mass Screened 109

3.5.3 Milky Way Observables 115

3.6 Conclusions 118

Chapter 4 Galactic Compton Wavelengths in $f(R)$ Screening Theories 122

4.1 Summary 122

4.2 Introduction 123

4.3 Theory 125

4.3.1 $f(R)$ Gravity 125

4.3.2 Compton Wavelength 127

4.4 Galaxy Model 129

4.4.1 Galactic Density Model 129

4.4.2 Separation Between Stars 130

4.5 Results 131

4.5.1 Compton Wavelength in Galaxies 131

4.5.2 Scalar Field Values in the Interstellar Medium 135
4.5.3 Fifth Forces Around Stars 138
4.6 Conclusions 138
Chapter 5 Lensing in Modified Gravity Theories 140
5.1 Summary 140
5.2 Introduction 141
5.3 Measurements of the RAR 144
5.4 Scalar Coupling Model 150
5.4.1 Constraints on the Photon Mass 153
5.5 Numerical and Statistical Modelling 154
5.5.1 Galactic Model 154
5.5.2 Mock Galaxy Sample 155
5.5.3 Numerical Scalar Field Solver 160
5.6 Fifth Force Contributions to the RAR 161
5.7 Scalar Modifications to RAR Observations 166
5.7.1 Scalar Impact on Lensing 167
5.7.2 Scalar Lensing RAR Results 172
5.8 Conclusions 174
Chapter 6 Conclusions 178
Bibliography 184
Appendices 238
Appendix A Metric Components for a Spherical Source 239
A.1 SIS Metric Components 240
A.2 NFW Metric Components 242
Appendix B General Radial Acceleration from Geodesic Equation 245
B.1 Exterior Schwarzschild Metric 248
B.2 Interior SIS Metric 249
B.3 Interior NFW Metric 250
B.4 Comparison of Radial Accelerations 251
Appendix C Lensing in Modified Gravity Theories 253

C.1 Exterior Schwarzschild Metric 253
C.2 Interior SIS Metric 255

List of Figures

1.1 A sketch of the symmetron effective potential, eq. (1.114). When $\rho > \rho_{\rm SSB}$ (red), the potential has a single minimum at $\phi = 0$. When $\rho < \rho_{\rm SSB}$ (blue), the symmetry is spontaneously broken, and the field falls into one of two minima at $\phi = \pm\phi_\infty$, while $\phi = 0$ becomes unstable. 53

1.2 Schematic of weak lensing geometry. A photon travels from a distant source, is deflected by a mass at an impact parameter b, and is observed by a telescope. The deflection angle is $\Delta\theta$. 62

2.1 A flowchart illustrating the pipeline used to estimate the galactic parameters, contained within black boxes, from a single base input parameter. Deterministic relations are shown in green, while empirical scaling relations and their associated intrinsic scatter are blue. The left branch of the flowchart pertains to the dark matter halo, while the right branch pertains to the baryonic disc. 67

3.1 Various panels illustrating the different stages of our numerical procedure, as described throughout section 3.4. All plots are zoomed in to $5R_{\rm disc}$, showing only the disc-dominated central region. Top left: input density profile, for an axisymmetric galaxy with $M_{\rm vir} = 10^{11.5}\,M_\odot$, rescaled by the cosmic mean density. Top right: coordinate grid, showing every *fifth* radial and azimuthal angle gridline. Bottom left, left half: f_R field profile rescaled by the background field value, $|f_{R0}| = 10^{-6.4}$. Bottom left, right half: the curvature-density ratio, eq. (3.3a). Bottom right, left half: symmetron field profile rescaled by its background field value, for the input parameters $M_{\rm sym} = 10^{-4.5}\,M_{\rm pl}$ and $L_{\rm c} = 10^{-1}\,{\rm kpc}$. Bottom right, right half: truncated scalar field profile to illustrate the symmetron screening condition, eq. (3.3b). . . . 98

3.2 Values of the $f(R)$ curvature-density ratio (top left), the $f(R)$ fifth force (top right), the symmetron field (bottom left) and the symmetron fifth force (bottom right), in the plane of the galactic disc, plotted against radial coordinates rescaled by r_s (the radius at which the screening surface meets the disc plane), across a range of theory parameters and galaxy masses. In the $f(R)$ case, $\log(|f_{R0}|) \in [-8, -5]$ and $\log(M_{\rm vir}/M_\odot) \in [10, 13.5]$, both in increments of 0.2. In the symmetron case, $\log(M_{\rm sym}/M_{\rm pl}) \in [-6.5, -3]$, $\log(L_{\rm c}/{\rm kpc}) \in [-3, 3]$ and $\log(M_{\rm vir}/M_\odot) \in [10, 13.5]$, all in increments of 0.5. Profiles are cut off at the extent of the galaxy, $2.2r_{\rm vir}$. Dashed vertical lines represent the location of the screening radius. Dashed horizontal lines correspond to the screening condition threshold. Purple lines on the symmetron plot indicate solutions that evade the fully unscreened central scalar field definition but are properly considered fully unscreened by the central Laplacian definition. 105

3.3 Screening surfaces across a range of theory parameters, in a galaxy with mass $M_{\rm vir} = 10^{11.5}\,M_\odot$, for $f(R)$ (top) and symmetron (bottom) models. In the symmetron case, we vary $M_{\rm sym}$ holding $L_{\rm c}$ fixed (bottom left) and vary $L_{\rm c}$ holding $M_{\rm sym}$ fixed (bottom right). Sky blue dashed lines are the calculated screening surfaces with theory parameters labelled. Grey dashed-dotted lines are approximate solutions: numerically integrating the critical potential (1.89) in the $f(R)$ case; isodensity contours equal to $\rho_{\rm SSB}$ in the symmetron case. In each case, the right-hand semi-circle plots the radial range of the galaxy out to $10\,r_{\rm NFW}$ (approximately 150 kpc), while the left-hand semi-circle zooms into the central region, out to $5R_{\rm disc}$ (approximately 8 kpc). The coloured background regions represent the adopted matter density profile, plotted as a fraction of the cosmic mean density. 107

3.4 Fraction of disc mass (left) and dark matter (right) screened, for a range of $f(R)$ (top) and symmetron parameters, with fixed $L_{\rm c} = 10^{-1}$ kpc (middle) and with fixed $M_{\rm sym} = 10^{-4.5}\,M_{\rm pl}$ (bottom). Sky blue dashed contours show where 50% of mass is screened. Grey dashed-dotted contours indicate where 50% of mass is screened when r_s is approximated: by numerically integrating eq. (1.89) for the $f(R)$ critical potential, or by finding isodensity contours equal to $\rho_{\rm SSB}$ for the symmetron model. Grey dotted lines correspond to the binary screening condition; solutions below this line would be considered 'fully screened'. Solid white lines separate the fully unscreened and partially screened solutions. 111

3.5 Positions where non-spherical screening surface intersects the disc plane of a Milky Way-like galaxy over $f(R)$ (top) and symmetron (bottom) parameter space. In the $f(R)$ plot, the dashed line shows the true r_s value, whereas the dashed-dotted line shows the approximate r_s values, derived by numerically integrating eq. (1.89) for the $f(R)$ critical potential. In the symmetron plots, the colourmap shows the true r_s value, the dashed line indicates where r_s is equal to the Milky Way centre-Solar System separation of 8 kpc, and the dashed-dotted line shows where the approximate r_s, derived by finding isodensity contours equal to $\rho_{\rm SSB}$, is equal to the Milky Way centre-Solar System separation. Dotted lines indicate the binary screening condition. In the symmetron plot, a solid white line separates the fully unscreened and partially screened solutions, and the white region shows where SSB does not occur, i.e. the cosmic background density, $\bar{\rho}$, is greater than $\rho_{\rm SSB}$. 116

4.1 An example solution for a Milky-Way-like galaxy with $M_{\rm vir} = 1.5 \times 10^{12} M_\odot$, and $f_{R0} = -10^{-6}$, plotted to a maximum radius of 10 kpc. Top left shows the field solution obtained from the numerical solver. Top right is the Compton wavelength, eq. (4.17). Bottom left shows the screened field value, eq. (4.1). Bottom right is the galactic density profile. This example illustrates a partially screened case, where the scalar field (and Compton wavelength) change dramatically at the screening surface, which is located within the stellar disc. . . 132

4.2 Comparison between average stellar separation (purple) and Compton wavelength (orange) as a function of galactocentric radius, in a Milky-Way-like galaxy with $M_{\rm vir} = 1.5 \times 10^{12} M_\odot$ and $f_{R0} = -10^{-6}$. Two curves are shown for the Compton wavelength: the numerical solution extracted from our solver (solid) and the analytic solution in the screened regime (eq. (4.1); dashed). The curve representing the stellar separation has been truncated at the point where the stellar density is subdominant to the cosmic mean density. The figure shows that the Compton wavelength is orders of magnitude smaller(larger) than the stellar separation in the screened(unscreened) regime. 133

4.3 Proportion (in percent) of the stellar mass within the region where the Compton wavelength (calculated numerically, assuming a smooth stellar profile) is larger than the stellar separation, across a range of f_{R0} and $M_{\rm vir}$ values. The top-left white region corresponds to fully unscreened solutions. This figure shows that the majority of galaxies that are not fully screened have stellar profiles with separations less than the Compton wavelength. 134

4.4 Comparisons of the screening radius assuming no stellar contribution to the galactic density ($r_s^{\rm DM}$) and assuming a smooth stellar density profile ($r_s^{\rm DM+SD}$). Left shows the absolute distance between the two r_s solutions, and right shows the ratio between them. In both cases, the upper-left white region corresponds to fully unscreened solutions. In the lower-right regions, the screening radii are larger than the extent of the stellar profile and thus are unchanged by ignoring the stellar contribution. In the right plot these correspond to ratios of 1, in the left we have masked these values. Assuming no stellar contribution has the largest impact on solutions where the screening radius is within the stellar disc, corresponding to the thin diagonal highlighted in the left plot, or the ratios with a value less than one in the right plot. 137

5.1 RAR of a statistical sample of 1000 galaxies, using the SIS (top) and NFW (bottom) models, plotted on top of the kinematic (SPARC) and lensing (Mistele) data points. Each green data point represents the mean acceleration values ($\pm 1\sigma$), evaluated at the corresponding $g_{\rm bar}$. In the data points from Mistele et al. (2024b) the error bars represent the 1σ statistical uncertainty on the mean in each bin; the yellow band represents the systematic uncertainties from interpolating between bins; and the grey band represents the additional systematic uncertainties from stellar mass estimates. The reduced chi-squared values in the legend represent the goodness of fit for each model to the lensing data points. 158

5.2 Scalar field profiles for a statistical sample of 1000 NFW galaxies, for the symmetron parameters $M_{\rm sym} = 10^{-3.5}\, M_{\rm pl}$ and $L_{\rm c} = 10^2\,\text{Mpc}$. Each line represents the scalar field value as a function of radius (left) and $g_{\rm bar}$ (right), illustrating the variation in field strength across different galaxies. 162

5.3 RAR of a statistical sample of 1000 galaxies, using the SIS (top) and NFW (bottom) models, plotted on top of the kinematic (SPARC) and lensing (Mistele) data points. Each pink data point represents the mean fifth force acceleration, eq. (B.24), evaluated at the corresponding $g_{\rm bar}$, for symmetron parameters $M_{\rm sym} = 10^{-3.5}\, M_{\rm pl}$, $L_{\rm c} = 10^2\,\text{Mpc}$, and $\phi_{\rm vev} = 2 \times 10^{-7}$. Other data points are explained in figure 5.1. 165

5.4 RAR of a statistical sample of 1000 galaxies, using the SIS (top) and NFW (bottom) models, plotted on top of the kinematic (SPARC) and lensing (Mistele) data points. Each red data point represents the mean fixed photon mass acceleration values ($\pm 1\sigma$), evaluated at the corresponding $g_{\rm bar}$ for symmetron parameters $M_{\rm sym} = 10^{-3.5}\, M_{\rm pl}$, $L_{\rm c} = 10^2\,\text{Mpc}$, and $\delta A = 0.1$, with a photon mass $m_\gamma = 0.2\,\text{eV}$. Other data points are explained in figure 5.1. Note, parameters are not necessarily best-fit parameters, but chosen to show the effects of the model. 175

5.5 RAR of a statistical sample of 1000 galaxies, using the SIS (top) and NFW (bottom) models, plotted on top of the kinematic (SPARC) and lensing (Mistele) data points. Each blue data point represents the mean fixed photon mass acceleration values ($\pm 1\sigma$), evaluated at the corresponding g_{bar} for symmetron parameters $M_{\mathrm{sym}} = 10^{-3.5}\, M_{\mathrm{pl}}$, $L_{\mathrm{c}} = 10^{2}\,\mathrm{Mpc}$. Here the photon mass is scalar dependent, with a vacuum expectation value given by $m_{\gamma} = M_{\mathrm{pl}}\phi_{\mathrm{vev}} = 2 \times 10^{-3}\,\mathrm{eV}$. Other data points are explained in figure 5.1. Note, parameters are not necessarily best-fit parameters, but chosen to show the effects of the model. 176

Abbreviations

ΛCDM Lambda Cold Dark Matter.

BAO Baryon Acoustic Oscillations.

BTFR Baryonic Tully-Fisher Relation.

CDR Central Density Relation.

CMB Cosmic Microwave Background.

DM Dark Matter.

EoM Equation of Motion.

ESD Excess Surface Density.

GR General Relativity.

KiDS Kilo-Degree Survey.

MCMC Markov Chain Monte Carlo.

MG Modified Gravity.

NFW Navarro–Frenk–White.

RAR Radial Acceleration Relation.

SHMR Stellar-Halo Mass Relation.

SIS Singular Isothermal Sphere.

SMF Stellar Mass Function.

SPARC Spitzer Photometry and Accurate Rotation Curves.

SSB Spontaneous Symmetry Breaking.

Conventions

Throughout this thesis we adopt several conventions, listed here for convenience. We work in natural units where $\hbar = c = 1$, except in chapter 4 where we work in reduced Planck units such that $8\pi G = \hbar = c = 1$. We adopt the mostly-positive metric signature $(-,+,+,+)$. Greek indices run over spacetime coordinates $(0,1,2,3)$, and we use the Einstein summation convention, where repeated indices are summed over. Vectors are denoted in bold (e.g. $\boldsymbol{r}$) and their magnitude by non-bold symbols (e.g. $r = |\boldsymbol{r}|$). Throughout this text $\ln(x) = \log_{\mathrm{e}}(x)$ is the natural logarithm, and $\log(x) = \log_{10}(x)$ denotes the base-10 logarithm. The scalar field ϕ is dimensionless, and φ is the scalar field normalised to its background vacuum value, $\varphi = \phi/\phi_{\mathrm{vev}}$. In relation to galactic masses, the capital M represents the total mass, whereas the lowercase $m = m(r)$ is the enclosed mass function. Except where explicitly stated otherwise, we assume cosmological parameters $\Omega_{0,m} = 0.3$, $\Omega_{0,\Lambda} = 0.7$, and $h = 0.7$.

Chapter 1

Introduction

1.1 Cosmological Model

1.1.1 General Relativity

In a now-famed 1675 correspondence between Isaac Newton and Robert Hooke, Newton said "if I have seen further, it is by standing on the shoulders of giants". This sentiment was equally applicable almost a quarter-millennia later, when Einstein released his theory of General Relativity (GR). The theory was a culmination of centuries of work in physics, mathematics, and philosophy, and has since become the cornerstone of modern cosmology.

Newtonian Gravity

Before venturing into GR, it is beneficial to review Newtonian gravitational physics, particularly from a field theory perspective. A particle of mass m in a gravitational potential field, $\Phi(\boldsymbol{r}, t)$, experiences a force

$$\boldsymbol{F} = -m\boldsymbol{\nabla}\Phi\,. \tag{1.1}$$

The form of the gravitational field is determined by the nearby mass distribution, $\rho(\boldsymbol{r}, t)$. For a static source with density $\rho(\boldsymbol{r})$, this relationship

between the field and the matter is in the form of the Poisson equation,

$$\nabla^2\Phi = 4\pi G\rho(\boldsymbol{r})\,, \tag{1.2}$$

where G is Newton's gravitational constant.

This can be easily recast into a more familiar form by considering a point mass, M, at the origin, i.e. $\rho(\boldsymbol{r}) = M\delta(\boldsymbol{r})$. Solving the Poisson equation in this case yields

$$\Phi_N(\boldsymbol{r}) = -\frac{GM}{r}\,, \tag{1.3}$$

where Φ_N is the usual Newtonian gravitational potential for a point mass. Substituting this into eq. (1.1) yields the inverse square law of gravitation,

$$\boldsymbol{F} = -\frac{GMm}{r^2}\hat{\boldsymbol{r}}\,. \tag{1.4}$$

Steps Towards General Relativity

This picture works well when describing static (or approximately static) matter sources. However, there is no reason to assume the Poisson equation, eq. (1.2), is valid for time-varying sources. Furthermore, assuming it does hold means any change in ρ instantly alters the value of Φ across all of space. This represents a non-local theory that violates causality — something Einstein was inherently interested in addressing, having published his theory of Special Relativity (Einstein, 1905).

In an effort to resolve this with his theory of General Relativity (Einstein, 1916), Einstein carefully considered the Equivalence Principle. In Newtonian gravity, the motion of a particle is determined through Newton's law of gravitation, eq. (1.4), and Newton's second law, $F = ma$. This results in the acceleration of a particle in a gravitational field being independent of its mass, i.e. all particles fall at the same rate in a gravitational field. This occurs because the inertial mass, m_i, and gravitational mass, m_g, are equal, i.e. $m_i = m_g = m$. However, there is no fundamental rea-

son why this should hold in Newtonian gravity; it is simply an empirical observation.

Einstein elevated this to a fundamental principle, the "equivalence principle", and built his theory of gravity around it. The same mass both causes and responds to gravity. As the famous rhetoric coined by John Wheeler goes: "Space tells matter how to move; Matter tells space how to curve" (Misner et al., 1973). This is the essence of GR, and is perfectly encapsulated in Einstein's field equations,

$$G_{\mu\nu} = 8\pi G T_{\mu\nu} \,. \tag{1.5}$$

Here $G_{\mu\nu}$ is the Einstein tensor, which encodes the curvature of spacetime, and $T_{\mu\nu}$ is the stress-energy tensor, which describes the distribution of matter and energy in spacetime. This equation can be considered a generalised version of the Poisson equation, eq. (1.2), now with time-dependence necessarily baked into the theory.

The Einstein field equations constitute a set of 16 component equations describing the motion of particles in our Universe. However, the tensors on each side are symmetric, i.e. $G_{\mu\nu} = G_{\nu\mu}$ and likewise for $T_{\mu\nu}$. This reduces the number of independent equations to 10. A full derivation of eq. (1.5) falls outside the remit of this introduction, but excellent derivations can be found in many textbooks, e.g. Wald (1984) and Carroll (2004). Instead, we will provide an overview of this equation and how it impacts our understanding of gravity.

How Geometry Tells Matter to Move

In GR, particles traverse along geodesics of spacetime, described by the geodesic equation

$$\frac{\mathrm{d}^2 x^\mu}{\mathrm{d}\tau^2} + \Gamma^\mu_{\alpha\beta} \frac{\mathrm{d}x^\alpha}{\mathrm{d}\tau} \frac{\mathrm{d}x^\beta}{\mathrm{d}\tau} = 0 \,, \tag{1.6}$$

where x^μ is the spacetime coordinate, τ is the proper time, and $\Gamma^\mu_{\alpha\beta}$ are the Christoffel symbols. In turn, the Christoffel symbols are given by

$$\Gamma^\mu_{\alpha\beta} = \frac{1}{2} g^{\mu\nu} \left(\partial_\alpha g_{\nu\beta} + \partial_\beta g_{\nu\alpha} - \partial_\nu g_{\alpha\beta} \right) , \tag{1.7}$$

where $g_{\mu\nu}$ is the metric tensor, and $g^{\mu\nu}$ its inverse, satisfying $g_{\mu\lambda} g^{\lambda\nu} = \delta^\nu_\mu$.

The metric tensor, hereafter referred to as the metric, is the fundamental object in GR, describing the geometric curvature of spacetime. It is symmetric in its indices,[1] i.e. $g_{\mu\nu} = g_{\nu\mu}$, and is used to calculate the line element,

$$\mathrm{d}s^2 = g_{\mu\nu} \mathrm{d}x^\mu \mathrm{d}x^\nu , \tag{1.8}$$

which describes an infinitesimal displacement vector. This displacement vector can be integrated to find the proper time or length between two points in spacetime.

In Minkowski spacetime, the metric is given by $\eta_{\mu\nu} = \mathrm{diag}(-1, 1, 1, 1)$. As such, $\partial_\alpha \eta_{\mu\nu} = 0$, and thus $\Gamma^\mu_{\alpha\beta} = 0$, resulting in trajectories that are straight lines. This spacetime is considered 'flat', and is the implicit backdrop for special relativity. In GR, the metric components are a function of the spacetime coordinates, and the Christoffel symbols are non-zero, resulting in curved trajectories.

With an understanding of geodesics and metrics, we are able to fully describe the left-hand side of Einstein's field equations, eq. (1.5). The Einstein tensor,

$$G_{\mu\nu} = R_{\mu\nu} - \frac{1}{2} g_{\mu\nu} R , \tag{1.9}$$

is a combination of the Ricci tensor, $R_{\mu\nu}$, and the Ricci scalar, R. The Ricci scalar is a contraction of the Ricci tensor, with the metric,

$$R = g^{\mu\nu} R_{\mu\nu} , \tag{1.10}$$

while the Ricci tensor is a contraction of the Riemann curvature tensor,

[1] This is a requirement in GR, ensuring the distance between two nearby points is the same irrespective of the direction measured.

$R^{\lambda}_{\sigma\mu\nu}$,

$$R_{\mu\nu} = R^{\lambda}_{\mu\lambda\nu}\,. \tag{1.11}$$

The Riemann tensor is itself built from first and second derivatives of the metric,

$$R^{\lambda}_{\sigma\mu\nu} = \partial_\mu \Gamma^{\lambda}_{\nu\sigma} - \partial_\nu \Gamma^{\lambda}_{\mu\sigma} + \Gamma^{\lambda}_{\mu\alpha}\Gamma^{\alpha}_{\nu\sigma} - \Gamma^{\lambda}_{\nu\alpha}\Gamma^{\alpha}_{\mu\sigma}\,. \tag{1.12}$$

From symmetries embedded in the Riemann tensor, one can derive the Bianchi identity

$$\nabla_\gamma R^{\lambda}_{\mu\nu\sigma} + \nabla_\nu R^{\lambda}_{\mu\sigma\gamma} + \nabla_\sigma R^{\lambda}_{\mu\gamma\nu} = 0\,. \tag{1.13}$$

This ultimately leads to the identity

$$\nabla^\mu G_{\mu\nu} = 0\,. \tag{1.14}$$

This identity is a powerful tool in GR. It is a geometric identity, holding true regardless of the form of the metric, that reduces the number of independent equations in the Einstein field equations from ten to six. However, the metric tensor $g_{\mu\nu}$ itself contains ten independent components, meaning the Einstein field equations alone do not fully fix the metric. The remaining four degrees of freedom reflect the coordinate invariance of general relativity: for any metric $g_{\mu\nu}$ that solves Einstein's field equations, eq. (1.5), one can perform an arbitrary coordinate transformation $x^\mu \to x'^\mu$ and the transformed metric $g'_{\mu\nu}$ will also satisfy the field equations.

How Matter Tells Spacetime to Curve

The right-hand side of eq. (1.5) is the energy-momentum tensor, $T_{\mu\nu}$, which describes the distribution of mass and energy in spacetime. It is a symmetric tensor, and its components describe the energy density, momentum density, and stress in the system. For a perfect fluid, the energy-momentum tensor is given by

$$T_{\mu\nu} = (\rho + p)u_\mu u_\nu + p g_{\mu\nu}\,, \tag{1.15}$$

where ρ is the (rest frame) energy density, p is the (rest frame) pressure, and $u_\mu = dx_\mu/d\tau$ is the four-velocity of the fluid. It is evident that this represents the source term in our equations, describing the contents of our spacetime, whereas the Einstein tensor is the curvature term, describing the resulting geometry of spacetime. For a given energy-momentum tensor, the Einstein field equations can be solved to find the metric, and thus the geometry of spacetime.[2]

Given the geometric identity in eq. (1.14), we find that the energy-momentum tensor is covariantly conserved, i.e.

$$\nabla^\mu T_{\mu\nu} = 0\,. \tag{1.16}$$

This conservation law represents the local conservation of energy and momentum in spacetime, and it is a key feature of GR. In section 1.3.1 we will show that this conservation law is violated in scalar-tensor theories of gravity.

Action Formulation of General Relativity

It will prove to be useful to also describe GR using action principles. The Einstein-Hilbert action represents the simplest[3] action that can be formulated for GR. It is given by

$$S_{\rm EH} = \frac{1}{16\pi G}\int \mathrm{d}^4x\sqrt{-g}R + S_{\rm m}[g_{\mu\nu},\psi_i]\,, \tag{1.17}$$

where g is the determinant of the metric, and $S_{\rm m}$ is the matter action for the Standard Model matter fields ψ_i. Varying this action with respect to the metric yields the Einstein field equations, eq. (1.5). Additionally,

[2] In appendix A, we follow this methodology to determine the metrics of commonly used dark matter density profiles.

[3] The term "simplest" here refers to the fact that R is the only curvature invariant that leads to field equations containing no more than second derivatives of the metric. Higher-order curvature invariants (such as R^2 or $R_{\mu\nu}R^{\mu\nu}$) generally lead to fourth-order field equations or introduce instability ghosts, while other low-order terms typically reduce to total derivatives that do not affect the equations of motion.

variation of the matter action produces the stress-energy tensor

$$T_{\mu\nu} = -\frac{2}{\sqrt{-g}}\frac{\delta S_{\mathrm{m}}}{\delta g^{\mu\nu}}\,. \tag{1.18}$$

1.1.2 The Standard Model of Cosmology

Early prescriptions of the universe were largely philosophical, with ideas ranging from a static, eternal universe to a cyclic universe. The first scientific model of the universe was proposed by Einstein in 1917 (Einstein, 1917), shortly after the publication of his theory of GR. Einstein applied his field equations, eq. (1.5), to the entire universe, assuming it was *homogeneous* and *isotropic* on large scales. However, this led to a problem: a universe filled with matter would inevitably collapse under its own gravity. Einstein's original solution was to modify his equations to allow for a static universe. This idea was soon superseded by new theoretical work and observational evidence, which instead showed the universe is expanding. Emerging from this work is the current standard model of cosmology, known as the Lambda Cold Dark Matter (ΛCDM) model. This model describes a universe that is homogeneous and isotropic on large scales, expanding, composed of ordinary matter, and two mysterious components: dark matter, and dark energy, which we will explain in the proceeding sections.

The Expanding Universe

In the early 20th century, the prevailing view of the universe was that it was static and unchanging. This view was shattered by Edwin Hubble in 1929, who discovered that galaxies were receding from us, and that the further away they were, the faster they were receding (Hubble, 1929). This observation, now referred to as Hubble's law, provided the first piece of evidence for the expanding universe and would form the foundation of modern cosmology and the ΛCDM model.

These observations were made possible by measurements of redshift, z. The redshift is a measure of the change in wavelength of light emitted from a source as it travels through space, and is given by

$$1 + z = \frac{\lambda_{\rm obs}}{\lambda_{\rm em}}\,, \tag{1.19}$$

where $\lambda_{\rm obs}$ is the observed wavelength, and $\lambda_{\rm em}$ is the emitted wavelength (in the rest frame), usually determined from the spectral emission lines of the source. Additionally, the redshift tells us about the relative motion of the source and observer, and is related to the velocity of the source, v via the relativistic Doppler effect

$$1 + z = \sqrt{\frac{1 + v/c}{1 - v/c}}\,, \tag{1.20}$$

where c is the speed of light. For small redshifts, $z \ll 1$, this relation becomes the rather simple $z \approx v/c$. An object moving away from us will have a positive redshift, whereas an object moving towards us will have a negative redshift, causing it to appear more blue.

Hubble found a linear relation between the redshift and the distance to the source, d, which he interpreted as a linear relation between the distance and the recessional velocity, v of the source. This is known as Hubble's law, and is given by

$$v = H_0 d\,, \tag{1.21}$$

where H_0 is the Hubble constant. Admittedly, Hubble's original work underestimated the distances to nearby galaxies, resulting in a value of $H_0 \approx 500\,\mathrm{km/s/Mpc}$, substantially larger than the currently (somewhat) accepted value of $H_0 \approx 70\,\mathrm{km/s/Mpc}$.

Prior to Hubble's discovery, there was a body of theoretical work on the expanding universe, including the work of Alexander Friedmann, Georges Lemaître, Howard Robertson and Arthur Walker (Friedmann, 1922, 1924; Lemaître, 1931, 1933; Robertson, 1935, 1936a,b; Walker, 1937). These

authors developed (and found solutions for) the FLRW metric,

$$\mathrm{d}s^2 = -\mathrm{d}t^2 + a(t)^2 \left[\mathrm{d}x^2 + \mathrm{d}y^2 + \mathrm{d}z^2\right] , \tag{1.22}$$

which describes a homogeneous and isotropic universe that is expanding or contracting over time. Here the expansion of the Universe is realised via the scale factor, $a(t)$.

The scale factor expresses the expansion of the universe as a function of time; normalised to $a(t_0) = 1$ at the present time, t_0, with $a(t < t_0) < 1$ and $a(t > t_0) > 1$. Explicitly put, a physical distance D measured at the present time will become $Da(t)$ at some time t. Additionally, photons emitted from distant sources at time t_{em} will traverse through this expanding spacetime, causing their wavelengths to be stretched, resulting in a redshift given by

$$1 + z = \frac{a(t_0)}{a(t_{em})} , \tag{1.23}$$

assuming the likely scenario the observer is a modern-day human.

The form of the spatial part of the FLRW metric presented here assumes that the universe is spatially flat, obeying Euclidean geometry. The FLRW metric can be generalised to include curvature, k — with $k = 0$ for a flat universe, $k = 1$ for a closed universe, and $k = -1$ for an open universe. In general, the form of the spatial coordinates is given by[4]

$$\mathrm{d}\boldsymbol{r}^2 = \frac{\mathrm{d}r^2}{1 - kr^2} + r^2 \mathrm{d}\Omega^2 , \tag{1.24}$$

where $\mathrm{d}\Omega^2 \equiv \mathrm{d}\theta^2 + \sin^2\theta \mathrm{d}\phi^2$ contains the angular components. Contemporary cosmological measurements suggest that the universe is (at least effectively) spatially flat (Planck Collaboration et al., 2020). As such, we will continue with the flat FLRW metric, eq. (1.22), for the remainder of this thesis.

[4]The dimensionless constant k can be chosen to take the values $-1, 0, +1$ by rescaling the radial coordinate r by the radius of curvature R_c. Specifically, if the curvature is non-zero, one transforms the physical radial coordinate $\tilde{r}$ via $r = \tilde{r}/R_c$, resulting in a dimensionless r and k.

The spatial coordinates contained within the FLRW metric, eq. (1.22), are comoving coordinates, which are a useful way to describe the expansion of the universe. Comoving coordinates are defined such that they remain constant as the universe expands, i.e. the comoving distance between two objects in space (with no peculiar velocity) remains constant as the universe expands. The comoving separation, x, is related to the physical separation, d, by

$$d = a(t)x\,. \tag{1.25}$$

From this expression, we find the recessional velocity is

$$v = \dot{d} = \dot{a}(t)x = \frac{\dot{a}}{a}d = H(t)d\,, \tag{1.26}$$

where dots represent derivatives with respect to time, and $H(t) = \dot{a}/a$ is the Hubble parameter. The Hubble parameter is a measure of the expansion rate of the universe, and is related to the Hubble constant by $H_0 = H(t_0)$. Evaluating eq. (1.26) at the present time, t_0, we rederive Hubble's law, eq. (1.21).

The mechanism driving the accelerated expansion of the universe is known as dark energy — a mysterious component of the universe that possesses a strong negative pressure, generating a repulsive gravitational effect. The simplest form of this dark energy is the cosmological constant (the Λ component of ΛCDM). Λ arises naturally in GR as an integration constant in the Einstein field equations,[5]

$$G_{\mu\nu} + \Lambda g_{\mu\nu} = 8\pi G T_{\mu\nu}\,, \tag{1.27}$$

or equivalently in the Einstein-Hilbert action, eq. (1.17), as an additional term

$$S_{\rm EH} = \frac{1}{16\pi G}\int \mathrm{d}^4x\sqrt{-g}\,(R - 2\Lambda) + S_{\rm m}[g_{\mu\nu}, \psi_i]\,. \tag{1.28}$$

[5]Einstein originally formulated his equations without this term, but found they predicted a collapsing universe. To force a static solution, which was the prevailing belief at the time, he introduced a non-zero Λ to carefully counteract gravitational collapse. He later considered this his "biggest blunder" when observations confirmed the universe was, in fact, expanding.

However it is typical to absorb the contribution into the energy-momentum tensor, $T_{\mu\nu}$, as a perfect fluid with equation of state $p_\Lambda = -\rho_\Lambda$. This approach allows us to treat the cosmological constant as a form of energy density in the universe — hence the general term "dark energy".

In the context of energy density, the cosmological constant could theoretically be explained as arising from the vacuum energy arising from quantum fluctuations of particle fields in empty spacetime. However, calculating this vacuum energy yields a value roughly 120 orders of magnitude higher than the observed value of the cosmological constant. This discrepancy is known as the "cosmological constant problem", and represents one of the major unsolved problems in modern physics (Weinberg, 1989; Carroll, 2001).

Dynamics of the Universe

The cosmological constant is not the only form of energy density in the universe. The universe is also filled with matter and radiation. These components are best described by a perfect fluid with equation of state

$$p = w\rho, \tag{1.29}$$

where w is the equation of state parameter. For non-relativistic matter $w = 0$, for radiation (and relativistic particles) $w = 1/3$, and for the cosmological constant $w = -1$, as stated earlier. The total energy density in the universe can be written as

$$\rho = \rho_m + \rho_r + \rho_\Lambda \,, \tag{1.30}$$

where ρ_m is the matter density, ρ_r is the radiation density, and ρ_Λ is the cosmological constant density.

Considering the FLRW metric as a solution to the Einstein field equations, eq. (1.5), we can derive the Einstein tensor components. For the

FLRW metric, the only non-zero components are

$$G_{00} = 3\left(\frac{\dot{a}}{a}\right)^2 \quad \text{and} \quad G_{ii} = -\left(2\ddot{a}a + \dot{a}^2\right) . \tag{1.31}$$

The corresponding energy-momentum tensor components are

$$T_{00} = \rho \quad \text{and} \quad T_{ii} = a^2 p \, . \tag{1.32}$$

From this, we arrive at two of the most useful and influential equations in cosmology: the Friedmann equation (Friedmann, 1922, 1924),

$$H^2 = \frac{8\pi G}{3}\rho \, , \tag{1.33}$$

and the continuity equation

$$\dot{\rho} + 3H(\rho + p) = 0 \, . \tag{1.34}$$

The continuity equation describes how the energy density evolves over time, depending on the type of energy and its equation of state defined in eq. (1.29). Meanwhile, the Friedmann equation describes how the expansion of the universe is related to the energy density.

There also exists a second Friedmann equation, often referred to as the acceleration equation, which comes from combining the Friedmann and continuity equations.

$$\ddot{a} = -\frac{4\pi G}{3}\left(\rho + 3p\right) a \, . \tag{1.35}$$

The acceleration equation (perhaps unsurprisingly) describes the acceleration of the universe in terms of the energy density and pressure. From this equation we see that if $\rho + 3p < 0$, then $\ddot{a} > 0$, and the universe is accelerating. This is the case for the cosmological constant, which has $p = -\rho_\Lambda$. For matter and radiation, $\rho + 3p > 0$, and the universe is decelerating.

In a universe comprising (or dominated by) a single one of the energy density components, it is possible to determine how the density and scale factor evolve over time. In a non-relativistic matter dominated universe

with $w = 0$,

$$\rho_m \propto a^{-3} \quad \text{and} \quad a \propto t^{2/3} \,. \tag{1.36}$$

In a radiation dominated universe with $w = 1/3$,

$$\rho_r \propto a^{-4} \quad \text{and} \quad a \propto t^{1/2} \,. \tag{1.37}$$

And lastly, in a cosmological constant dominated universe with $w = -1$,

$$\rho_\Lambda \propto \text{constant} \quad \text{and} \quad a \propto \mathrm{e}^{H_0 t} \,. \tag{1.38}$$

For our universe with multiple components, it is convenient to express the energy density in terms of the critical density, ρ_c, which is the energy density required for a flat ($k = 0$) universe, given by

$$\rho_c = \frac{3H^2}{8\pi G} \,. \tag{1.39}$$

The critical density is a useful quantity, as it allows us to express the energy density in terms of the density parameters, Ω_i, which are defined as

$$\Omega_i = \frac{\rho_i}{\rho_c} \,. \tag{1.40}$$

The density parameters are dimensionless quantities that describe the contribution of each component to the total energy density of the universe. The total density parameter is given by $\Omega = \sum_i \Omega_i$, and should equal unity for a flat universe. With this reparametrisation the Friedmann equation, eq. (1.33), can be rewritten as

$$H^2 = H_0^2 \left(\Omega_{0,r} a^{-4} + \Omega_{0,m} a^{-3} + \Omega_{0,\Lambda} \right) \,, \tag{1.41}$$

where 0 subscripts denote present day values. From this representation of the Friedmann equation we see that at early times, $a \ll 1$, the radiation component dominates, followed by the matter. But eventually the cosmological constant will dominate, and the universe will enter an accelerated expansion phase. This is the current state of the universe.

The Hot Big Bang

One interesting prediction of the expanding universe model described thus far is the existence of a hot, dense early universe. Reversing the expansion of the universe back in time, we find that the universe was once much smaller and denser than it is today. This leads to the prediction of a 'Big Bang singularity' where the density and temperature of the universe become infinite. While this singularity is likely an artefact of our classical description of gravity breaking down at high energies, the surrounding theory suggesting that the early universe was once a hot, dense plasma of particles and radiation is supported by our observations. This understanding has come to be known as the "Big Bang Model".

In this picture, the Universe began in a hot, dense state approximately 13.8 billion years ago, and has been expanding and cooling ever since. As the universe expanded, it underwent a series of phase transitions, leading to the formation of the first atoms, stars, and galaxies. The Big Bang model is supported by a wealth of observational evidence, including the relative abundance of light elements such as hydrogen and helium, the large-scale structure of the universe, and the cosmic microwave background radiation.

The first stage of the Universe is thought to have been a period of rapid expansion known as inflation, which occurred within the first fraction of a second after the Big Bang. During this period, the universe expanded exponentially, smoothing out any initial inhomogeneities. The details of this process are beyond the scope of this thesis and are omitted for brevity, but inflation itself is an extremely interesting and active area of research. For an extensive overview see e.g. Liddle and Lyth (2000); Lyth and Liddle (2009); Baumann (2022). What is key for us is that inflation provides a mechanism to explain the observed homogeneity and isotropy of the universe on large scales, as well as the nearly scale-invariant spectrum of primordial density perturbations that seeded the formation of galaxies and large-scale structure. These perturbations are thought to have arisen from quantum

fluctuations during inflation, which were stretched to macroscopic scales by the rapid expansion of the universe.

The most compelling evidence for the Big Bang model comes from the discovery of the Cosmic Microwave Background (CMB) by Penzias and Wilson (1965). The CMB is a nearly uniform background of microwave radiation that fills the universe, representing the remnant of the hot, dense plasma that existed in the early universe. It results from the universe cooling sufficiently for protons and electrons to combine and form neutral hydrogen atoms, allowing photons to travel freely through space. This event, known as recombination,[6] occurred approximately 380,000 years after the Big Bang, at a redshift of $z = 1100$, when the universe had cooled to a temperature of around 3000 K. Since the universe has expanded significantly since then, the CMB photons have been redshifted into the microwave frequency band.

This nearly uniform background of microwave radiation exhibits remarkable homogeneity and isotropy, with a blackbody spectrum at approximately 2.7 K and temperature fluctuations no larger than $\Delta T/T \sim 10^{-5}$ (once the dipole anisotropy due to the Earth's motion is subtracted). These small perturbations encode the initial conditions for structure formation, providing a wealth of information about the early universe and the density fluctuations that eventually led to the formation of galaxies and large-scale structure. The CMB has been measured with incredible precision by a series of experiments, including COBE (Smoot et al., 1992), WMAP (Bennett et al., 2013), and Planck (Planck Collaboration et al., 2020). These measurements deliver increasingly stringent constraints on cosmological parameters. In terms of our density parameters defined earlier, eq. (1.40), Planck Collaboration et al. (2020) find $\Omega_{0,m} \approx 0.31$, $\Omega_{0,r} \approx 9 \times 10^{-5}$, and $\Omega_{0,\Lambda} \approx 0.69$. Of the matter component, only roughly 15% is thought to be ordinary (baryonic) matter, with the remaining 85% being dark matter.

[6]The name recombination is misleading, since the protons and electrons had not previously combined before this point, yet the name has stuck for historical reasons.

Dark Matter

Up to this point we have neglected to mention the CDM component of ΛCDM. CDM refers to Cold Dark Matter, a hypothetical form of matter that does not interact electromagnetically and thus cannot be observed directly. Not much is known of the exact form of Dark Matter (DM), but it is cosmologically consistent with a perfect fluid with negligible pressure (Blumenthal et al., 1984), hence the term 'cold'. The existence of dark matter is inferred from its gravitational effects on visible matter, such as the rotation curves of galaxies (Kapteyn, 1922; Oort, 1932; Babcock, 1939; Bosma, 1981; Rubin, 1983), mass measurements of galaxies through gravitation lensing (Abbott et al., 2018), and the large-scale structure of the universe (Tegmark et al., 2004).

Dark matter plays a crucial role in the formation of our present-day Universe. Without its presence, the formation of galaxies and large-scale structure would be difficult to explain. Dark matter provides the gravitational wells into which ordinary matter falls, leading to the formation of galaxies and clusters of galaxies. The presence of dark matter is also necessary to explain the observed anisotropies in the CMB, as it affects the growth of density fluctuations in the early universe. Indeed, cross-correlating the CMB with large-scale structure surveys reveals a strong correlation (Boughn and Crittenden, 2004; Giannantonio et al., 2008), providing direct evidence for the connection between primordial fluctuations and present-day cosmic structure.

Structure Formation in ΛCDM

In the present day, the Universe retains its homogeneous and isotropic properties, but only on the largest scales ($\gtrsim$ 100 Mpc). On smaller scales, we observe an intricate cosmic web of overdense nodes connected by filaments and walls, interspersed with underdense voids. This rich structure, clearly

visible in modern galaxy surveys and simulations, contrasts sharply with the smooth appearance of the cosmic microwave background, yet both can be understood within the framework of linear perturbation theory applied to small primordial fluctuations against a homogeneous background.[7]

To quantify the primordial fluctuations found in the early universe, we define the density contrast as

$$\delta(\boldsymbol{x}, t) = \frac{\rho_m(\boldsymbol{x}, t) - \bar{\rho}_m(t)}{\bar{\rho}_m(t)}\,, \tag{1.42}$$

where $\rho_m(\boldsymbol{x}, t)$ is the local matter density at position $\boldsymbol{x}$ and time t, and $\bar{\rho}_m(t)$ is the background (average) matter density. Regions with $\delta > 0$ are overdense, whilst regions with $\delta < 0$ are underdense. In the early universe, these density fluctuations were extremely small, with $|\delta| \ll 1$, allowing them to be treated using linear perturbation theory.

The statistical properties of these density fluctuations are characterised by the matter power spectrum, $P(k)$, which describes the variance of density fluctuations as a function of spatial scale. The power spectrum is defined through the Fourier transform of the density field:

$$\langle \tilde{\delta}(\boldsymbol{k}) \tilde{\delta}^*(\boldsymbol{k}') \rangle = (2\pi)^3 \delta_D(\boldsymbol{k} - \boldsymbol{k}') P(k)\,, \tag{1.43}$$

where $\tilde{\delta}(\boldsymbol{k})$ is the Fourier transform of the density contrast, δ_D is the Dirac delta function, and the angle brackets denote ensemble averaging. The power spectrum quantifies the amplitude of fluctuations on different scales: large k corresponds to small physical scales x, whilst small k corresponds to large scales, according to the relation $k = 2\pi/x$.

The formation of cosmic structure begins with nearly scale-invariant density perturbations, as predicted by inflationary theory, characterised by a primordial power spectrum $P(k) \propto k^n$ with spectral index $n \approx 0.96$

[7] While linear perturbation theory accurately describes the initial conditions and early growth of these structures, understanding their late-time evolution into the highly non-linear cosmic web observed today requires methods beyond linear theory, such as N-body numerical simulations.

(Planck Collaboration et al., 2020). During the radiation-dominated era, perturbations on scales larger than the horizon grow logarithmically, whilst subhorizon perturbations oscillate and are effectively suppressed. After matter-radiation equality, this suppression ends and perturbations begin to grow on all scales throughout the matter-dominated era.

For baryons, the situation is more complex: prior to recombination, they remain tightly coupled to photons through Thomson scattering and cannot collapse to form structure independently. The acoustic oscillations of this tightly coupled baryon-photon fluid leave characteristic imprints in both the CMB angular power spectrum and the large-scale distribution of galaxies as Baryon Acoustic Oscillations (BAO) (Eisenstein et al., 2005; Percival et al., 2010; Beutler et al., 2011). After recombination, baryons decouple from photons and fall into the pre-existing dark matter gravitational wells that have been growing throughout the matter-dominated era.

Once density perturbations become non-linear ($\delta \sim 1$), linear perturbation theory breaks down and the fluctuations undergo gravitational collapse to form virialised dark matter haloes. This bottom-up structure formation process occurs first at the smallest scales in cold dark matter models, with larger structures forming through the hierarchical merging of smaller haloes. During virialisation, shock-heated gas reaches hydrostatic equilibrium within the dark matter potential well. If this gas can cool efficiently through radiative processes, it collapses further to form dense, star-forming structures at the halo centre[8] — the galaxies that serve as the primary observational tracers of cosmic structure and the focus of gravitational physics tests explored in this thesis.

[8]In the largest haloes ($M \gtrsim 10^{15}\, M_\odot$) the gas cannot efficiently cool to form new stars. In this case, while the halo still hosts a massive population of galaxies (formed in subhaloes prior to accretion), the central hot gas reservoir remains largely diffuse. These structures are known as galaxy clusters.

1.1.3 Beyond ΛCDM

Despite the many successes of the ΛCDM model, several open questions and tensions motivate the exploration of alternative cosmological models. We will broadly outline three categories of issues: the Hubble tension, the lack of dark matter detection, and small-scale structure problems.

The latter of these issues, small-scale structure problems arise from discrepancies between the predictions of ΛCDM simulations and observations of galactic physics on small scales. For instance, Moore et al. (1999b) found that ΛCDM simulations predict a cuspy density profile for dark matter haloes, whereas observations of dwarf galaxies suggest a cored profile. This is known as the core-cusp problem. Additionally, Klypin et al. (1999) and Moore et al. (1999a) found that ΛCDM simulations predict a large number of subhaloes within larger haloes, whereas observations of the Milky Way and other galaxies suggest a much smaller number of satellite galaxies. This is known as the missing satellites problem. This problem is the easiest to pass off as a misunderstanding in other non-ΛCDM related physics, e.g. more accurately simulating the complex baryonic physics occuring in galaxies, that is either not resolved, or not including within the current simulations.

The lack of dark matter detection is self-explanatory. Despite numerous attempts to directly detect dark matter particles through experiments such as LUX (Akerib et al., 2017), XENON1T (Aprile et al., 2018), and PandaX-II (Cui et al., 2017), no conclusive evidence for dark matter has been found. This has led to the exploration of alternative dark matter models, including, but not limited to, self-interacting dark matter, fuzzy dark matter , and axion-like particles (see Spergel and Steinhardt (2000), Hu et al. (2000) and Marsh (2016) for an overview of each respective theory).

Last, but certainly not least, the Hubble tension has emerged as a significant challenge to the ΛCDM model. This tension refers to the discrepancy

between the value of the Hubble constant, H_0, measured from the local universe using Cepheid variables and Type Ia supernovae (Riess et al., 2019, 2021), and the value inferred from the CMB using ΛCDM (Planck Collaboration et al., 2020). The local measurements find $H_0 \approx 74$ km/s/Mpc, whereas the CMB measurements find $H_0 \approx 67$ km/s/Mpc. This discrepancy is currently at the level of $4-6\sigma$, depending on the datasets used, and has led to speculation that new physics beyond ΛCDM may be required to resolve this tension. Researchers working on early universe measurements argue this tension arises from systematics in the local measurements. Meanwhile, those working on local measurements suggest the tension comes from issues with the cosmological model used to extrapolate the early universe Hubble value to the present day. Regardless of which perspective is correct (possibly neither, or a combination of both), this tension has sparked significant interest in the cosmology community, leading to the exploration of a wide range of alternative models. Proposed solutions include early dark energy models (Poulin et al., 2019), modifications to the dark matter sector (Vattis et al., 2019), and interactions between dark matter and dark energy (Kumar et al., 2019; Di Valentino et al., 2020). For a review of efforts to resolve the Hubble tension see Di Valentino et al. (2021); Abdalla et al. (2022).

The likelihood that the universe does not contain a cosmological constant (Λ), but instead a dynamical dark energy component, has gained considerable traction in recent years, especially given recent DESI results (Adame et al., 2025) — who find a 2.6σ preference for dynamical dark energy, when combined with CMB measurements; upgraded to a 3.9σ preference when combined with CMB and supernova measurements. Dynamical dark energy models, which allow for a time-varying equation of state, have been proposed as a means to alleviate the Hubble tension and provide a more flexible framework for understanding cosmic acceleration. Examples of such models include quintessence (Peebles and Ratra, 1988; Caldwell et al., 1998), k-essence (Armendariz-Picon et al., 2001), and phantom en-

ergy (Caldwell, 2002). For an encyclopedic overview of dynamical dark energy models see Copeland et al. (2006). These models typically involve a scalar field that evolves over time, leading to a time-varying equation of state parameter, $w(z)$, where z is the redshift. Observational constraints on these models come from a variety of sources, including supernovae, BAO, CMB, and large-scale structure surveys. Current data suggest that w is close to -1, consistent with a cosmological constant, but there remains room for dynamical dark energy models within the observational uncertainties.

With these unresolved issues in mind, it is clear that there is a need to explore alternative cosmological models that can address these tensions and provide a more complete understanding of the universe. One frequently utilised tool to explore these alternative models is scalar fields. Scalar fields are a natural extension of the Standard Model of particle physics and can be used to model a wide range of phenomena, including dark energy and dark matter. Scalar fields are particularly appealing for cosmological applications, as they can lead to rich phenomenology while remaining relatively simple to implement.

One caveat to their simplicity is that the introduction of a scalar field often necessitates couplings between the scalar field and existing matter fields. In turn, this can lead to fifth forces and violations of the equivalence principle, which are tightly constrained by local tests of gravity. To address these issues, various screening mechanisms have been proposed, which allow scalar fields to have significant effects on cosmological scales while remaining consistent with local tests of gravity. Examples of such mechanisms include chameleon screening (Khoury and Weltman, 2004b) and symmetron screening (Hinterbichler et al., 2011). The impact of these theories, especially on galactic scales, is a key focus of this thesis, and more detail is provided on their implementation in section 1.3.

1.2 Galaxies

Galaxies represent some of the most fundamental structures in the observable universe, serving as both the primary tracers of cosmic evolution and natural laboratories for testing gravitational physics. These gravitationally bound systems of stars, gas, dust, and dark matter range from dwarf galaxies containing millions of stars to massive ellipticals with over a trillion stars and total masses exceeding $10^{13}\,M_\odot$. Most importantly for this thesis, galaxies provide unique opportunities to probe gravitational physics across scales inaccessible to laboratory experiments, potentially revealing new insights into the nature of gravity itself.

In this section, we discuss the historical development of galactic studies, and finally review the modern understanding of galactic structure and dynamics. This background sets the stage for the subsequent chapters, which explore how galaxies can be used to test theories of gravity beyond GR.

1.2.1 Historical Development of Galactic Studies

The systematic understanding of galaxies as fundamental cosmic structures emerged through centuries of observational breakthroughs that transformed our conception of the Universe's scale and structure. Before venturing into the detailed astrophysical properties of galaxies, it is both entertaining and instructive to briefly review the historical observations that established galaxies as distinct entities and laid the groundwork for modern extragalactic astronomy.

Early philosophical speculation about the nature of the Milky Way[9] can be traced to ancient Greece, where Democritus (450–370 BCE) proposed that the bright band across the night sky consisted of distant stars. This contrasted with the popular Aristotelian view that the Milky Way was an

[9]The name "Milky Way Galaxy" is a modern tautology, as the word galaxy itself derives from the ancient Greek name for our own galaxy, *galaxías*, which means "milky".

atmospheric phenomenon. This atmospheric hypothesis was quantitatively disproved by the renowned Arabic astronomer Ibn al-Haytham[10] (965–1040 CE), who noted that the parallax of stars in the Milky Way was much smaller than the lunar parallax, proving the celestial nature of the Milky Way (Eckart, 2018; Eckart and Idriz, 2023). The first empirical evidence supporting the stellar model came in 1610 when Galileo Galilei used his telescope to resolve the Milky Way into "a huge number of faint stars" (Galilei, 1989). This period marked the beginning of telescopic astronomy.

The 18th and 19th centuries witnessed systematic efforts to map galactic structure and identify similar systems beyond our own. William Herschel's ambitious star-counting surveys in 1785 produced the first quantitative model of the Milky Way's shape, though his assumption that the Solar System lay near the galactic centre would later prove incorrect (Herschel, 1785). Meanwhile, observers began cataloguing "nebulous" objects throughout the sky. Charles Messier's catalogue of 110 nebular objects[11] (Messier, 1781) and William Herschel's subsequent catalogue of 5,000 nebulae laid the groundwork for distinguishing between galactic and extragalactic phenomena. These works constitute some of the earliest galactic surveys.

The early 20th century brought revolutionary discoveries that established modern extragalactic astronomy. Edwin Hubble's observations with the 100-inch Hooker Telescope at Mount Wilson in the 1920s definitively resolved the "Great Debate" between Harlow Shapley and Heber Curtis by identifying individual Cepheid variable stars in spiral nebulae, proving these objects were "island universes" far beyond the Milky Way (Hubble, 1925).

[10] Outside of astronomy, Ibn al-Haytham's foundational Book of Optics pioneered the modern scientific method and correctly theorised that vision results from light reflecting off an object and entering the eye. He was justly cited in the work of scholars for centuries, including Roger Bacon, Christiaan Huygens, Issac Newton, Johannes Kepler and Galileo Galilei.

[11] Ironically, Messier was primarily interested in observing comets and kept this now-famed catalogue to help other comet-hunters actively avoid these permanent 'nuisance' objects.

These breakthroughs effectively divided astronomy into galactic and extragalactic subfields, each with distinct methodological approaches. Galactic astronomy focused on detailed studies of stellar populations, kinematics, and structure within the Milky Way, while extragalactic astronomy emerged as a powerful tool for cosmological investigations.

1.2.2 Modern Galactic Astronomy

The mid-20th century saw the development of systematic classification schemes for galaxies, most notably Edwin Hubble's morphological sequence (Hubble, 1926), which organised galaxies into ellipticals, spirals, and irregulars based on their visual appearance. This classification provided a framework for understanding galactic diversity and evolution. Galaxies can be broadly classified into two primary morphological categories. Early-type galaxies (ellipticals and lenticulars) exhibit smooth, featureless light distributions dominated by old stellar populations with minimal star formation. These systems follow well-defined scaling relations between size, luminosity, and velocity dispersion (Faber et al., 1987). Late-type galaxies (spirals and irregulars) display prominent disc structures with spiral arms, central bulges, and active star formation regions.

The advent of large-scale photographic surveys in the mid-20th century, such as the Palomar Observatory Sky Survey (POSS) (Minkowski and Abell, 1963), enabled the discovery of thousands of galaxies, facilitating statistical studies of their properties. The latter half of the 20th century witnessed the rise of multi-wavelength astronomy, with radio, infrared, ultraviolet, and X-ray observations revealing new facets of galactic structure and activity (Condon, 1992; Neugebauer et al., 1984; Code et al., 1970; Giacconi et al., 1962).

The late 20th and early 21st centuries have been defined by the era of large digital sky surveys, which have marked a transformational shift

from individual galaxy studies to statistical analyses of millions of systems. The Sloan Digital Sky Survey (SDSS) (York et al., 2000) has been particularly influential, providing detailed imaging and spectroscopy for millions of galaxies and enabling precise measurements of their redshifts, stellar masses, star formation rates, and internal kinematics. Other major surveys such as the Two-Degree Field Galaxy Redshift Survey (2dFGRS) (Colless et al., 2001) and the Dark Energy Survey (DES) (Abbott et al., 2018) have further expanded our knowledge of galactic populations across cosmic time, whilst the recently launched telescopes JWST (Gardner et al., 2006; Jakobsen et al., 2022) and Euclid (Laureijs et al., 2011; Euclid Collaboration et al., 2025) promise to extend these capabilities further.

Thanks in part to this overwhelming amount of new data, we now have precise measurements of key galactic properties. One of the most fundamental measured parameters is the luminosity — the amount of electromagnetic energy emitted by a galaxy (per unit time). When integrated over all wavelengths, this quantity is referred to as the bolometric luminosity. The distribution of luminosities in a given galaxy population can be well described by a luminosity function. The Schechter function (Schechter, 1976) provides a convenient parametric form for the luminosity function:

$$n(L)\mathrm{d}L = n^* \left(\frac{L}{L^*}\right)^{\alpha} \exp\left(-\frac{L}{L^*}\right) \frac{\mathrm{d}L}{L^*}\,, \tag{1.44}$$

where $n(L)$ is the number density of galaxies with luminosity L within the interval $\mathrm{d}L$. The other parameters are free parameters to be fitted: n^* is a normalisation constant, L^* is the characteristic luminosity at the knee of the function, and α describes the faint-end slope. The faint-end slope, α, is of particular interest as it encodes information about the efficiency of galaxy formation in low-mass dark matter haloes, which is sensitive to feedback processes and the nature of dark matter itself (Benson et al., 2003). The exact values of these fitting parameters depend on the galaxy population, redshift, and wavelength band considered (see e.g. Norberg et al. (2002); Madgwick et al. (2002); Cole et al. (2005)). Overall, the Schechter function

provides excellent agreement with observed luminosity distributions across a wide range of environments (Blanton et al., 2001).

Alongside this wealth of observational data, high-powered modern cosmological simulations within the ΛCDM framework (Navarro et al., 1996; Vogelsberger et al., 2014; Schaye et al., 2015; Pillepich et al., 2018) provide essential theoretical context for interpreting these observations. In particular, they enable direct comparisons between astrophysical predictions and data whilst highlighting areas where our understanding of galactic physics remains incomplete.

From the perspective of testing gravitational physics, galaxies offer several unique advantages. They probe gravitational fields across an enormous dynamic range, from dense central regions where gravitational potential wells are deepest, to diffuse outer regions where potentials are much shallower. This range encompasses the regime where modifications to GR are predicted to become most apparent in many alternative theories of gravity (discussed more in section 1.3). Furthermore, galaxies exist in diverse environments, from isolated systems to dense cluster cores, providing different testing grounds for environmental dependencies of gravitational physics. Their well-understood stellar populations enable precise determinations of baryonic mass distributions, whilst their rotation curves and velocity dispersions directly trace the underlying gravitational potential. Combined with weak gravitational lensing measurements that extend to hundreds of kiloparsecs beyond the visible galaxy (Brouwer et al., 2017), these observations provide comprehensive probes of gravitational physics across vast galactic scales.

Additionally, statistical astronomy has revealed remarkable empirical scaling relations that provide stringent tests of gravitational physics. The Baryonic Tully-Fisher Relation (BTFR) connects galactic baryonic mass to asymptotic rotation velocity across four orders of magnitude (McGaugh, 2012). The Central Density Relation (CDR) links the central surface den-

sity of galactic discs to rotation curve steepness (Donato et al., 2009). Most fundamentally, the Radial Acceleration Relation (RAR) demonstrates a universal correlation between the gravitational acceleration inferred from baryonic matter alone and the total observed acceleration (McGaugh et al., 2016; Brouwer et al., 2021; Mistele et al., 2024b). What is most surprising to modern astronomers and cosmologists alike is the small scatter in these relations, which is difficult to reconcile with the stochastic nature of galaxy formation in ΛCDM.

The RAR is particularly significant as it directly probes the relationship between visible matter and the gravitational potential without assumptions about dark matter distributions. Measured using the SPARC sample of galaxies with high-quality rotation curves (Lelli et al., 2016), it shows remarkable universality across diverse galaxy types and environments. The BTFR and CDR emerge as natural consequences of this more fundamental relation, which encodes the basic relationship between matter and gravity in galactic systems. We discuss the RAR in more detail, and as a test of modified gravity, in Chapter 5.

1.2.3 Galactic Density Models

To model galaxies theoretically, we require parametric descriptions of their mass distributions. Galaxies are complex, multi-component systems comprising dark matter, stars, gas, dust, and central supermassive black holes. Each component exhibits a distinct spatial distribution that must be described by appropriate density profiles. In this section, we outline the most commonly used density profiles for galactic components, focusing primarily on the dark matter halo and stellar disc. In later chapters, we describe the empirical relations between their various scales and parameters, which are essential for constructing realistic galaxy models (see section 2.1).

Dark Matter Component

We begin with the most dominant of these components: the dark matter halo. The mass in a galaxy is predominantly dark matter, with haloes typically containing $\sim 90\%$ of the total galactic mass. These haloes extend far beyond the visible extent of the galaxy, reaching several hundred kiloparsecs. The standard approach is to model dark matter haloes as spherically symmetric, although simulations (Schneider et al., 2012) and weak lensing observations (Schrabback et al., 2021) predict them to be triaxial. This does not pose a problem for the methods employed in this thesis since the ellipticity is small,[12] $\langle|\epsilon|\rangle = 0.174 \pm 0.046$ (Schrabback et al., 2021), but it is worth noting that this constitutes a common simplifying assumption nonetheless.

The mass of a dark matter halo is usually expressed in terms of the virial mass, $M_{\rm vir}$, which represents the mass of a gravitationally bound system under the assumption that the virial theorem holds. Similarly, the closely related virial radius, $r_{\rm vir}$, is the radius within which the virial theorem applies. The virial theorem states that for a gravitationally bound system in equilibrium, the total kinetic energy, K, and the total potential energy, U, are related by

$$2K + U = 0\,. \tag{1.45}$$

A more direct definition of the virial radius is the radius within which the average density equals some multiple of the critical density of the universe, ρ_c, given by eq. (1.39),

$$\langle\rho(< r_{\rm vir})\rangle = \Delta_c \rho_c\,, \tag{1.46}$$

where Δ_c is the overdensity parameter. Given this definition of the virial radius, the virial mass can be calculated as

$$M_{\rm vir} = \frac{4\pi}{3}\Delta_c \rho_c r_{\rm vir}^3\,. \tag{1.47}$$

[12] Additionally, the ellipticity is radially dependent, such that the haloes are more spherical in the inner regions where we mainly focus our attention.

The value of Δ_c is not uniquely defined; rather, it is a function of redshift and the cosmological model employed. For example, taking Δ_c from the solution to a spherical top-hat collapse of a singular isothermal sphere of dark matter (defined below in eq. (1.54)), Bryan and Norman (1998) find

$$\Delta_c(z) = 18\pi^2 + 82x - 39x^2\,, \tag{1.48}$$

where $x = \Xi(z) - 1$, and

$$\Xi(z) = \frac{\Omega_{0,m}(1+z)^3}{\Omega_{0,m}(1+z)^3 + \Omega_{0,\Lambda}}\,. \tag{1.49}$$

Given the now apparent complexity of this definition, its inherent simplifying assumptions, and the fact that cosmological parameters are rarely consistent across the literature, it is instead common practice to assume a fixed value for Δ_c. A typical choice is $\Delta_c = 200$, which we adopt throughout this thesis. The definition of virial mass in this case is often quoted in the literature as M_{200c}, or (somewhat lazily) as M_{200}. Other common choices include $\Delta_c = 100$, 500, or 1000. Additionally, some authors define the virial radius in terms of the mean matter density of the universe, ρ_m, rather than the critical density.[13] This results in a larger virial radius and mass for the same halo, since $\rho_m = \Omega_m \rho_c < \rho_c$.

The most commonly used model for dark matter haloes is the Navarro–Frenk–White (NFW) profile (Navarro et al., 1996), which provides an empirical fit to the results of N-body simulations of cold dark matter. The NFW profile is given by

$$\rho(r) = \frac{\rho_{\rm NFW}}{\dfrac{r}{r_{\rm NFW}}\left(1 + \dfrac{r}{r_{\rm NFW}}\right)^2}\,, \tag{1.50}$$

where r is the spherical radial coordinate, and $\rho_{\rm NFW}$ and $r_{\rm NFW}$ are the characteristic density and length scale, respectively. These parameters are often re-expressed in terms of the virial mass, $M_{\rm vir}$, and concentration

[13] In such cases, the virial mass may be quoted as M_{200m}. This is likewise often abbreviated as M_{200}, much to the dismay of many a PhD student attempting to reproduce results across multiple studies.

parameter, $c_{\rm vir}$,[14] defined as

$$c_{\rm vir} = \frac{r_{\rm vir}}{r_{\rm NFW}} \,. \tag{1.51}$$

The concentration parameter describes how centrally concentrated the dark matter halo is, with higher values indicating more mass concentrated at smaller radii. The concentration parameter is not a free parameter; instead, it is found to correlate with the virial mass, with lower-mass haloes being more concentrated than higher-mass haloes. This correlation is known as the concentration-mass relation and has been studied extensively in both simulations and observations (Dutton and Macciò, 2014; Ludlow et al., 2016).

The NFW profile exhibits a characteristic 'cuspy' inner density profile, with $\rho \propto r^{-1}$ at small radii and $\rho \propto r^{-3}$ at large radii. This cuspy profile has been a point of contention in the literature, as observations of dwarf galaxies and low surface brightness galaxies often reveal shallower inner density profiles, known as 'cores' (de Blok et al., 2001a,b). This discrepancy is known as the core-cusp problem and represents an active area of research in both simulations and observations. Various solutions have been proposed, most notably baryonic feedback processes that can flatten the inner density profile (Pontzen and Governato, 2012).

By integrating the NFW profile, eq. (1.50), we derive the enclosed mass function

$$\begin{aligned} m(r) &= \int_0^r 4\pi r'^2 \rho(r')\,{\rm d}r' \\ &= 4\pi\rho_{\rm NFW} r_{\rm NFW}^3 \left[\ln\left(1+\frac{r}{r_{\rm NFW}}\right) - \frac{r/r_{\rm NFW}}{1+r/r_{\rm NFW}}\right] . \end{aligned} \tag{1.52}$$

The total mass ($r \to \infty$) diverges logarithmically; however, in practice the NFW profile is truncated. The truncation radius is often taken to be the virial radius, $r_{\rm vir}$. A more physically motivated truncation radius is

[14] Throughout this thesis we denote the concentration parameter as $c_{\rm vir}$ to align it stylistically with the virial mass and to distinguish it from the speed of light.

the splashback radius, $r_{\rm SB}$, which represents the radius at which infalling matter reaches its first apocentre after turnaround (Diemer and Kravtsov, 2014; More et al., 2015). The splashback radius is typically found to be roughly $1.5 \sim 2$ times the virial radius (More et al., 2015; Deason et al., 2020; Giocoli et al., 2024); however, it is a function of the mass accretion rate of the halo and can vary from halo to halo (Diemer et al., 2017).

The NFW profile has been shown to provide an excellent fit to the dark matter haloes of galaxies in simulations and is widely used in both theoretical and observational studies. However, it is worth noting that there are alternative, equally viable models for dark matter haloes. One such model is the Einasto profile (Einasto, 1965)

$$\rho(r) = \rho_{-2} \exp\left\{-\frac{2}{\alpha}\left[\left(\frac{r}{r_{-2}}\right)^{\alpha} - 1\right]\right\}, \tag{1.53}$$

where ρ_{-2} and r_{-2} are the density and radius at which the logarithmic slope of the density profile equals -2, and α is a shape parameter that describes the curvature of the profile. The Einasto profile has been shown to provide a superior fit to the inner regions of dark matter haloes in simulations, particularly for massive clusters (Merritt et al., 2006; Gao et al., 2008).

Other models include the Burkert profile (Burkert, 1995), the cored NFW profile (Read and Gilmore, 2005), and many others (Merritt et al., 2006; Dehnen and McLaughlin, 2005; Cardone et al., 2005). However, for the purposes of this thesis, we focus primarily on the NFW profile as it is the most widely used and well-studied model for dark matter haloes.

In chapter 5, we additionally test our results using a simpler dark matter density model: the Singular Isothermal Sphere (SIS) profile

$$\rho(r) = \frac{\sigma_v^2}{2\pi G r^2}, \tag{1.54}$$

where σ_v is the velocity dispersion. This model represents an idealised gas of dark matter particles with a Gaussian velocity distribution. It is frequently employed as a simple model for dark matter haloes in lensing

studies (Schneider et al., 1992; Bartelmann and Schneider, 2001a; Brouwer et al., 2021), in which it provides a reasonable approximation to the outer regions of galaxies where the rotation curve is flat. The enclosed mass function for the SIS profile is

$$m(r) = \frac{2\sigma_v^2 r}{G}\,. \tag{1.55}$$

The SIS profile exhibits a density singularity at $r = 0$ and a divergent total mass at $r = \infty$, similar to the NFW case. The same practical solutions employed for the NFW halo can be applied here to circumvent these issues.

Stellar Disc Component

The second most important component of a galaxy is the stellar disc. In this work, we focus our attention on late-type spiral galaxies. In spiral galaxies, the stellar disc typically contains approximately 5% of the total galactic mass and extends to several tens of kiloparsecs. The stellar disc contains the majority of the galaxy's stars and thus constitutes the primary visible component. Many different models exist for the stellar disc, depending on the type of galaxy being modelled, but they most commonly adopt an exponential profile in the disc plane (Freeman, 1970).

The model we adopt is the double exponential disc model (Jurić et al., 2008; Binney and Tremaine, 2008), which describes the stellar density as a function of both the cylindrical radial distance from the galactic centre, R, and the vertical distance from the galactic plane, z. The density profile is given by

$$\rho(R, z) = \frac{\Sigma_{\rm disc}}{2z_{\rm disc}} \mathrm{e}^{-R/R_{\rm disc}} \mathrm{e}^{-|z|/z_{\rm disc}}\,, \tag{1.56}$$

where $\Sigma_{\rm disc}$ is the central surface density of the disc, $R_{\rm disc}$ is the radial scale length, and $z_{\rm disc}$ is the vertical scale height. The radial scale length describes how rapidly the density decreases with increasing radius, while the vertical scale height describes how rapidly the density decreases with increasing height above or below the galactic plane. By integrating the

double exponential disc profile, eq. (1.56), we can derive the enclosed mass function

$$\begin{aligned} m(R) &= \int_{-\infty}^{\infty} \int_{0}^{R} 2\pi R' \rho(R', z)\, \mathrm{d}R' \mathrm{d}z \\ &= 2\pi \Sigma_{\mathrm{disc}} R_{\mathrm{disc}}^2 \left[1 - \left(1 + \frac{R}{R_{\mathrm{disc}}} \right) \mathrm{e}^{-R/R_{\mathrm{disc}}} \right] . \end{aligned} \tag{1.57}$$

The double exponential disc model has been shown to provide an excellent fit to the stellar discs of spiral galaxies in both observations and simulations (de Jong, 1996; Kregel et al., 2002). The stellar disc is often decomposed into thin and thick disc components, each with their own scale heights and scale lengths (Gilmore and Reid, 1983; Jurić et al., 2008). However, for the purposes of this thesis, we adopt a single disc component for simplicity.

Other Galactic Components

In addition to the dominant dark matter and stellar disc components, galaxies often contain several other components that can contribute to the overall mass distribution. These include the gas component, central bulge, satellite systems, and the central supermassive black hole.

The gas component of a galaxy is the largest of these additional components, potentially containing a similar amount of mass to the stellar disc in certain galaxy types. This gaseous reservoir is dominated by neutral atomic hydrogen (HI), which can be directly observed and mapped using the 21-cm hyperfine transition line. In the denser central regions, molecular hydrogen (H_2) becomes significant, typically traced via carbon monoxide (CO) emission lines since cold H_2 lacks a permanent dipole moment. The gas component is typically modelled using an exponential profile similar to the stellar disc, but with a larger scale length and scale height (Binney and Tremaine, 2008). The gas component can contain both atomic and molecular gas, with the latter being more concentrated in the central regions

of the galaxy. Despite comprising a not insignificant fraction of the total mass, the gas component is often neglected in studies of galaxy dynamics due to its relatively low density and the difficulty in measuring its distribution. For the purposes of our analysis, we assume the stellar disc provides a good representation of the entire baryonic mass distribution, and thus we do not explicitly model an additional gas component.

The central bulge is a roughly spheroidal component located at the centre of the galaxy, typically containing older stellar populations with little ongoing star formation. Observations reveal that galactic bulges are often triaxial, boxy structures — sometimes described as "peanut-shaped" (McWilliam and Zoccali, 2010; Nataf et al., 2010; Ness et al., 2012). The bulge density profile can be modelled using various forms, such as the exponential cutoff profile employed by Bissantz and Gerhard (2002). For spiral galaxies, the bulge typically contains only a small fraction of the total galactic mass (often around 1%) and extends to a few kiloparsecs from the galactic centre, though its exact mass and extent can vary significantly depending on the galaxy type and the specific region considered in observational studies.

Satellite systems, such as globular clusters and dwarf galaxies, can also contribute to the overall mass distribution of a galaxy. These systems are typically modelled using a variety of density profiles, including the Plummer profile (Plummer, 1911) and the King profile (King, 1962). Satellite systems typically contain $\lesssim 1\%$ of the total galactic mass and extend to several hundred kiloparsecs.

Finally, most galaxies contain a central supermassive black hole, which can have a significant impact on the dynamics of the central regions of the galaxy. The mass of the supermassive black hole is typically correlated with the properties of the bulge, such as its velocity dispersion and luminosity (Kormendy and Ho, 2013). Despite its unrivalled coolness, and mass-based name, the supermassive black hole typically contains a minuscule fraction

($\lesssim 0.001\%$) of the total galactic mass.

With this, we have provided a brief overview of the most commonly used density profiles for the various components of a galaxy. In later chapters, we describe how these components are combined to create realistic galaxy models, and how their parameters are determined from observations (see section 2.1). We shall utilise these density profiles as the matter sourcing the scalar field in our modified gravity analysis.

1.3 Screened Modified Gravity Theories

1.3.1 General Scalar-Tensor Model

Our investigation into Modified Gravity (MG) theories focuses exclusively on scalar-tensor theories. In the Einstein frame,[15] these theories are described by the general scalar-tensor action

$$S = \frac{1}{8\pi G}\int \mathrm{d}^4x\sqrt{-g}\left[\frac{R}{2} - \frac{1}{2}\nabla_\mu\phi\nabla^\mu\phi - V(\phi)\right] + S_m\left[\tilde{g}_{\mu\nu}, \psi_i^{SM}\right] , \quad (1.58)$$

composed of an Einstein-Hilbert term, a canonical kinetic term for the scalar field, and a potential term. Here ϕ is a canonically normalised scalar field with potential $V(\phi)$,[16] and S_m represents the matter action for the Standard Model fields, ψ_i^{SM}. These theories include a conformal coupling to matter, meaning that matter fields now move on geodesics of the Jordan frame metric

$$\tilde{g}_{\mu\nu} = A^2(\phi)g_{\mu\nu} . \quad (1.59)$$

Deviations from GR arise from the non-minimal conformal coupling function, $A(\phi)$. Both frames yield identical classical observables. For ease of calculation, the analysis within this thesis focuses solely on the Einstein frame, where there is a direct coupling between matter and the scalar field,

[15] In the Einstein frame, $g_{\mu\nu}$, the Einstein field equations are unchanged, but matter no longer moves on geodesics of the metric due to scalar modifications.

[16] Throughout this thesis, we adopt a dimensionless scalar field, ϕ, and a potential with dimensions of inverse length squared, i.e. mass squared in natural units.

and the pure gravitational action does not depend explicitly on the scalar field.

The inclusion of this conformal coupling, particularly in the matter action S_m, results in the energy-momentum tensor for matter no longer being covariantly conserved, as it was in the GR case, eq. (1.16). Instead, it satisfies the modified covariant conservation law,

$$\nabla_\mu T^{\mu\nu} = \beta(\phi) T \nabla^\nu \phi \,, \tag{1.60}$$

where $T = g_{\mu\nu} T^{\mu\nu}$ is the trace of the energy-momentum tensor, and the coupling function β is defined as

$$\beta(\phi) \equiv \frac{\mathrm{d}\ln A}{\mathrm{d}\phi} \,. \tag{1.61}$$

In the low-energy Newtonian limit, this non-conservation of the energy-momentum tensor results in a modified Newtonian force law,

$$\ddot{\boldsymbol{x}} + \boldsymbol{\nabla}\Phi_N = -\beta(\phi)\boldsymbol{\nabla}\phi \,. \tag{1.62}$$

A step-by-step derivation of this equation starting from the GR geodesic equation (eq. 1.6) can be found in appendix B.

The additional scalar term in eq. (1.62) is known as the **fifth force**. Explicitly put,

$$\boldsymbol{a}_5 = -\beta(\phi)\boldsymbol{\nabla}\phi \,, \tag{1.63}$$

where a_5 is the acceleration due to the fifth force. This fifth force is the key signature of scalar-tensor theories and represents the primary target of observational constraints. In most cases, this fifth force cannot be left to act freely, as it would lead to violations of well-tested gravitational physics in the Solar System and on Earth. To evade these constraints, many scalar-tensor theories adopt specific forms of the potential and coupling function to implement "screening mechanisms". These screening mechanisms suppress the fifth force in high-density environments, whilst allowing it to operate in low-density environments, such as galactic outskirts. We will

revisit these screening mechanisms in more detail in the forthcoming sections.

In order to determine the fifth forces in a given system, we require the scalar field profile, $\phi(x_\mu)$, which we obtain by solving the scalar field's Equation of Motion (EoM). One can derive the equation of motion by extremising the general scalar-tensor action, eq. (1.58), with an energy-momentum tensor for the matter fields that assumes matter is a non-relativistic, perfect fluid with matter density ρ. Doing so will result in the following equation of motion for the scalar field:

$$\Box\phi = \frac{\mathrm{d}V(\phi)}{\mathrm{d}\phi} + 8\pi G\beta(\phi)\rho\,. \tag{1.64}$$

It is clear from the second term on the right-hand side that the scalar field is sourced not only by the potential $V(\phi)$, but also by the local environment through the matter density, ρ. It is possible to rewrite this equation in terms of an effective potential, given by

$$V_{\text{eff}}(\phi) \equiv V(\phi) + 8\pi G \ln A(\phi)\rho\,, \tag{1.65}$$

so that the dynamics of the scalar field are governed by the effective potential,

$$\Box\phi = \frac{\mathrm{d}V_{\text{eff}}(\phi)}{\mathrm{d}\phi}\,. \tag{1.66}$$

1.3.2 Solving the General Scalar Field Equation of Motion

While the general form of the scalar equation of motion is highly non-linear and cannot be solved in closed form, it is possible to determine a solution given a sufficiently symmetric source term, and several simplifying assumptions. It will prove to be useful to detail the steps and results of this derivation, as they provide key insights into the behaviour of scalar-tensor theories.

To start, consider a static, spherically symmetric source, $\delta\rho(r)$, with radius R and total mass M, embedded in a constant background density $\bar{\rho}$. Under these assumptions, the scalar field equation of motion can be written as

$$\nabla^2\phi = \frac{\mathrm{d}V}{\mathrm{d}\phi} + 8\pi G\beta(\phi)\rho(r)\,, \tag{1.67}$$

where $\rho(r) = \bar{\rho} + \delta\rho(r)$ is the total density. We will solve this equation in three scenarios: the source mass being fully screened, fully unscreened, and partially screened.

Fully Screened Solution

In fully screened regime, the object is sufficiently dense such that the field minimises the effective potential everywhere inside the object, $\phi \to \phi_{\min}(\bar{\rho}+\delta\rho)$. Far from the object, in the background medium, the field minimises the effective potential, $\phi \to \bar{\phi} \equiv \phi_{\min}(\bar{\rho})$. In both regions the field is constant and thus the fifth force vanishes, hence the object is fully screened. But, necessarily, as we transition between these regions there must exist some "thin shell" where the field gradient, and thus the fifth force eq. (1.63), is non-zero. In practice, this thin shell of mass contributing to the fifth force is extremely thin and thus the fifth force is heavily suppressed. This will become more apparent once we have examined the other scenarios.

Fully Unscreened Solution

Considering instead an object where the scalar field minimises the effective potential far from the object, $\phi \to \bar{\phi}$, but does not minimise the effective potential inside the object. In this case, we make the first assumption: that the field can be expressed as a linear perturbation about the background, $\phi = \bar{\phi} + \delta\phi$, where $\delta\phi$ is small, i.e. neglecting terms of $\mathcal{O}(\delta\phi^2)$ and higher powers. The equation of motion is then written as

$$\nabla^2(\bar{\phi}+\delta\phi) = \left.\frac{\mathrm{d}V}{\mathrm{d}\phi}\right|_{\bar{\phi}+\delta\phi} + 8\pi G\beta(\bar{\phi}+\delta\phi)(\bar{\rho}+\delta\rho)\,. \tag{1.68}$$

To simplify the terms in this equation we Taylor expand around the background field value, $\bar{\phi}$.

Perturbatively expanding the coupling function around the background field, we have

$$\beta(\bar{\phi}+\delta\phi) \approx \beta(\bar{\phi}) + \left.\frac{\mathrm{d}\beta}{\mathrm{d}\phi}\right|_{\bar{\phi}} \delta\phi\,. \tag{1.69}$$

Here we make a second assumption: that the coupling function is weakly dependent on ϕ, and thus $\beta(\bar{\phi}) \gg \left.\frac{\mathrm{d}\beta}{\mathrm{d}\phi}\right|_{\bar{\phi}} \delta\phi$. This is justified as it ensures that the conformal factor $A(\phi)$ remains close to unity, ensuring that small changes in the Einstein frame are not amplified in the Jordan frame.

Similarly, for the potential term, we can Taylor expand around the background field value, $\bar{\phi}$,

$$\left.\frac{\mathrm{d}V}{\mathrm{d}\phi}\right|_{\bar{\phi}+\delta\phi} \approx \left.\frac{\mathrm{d}V}{\mathrm{d}\phi}\right|_{\bar{\phi}} + \left.\frac{\mathrm{d}^2V}{\mathrm{d}\phi^2}\right|_{\bar{\phi}} \delta\phi\,. \tag{1.70}$$

The second derivative of the potential can be interpreted as the mass of the scalar field, $m_\phi^2 = \frac{\mathrm{d}^2V}{\mathrm{d}\phi^2}$, which is inversely proportional to the Compton wavelength of the scalar field, $\lambda_\phi = m_\phi^{-1}$.

With this, our resulting equation of motion becomes

$$\nabla^2\delta\phi = \left.\frac{\mathrm{d}V}{\mathrm{d}\phi}\right|_{\bar{\phi}} + \bar{\lambda}_{\mathrm{C}}^{-2}\delta\phi + 8\pi G\beta(\bar{\phi})(\bar{\rho}+\delta\rho)\,, \tag{1.71}$$

where $\bar{\lambda}_{\mathrm{C}} = \lambda_{\mathrm{C}}(\phi=\bar{\phi})$ is the background Compton wavelength. We reduce this further by recalling that $\bar{\phi}$ minimises the effective potential in the background medium, and thus $\left.\frac{\mathrm{d}V}{\mathrm{d}\phi}\right|_{\bar{\phi}} + 8\pi G\beta(\bar{\phi})\bar{\rho} = 0$. This leaves us with the much simpler equation of motion

$$\nabla^2\delta\phi = \bar{\lambda}_{\mathrm{C}}^{-2}\delta\phi + 8\pi G\beta(\bar{\phi})\delta\rho\,, \tag{1.72}$$

which we are now able to solved in two regions, inside ($r < R$) and outside ($r > R$) the object.

Inside the object we make a third simplifying assumption: that the first term on the right-hand side of eq. (1.72) is negligible, since a cosmologically

relevant theory will have $\bar{\lambda}_{\rm C} \gg R$. This allows us to write the equation of motion as

$$\frac{1}{r^2}\frac{\mathrm{d}}{\mathrm{d}r}\left(r^2\frac{\mathrm{d}\delta\phi}{\mathrm{d}r}\right) = 8\pi G\beta(\bar{\phi})\delta\rho\,, \tag{1.73}$$

which results in the first order differential equation

$$\frac{\mathrm{d}\delta\phi}{\mathrm{d}r} = 2\beta(\bar{\phi})\frac{Gm(r)}{r^2}\,, \tag{1.74}$$

where $m(r) = \int_0^r 4\pi r'^2\delta\rho(r')dr'$ is the mass within radius r, and the boundary condition $\frac{\mathrm{d}\delta\phi}{\mathrm{d}r}\big|_{r=0} = 0$ has been applied.

Outside the object the density perturbation vanishes, $\delta\rho = 0$, and we can no longer neglect the first term on the right-hand side of eq. (1.72), resulting in the following equation of motion:

$$\frac{1}{r^2}\frac{\mathrm{d}}{\mathrm{d}r}\left(r^2\frac{\mathrm{d}\delta\phi}{\mathrm{d}r}\right) = \bar{\lambda}_{\rm C}^{-2}\delta\phi\,. \tag{1.75}$$

This equation is a homogeneous second-order differential equation, analogous to the Helmholtz equation. The first step in solving this is to make the substitution $\delta\phi(r) = y(r)/r$, which yields the equation

$$\frac{\mathrm{d}^2 y}{\mathrm{d}r^2} - \bar{\lambda}_{\rm C}^{-2}y = 0\,. \tag{1.76}$$

This second-order differential equation has the general solution

$$y(r) = Ae^{r/\bar{\lambda}_{\rm C}} + Be^{-r/\bar{\lambda}_{\rm C}}\,, \tag{1.77}$$

and so our field perturbation is given by

$$\delta\phi(r) = \frac{A}{r}e^{r/\bar{\lambda}_{\rm C}} + \frac{B}{r}e^{-r/\bar{\lambda}_{\rm C}}\,. \tag{1.78}$$

In order for $\delta\phi \to 0$ as $r \to \infty$, we must set $A = 0$. We then find B by matching the first derivative of the interior solution at the surface of the object, $r = R$. The derivative of our exterior solution at the boundary is given by

$$\left.\frac{\mathrm{d}\delta\phi}{\mathrm{d}r}\right|_{r=R} = -\frac{B}{R^2}\left(1 + \frac{R}{\bar{\lambda}_{\rm C}}\right)e^{-R/\bar{\lambda}_{\rm C}} \approx -\frac{B}{R^2}\,, \tag{1.79}$$

where we have again used $R \ll \bar{\lambda}_{\rm C}$. Comparing this with the interior

solution, eq. (1.74), we find

$$B = -2\beta(\bar{\phi})GM, \tag{1.80}$$

and so the full solution for the exterior field perturbation is given by

$$\delta\phi(r) = -2\beta(\bar{\phi})\frac{GM}{r}e^{-r/\bar{\lambda}_{\rm C}}\,. \tag{1.81}$$

This field profile has an associated gradient profile

$$\begin{aligned}\frac{\mathrm{d}\delta\phi}{\mathrm{d}r} &= 2\beta(\bar{\phi})\frac{GM}{r^2}\left(1+\frac{r}{\bar{\lambda}_{\rm C}}\right)e^{-r/\bar{\lambda}_{\rm C}} \\ &\approx 2\beta(\bar{\phi})\frac{GM}{r^2}e^{-r/\bar{\lambda}_{\rm C}}\,.\end{aligned} \tag{1.82}$$

The above approximation can be applied since we are already assuming $R \ll \bar{\lambda}_{\rm C}$, and by the time we reach $r \sim \bar{\lambda}_{\rm C}$ the expression is exponentially suppressed, so the multiplicative factor is effectively unity.

With this, we have a complete solution for the scalar field perturbation both inside and outside the object. The fifth force, eq. (1.63), can then be calculated using these solutions. Inside the object, the fifth force is given by

$$a_5 = -2\beta^2(\bar{\phi})\frac{Gm(r)}{r^2}\,, \tag{1.83}$$

while outside the object it is given by

$$a_5 = -2\beta^2(\bar{\phi})\frac{GM}{r^2}e^{-r/\bar{\lambda}_{\rm C}}\,. \tag{1.84}$$

It is now apparent that a fully unscreened object exerts a fifth force proportional to the standard Newtonian gravitational force, acting to enhance the gravitational effect of the object. Outside the source this fifth force is exponentially suppressed,[17] as shown in eq. (1.84).

[17]This type of exponential suppression is oftentimes referred to as a "Yukawa suppression", in reference to the form $e^{-r/\lambda_{\rm C}}$ found in Yukawa's original work on strong force screening mechanisms (Yukawa, 1935).

Partially Screened Solution

Finally, we consider the case of a partially screened object. In this scenario, the object is sufficiently dense such that the field minimises the effective potential inside the object, $\phi \to \phi_{\rm min}(\bar{\rho} + \delta\rho)$, but only within some radius $r_s < R$. This radius, r_s, is known as the "**screening radius**". Inside this radius, $0 < r < r_s$, the field minimises the effective potential and thus the fifth force vanishes. Outside this radius, $r_s < r < R$, the field can be solved in a similar manner as in the fully unscreened case, except now the inner boundary condition is evaluated at the screening radius, instead of $r = 0$.

Explicitly, one should solve eq. (1.73) to find

$$\frac{\mathrm{d}\delta\phi}{\mathrm{d}r} = 2\beta(\bar{\phi})\frac{G\left(m(r) - m(r_s)\right)}{r^2}\,, \tag{1.85}$$

having applied the inner boundary condition $\frac{\mathrm{d}\delta\phi}{\mathrm{d}r}\big|_{r=r_s} = 0$. The methodology to solve the exterior field remains unchanged. However, by matching the field gradient solution to the screened interior solution at $r = R$ we instead arrive at

$$\frac{\mathrm{d}\delta\phi}{\mathrm{d}r} = 2\beta(\bar{\phi})\frac{G\left(M - m(r_s)\right)}{r^2}\,. \tag{1.86}$$

In terms of fifth forces, eq. (1.63),

$$a_5 = \begin{cases} 0 & \text{for } r \leq r_s \\ -2\beta^2(\bar{\phi})\dfrac{Gm(r)}{r^2}\left(1 - \dfrac{m(r_s)}{m(r)}\right) & \text{for } r_s < r < R \\ -2\beta^2(\bar{\phi})\dfrac{GM}{r^2}\left(1 - \dfrac{m(r_s)}{M}\right)\mathrm{e}^{-r/\bar{\lambda}_{\rm C}} & \text{for } r \geq R \end{cases} \tag{1.87}$$

In the above equation, we recognise that the fifth force is sourced only by the mass enclosed between the screening radius and the outer radius (or the radial position for $r_s < r < R$). This effect, briefly mentioned earlier, is known as the **thin-shell effect**, and is one of the key mechanisms by which fifth forces are suppressed. In the fully screened case $r_s \to R$, resulting in a negligible amount of mass contributing to the fifth force. Meanwhile in

the fully unscreened scenario, $r_s \to 0$ and all the mass sources fifth forces.

1.3.3 Approximations for the Screening Radius

Given the importance of the thin-shell effect, it is paramount to determine the screening radius, r_s, for a given object. Indeed, the work we conduct in chapter 3 is dedicated to developing accurate methods to calculate the screening radius. Here we establish the prerequisites for that work by deriving the commonly used approximations for the screening radius.

Our starting point is the partially screened interior solution for the gradient of the scalar field, eq. (1.85). Integrating this equation from the screening radius, where $\phi \approx \phi_{\rm min}(\rho(r_s))$, to infinity, where the field assumes the background value, $\bar{\phi}$, we find

$$\bar{\phi} - \phi_{\rm min}(\rho(r_s)) = \frac{2G\beta(\bar{\phi})}{c^2}\left(\frac{m(r_s)}{r_s} + \int_{r_s}^{\infty}\frac{m(r)}{r^2}{\rm d}r\right) . \tag{1.88}$$

Subsequently, integrating by parts and using the definition of the enclosed mass $m(r)$, we find the expression

$$\chi \equiv \frac{\bar{\phi}}{2\beta(\bar{\phi})} = 4\pi G\int_{r_s}^{\infty} r\delta\rho(r){\rm d}r\,, \tag{1.89}$$

where the $\phi_{\rm min}(\rho(r_s))$ term has been dropped since it is assumed the screening mechanism acts to force the field to smaller values inside high-density objects, thus $\phi_{\rm min}(\rho(r_s)) \ll \bar{\phi}$. Performing this integral for given model parameters, $\{\bar{\phi}, \beta(\bar{\phi})\}$, and density profile, $\delta\rho(r)$, yields the screening radius, r_s.

To obtain the above expression several assumptions have been made. Specifically: that the field reaches its minimum value inside the object, that this minimum value can be neglected, that the theory can be linearised in the region containing the screening radius, that the scalar mass is negligible in this region, and that the coupling function $\beta(\phi)$ is constant throughout. We further discuss the validity of these assumptions in chapter 3.

Here we have introduced the parameter χ, which we hereby refer to as the **critical potential**. This parameter is a property of the theory, dependent on the background field value and coupling function — independent of the object being screened. The parameter χ is provocatively named the critical potential since eq. (1.89) can be rewritten in terms of the Newtonian potential, Φ_N. This yields the equivalent expression

$$\chi = -\left(\Phi_N(r_s) + r_s \left.\frac{\mathrm{d}\Phi_N}{\mathrm{d}r}\right|_{r_s}\right), \tag{1.90}$$

where $\bar{\phi} = \phi(\bar{\rho})$ is the background field solution and $\Phi_N(r)$ is the Newtonian potential.

One can use the critical potential to approximate the screening radius, given some model parameters. If eq. (1.89), or equivalently eq. (1.90), has no solution for r_s, this corresponds to a fully unscreened object, i.e. all the mass sources fifth forces. Since $\Phi_N < 0$ and $\frac{\mathrm{d}\Phi_N}{\mathrm{d}r} > 0$, an object must be fully unscreened when $\chi > |\Phi_N|$, where the Newtonian potential is measured at the surface of the object. Conversely, this indicates that only objects with $\chi < |\Phi_N|$ are partially screened (or fully screened, i.e. r_s is larger than the extent of the object, in the case $\chi \ll |\Phi_N|$).

1.3.4 Screening Mechanisms

The final insight we gain from our approximate solutions to the scalar field equation of motion is a method to categorise different screening mechanisms. As it stands, the fifth forces arising from scalar contributions to the gravitational field are in direct conflict with observations. To avoid these constraints, scalar-tensor theories must include screening mechanisms that suppress the fifth force in high-density environments. These mechanisms are necessary to ensure that the theory is consistent with the stringent constraints on deviations from GR in the Solar System and in laboratory experiments, which we will revisit in more detail in section 1.3.8.

Looking at the fifth force equations eqs. (1.87), we find the fifth force can be written generally as

$$\frac{a_5}{a_N} \propto S(M,R)\beta^2(\bar{\phi})\mathrm{e}^{-r/\bar{\lambda}_\mathrm{C}}\,, \tag{1.91}$$

where a_N is the Newtonian gravitational force, and $S(M,R)$ is a model-dependent function that depends on the mass sourcing the fifth force. It stands to reason that there are three ways in which one can suppress this fifth force:

1. Not all the mass contributes to the fifth force, i.e. $S(M,R) \ll 1$. This is the thin-shell effect, discussed in detail above.

2. The coupling function is small, i.e. $\beta(\bar{\phi}) \ll 1$. This is known as weak coupling screening.

3. The scalar field is very massive, i.e. $\bar{\lambda}_\mathrm{C} \ll r$, resulting in short-range fifth forces. This is sometimes referred to as large mass screening.

The most straightforward way to suppress fifth forces would be to choose theory parameters such that one of the last two conditions is satisfied on all scales. However, this is not particularly satisfying as it does not allow for interesting phenomenology on cosmological scales. Fortunately, given the dynamical scales observed in cosmology, it is possible to choose theory parameters such that fifth forces are negligible in easily testable environments, such as the Solar System, while still allowing for interesting phenomenology on larger scales.

Many screening mechanisms have been proposed in the literature, and they can be broadly categorised into groups based on which of the above conditions they satisfy. Models that satisfy a combination of the first and third conditions are known as **chameleon** models (covered in section 1.3.5). Models that satisfy a combination of the first and second condition are known as **symmetron** models (covered in section 1.3.7).

There are a litany of other models not considered in this thesis. One prominent example is the dilaton model (Damour and Polyakov, 1994), which, like the symmetron, satisfies the second condition by driving the coupling strength to zero in dense environments. Another major class of models, known as Vainshtein (or Vainshtein-like) models, screen fifth forces via an entirely different mechanism. These models, which include Dvali-Gabadadze-Porrati (DGP) gravity (Dvali et al., 2000) and Galileon theories (Nicolis et al., 2009), rely on non-linear derivative self-interactions in the kinetic term of the action. This results in the suppression of fifth forces within the Vainshtein radius, effectively decoupling the scalar field from matter in high-density regions (Vainshtein, 1972; Babichev and Deffayet, 2013).

See also Mota and Shaw (2007); Dehnen et al. (1992); Gessner (1992); Damour and Polyakov (1994); Pietroni (2005); Olive and Pospelov (2008) for even more screening mechanisms, or Koyama (2016); Saridakis et al. (2021a) for an impressively extensive overview of modified gravity

In this thesis, we focus exclusively on chameleon and symmetron screening. This choice is broadly motivated by two factors. Firstly, our initial investigation (chapter 3) was conceived in response to specific constraints placed on $f(R)$ chameleon gravity, necessitating a detailed examination of that specific mechanism. Secondly, the screening in chameleon and symmetron models arises from the potential and coupling functions, leading to field equations that are essentially non-linear Poisson equations. These are considerably more amenable to the numerical methods developed in this work than Vainshtein mechanism models, which involve complex non-linear derivative terms that are notoriously difficult to simulate.

1.3.5 Chameleon

As outlined in the previous subsection, chameleon models are a class of scalar-tensor theories that screen primarily via a density-dependent scalar mass, leading to the presence of short-range fifth forces. A wide array of potentials and coupling functions can be written to achieve this. Here we focus on the existing literature, with power-law potentials and exponential coupling functions (Khoury and Weltman, 2004a,b),

$$V(\phi) = \frac{V_0^{4+n}}{\phi^n} \quad \text{and} \quad A(\phi) = e^{\beta\phi}\,. \tag{1.92}$$

Here V_0 is a constant scale parameter controlling the energy scale of the potential, n is an integer, and β is a constant coupling parameter. In applications to cosmology, V_0 is typically chosen to be of order the dark energy scale, such that the potential drives the late-time acceleration of the Universe. n is typically taken to be a positive integer, $n > 0$, to ensure the potential is a monotonically decreasing function of ϕ. For simplicity it is often assumed $n = 1$.

In such a theory, the effective potential, eq. (1.65), is given by

$$V_{\rm eff}(\phi) = \frac{V_0^{4+n}}{\phi^n} + 8\pi G\rho\beta\phi\,. \tag{1.93}$$

Assuming the bare potential is monotonically decreasing, i.e. $n > 0$, the effective potential will have a minimum at

$$\phi_{\rm min}(\rho) = \left(\frac{nV_0^{4+n}}{8\pi G\rho\beta}\right)^{\frac{1}{n+1}}\,, \tag{1.94}$$

with an associated scalar mass

$$m_\phi^2(\rho) = \left.\frac{{\rm d}^2V_{\rm eff}}{{\rm d}\phi^2}\right|_{\phi_{\rm min}} = n(n+1)V_0^{4+n}\left(\frac{8\pi G\rho\beta}{nV_0^{4+n}}\right)^{\frac{n+2}{n+1}}\,. \tag{1.95}$$

Therefore, the Compton wavelength of the scalar field, $\lambda_{\rm C}(\rho) = m_\phi^{-1}(\rho)$, is a decreasing function of the local matter density, ρ. In high-density environments, such as the Solar System or the centres of galaxies, the scalar

field is very massive and thus the fifth force is short-ranged and negligible. Meanwhile, in low-density environments, such as the outskirts of galaxies or cosmic voids, the scalar field is light, so the fifth force can be long-ranged and have interesting phenomenology.

1.3.6 $f(R)$ Gravity

In chapters 3 and 4 we specialise to a particular chameleon model known as Hu-Sawicki $f(R)$ gravity. The Hu-Sawicki model is a subclass of $f(R)$ gravity, which allows for higher-order curvature terms in the Einstein-Hilbert action. We choose to work with $f(R)$ chameleon screening because of its simplicity as a model and its ubiquity in the literature. In this section, we briefly review $f(R)$ gravity and the specific choice of $f(R)$ leading to the Hu-Sawicki model.

$f(R)$ gravity is a natural and well-motivated extension of General Relativity with applications across an enormous range of scales and physical phenomena. Historical interest in higher-order gravitational theories began soon after the formulation of GR with Weyl (1919) and continued through Eddington (1923), initially driven by scientific curiosity about Einstein's newly proposed theory. Modern $f(R)$ theories have proven remarkably versatile, providing frameworks for inflation through curvature-driven scenarios (Starobinsky, 1980), addressing late-time cosmic acceleration as alternatives to dark energy (Capozziello and Fang, 2002; Carroll et al., 2004), and enabling studies of strong gravity modifications near black holes and neutron stars (Yunes and Pretorius, 2009). For a general review of $f(R)$ gravity, see Sotiriou and Faraoni (2010).

As earlier mentioned, $f(R)$ theories modify GR by replacing the Ricci scalar, R, in the Einstein-Hilbert action eq. (1.17) with the generalised

$R + f(R)$,[18] allowing for higher-order curvature terms in the action,

$$S = \frac{1}{16\pi G}\int \mathrm{d}^4x\sqrt{-\tilde{g}}\left[R + f(R)\right] + S_m\left[\tilde{g}_{\mu\nu}, \psi_i^{SM}\right] , \tag{1.96}$$

where $R = R(\tilde{g})$. This action can be recast in the form of the general scalar-tensor action eq. (1.58) with the field redefinition (Brax et al., 2008)

$$\phi = -\frac{\ln(1+f_R)}{2\beta(\phi)} , \qquad V(\phi) = \frac{Rf_R - f(R)}{2(1+f_R)^2} \qquad \text{and} \qquad \beta(\phi) = \frac{1}{\sqrt{6}} , \tag{1.97}$$

where

$$f_R \equiv \frac{\mathrm{d}f(R)}{\mathrm{d}R} \tag{1.98}$$

acts as the scalar field of the theory.

Extremising the $f(R)$ action eq. (1.96) with respect to the metric results in a set of modified Einstein field equations,

$$G_{\mu\nu} + f_R R_{\mu\nu} - \frac{1}{2}f(R)g_{\mu\nu} + g_{\mu\nu}\nabla^2 f_R - \nabla_\mu\nabla_\nu f_R = 8\pi G T_{\mu\nu} . \tag{1.99}$$

Taking the trace yields the scalar equation of motion

$$3\Box f_R - R + f_R R - 2f(R) = -8\pi G\rho . \tag{1.100}$$

assuming the matter consists of non-relativistic particles, such that $T \approx -\rho$. At this point one can take the Newtonian limit, with the assumptions $|f_R| \ll 1$ and $|\nabla f_R| \gg \partial_t f_R$ (the latter is known as the quasi-static approximation), resulting in the scalar equation of motion for f_R and a modified Poisson equation:

$$\nabla^2 f_R = \frac{1}{3}\left(\delta R - 8\pi G\delta\rho\right) , \tag{1.101}$$

$$\nabla^2\Phi = \frac{16\pi G}{3}\delta\rho - \frac{1}{6}\delta R . \tag{1.102}$$

Here $\delta\rho$ is the density perturbation and δR is the curvature perturbation, such that $R = \bar{R} + \delta R$.

[18]The literature is somewhat split between this expression of $f(R)$, and an equivalent version where the Ricci scalar is absorbed into the function. The results and observables are identical, but the choice of formulation can result in differences in between calculations.

Assuming this theory exhibits a chameleon screening mechanism, in the screened region the field acts to minimise the effective potential, i.e. $\delta R = 8\pi G\delta\rho$, and thus the modified Poisson equation reduces to the standard Poisson equation, $\nabla^2\Phi = 4\pi G\delta\rho$, eq. (1.2). In unscreened regions $\delta R \ll 8\pi G\delta\rho$, and the modified Poisson equation becomes $\nabla^2\Phi = 16\pi G\delta\rho/3$. Comparing this to the standard Poisson equation, we see a factor of $1/3$ enhancement of the gravitational force. This can equally be interpreted as a modification to the gravitational constant, i.e. $G_{\rm eff} = \frac{4}{3}G$, and is exactly encapsulated by $\beta = \sqrt{1/6}$ in the fifth force equation for an unscreened region, eq. (1.83).

Hu-Sawicki $f(R)$

For specific choices of the functional form of $f(R)$, the theory exhibits the chameleon screening mechanism. Several forms of $f(R)$ can achieve this, for example Faulkner et al. (2007); Starobinsky (2007); Navarro and Van Acoleyen (2007). We adopt the commonly used Hu-Sawicki model (Hu and Sawicki, 2007). In this model

$$f(R) = -\frac{am^2}{1 + (R/m^2)^{-n}}\,, \tag{1.103}$$

where a and n are positive dimensionless parameters, and m is a dimensionful parameter.[19] For simplicity, we choose $n = 1$, in line with the bulk of the current literature. In such a case, the scalar of the theory is given by

$$f_R = -\frac{am^4}{(R + m^2)^2}\,, \tag{1.104}$$

and the background value is simply

$$f_{R0} = -\frac{am^4}{(R_0 + m^2)^2}\,, \tag{1.105}$$

[19]Note that a here is unrelated to the scale factor $a(t)$.

where R_0 is the present-day background Ricci scalar.[20] For a flat FLRW metric, R_0 is given by

$$R_0 = 3H_0^2(\Omega_m + 4\Omega_\Lambda)\,. \tag{1.106}$$

Currently the model has two free parameters a and m; however these can be related by requiring that the action returns to GR + ΛCDM (eq. 1.28) in the high curvature limit, i.e.

$$f(R) \approx -am^2 = -2\Lambda\,, \tag{1.107}$$

when $R \gg m^2$. This allows us to describe the theory in terms of one free model parameter, a or m, which we instead express as the present-day background field value f_{R0}. To do this one must simultaneously solve equations (1.105), (1.106) and (1.107), which leads to the following relations:

$$a = -\frac{4\Omega_\Lambda^2}{(\Omega_m + 4\Omega_\Lambda)^2}\frac{1}{f_{R0}} \quad \text{and} \quad m^2 = -\frac{3H_0^2(\Omega_m + 4\Omega_\Lambda)^2}{2\Omega_\Lambda}f_{R0}\,. \tag{1.108}$$

From this definition of m and the definition of R_0, eq. (1.106), we see that the high curvature limit ($R \gg m^2$) is equivalent to $|f_{R0}| \ll 1$, which is necessarily satisfied for the theory to be consistent with local tests of gravity (Hu and Sawicki, 2007).

In Hu-Sawicki $f(R)$, the equation of motion is given by eq. (1.101), with the curvature perturbation

$$\delta R = R_0\left[\sqrt{\frac{f_{R0}}{f_R}} - 1\right]\,, \tag{1.109}$$

which follows from the ratio of eq. (1.104) and eq. (1.105), in the high-curvature limit.[21] The outline of our numerical methods to solve the EoM and determine the field profile is given in section 2.2. The fifth force accel-

[20] Here, and throughout this thesis, zero subscripts are used to denote present-day background values evaluated at $z = 0$.

[21] Technically R is a function of the expansion rate $a(t)$; however, in this thesis we are primarily interested in local measurements where $a(t) \approx a_0 \equiv 1$.

eration, eq. (1.63), caused by our scalar field is given by

$$\boldsymbol{a}_5 = \frac{1}{2}\boldsymbol{\nabla} f_R \,, \tag{1.110}$$

where we have again assumed $f_R \ll 1$. The Compton wavelength of this theory is discussed in great detail in chapter 4; here we state the background Compton wavelength

$$\lambda_{\rm C} \approx 32\sqrt{\frac{f_{R0}}{10^{-4}}}\,{\rm Mpc}\,, \tag{1.111}$$

as given in Cabré et al. (2012), based on Hu and Sawicki (2007).

1.3.7 Symmetron

In contrast to chameleon models, where screening arises due to a variable scalar mass, symmetron models screen by suppressing the coupling to matter in dense regions (Hinterbichler and Khoury, 2010). This is achieved through a density-dependent Spontaneous Symmetry Breaking (SSB), given the correct form of potential and coupling in the scalar-tensor action, eq. (1.58). In our case, we choose to work with a quartic potential and quadratic coupling, each possessing a $\mathbb{Z}_2$ symmetry ($\phi \to -\phi$),

$$V(\phi) = \frac{1}{L_{\rm pl}^2}\left[-\frac{1}{2}\left(\frac{\mu}{M_{\rm pl}}\right)^2\phi^2 + \frac{1}{4}\lambda\phi^4\right], \tag{1.112}$$

$$A(\phi) = 1 + \frac{1}{2}\left(\frac{M_{\rm pl}}{M_{\rm sym}}\right)^2\phi^2\,, \tag{1.113}$$

where $M_{\rm pl}^2 \equiv \hbar c/8\pi G$ is the reduced Planck mass and $L_{\rm pl}^2 \equiv 8\pi G\hbar/c^3$ is the reduced Planck length. This model has three free parameters: the mass scale $M_{\rm sym}$ controlling the strength of the coupling to matter, the mass scale μ representing the bare tachyonic mass of the scalar field, and the dimensionless λ governing the scalar self-interactions. In the coupling function above, and throughout the remainder of this thesis, we assume that $\phi \ll M_{\rm sym}/M_{\rm pl}$ to suppress higher-order terms in $A(\phi)$.

This choice of potential and coupling results in an effective potential

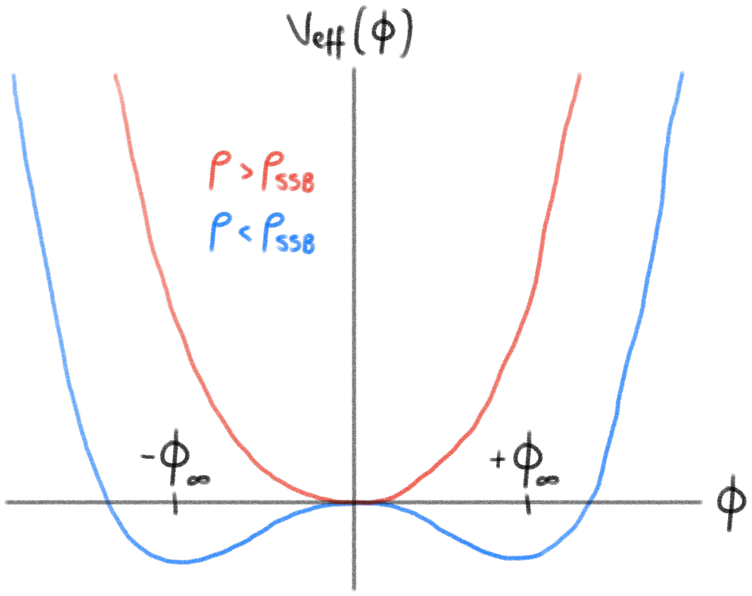


Figure 1.1: A sketch of the symmetron effective potential, eq. (1.114). When $\rho > \rho_{\rm SSB}$ (red), the potential has a single minimum at $\phi = 0$. When $\rho < \rho_{\rm SSB}$ (blue), the symmetry is spontaneously broken, and the field falls into one of two minima at $\phi = \pm\phi_\infty$, while $\phi = 0$ becomes unstable.

eq. (1.65) with the necessary SSB properties,

$$V_{\rm eff}(\phi) = \frac{1}{2L_{\rm c}^2}\left[\frac{1}{2}\left(\frac{\rho}{\rho_{\rm SSB}} - 1\right)\phi^2 + \frac{\lambda}{4}\left(\frac{M_{\rm pl}}{\mu}\right)^2\phi^4\right], \tag{1.114}$$

where $L_{\rm c}$ and $\rho_{\rm SSB}$ are the background Compton wavelength and SSB density scale, respectively, expressed as

$$L_{\rm c}^2 = \frac{1}{2}\left(\frac{M_{\rm pl}}{\mu}\right)^2 L_{\rm pl}^2\,, \tag{1.115}$$

$$\rho_{\rm SSB} = \left(\frac{M_{\rm sym}\mu}{M_{\rm pl}^2}\right)^2 \frac{M_{\rm pl}}{L_{\rm pl}^3}\,. \tag{1.116}$$

This effective potential possesses a $\mathbb{Z}_2$ symmetry, $\phi \to -\phi$. A sketch of the effective potential is shown in figure 1.1. When $\rho > \rho_{\rm SSB}$, the effective potential has a single minimum at $\phi = 0$, and the theory is symmetric. In this regime, the coupling to matter vanishes, and thus the fifth force is screened. When $\rho < \rho_{\rm SSB}$, the minimum at $\phi = 0$ becomes unstable, and the field rolls into one of the two new minima at $\phi = \pm\phi_\infty$, spontaneously breaking the symmetry.

As in the general case, eq. (1.64), taking the derivative of the effective potential eq. (1.114) with respect to ϕ yields the static symmetron equation of motion for non-relativistic matter,

$$\nabla^2\phi = \frac{1}{2L_{\rm c}^2}\left[\left(\frac{\rho}{\rho_{\rm SSB}} - 1\right)\phi + \lambda\left(\frac{M_{\rm pl}}{\mu}\right)^2\phi^3\right]. \tag{1.117}$$

We find the vacuum field value by considering solutions to eq. (1.117) in an infinite box of density ρ. When $\rho > \rho_{\rm SSB}$, the field is screened and $\phi = 0$. If $\rho < \rho_{\rm SSB}$, then our scalar field falls into one of two solutions

$$\phi = \pm\phi_\infty \equiv \pm\phi_{\rm vev}\sqrt{1 - \frac{\rho}{\rho_{\rm SSB}}}\,, \tag{1.118}$$

where $\phi_{\rm vev}$ is the vacuum expectation value given by

$$\phi_{\rm vev} = \frac{1}{\sqrt{\lambda}}\frac{\mu}{M_{\rm pl}}\,. \tag{1.119}$$

It is possible to reduce the three-parameter equation of motion given in eq. (1.117), to a two-parameter one by rescaling the field by its vacuum expectation value, $\varphi = \phi/\phi_{\rm vev}$. Doing so, we obtain the simpler two-parameter equation of motion,

$$\nabla^2\varphi = \frac{1}{2L_{\rm c}^2}\left[\left(\frac{\rho}{\rho_{\rm SSB}} - 1\right) + \varphi^2\right]\varphi\,. \tag{1.120}$$

This is the equation of motion we will solve numerically for input parameters $M_{\rm sym}$ and $L_{\rm c}$, as outlined in section 2.2. We choose to work with $M_{\rm sym}$ and $L_{\rm c}$ as our free parameters since they have more a direct physical interpretation, i.e. the vacuum value of the coupling strength and Compton wavelength of the theory, respectively.

The acceleration that a test particle experiences due to the scalar fifth force, eq. (1.63), is given by

$$\boldsymbol{a}_5 = -\phi_{\rm vev}^2\left(\frac{M_{\rm pl}}{M_{\rm sym}}\right)^2\varphi\boldsymbol{\nabla}\varphi\,. \tag{1.121}$$

Note that despite reducing the equation of motion to two parameters, the theory remains a three-parameter one, as the scaling of the fifth force with

$\phi^2_{\rm vev}$ reintroduces a dependence on λ. In essence, the shape of the field profile is determined by $M_{\rm sym}$ and $L_{\rm c}$, while the strength of the fifth force is scaled by λ.

The λ parameter can be tuned (in terms of the other model parameters) to ensure that fifth forces are similar in strength to gravitational forces. One can also choose the parameter μ (or equivalently $L_{\rm c}$) in terms of $M_{\rm sym}$ such that $\rho_{\rm SSB}$ is of the order of the current mean density of the Universe. This ensures the theory is screened in high-density environments, such as the Solar System, and the symmetry is broken only in low-density environments today. Depending on the chosen scale, this effect will impact the growth of structure in the late Universe (Davis et al., 2012a) or affect measurements of the Hubble constant (Hinterbichler et al., 2011; Jain et al., 2013; Högås and Mörtsell, 2023). Additionally, due to the symmetry-breaking nature of the theory, the Universe is expected to be filled with symmetron domain walls, which provide another phenomenological observational tool (Christiansen et al., 2024).

1.3.8 Tests of Gravity

There exists a breadth of literature across an enormous range of scales testing the validity of GR and constraining deviations from it. In this section, we provide a whistle-stop tour of some of these tests, focusing on those that yield the tightest constraints on Hu-Sawicki $f(R)$ and symmetron models. We refer the reader to Will (2014) for a comprehensive review of tests of GR, and to Koyama (2016); Saridakis et al. (2021a) for reviews of tests of modified gravity, as well as Burrage and Sakstein (2018) for a chameleon and symmetron focused review. Broadly speaking, tests of modified gravity can be categorised into three types: laboratory tests, Solar System tests, and astrophysical tests.

Laboratory Tests

Laboratory tests of gravity are typically performed in controlled environments, often within vacuum chambers, allowing for unmatched precision. These tests either directly measure fifth forces by searching for deviations from the inverse-square law of gravity, or they search for novel interactions between matter and dark energy. Such experiments include:

- Torsion balance experiments (Adelberger et al., 2003; Lambrecht et al., 2005; Kapner et al., 2007; Zhao et al., 2021)
- Casimir force experiments (Lamoreaux and Buttler, 2005; Decca et al., 2007, 2010; Lambrecht and Reynaud, 2011; Brax et al., 2007; Brax et al., 2010; Almasi et al., 2015)
- Levitated force sensors (Geraci et al., 2010; Rider et al., 2016; Yin et al., 2022)
- Atom interferometry (Burrage et al., 2015a; Hamilton et al., 2015; Burrage and Copeland, 2016; Elder et al., 2016; Burrage et al., 2016; Jaffe et al., 2017; Bertoldi et al., 2021)
- Precision atomic tests (Simon et al., 1980; Schwob et al., 1999; Jaeckel and Roy, 2010; Brax and Burrage, 2011)
- Neutron experiments (Brax and Pignol, 2011; Ivanov et al., 2013; Cronenberg et al., 2015)

Of these experiments, torsion balance and atom interferometry tests currently provide the tightest constraints on chameleon models, ruling out large portions of parameter space.

Torsion balance experiments search for deviations from the inverse-square law of gravity at sub-millimetre scales. These experiments involve two suspended masses, one of which acts as a source mass, while the other

acts as a test mass. The masses are arranged in such a way to precisely cancel out inverse-square forces, making them highly sensitive to fifth forces. In Eöt-Wash versions (Adelberger et al., 2003; Lambrecht et al., 2005; Kapner et al., 2007), the masses are cylindrical discs, with holes in them to generate a torque from higher multipole moments. The source mass is rotated to cancel out the Newtonian torque, leaving only modified gravity effects. It should be noted that these experiments are typically performed in vacuum chambers to reduce noise and environmental factors. This means the tests are limited to scalar models with a sufficiently small Compton wavelength, such that the field is able to vary within the vacuum chamber, inducing fifth forces through the scalar gradient. This makes their application to astrophysically-relevant symmetron models with large Compton wavelengths difficult.

Atom interferometry experiments use the wave-like nature of atoms to precisely measure gravitational acceleration effects. In these experiments, cold atoms in a quantum superposition are driven down two paths using laser pulses. One path passes close to a source mass, producing GR and fifth forces, while the other path is kept far away. The two paths are then recombined, and the interference pattern is measured. Any difference in the phase of the two paths can be attributed to the gravitational interaction of the atoms near the source mass. Atoms in a vacuum chamber are unscreened for a large range of parameters. As such, atom interferometry can be applied to a wide range of scalar field models, making them particularly useful for testing chameleon and symmetron models (Jaffe et al., 2017; Burrage et al., 2016). Space-based atomic interferometry experiments have also been proposed, which would allow for even greater sensitivity at large Compton wavelengths (Bertoldi et al., 2021).

Between these two types of experiments (Zhao et al., 2021; Jaffe et al., 2017) (and with little help from levitated force sensors (Yin et al., 2022)), the $n = 1$ chameleon model, eq. (1.92), is constrained for the whole param-

eter space relevant to dark energy, i.e. $V_0 = \Lambda_{\rm DE} \sim 2.4 \times 10^{-3}\,{\rm eV}$, effectively ruling out the $(n = 1)$ chameleon model as a dark energy candidate. Current constraints for symmetron models from atom interferometry experiments place bounds on $10^{-3} \lesssim M_{\rm sym}/{\rm GeV} \lesssim 10^{2}$ for $10^{-5} \lesssim \mu/{\rm eV} \lesssim 10^{-4}$ (Burrage et al., 2016; Jaffe et al., 2017).

Solar System Tests

Tests of gravity within the Solar System rely on high-precision measurements of the motion of the Moon, planets, and spacecraft. These investigations can be broadly divided into two categories: tests of the inverse-square law and tests of the equivalence principle. Key examples include

- Lunar laser ranging (Williams et al., 2004; Hofmann and Müller, 2018)
- Planetary dynamics (Ruggiero and Iorio, 2007; Iorio, 2007b,a, 2009; Fienga et al., 2010, 2011; Fienga and Minazzoli, 2024)
- Satellite and spacecraft tests (Bertotti et al., 2003; Everitt et al., 2011; Touboul et al., 2017, 2019)
- Deflection of light (Shapiro et al., 2004)

These experiments predominantly probe for violations of the equivalence principle and have consistently yielded results in strong agreement with General Relativity (GR). For instance, lunar laser ranging experiments measure the Earth-Moon separation by bouncing laser beams off retroreflectors placed on the Moon's surface during the Apollo missions. Using this technique, Hofmann and Müller (2018) confirmed that the equivalence principle is satisfied to an exceptional degree of precision, finding $\Delta m_g/m_i \lesssim 10^{-14}$.

In the context of modified gravity theories, this strong agreement with GR suggests that any alternative gravitational effects are screened within

the Solar System. For this to occur, the screening mechanism must operate on a galactic scale, screening the Milky Way out to the Solar System. In chapter 3, we show the parameters this requirement corresponds to for Hu-Sawicki $f(R)$ gravity and the symmetron model, figure 3.5.

Astrophysical Tests

Astrophysical tests of gravity leverage observations of celestial objects and large-scale structures to probe gravitational interactions over vast distance and energy scales that are inaccessible to laboratory experiments. As such, these tests often provide complementary constraints to laboratory and Solar System tests, probing different regimes of gravitational interactions. A non-exhaustive list of astrophysical tests include:

- Distance indicators (Knox et al., 2006; Sakstein, 2013; Jain et al., 2013; Desmond et al., 2019b; Desmond and Sakstein, 2020; Högås and Mörtsell, 2023)
- Stellar structure (Davis et al., 2012b; Sakstein, 2013; Sakstein et al., 2014; Sakstein, 2015a,b)
- Galaxy clusters (Terukina et al., 2014; Wilcox et al., 2016; Pizzuti et al., 2020)
- Galactic dynamics (Hui et al., 2009; Keselman et al., 2009; Jain and VanderPlas, 2011; Vikram et al., 2013; Desmond et al., 2018b,a; Naik et al., 2020; Desmond and Ferreira, 2020)
- Rotation curves (Vikram et al., 2014; Naik et al., 2018, 2019; Landim et al., 2024)
- Weak lensing (Jain and Taylor, 2003; Song, 2006; Amendola et al., 2008; Schmidt, 2008; Thomas et al., 2009; Liu et al., 2016; Martinet et al., 2021; Davies et al., 2024)

See also Baker et al. (2019); Sakstein (2020) for an overview of astrophysical tests.

These tests are most relevant to the work presented in this thesis, and we will reference them in later chapters where appropriate. Here we briefly highlight a few of the most pertinent tests. In particular, for Hu-Sawicki $f(R)$ gravity, the most stringent constraints come from measurements of galactic dynamics, thanks in large part to the vast range of densities probed across the extent of a galaxy. Currently, the most robust bounds on $f(R)$ gravity lie at $|f_{R0}| \lesssim 10^{-8}$, thanks to two independent constraints from measurements by Desmond and Ferreira (2020) and Landim et al. (2024). These tests rely on the fact that in $f(R)$ gravity, different components of a galaxy can be screened to different degrees, leading to observable disparities. For example, in Desmond and Ferreira (2020) (and previous work in the series (Desmond et al., 2018c,b,a)), the authors search for offsets between the self-screened stellar component and diffuse gaseous components of galaxies, as well as the secondary effect of the warping of stellar discs as a result of the now offset centres of mass. Finding no statistical correlation between these effects and the expected fifth force exerted by external galaxies (determined in part by state-of-the-art fifth force mapping of our local Universe (Desmond et al., 2018c)), the authors place tight constraints on f_{R0}. In a similar, albeit different, approach, Landim et al. (2024) used the SDSS-IV MaNGA Survey (Bundy et al., 2015) to search for differences in the ratios of rotational speeds between the stellar and gaseous components of galaxies.

For symmetron models, the constraints are more complex. This is due in part to the more recent development of the model, the larger parameter space, and the non-trivial relationship between symmetron and other commonly studied modified gravity models. Consequently, the symmetron model is currently less well-constrained than chameleon models. Typically, results focus on constraining one of the parameters while fixing the others,

or performing tests for specific choices of all three parameters. Producing a definitive map of symmetron constraints could itself prove to be an insightful thesis topic.

1.4 Weak Lensing

Gravitational lensing is the deflection of light rays by massive objects, an effect predicted by GR and confirmed by numerous observations (Eddington, 1919; Dyson et al., 1920). In the weak lensing regime, the deflections are small, leading to subtle distortions in the shapes of background galaxies. These distortions — otherwise known as 'cosmic shear' — can be statistically measured to infer the mass distribution of foreground structures, such as galaxies and galaxy clusters (Bartelmann and Schneider, 2001b; Hoekstra and Jain, 2008; Kilbinger, 2015). [22] Weak lensing is a powerful tool for testing gravity on cosmological scales, as it directly probes the gravitational mass and can be used to map the distribution of dark matter, or as a measure of cosmic structure growth and thus inferred dark energy properties (Troxel and Ishak, 2015; Mandelbaum, 2018).

In chapter 5, we will explore the use of weak lensing to test modified gravity theories, developing new methodology to determine the effect of conformally coupled scalars on weak lensing, and considering the particular case of symmetron models. As such, it is pertinent to briefly introduce the formalism of weak lensing here. We refer the reader to Bartelmann and Schneider (2001b); Hoekstra and Jain (2008); Kilbinger (2015) for comprehensive reviews of weak lensing.

In weak lensing, the photon is assumed to travel from $r = \infty$, approach the mass at some minimum distance b, known as the impact parameter,

[22] We note that 'cosmic shear' technically refers only to the anisotropic stretching of background images. The other component of weak lensing is convergence, or magnification, which describes the isotropic scaling of the image size. While shear is the primary observable for shape measurement, both effects are integral to the full description of weak lensing.

get an impulse from the mass, and then escape back to $r = \infty$, having been deflected into the observers telescope. In this approximation, the mass acts as a thin lens, i.e. the deflection occurs instantaneously at the point of closest approach. Immediately prior to the graviational imparting of momentum, the photon will be deflected by an angle $\Delta\theta$. See figure 1.2 for a schematic of this setup.

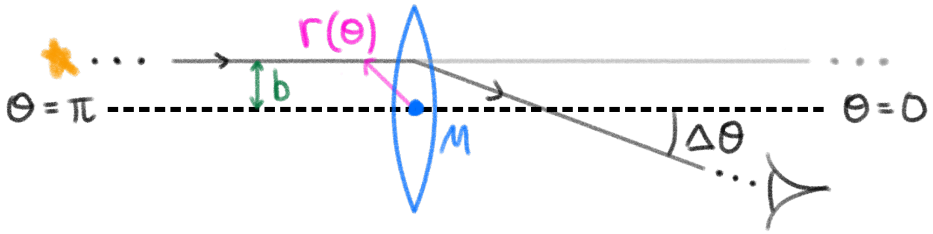


Figure 1.2: Schematic of weak lensing geometry. A photon travels from a distant source, is deflected by a mass at an impact parameter b, and is observed by a telescope. The deflection angle is $\Delta\theta$.

A good starting point for our calculation is the exterior Schwarzschild metric, which describes the spacetime around a static point mass, M,

$$\mathrm{d}s^2 = -\left(1 - \frac{2GM}{r}\right)\mathrm{d}t^2 + \left(1 - \frac{2GM}{r}\right)^{-1}\mathrm{d}r^2 + r^2(\mathrm{d}\vartheta^2 + \sin^2\vartheta\mathrm{d}\theta^2) \tag{1.122}$$

where $\vartheta \in [0, \pi]$ and $\theta \in [0, 2\pi)$ are the usual spherical coordinates. We can set $\vartheta = \pi/2$ and $\dot{\vartheta} = 0$ without loss of generality. Our system is static and spherically symmetric. These symmetries will necessarily result in the conserved quantities

$$E = -\left(1 - \frac{2GM}{r}\right)\frac{\mathrm{d}t}{\mathrm{d}\tau} \qquad \text{and} \qquad h = r^2\frac{\mathrm{d}\theta}{\mathrm{d}\tau}\,. \tag{1.123}$$

Here E is the rest energy per unit mass of the test particle, and h is the angular momentum per unit mass. The path of a photon in this spacetime is given by the null geodesic condition, $ds^2 = 0$. This leads to the equation of motion for a photon,

$$\frac{1}{2}\left(\frac{\mathrm{d}r}{\mathrm{d}\tau}\right)^2 + \left(1 - \frac{2GM}{r}\right)\frac{h^2}{2r^2} = \frac{E^2}{2}\,. \tag{1.124}$$

To better understand the deflection of light rays it is useful to adopt the inverse radial coordinate, $u = 1/r$. Using the conserved quantities, we can rewrite the equation of motion, eq. (1.124) as,

$$\left(\frac{\mathrm{d}u}{\mathrm{d}\theta}\right)^2 + u^2\left(1 - 2GMu\right) = \frac{E^2}{h^2}\,. \tag{1.125}$$

The turning point of the photon trajectory occurs when $du/d\theta = 0$, at $r = b$. From this knowledge, and the above equation, we find that

$$\frac{E^2}{h^2} = \frac{1}{b^2}(1 - \frac{2GM}{b})\,. \tag{1.126}$$

which reduces to $h \approx bE$ in the the weak field limit, $GM/b \ll 1$. Differentiating the equation of motion, eq. (1.125), with respect to θ yields,

$$\frac{\mathrm{d}^2u}{\mathrm{d}\theta^2} + u = 3GMu^2\,. \tag{1.127}$$

This equation demonstrates a clear relationship between the gravitational mass, M, and the curvature of the photon path, encoded within $u(\theta)$.

We can solve equation (1.127) perturbatively in the weak field limit, i.e. $u \approx u_0 + \frac{GM}{b}u_1$, solving u_0 to zeroth order in GM/b and u_1 to first order. To find u_0 we neglect the mass term on the right-hand side, resulting in

$$\frac{\mathrm{d}^2u_0}{\mathrm{d}\theta^2} + u_0 = 0\,, \tag{1.128}$$

which has the general solution

$$u_0(\theta) = \frac{\sin\theta}{b}\,, \tag{1.129}$$

where we have applied the boundary condition $u_0(\pi/2) = 1/b$. This solution is the straight line trajectory, in figure 1.2, i.e. $y \equiv r\sin\theta = b$. Now solving to leading order in GM/b, the equation of motion for u_1 is

$$\frac{\mathrm{d}^2u_1}{\mathrm{d}\theta^2} + u_1 = 3bu_0^2 = \frac{3\sin^2\theta}{b}\,. \tag{1.130}$$

This results in the general solution

$$u_1(\theta) = A\cos\theta + B\sin\theta + \frac{1}{2b}\left(3 + \cos 2\theta\right)\,. \tag{1.131}$$

The constants A and B associated with the complimentary solution can be determined by matching them to the straight line initial trajectory, i.e. $u_1 \to 0$ as $\theta \to \pi$. This leads to $A = 2/b$ and $B = 0$. Thus, the full solution to first order is

$$u(\theta) = \frac{\sin\theta}{b} + \frac{GM}{2b^2}\left(3 + 4\cos\theta + \cos 2\theta\right) . \tag{1.132}$$

To determine the total deflection angle, $\Delta\theta$, one must consider the asymptotic behaviour of the photon trajectory as $r \to \infty$, or equivalently $u \to 0$. For the straight line solution this occurs at $\theta = 0$. However for the full solution, the mass causes a deflection to $\theta = -\Delta\theta$ (see figure 1.2). Assuming this deflection angle is small, such that $\sin\theta \approx \theta$ and $\cos\theta \approx 1$, we find

$$\Delta\theta \approx \frac{4GM}{b} . \tag{1.133}$$

This is the classic result for the deflection of light by a point mass in GR, and was used to verify the theory during the solar eclipse of 1919 (Eddington, 1919). Assuming the light barely grazes the surface of the Sun, such that $b = R_\odot$, and given $M = M_\odot$, we expect (and measure) a deflection angle of $\Delta\theta \approx 1.8''$.

Chapter 2

Methodology

The work in this chapter develops the foundational methods required to model galaxies and the scalar fields within them. To provide a clear and centralised reference, and to avoid repetition, these methodologies are described in full here. They form the basis for the results presented in Chapters 3, 4, and 5, with any specific adaptations noted in the relevant sections. The contents of this chapter are largely based on our published work within Burrage et al. (2024).

2.1 Galactic Parameter Pipeline

In section 1.2.3, we introduced our models for the components of a galaxy: the NFW profile for the dark matter halo, eq. (1.50), and the exponential disc profile for the baryonic disc, eq. (1.56). Each of these profiles introduces several parameters that must be specified to fully define the density profile of a given galaxy. In total, we have five parameters: two for the NFW profile ($\rho_{\rm NFW}$ and $r_{\rm NFW}$) and three for the disc profile ($\Sigma_{\rm disc}$, $R_{\rm disc}$, and $z_{\rm disc}$). The work in this section invokes a series of empirical scaling relations to estimate these five parameters from a single base input parameter ($M_{\rm vir}$ or $M_{\rm disc}$). An overview of the pipeline is given in figure 2.1, and the details of each step are given in the remainder of this section. We do this to simplify our analysis, reducing the dimensionality of our galactic

models, and allowing us to focus on the impact of the scalar field parameters, whilst also retaining the ability to model a wide range of realistic galaxies.

It is important to note that by determining galaxy properties via a hierarchical series of one-dimensional scaling relations (e.g., determining stellar mass solely from halo mass, then radius solely from stellar mass), we are making a simplifying assumption. Ideally, one would determine parameters by sampling from a single N-dimensional joint probability distribution that captures the complex correlations between all five parameters simultaneously. However, constructing such a distribution requires a homogeneous dataset where all properties are measured for the same large population of galaxies, which is not currently available. By composing widely accepted 1-D relations, we implicitly assume that the parameters are conditionally independent given the preceding step in the pipeline (effectively a Markov-like assumption).

While the set of galactic density parameters are necessary to fully define the density profile of a given galaxy, they are not all directly observable and cannot always be taken as direct inputs from observational data. In fact, depending on the scope of the survey, the main parameters that we can typically observe are twofold: the flux (perceived brightness) and the redshift. From these two fundamental measurements, many other parameters can be implied. For example, from the redshift we can estimate the distance to the galaxy, assuming a cosmological model. From the distance and flux, we can calculate the luminosity (the intrinsic brightness) of the galaxy. From the luminosity, we can estimate the stellar mass of the galaxy, assuming a mass-to-light ratio. Additionally, from the observed light, we can measure the broadening of spectral lines, which can model the velocity dispersion of the galaxy, which relates to the virial mass of the galaxy.

All of these galactic properties are interconnected, and empirical relations exist that associate them to one another. As such, any one of them

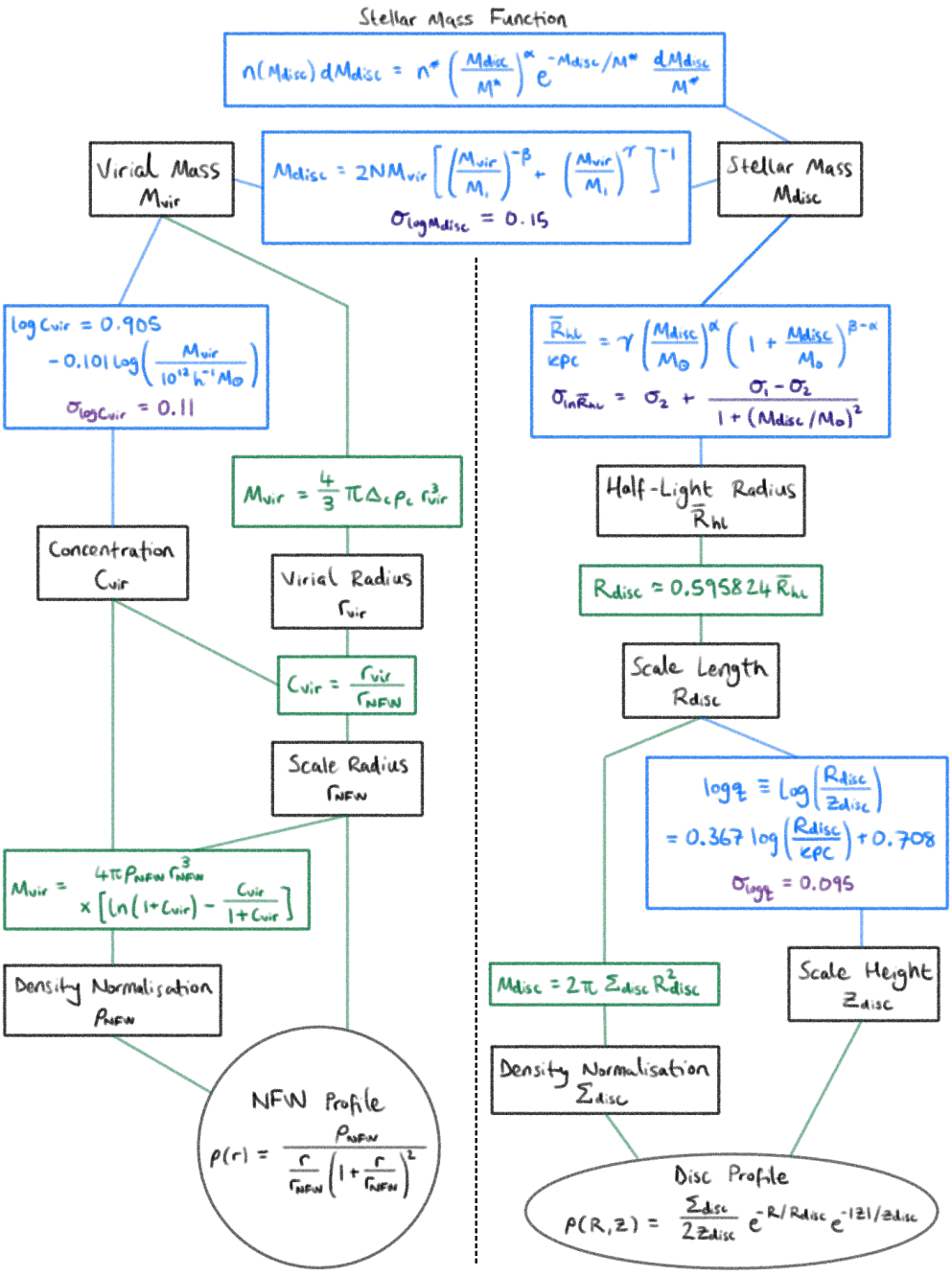


Figure 2.1: A flowchart illustrating the pipeline used to estimate the galactic parameters, contained within black boxes, from a single base input parameter. Deterministic relations are shown in green, while empirical scaling relations and their associated intrinsic scatter are blue. The left branch of the flowchart pertains to the dark matter halo, while the right branch pertains to the baryonic disc.

can serve as a reliable metric for the galaxy and provide a foundation from which to determine the other unmeasurable parameters. In chapters 3 and 4, we use the virial mass, $M_{\rm vir}$, as our base input parameter, from which we estimate all five required density parameters ($\rho_{\rm NFW}$, $r_{\rm NFW}$, $\Sigma_{\rm disc}$, $R_{\rm disc}$, and $z_{\rm disc}$) using a series of empirical scaling relations. In chapter 5, we modify this approach by starting with a Stellar Mass Function (SMF), thereby using the stellar mass as our base input parameter.

2.1.1 Galactic Parameter Relations

Mass Relations

Regardless of the choice of starting parameter ($M_{\rm vir}$ or $M_{\rm disc}$), the initial step of our pipeline is the same: estimate one with the other using an empirical Stellar-Halo Mass Relation (SHMR). The SHMR is well-studied, and many unique versions exist in the literature, established using different methods and datasets. However, they all broadly agree with one another, so the choice of SHMR is not critical to our results. We adopt the SHMR from Moster et al. (2013), which is determined by matching ΛCDM simulations to observations using a method called 'abundance matching' (a technique that assumes lighter galaxies reside in lighter haloes, matching the two populations by their respective number densities). This SHMR is defined by eq. 2 in Moster et al. (2013):

$$M_{\rm disc} = 2NM_{\rm vir}\left[\left(\frac{M_{\rm vir}}{M_1}\right)^{-\beta} + \left(\frac{M_{\rm vir}}{M_1}\right)^{\gamma}\right]^{-1}, \tag{2.1}$$

where the four fitting parameters and related errors are given in table 3 of Moster et al. (2013). The above equation represents the mean value of the SHMR. Since two galaxies with the same halo mass can have different stellar masses due to differing halo concentrations, formation histories, environments, etc., there is intrinsic scatter about this mean relation. The intrinsic scatter on the resulting stellar mass is modelled as log-normal with

$\sigma_{\log M_{\rm disc}} \approx 0.15\,\mathrm{dex}$ (see the text preceding § 3.1 in Moster et al. (2013)). This relation is used bidirectionally: to determine $M_{\rm disc}$ from $M_{\rm vir}$ in chapters 3 and 4, and to determine $M_{\rm vir}$ from $M_{\rm disc}$ in chapter 5.

In the remainder of this section, we detail the other scaling relations we use to estimate our five density parameters from the two masses, $M_{\rm vir}$ and $M_{\rm disc}$.

NFW Parameters

For the dark matter component, an NFW profile, eq. (1.50), is uniquely defined in terms of one of two parameter sets: $\rho_{\rm NFW}$ and $r_{\rm NFW}$, or $M_{\rm vir}$ and $c_{\rm vir}$. Knowledge of either set allows us to derive the other, as we demonstrate at the end of this subsection. We choose to parameterise the NFW profile with $M_{\rm vir}$ and $c_{\rm vir}$, since the virial mass is more physically relevant and we already have $M_{\rm vir}$ as an input parameter. Therefore, we need only employ a single empirical relation between the virial mass and concentration parameter to fully describe the density profile. For this, we use equation 8 of Dutton and Macciò (2014),

$$\log c_{\rm vir} = 0.905 - 0.101 \log \left(\frac{M_{\rm vir}}{10^{12} h^{-1} M_\odot} \right) , \tag{2.2}$$

where h is the Hubble parameter, taken to be 0.7. This relation reflects the well-known result from ΛCDM simulations that more massive dark matter haloes are less centrally concentrated. The intrinsic scatter is log-normal with $\sigma_{\log c_{\rm vir}} = 0.11$ (see the end of §4.1 in Dutton and Macciò (2014)).

At this point, $\rho_{\rm NFW}$ and $r_{\rm NFW}$ can be obtained from $M_{\rm vir}$ and $c_{\rm vir}$ through simultaneous solution of

$$M_{\rm vir} = \frac{4}{3} \pi \Delta_c \rho_c r_{\rm vir}^3 , \tag{2.3}$$

$$r_{\rm vir} = c_{\rm vir} r_{\rm NFW} , \tag{2.4}$$

$$M_{\rm vir} = 4\pi \rho_{\rm NFW} r_{\rm NFW}^3 \left[\ln(1 + c_{\rm vir}) - \frac{c_{\rm vir}}{1 + c_{\rm vir}} \right] , \tag{2.5}$$

which are derived, respectively, from the definition of the virial mass, eq. (1.47), the definition of the concentration parameter, eq. (1.51), and the formula for the enclosed mass at a given radius under the NFW profile, eq. (1.52), evaluated at the virial radius.

Galactic Disc Parameters

We now aim to define the three parameters ($R_{\rm disc}$, $z_{\rm disc}$, and $\Sigma_{\rm disc}$) of the galactic disc profile, eq. (1.56), from the stellar mass $M_{\rm disc}$. To begin, we perform the intermediate step of relating the stellar mass to the half-light radius $\overline{R}_{\rm hl}$, which is, perhaps unsurprisingly, the radius that contains half of the galaxy's light. This relation comes from the observational results of Shen et al. (2003), who studied the size distribution of over 140,000 galaxies from the Sloan Digital Sky Survey (SDSS). We use their results for late-type (i.e., disc) galaxies, specifically equation 18 of Shen et al. (2003):

$$\frac{\overline{R}_{\rm hl}}{\rm kpc} = \gamma \left(\frac{M_{\rm disc}}{M_\odot}\right)^{\alpha} \left(1 + \frac{M_{\rm disc}}{M_0}\right)^{\beta-\alpha} , \tag{2.6}$$

where the fitting parameters (α, β, γ, and M_0) take the values from the bottom row of table 1 in Shen et al. (2003). The intrinsic scatter about this relation is mass-dependent and is given by eq. 19 of Shen et al. (2003):

$$\sigma_{\ln \overline{R}_{\rm hl}} = \sigma_2 + \frac{\sigma_1 - \sigma_2}{1 + (M_{\rm disc}/M_0)^2} , \tag{2.7}$$

where M_0, σ_1, and σ_2 again take the values from the bottom row of table 1 in Shen et al. (2003).

Next, we relate the half-light radius (and thus the stellar mass) to the disc scale length, $R_{\rm disc}$. By assuming a constant mass-to-light ratio within the galaxy, we can use the half-light radius as a proxy for the half-mass radius.[1] This allows us to relate $R_{\rm disc}$ to $\overline{R}_{\rm hl}$ via the enclosed mass for a

[1] Realistically, the mass-to-light ratio decreases with radius as central stellar populations are typically older and have a higher mass-to-light ratio. This implies the mass is more concentrated than the light, meaning the half-mass radius is slightly smaller than the half-light radius. However, this effect is small compared to the intrinsic scatter in the size-mass relation.

stellar disc, eq. (1.57),

$$\begin{aligned}
\frac{1}{2}M_{\rm disc}(R\to\infty) &= M_{\rm disc}(R=\overline{R}_{\rm hl}) \\
\frac{1}{2}\left(2\pi\Sigma_{\rm disc}R_{\rm disc}^2\right) &= 2\pi\Sigma_{\rm disc}R_{\rm disc}^2\left[1-\left(1+\frac{\overline{R}_{\rm hl}}{R_{\rm disc}}\right)\mathrm{e}^{-\overline{R}_{\rm hl}/R_{\rm disc}}\right] \\
\Rightarrow \frac{1}{2} &= 1-\left(1+\frac{\overline{R}_{\rm hl}}{R_{\rm disc}}\right)\mathrm{e}^{-\overline{R}_{\rm hl}/R_{\rm disc}}\,. \qquad (2.8)
\end{aligned}$$

This can be rearranged to give an implicit equation for $R_{\rm disc}$ in terms of $\overline{R}_{\rm hl}$, which can be solved using the Lambert function, $W_n(z)$, defined as the inverse function of the relation $we^w = z$. In our case, this yields the solution

$$R_{\rm disc} = -\overline{R}_{\rm hl}\left(1+W_{-1}\left(-\frac{1}{2e}\right)\right) \approx 0.595824\overline{R}_{\rm hl}\,, \qquad (2.9)$$

where $W_{-1}(x)$ is the $n=-1$ solution to the Lambert W_n function.

With the disc scale length defined, we can now determine the disc surface density, $\Sigma_{\rm disc}$, via the enclosed mass of the stellar disc, equation (1.57). As in the previous paragraph, the total disc mass is given by

$$M_{\rm disc}(R\to\infty) = 2\pi\Sigma_{\rm disc}R_{\rm disc}^2\,, \qquad (2.10)$$

which can be simply rearranged to give $\Sigma_{\rm disc}$ in terms of $M_{\rm disc}$ and $R_{\rm disc}$.

Finally, we employ one last observational relation to determine the disc scale height, $z_{\rm disc}$, in terms of the disc scale radius $R_{\rm disc}$. For this, we utilise eq. 1 of Bershady et al. (2010):

$$\log(q) \equiv \log\left(\frac{R_{\rm disc}}{z_{\rm disc}}\right) = 0.367\log\left(\frac{R_{\rm disc}}{\rm kpc}\right) + 0.708\,. \qquad (2.11)$$

Rearranging this expression gives $z_{\rm disc}$ in terms of $R_{\rm disc}$. The intrinsic scatter about this relation is given by $\sigma_{\log q} = 0.095$, which we assume to be log-normally distributed.

2.1.2 Galactic Parameter Generation

In chapters 3 and 4, we use the virial mass, $M_{\rm vir}$, as our base input parameter,[2] from which we estimate all five required density parameters ($\rho_{\rm NFW}$, $r_{\rm NFW}$, $\Sigma_{\rm disc}$, $R_{\rm disc}$, and $z_{\rm disc}$) using the series of empirical scaling relations described in the above section, and outlined in figure 2.1. These works focus on the impact of scalar fields on the dynamics of individual galaxies. As such, we are interested in testing our model over a range of galactic masses, rather than a statistically relevant population of galaxies. To this end, we generate parameters for these works using the pipeline described above, assuming all galactic density parameters take their mean values, i.e. assuming no scatter on the relations laid out. This results in a deterministic mapping from $M_{\rm vir}$ to the five density parameters, essentially creating a 'maximally typical' galaxy for each choice of $M_{\rm vir}$.

In chapter 5, we wish to compare our results to a statistical analysis of observations taken from a real galaxy survey. This means we must determine our results from a statistically relevant sample of mock galaxies. This requires us to incorporate an intrinsic scatter on the various empirical relations described above, ensuring our sample is representative of the diverse range of real galaxies. We thus modify our approach by starting with a stellar mass function (SMF), representative of the observed distribution of stellar masses in the local universe. This slightly alters the flow of our pipeline, as the halo mass, $M_{\rm vir}$, is no longer the input parameters, instead it is now estimated from the stellar mass distribution sampled from the SMF.

There are many ways to construct a SMF, and we detail the specific method we use in chapter 5. Given the close relation between the luminosity and stellar mass of a galaxy, SMFs share a similar distribution to luminosity

[2]The choice of the base input parameter between $M_{\rm vir}$ and $M_{\rm disc}$ is somewhat arbitrary, but we find it more convenient to work with $M_{\rm vir}$ as it is more directly related to the total galactic mass, and thus the gravitational potential well of the galaxy.

functions, and are often modelled using a Schechter function (Schechter, 1976), as we introduced in equation (1.44). The Schechter function for a SMF is defined as

$$n(M_{\rm disc})\mathrm{d}M_{\rm disc} = n^\star \left(\frac{M_{\rm disc}}{M^\star}\right)^\alpha \exp\left(-\frac{M_{\rm disc}}{M^\star}\right)\frac{\mathrm{d}M_{\rm disc}}{M^\star}\,, \tag{2.12}$$

where $n(M_{\rm disc})\mathrm{d}M_{\rm disc}$ is the number density of galaxies with stellar masses in the interval $\mathrm{d}M_{\rm disc}$, and $n^\star$, $M^\star$, and α are fitting parameters (see e.g. (Baldry et al., 2008, 2012; Kelvin et al., 2014) for reference parameters.)[3]

From the SMF distribution, we generate a representative sample of galaxies by randomly sampling stellar masses. For each sampled stellar mass, we then utilise the SHMR to determine the corresponding halo mass, $M_{\rm vir}$, randomly sampling from the full distribution of halo masses given that stellar mass, thus incorporating the natural scatter in the empirical relation. This process is repeated for each of the relations detailed in the previous section, making sure to include the intrinsic scatter of the relation where stated. Incorporating intrinsic scatter at each step of the pipeline ensures that our sample of galaxies is diverse and statistically relevant.

To implement this pipeline to generate a large number of mock galaxies, representative of a realistic population, one could simply use standard forward modelling; sampling sequentially from the log-normal distributions of each scaling relation. However, we explicitly adopt a Markov Chain Monte Carlo (MCMC) framework to facilitate future parameter estimation. In a full analysis comparing modified gravity predictions to observational data, the specific properties of individual galaxies (masses, concentrations, etc.) act as 'nuisance parameters'. The MCMC framework is chosen because it naturally allows for these nuisance parameters to be 'marginalized over', isolating the posterior distributions of the modified gravity parameters of interest. In the remainder of this section, we detail how this methodology

[3]These works often adopt a double-Schechter function to model the SMF, which is a sum of two Schechter functions with different slope and normalisation parameters (α and $n^\star$ respectively).

is applied to generate a sample of galactic parameters that are representative of the full distributions, given the SMF as our prior 'data', and the empirical relations as our likelihoods.

Aside: Bayesian Statistics and MCMC Methods

Before detailing the MCMC method we use to generate our mock galaxy sample, we first provide a brief overview of Bayesian statistics and MCMC methods. This is intended as a concise introduction to the concepts and terminology used in this work, and is not meant to be a comprehensive review of the field. For a more detailed introduction, with a specific focus on cosmology we refer the reader to Trotta (2017).

Bayesian inference is a statistical method that updates the probability of a model as more evidence or information becomes available. It is based on Bayes' theorem, which mathematically inverts conditional probabilities to relate the probability of a model, given some data, to the probability of observing the data, given the model. This is expressed as

$$\mathcal{P}(\theta|D) = \frac{\mathcal{L}(D|\theta)\Pi(\theta)}{P(D)}\,, \tag{2.13}$$

where the terms are defined as follows:

- The **posterior**, $\mathcal{P}(\theta|D)$, is the probability distribution for the model parameters, $\theta = \{\theta_i\}$ after accounting for the data, $D = \{d_j\}$. It is the key distribution we wish to calculate.
- The **likelihood**, $\mathcal{L}(D|\theta)$, evaluates how probable our specific, observed data is, given a proposed model. It is a function of the model parameters for the fixed measured data.[4]
- The **prior**, $\Pi(\theta)$, is our initial belief about the model before observing

[4]It should be noted that the likelihood is actually a probability distribution over the data space, D, but because the data is fixed it is understood as a function of the model parameters, θ.

the data. Usually taken to be a flat prior within some bounds,[5] or a specialized non-informative prior (e.g. Jeffreys), unless there is a strong motivation to do otherwise.

- The **marginal likelihood**,[6] $P(D)$, is a normalisation factor that ensures the posterior is a valid probability distribution.

For continuous parameters, these terms are probability density functions, but Bayes' theorem is equally applicable to discrete parameters.

While elegant, calculating the posterior distribution directly can be challenging, especially for complex models with high-dimensional parameter spaces. Specifically, a brute-force grid search is computationally expensive due to the high dimensionality. Furthermore, obtaining a normalised probability distribution requires calculating the marginal likelihood, which involves a prohibitively expensive multi-dimensional integral. This is where Markov Chain Monte Carlo (MCMC) methods prove invaluable. MCMC methods are a class of algorithms that allow us to generate samples from the posterior distribution without having to calculate the normalisation explicitly. They work by constructing a Markov chain that stochastically explores the parameter space, generating a large set of samples that are representative of the posterior. From this set of samples, one can estimate the posterior distribution for a given model parameter, $\mathcal{P}(\theta_i|\{d_j\})$, by binning in θ_i space. In our case, we will utilise the sampled values of $\{\theta_i\}$ as valid representatives of the full posterior distribution. There are many different MCMC algorithms, each with its own strengths and weaknesses. Some of the most commonly used MCMC algorithms include the Metropolis-Hastings algorithm, the Gibbs sampler, and the Hamiltonian Monte Carlo (HMC) method. Each of these algorithms has its own way of proposing new samples and accepting or rejecting them based on the

[5] Note that a "flat" prior is not truly uninformative, as its shape depends on the parameterisation. For example, a prior that is uniform in a parameter θ is non-uniform in $\log\theta$.

[6] Also commonly referred to as the Bayesian evidence.

posterior distribution.

In practice, for MCMC methods, we often work with the logarithm of the posterior. The motivation for this is that the log-posterior is numerically more stable, and easier to work with, as it transforms products into sums. The log-posterior is given by

$$\ln \mathcal{P}(\theta|D) = \ln \mathcal{L}(D|\theta) + \ln \Pi(\theta) + \text{constant}\,. \tag{2.14}$$

Here the constant term is the logarithm of the marginal likelihood. Since the proportionality $\mathcal{P}(\theta|D) \propto \mathcal{L}(D|\theta)\Pi(\theta)$ is sufficient to assess the relative probability of samples, the constant, and therefore the marginal likelihood, is not required in MCMC sampling.

Assuming the model parameters are a priori independent from one another, the total log-prior can be expressed as the sum of the individual log-priors for each parameter, i.e.,

$$\ln \Pi(\theta) = \sum_i \ln \Pi_i(\theta_i)\,. \tag{2.15}$$

If we adopt flat priors, then for each parameter θ_i,

$$\Pi_i(\theta_i) = \begin{cases} \text{constant}, & \theta_i \in [\theta_{i,\min}, \theta_{i,\max}] \\ 0, & \text{otherwise} \end{cases}\,. \tag{2.16}$$

The priors enforce hard boundaries on the parameter values. In practice, this means that the prior can be used to exclude unphysical parameter values from consideration, preventing the MCMC algorithm from unnecessarily exploring these regions.

For the likelihood, if we assume that the data points are independent and normally distributed, this means that the total log-likelihood can be expressed as the sum of the individual log-likelihoods for each data point, i.e.,

$$\ln \mathcal{L}(D|\theta) = \sum_j \ln \mathcal{L}_j(d_j|\{\theta_i\})\,, \tag{2.17}$$

and that the individual likelihoods take the form of a Gaussian distribution:

$$\mathcal{L}_j(d_j|\{\theta_i\}) = \frac{1}{\sqrt{2\pi\sigma_j^2(\{\theta_i\})}} \exp\left(-\frac{1}{2}\frac{(d_j - \mu_j(\{\theta_i\}))^2}{\sigma_j^2(\{\theta_i\})}\right), \tag{2.18}$$

where $\mu_j(\{\theta_i\})$ and $\sigma_j^2(\{\theta_i\})$ are the mean and variance of the Gaussian distribution for the j-th data point. In general, μ_j and σ_j^2 (and thus $\mathcal{L}_j$) can depend on the full set of parameters $\{\theta_i\}$, or on a subset of them. In the special case where the variance is constant throughout the parameters space, $\sigma_j^2(\{\theta_i\}) = \sigma_j^2$, the Gaussian denominator term can be readily ignored as a constant contribution, which does not impact the relative probability of samples, and thus does not impact the MCMC sampling. In this case, the log-likelihood simplifies to

$$\ln \mathcal{L}(D|\theta) = -\frac{1}{2}\sum_j \left(\frac{d_j - \mu_j(\{\theta_i\})}{\sigma_j}\right)^2 + \text{constant}\,. \tag{2.19}$$

With this we have fully described the log-posterior, which can be evaluated for any set of parameters $\{\theta_i\}$, for a fixed dataset $D = \{d_j\}$. This allows us to use MCMC methods to generate samples from the posterior distribution, which can then be used as a valid representation of the parameters obeying the statistical influence of posterior distribution. In the proceeding section we demonstrate how this framework applies to our methods of sampling statistically relevant mock galaxies from the galactic scaling relations in section 2.1.1.

Galactic Parameter MCMC Sampling

To generate a statistically relevant population of mock galaxies we wish to sample over the galactic parameters, $\theta = \{\rho_{\rm NFW}, r_{\rm NFW}, \Sigma_{\rm disc}, R_{\rm disc}, z_{\rm disc}\}$, given the data of the stellar mass function, $D = \text{SMF}$. In actuality, the galactic parameters can themselves be entirely determined from the set $\theta = \{M_{\rm disc}, \overline{R}_{\rm hl}, q, M_{\rm vir}, c_{\rm vir}\}$, where each one of these parameters is the output of an empirical scaling relation, listed in the previous section (see equations

(2.12), (2.1), (2.2), (2.6), and (2.11) respectively, or see the blue relations in figure 2.1). In actuality again, we want to sample over the log of these scaling relation parameters, $\theta = \{\log M_{\rm disc}, \ln \overline{R}_{\rm hl}, \log q, \log M_{\rm vir}, \log c_{\rm vir}\}$. The reason for this is twofold: to reduce the dynamic range in numerical calculations, allowing us to adopt flat priors on the log-parameters, and to more directly relate quantities to their quoted log-scatter values. Thus we wish to let our MCMC algorithm explore the posterior distribution

$$\mathcal{P}(\theta|D) = \mathcal{P}(\{\log M_{\rm disc}, \ln \overline{R}_{\rm hl}, \log q, \log M_{\rm vir}, \log c_{\rm vir}\}|\text{SMF})\,. \tag{2.20}$$

Since the galactic parameters are related to one another in a hierarchical manner, we can decompose the likelihood as follows:

$$\begin{aligned}\mathcal{L}(D|\theta) = {} & \mathcal{L}(\text{SMF}|\log M_{\rm disc}) \\ & \times \mathcal{L}(\log M_{\rm disc}|\ln \overline{R}_{\rm hl})\mathcal{L}(\ln \overline{R}_{\rm hl}|\log q) \\ & \times \mathcal{L}(\log M_{\rm disc}|\log M_{\rm vir})\mathcal{L}(\log M_{\rm vir}|\log c_{\rm vir})\,.\end{aligned} \tag{2.21}$$

The SMF is itself a probability distribution, and since it is our initial 'observable' data, there is no intrinsic scatter associated with it. Each of the other likelihoods can be modelled as a log-normal distribution about the relevant scaling relation, with a standard deviation given by the intrinsic scatter on that relation.

The one caveat to this is the term $\mathcal{L}(\log M_{\rm disc}|\log M_{\rm vir})$, which is the likelihood associated with the *inverse* of the SHMR. An incorrect handling of this term would be to simply use the same log-normal distribution as the forward relation, $\mathcal{L}(\log M_{\rm vir}|\log M_{\rm disc})$, but with the mean and standard deviation swapped. This corresponds to an incorrect inversion because the SHMR is not a simple linear relation, but rather a more complex function; doing so would introduce an Eddington/Malmquist-like bias to our sampling. Instead, one should construct a numerical inverse SHMR, using e.g. interpolation, and then determine the appropriate scatter to use for the inverse relation. The scatter on the forward relation, $\sigma_{\log M_{\rm disc}} = 0.15$, can be

related to the inverse scatter via $\sigma_{\log M_{\rm vir}} = \left|\frac{{\rm dlog}\, M_{\rm vir}}{{\rm dlog}\, M_{\rm disc}}\right| \sigma_{\log M_{\rm disc}}$, which can be evaluated numerically, or analytically if the SHMR is simple enough. For the SHMR we use, eq. (2.1), the inverse log scatter is given by

$$\sigma_{\log M_{\rm vir}} = \left[1 - \frac{\gamma x^{\gamma} - \beta x^{-\beta}}{x^{\gamma} + x^{-\beta}}\right]^{-1} \sigma_{\log M_{\rm disc}}\,, \tag{2.22}$$

where $x = M_{\rm vir}/M_1$, and γ, β and M_1 are the constant fitting parameters of the SHMR given in Moster et al. (2013). This ensures that the scatter on the inverse relation is correctly accounted for, preventing any bias in our sampling.

With this, the final log-likelihood is given by

$$\begin{aligned}
\ln \mathcal{L}(D|\theta) = \; & \ln({\rm SMF}(\log M_{\rm disc})) \\
& - \frac{1}{2}\left(\frac{\ln \overline{R}_{\rm hl} - \mu_{\ln \overline{R}_{\rm hl}}(\log M_{\rm disc})}{\sigma_{\ln \overline{R}_{\rm hl}}(\log M_{\rm disc})}\right)^2 - \ln(\sigma_{\ln \overline{R}_{\rm hl}}(\log M_{\rm disc})) \\
& - \frac{1}{2}\left(\frac{\log q - \mu_{\log q}(\ln \overline{R}_{\rm hl})}{\sigma_{\log q}}\right)^2 \\
& - \frac{1}{2}\left(\frac{\log M_{\rm vir} - \mu_{\log M_{\rm vir}}(\log M_{\rm disc})}{\sigma_{\log M_{\rm vir}}}\right)^2 - \ln(\sigma_{\log M_{\rm vir}}) \\
& - \frac{1}{2}\left(\frac{\log c_{\rm vir} - \mu_{\log c_{\rm vir}}(\log M_{\rm vir})}{\sigma_{\log c_{\rm vir}}}\right)^2 .
\end{aligned} \tag{2.23}$$

To be explicit about the terms in the above equation:

- ${\rm SMF}(\log M_{\rm disc})$ is the stellar mass function, given by eq. (2.12).
- $\mu_{\ln \overline{R}_{\rm hl}}(\log M_{\rm disc})$ and $\sigma_{\ln \overline{R}_{\rm hl}}(\log M_{\rm disc})$ are the mean and standard deviation of the stellar mass-size relation, given by equations (2.6) and (2.7) respectively. The non-constant nature of the standard deviation means we must retain the Gaussian denominator term.
- $\mu_{\log q}(\ln \overline{R}_{\rm hl})$ is the mean of the disc scale height relation, given by eq. (2.11), with an intrinsic scatter $\sigma_{\log q} = 0.095$.
- $\mu_{\log M_{\rm vir}}(\log M_{\rm disc})$ is the mean of the inverse stellar-halo mass relation, given by eq. (2.1), with $\sigma_{\log M_{\rm vir}}$ given by eq. (2.22).

- $\mu_{\log c_{\rm vir}}(\log M_{\rm vir})$ is the mean of the halo mass-concentration relation, given by eq. (2.2), with $\sigma_{\log c_{\rm vir}} = 0.11$.
- The constant term is an arbitrary normalisation factor, coming from the prior, that does not affect the MCMC sampling.

We employ a `Python` based affine-invariant ensemble sampler `emcee` (Foreman-Mackey et al., 2013) to sample from this log-posterior distribution. The algorithm initialises a set of walkers arbitrarily within the parameter space, which then disperse and explore the distribution during a 'burn-in' phase. We ensure that the walkers are sufficiently burnt in before recording the full sample, verifying that they have reached a stable equilibrium distribution through visual inspection of the chains and their log probabilities.

Since the steps taken by MCMC walkers are dependent on their previous positions, the raw samples in a chain are correlated. To generate a population of independent mock galaxies, we must therefore post-process the chains. We calculate the maximum integrated autocorrelation time, τ, which estimates the number of steps required for the chain to 'forget' its initial state. We then 'thin' the chains by keeping only every τ-th sample. Throughout this process, we ensure the initial chain is large enough that the effective sample size, $n_{\rm eff} \approx n_{\rm chain}/\tau$, remains larger than the required number of sampled galaxies. This process yields a set of independent parameter vectors θ, each representing a unique galaxy realisation that correctly captures the intrinsic scatter and correlations of the underlying empirical relations.

Bayesian Inference for Modified Gravity Parameters

Although not utilised within this thesis, it is worth noting that Bayesian inference and MCMC methods are powerful tools that can be used to constrain the parameters of modified gravity theories using observational data,

D. In such cases, the model, θ, is the set of modified gravity parameters, and the galactic parameters are demoted to so called "nuisance parameters", $\{\psi_i\}$. The posterior distribution is then determined by "marginalising over" these nuisance parameters, i.e. integrating them out of the posterior:

$$\mathcal{P}(\theta|D) = \int \mathcal{P}(\theta, \{\psi_i\}|D) \mathrm{d}\psi_1 \mathrm{d}\psi_2 \ldots . \tag{2.24}$$

This integral can be evaluated using MCMC methods by simply including the nuisance parameters in the MCMC sampling, thereby generating samples of both the modified gravity parameters and the nuisance parameters. The posterior distribution for the modified gravity parameters is then easily estimated by binning in the modified gravity parameter space, effectively marginalising over the nuisance parameters. This approach allows us to account for uncertainties in the galactic parameters when constraining the modified gravity parameters, leading to more robust and reliable results. Indeed, the tightest constraints on $f(R)$ gravity to date have been obtained using this method (Desmond and Ferreira, 2020).

2.2 Numerical Methods

Due to the highly non-linear nature of the scalar-tensor theories we consider, analytical (or approximate analytical) solutions demand highly symmetrical, simple sources and/or idealised scalar field behaviour (Hui et al., 2009; Khoury and Weltman, 2004b; Mota and Shaw, 2007; Davis et al., 2012b; Sakstein, 2013; Burrage and Sakstein, 2016; Burrage et al., 2015b). Realistic galaxies are not perfectly symmetrical, and therefore we must resort to numerical methods to solve the equations of motion for the scalar fields. In this section, we briefly outline the numerical methods previously employed in the literature and describe the numerical solver we use to determine the scalar field profile.

Broadly speaking, numerical methods for solving the scalar field EoM

can be divided into two categories: grid-based methods and particle-based methods. Grid-based methods discretise the spatial domain into a grid, or mesh, and solve the EoM on this grid using finite difference or finite element methods. Particle-based methods, on the other hand, represent the matter distribution as a collection of particles and solve the EoM using techniques such as smoothed particle hydrodynamics or N-body simulations.

Extensive literature exists for both methods. For grid-based methods, see for example Bose et al. (2017); Naik et al. (2018); Briddon et al. (2021); Ruan et al. (2022). For particle-based methods, see for example Puchwein et al. (2013); Winther et al. (2015); Arnold et al. (2016, 2019). There also exist numerous emulators and machine learning methods to predict cosmological observables, such as the predicted power spectrum in modified gravity models; see for example Ramachandra et al. (2021); Arnold et al. (2022); Bai and Xia (2024); Hoyland et al. (2025); Gondhalekar et al. (2025).

2.2.1 Numerical Solver

Using the axisymmetric galaxy density profiles from the section 2.1.1, we solve the $f(R)$ and symmetron equations of motion, given by eqs. (1.101) and (1.120) respectively. We do this using a numerical solver based on that employed by Naik et al. (2018), updated to incorporate some optimisations suggested by Bose et al. (2017) and to include the symmetron. The solver is ultimately a two-dimensional version of the $f(R)$ solver used in the cosmological simulation code MG-GADGET (Puchwein et al., 2013): it constructs a coordinate grid, discretises the EoM on this grid, then solves this discretised EoM using an iterative Gauss-Seidel method.

Although a cylindrical polar coordinate system might seem the natural choice for the axisymmetric galaxy profiles we adopt, we instead use a two-dimensional spherical polar system (neglecting the azimuthal coordinate).

This is because the radial range of our grid should stretch from the galactic centre to several Compton wavelengths (eqs. (1.111) and (1.115)) beyond the galaxy's edge; the dynamic range is such that a spherical coordinate system better enables us to use a variable grid resolution with smaller cells in the central region and larger cells further out. Specifically, we use a logarithmic radial discretisation, i.e. cells are equally spaced in the coordinate[7] $u \equiv \ln(r/[\text{chosen length scale}])$, producing higher resolution at smaller radii, as required. Similarly, in the polar direction, θ, because the galaxy has a disc, we need a higher resolution near the disc-plane $\theta \approx \pi/2$ than at the poles. We can achieve this by discretising in the coordinate $v \equiv \cos\theta$. In principle, one could assume mirror symmetry about the disc plane and restrict v to the range $[0, 1]$, but we are often interested in the behaviour of the scalar field in the disc plane, and so wish to avoid pushing the disc plane to the boundary of the grid. We thus discretise v in the range $[-1, 1]$.[8]

In $u-v$ coordinates, the Laplace operator acting on a function f (dropping the azimuthal term) is

$$D \equiv \nabla^2 f = \frac{1}{r^3}\frac{\partial}{\partial u}\left(r\frac{\partial f}{\partial u}\right) + \frac{1}{r^2}\frac{\partial}{\partial v}\left((1-v^2)\frac{\partial f}{\partial v}\right) . \tag{2.25}$$

For later convenience, we have only expressed the derivatives in terms of u, while keeping other factors that contain r, as the conversion to u is straightforward.

We construct a regular grid in $u - v$ space. We use 512 radial (u) cells in the range $[0.05, 10^4]$ kpc, and 201 angular (v) cells. Despite the large dynamic range, our non-linear discretisation naturally concentrates grid cells in the central galactic regions, providing high precision where it is most needed. One could use a significantly smaller grid (e.g. 128 radial and

[7] Note that r is a dimensionful parameter, but choosing units here is redundant as they will be eliminated in later equations, where we are only interested in the change of u.

[8] A visualisation of the coordinate grid, out to a maximum radius of $5R_{\text{disc}}$, is given in the top-right panel of figure 3.1.

51 angular cells) and still achieve sufficient precision for the analysis within this thesis. Nevertheless, we opt to use this higher resolution grid to ensure the accuracy of our results, while remaining computationally efficient for extensive parameter space searches. The maximum radial extent of $10^4\,\mathrm{kpc}$ is several times larger than any galaxy scale considered in this work, so the field can reach the background value outside of the galaxy. By using an odd number of angular cells, we ensure that one row of the grid is centred on the disc plane. Each grid cell is labelled with indices (i, j), where i represents the u-coordinate and j represents the v-coordinate, i.e. $u = u_i$ and $v = v_j$ at cell (i, j). All other quantities (density, scalar field etc.) can be discretised on this grid. For example, we can write ρ_{ij} to represent the density at the *centre* of cell (i, j).

The Laplace operator acting on a function f, eq. (2.25), can then be discretised as

$$\begin{aligned} D_{ij} = &\frac{1}{h_u^2 r_i^3}\left[f_{i+1,j} r_{i+1/2} + f_{i-1,j} r_{i-1/2} - f_{ij}\left(r_{i+1/2} + r_{i-1/2}\right)\right] \\ &+ \frac{1}{h_v^2 r_i^2}\left[f_{i,j+1} s_{j+1/2}^2 + f_{i,j-1} s_{j-1/2}^2 - f_{ij}\left(s_{j+1/2}^2 + s_{j-1/2}^2\right)\right] , \end{aligned} \tag{2.26}$$

where h_u and h_v are the (constant) grid spacings in u and v respectively, and $s \equiv \sin\theta$, so that $s_j^2 = 1 - v_j^2$. Note that half-integer subscripts (e.g. $r_{i+1/2}$) indicate quantities evaluated at the cell edges rather than the cell centres.

We can now proceed to discretising the EoMs, eqs. (1.101) and (1.120). In the $f(R)$ case, we follow Bose et al. (2017) in redefining the scalar field as $\varphi \equiv (f_R/f_{R0})^{1/2}$. Consequently, the discretised forms of the symmetron and $f(R)$ EoM both turn out to be cubic equations of the form

$$\mathcal{L}_{ij} \equiv \varphi_{ij}^3 + p_{ij}\varphi_{ij} + q_{ij} = 0\,, \tag{2.27}$$

where the coefficients p_{ij} and q_{ij} are given in the $f(R)$ case by

$$\begin{aligned} p_{ij} &\equiv -\frac{1}{A_{ij}}\left(B_{ij}(\varphi^2) + \frac{8\pi G\delta\rho_{ij}}{3c^2 f_{R0}} + \frac{R_0}{3f_{R0}}\right); \\ q_{ij} &\equiv \frac{1}{A_{ij}}\frac{R_0}{3f_{R0}}, \end{aligned} \tag{2.28}$$

and in the symmetron case by

$$\begin{aligned} p_{ij} &\equiv \frac{\rho_{ij}}{\rho_{\rm SSB}} + 2L_{\rm c}^2 A_{ij} - 1; \\ q_{ij} &\equiv -2L_{\rm c}^2 B_{ij}(\varphi), \end{aligned} \tag{2.29}$$

and the objects A_{ij} and B_{ij} are given in turn by

$$\begin{aligned} A_{ij} &= \frac{r_{i+1/2} + r_{i-1/2}}{r_i^3 h_u^2} + \frac{s_{j+1/2}^2 + s_{j-1/2}^2}{r_i^2 h_v^2}; \\ B_{ij}(\psi) &= \frac{r_{i+1/2}\psi_{i+1,j} + r_{i-1/2}\psi_{i-1,j}}{r_i^3 h_u^2} + \frac{s_{j+1/2}^2\psi_{i,j+1} + s_{j-1/2}^2\psi_{i,j-1}}{r_i^2 h_v^2}, \end{aligned} \tag{2.30}$$

where ψ represents the argument of $B_{i,j}$, i.e. φ^2 in the $f(R)$ case and φ in the symmetron case.

Before proceeding to solve eq. (2.27) we must specify our boundary conditions and initial field profile guesses, which we will iteratively converge to the true solution. Our grid has four boundaries: $v = -1, 1$ (i.e. $\theta = \pi, 0$) and $u = \ln r_{\rm min}, \ln r_{\rm max}$. At the first three, we impose $\partial\varphi/\partial v, \partial\varphi/\partial u = 0$. At the outer radial boundary, we instead impose $\varphi = \varphi_\infty$, i.e. the cosmic background value of the scalar field. In the $f(R)$ case, this is simply f_{R0}; in the symmetron case, this is the field value that minimises the effective potential eq. (1.118) evaluated at the cosmic matter density. For initial guesses, in the $f(R)$ case we simply set $\varphi = 1$ everywhere, and allow the solver to converge on the correct profile. For the symmetron case, we speed up the convergence by setting the field to 1 everywhere, except in the region where $\rho > \rho_{\rm SSB}$ which is assumed to be screened and thus the field is set to 0.

We solve eq. (2.27) using a Gauss-Seidel iteration method. Here, our 2D grid is decomposed into a chequerboard pattern, i.e. we alternately assign

cells with 'red' and 'black' labels. Each iteration n is then comprised of two halves: a red sweep and a black sweep. During the 'red sweep', the scalar field value is changed in all of the red cells using a Newton-Raphson update,

$$\varphi_{i,j}^{n} = \varphi_{i,j}^{n-1} - \frac{\mathcal{L}_{i,j}}{\mathcal{L}'_{i,j}}\,, \tag{2.31}$$

where $\mathcal{L}' \equiv \partial\mathcal{L}/\partial\varphi = 3\varphi^2 + p$. Note that $\mathcal{L}_{i,j}$ here is evaluated using φ^{n-1}, i.e. the values of φ calculated at the previous Gauss-Seidel iteration (or the initial guess in the case $n = 1$).

Next, we perform a 'black sweep' in which the scalar field is updated in all of the black cells using the same expression. There is however one key difference in the black sweep: rather than using the remaining values from the previous Gauss-Seidel iteration $(n-1)$ as was done during the red sweep, we use the neighbouring red cell values that have just been updated during the red sweep, i.e. in the first half of iteration n.

This iterative process repeats, updating the field values at each grid point until a converged solution is obtained. The iteration stops when the difference between the field in the previous step and the current one is less than a given threshold. In the $f(R)$ case we use a threshold of 10^{-7}, and in the symmetron case we use 10^{-14}. These thresholds were selected by comparing solutions against those obtained with significantly stricter tolerances. We found that the resulting field profiles and derived fifth forces differed by negligible amounts, confirming physical convergence. The symmetron requires a particularly stringent threshold compared to the $f(R)$ case; choosing a laxer threshold can cause the innermost field value to prematurely stall at a small, non-zero value in regions that should be fully screened ($\phi = 0$).

The left semicircles in the bottom row of figure 3.1 show outputs of the solver for the same example galaxy shown in the upper left panel of the figure, with a mass $M_{\rm vir} = 10^{11.5}\,M_\odot$, theory parameters of $f_{R0} = -10^{-6.4}$

in the $f(R)$ case, $M_{\rm sym} = 10^{-4.5}\, M_{\rm pl}$ and $L_{\rm c} = 10^{-1}\,{\rm kpc}$ in the symmetron case. In both cases, the field solutions are plotted to a maximum radius of $5R_{\rm disc}$.

Chapter 3

Accurate Computation of the Screening of Scalar Fifth Forces in Galaxies

Declaration: This chapter is based on the published paper: *Accurate Computation of the Screening of Scalar Fifth Forces in Galaxies*, (Burrage et al., 2024). The source code and plotting scripts are publicly available at github.com/Bradley-March/GalacticScreeningConditions.

3.1 Summary

Screening mechanisms allow light scalar fields to dynamically avoid the constraints that come from our lack of observation of a long-range fifth force. Galactic scale tests are of particular interest when the light scalar is introduced to explain the dark matter or dark energy that dominates our cosmology. To date, much of the literature that has studied screening in galaxies has described screening using simplifying approximations. In this work, we calculate numerical solutions for scalar fields with screening mechanisms in galactic contexts, and use these to derive new, precise conditions governing where fifth forces are screened. We show that the commonly used binary screened/unscreened threshold can predict a fifth force signal in situations where a fuller treatment does not, leading us to

conclude that existing constraints might be overestimated. We show that various other approximations of the screening radius provide a more accurate proxy to screening, although they fail to exactly reproduce the true screening surface in certain regions of parameter space. As a demonstration of our scheme, we apply it to an idealised Milky Way and thus identify the region of parameter space in which the solar system is screened.

3.2 Introduction

Attempts to resolve long-standing complications within the dark sector often introduce a new scalar field which naturally couples to the gravitational sector, causing modifications to standard gravity, General Relativity (GR), in the form of scalar *fifth forces*. However, such deviations from GR are tightly constrained by lab-based experiments testing the inverse-square law and tests of Solar System dynamics, as detailed in section 1.3.8. To avoid such constraints, scalar-tensor theories with *screening* propose that the scalar field is environment-dependent, allowing for modifications to GR on certain scales whilst suppressing fifth forces on other scales (Joyce et al., 2015; Koyama, 2016; Ishak, 2019; Burrage and Sakstein, 2018; Brax et al., 2022; Saridakis et al., 2021b; Vardanyan and Bartlett, 2023).

In this chapter, we study chameleon (Khoury and Weltman, 2004b,a) and symmetron (Hinterbichler and Khoury, 2010; Hinterbichler et al., 2011) screening models, as described in sections 1.3.6 and 1.3.7. For related work on other scalar theories see Mota and Shaw (2007); Dehnen et al. (1992); Gessner (1992); Damour and Polyakov (1994); Pietroni (2005); Olive and Pospelov (2008); Dvali et al. (2000); Vainshtein (1972). Chameleon and symmetron theories introduce a density-dependent scalar potential that screens the fifth force in areas of high density or deep gravitational potential, such as in stellar interiors or the centres of galaxies.

Much of the recent literature has studied the behaviour of these the-

ories on galactic scales, where the screening phenomenon leads to a rich phenomenology, such as equivalence principle violations and other kinematic signatures (Hui et al., 2009; Jain and VanderPlas, 2011; Bartlett et al., 2021; Desmond et al., 2018b,a, 2019a; Desmond and Ferreira, 2020; Naik et al., 2020; Vikram et al., 2013; Pedersen and Stubbs, 2023; Naik et al., 2018, 2019; Vikram et al., 2014; Lombriser and Peñarrubia, 2015; Burrage et al., 2017; Cataldi et al., 2022; O'Hare and Burrage, 2018; Högås and Mörtsell, 2023). The recent interest in galactic scales is a result of two circumstances: the fact that galaxies inhabit an unconstrained "desert" in modified gravity parameter space (Baker et al., 2019), and the recent advent of vast datasets from various galaxy surveys (Almeida et al., 2023; Lavaux and Hudson, 2011; DESI Collaboration et al., 2023).

In this work, we investigate the non-linear nature of screening theories in the galactic regime by utilising a numerical solver, based on Puchwein et al. (2013); Naik et al. (2018); Bose et al. (2017), to determine the true scalar field profile inside our static model galaxies. Guided by these field solutions, we obtain empirical rules describing the locations of screening surfaces and compare these results with those of the common approximations. We discuss the implications of the proper non-linear treatment of these theories and how our findings can impact observables and constraints established using simplified methods. These results will form the foundation for a reevaluation of galaxy-based constraints in the near future, using methods that we have explored and tested in this chapter. This reanalysis will enable us to provide a quantitative estimate of the impact of using various standard approximations to screening, compared to our precise numerical methods that consider partial screening.

The outline for this chapter is as follows. In section 3.3 we present an overview of the general scalar-tensor theory, as well as our specific chameleon and symmetron models. In section 3.4 we describe our methods to solve the theories numerically, including the galactic model we use, the

mechanics behind the numerical solver, and the criteria used to define the screened and unscreened regions. Section 3.5 outlines the results of our investigation. Our conclusions are laid out in section 3.6.

3.3 Theory

3.3.1 Scalar-Tensor Gravity

We work within the framework of scalar-tensor theories of gravity, described in full in section 1.3.1. For the reader's convenience, here and throughout the remaining results sections, we restate key equations (without renumbering) that are relevant to the chapter. The canonical dimensionless scalar field, ϕ, obeys the equation of motion (1.64), restated here for convenience,

$$\Box\phi = \frac{\mathrm{d}V_{\mathrm{eff}}}{\mathrm{d}\phi}\,,$$

where the effective potential for non-relativistic matter is given by eq. (1.65),

$$V_{\mathrm{eff}}(\phi) = V(\phi) + 8\pi G \ln A(\phi)\rho\,.$$

Here $V(\phi)$ is the bare scalar potential, ρ is the matter density, and $A(\phi)$ is the conformal coupling to matter (such that matter fields now move on geodesics of the Jordan frame metric, $\tilde{g}_{\mu\nu} = A^2(\phi)g_{\mu\nu}$), in turn related to the coupling function $\beta(\phi)$ via eq. (1.61),

$$\beta(\phi) \equiv \frac{\mathrm{d}\ln A(\phi)}{\mathrm{d}\phi}\,.$$

Such theories admit fifth forces, given by eq. (1.63),

$$\boldsymbol{a}_5 = -\beta(\phi)\boldsymbol{\nabla}\phi\,,$$

which act to enhance gravitational forces, if left unscreened.

3.3.2 Astrophysical Screening Approximations

The crux of this chapter is to accurately determine the location of the screened region inside galaxies, defined by what we term the 'screening surface': the interface between the screened central region and the unscreened outskirts of a partially screened object. To determine this, we use numerical solutions of scalar EoM. These results will then be compared with the approximate methods that are commonly used in the literature.

One prevalent method for approximating screening surfaces considers a static, spherically symmetric source, $\delta\rho(r)$, in a constant density background, $\bar{\rho}$, e.g. a star embedded in the galactic medium or a dark matter halo embedded in the cosmological background, as in Hui et al. (2009); Davis et al. (2012b); Sakstein (2013); Burrage and Sakstein (2016). For such an object, the screening surface will necessarily be a sphere with radius r_s, the 'screening radius'. The general EoM, eq. (1.64), is then solved in a piecewise manner, as described in full in section 1.3.2 and 1.3.3, to obtain equations (1.89) and (1.90), restated here for convenience,

$$\begin{aligned}\chi \equiv \frac{\bar{\phi}}{2\beta(\bar{\phi})} &= 4\pi G \int_{r_s}^{\infty} r\delta\rho(r)\mathrm{d}r\,, \\ &= -\left(\Phi_N(r_s) + r_s \left.\frac{\mathrm{d}\Phi_N}{\mathrm{d}r}\right|_{r_s}\right)\,,\end{aligned}$$

where $\bar{\phi} = \phi(\bar{\rho})$ is the background field solution, $\Phi_N(r)$ is the Newtonian potential, and χ is the '**critical potential**'.

The critical potential is a function of the model parameters ($\bar{\phi}$ and $\beta(\bar{\phi})$), and can be calculated for any given scalar-tensor theory. It is a measure of how deep an object's gravitational potential must be in order to be screened. If there is no solution for r_s for a given χ in the above equations, then the object is fully unscreened. If a solution exists, then the object is partially (or fully) screened, with the screening radius given by the solution r_s. Given that $\Phi_N < 0$ and $\frac{\mathrm{d}\Phi_N}{\mathrm{d}r} > 0$, the object must be fully unscreened when $\chi > |\Phi_N|/c^2$, where the Newtonian potential is evaluated

at the surface of the object. Conversely, objects with $\chi < |\Phi_N|/c^2$ are partially screened (or fully screened if $\chi \ll |\Phi_N|/c^2$).

The critical potential serves as a starting point for two approaches commonly seen in the literature for approximating the screening of astrophysical objects. In the first approach, the implicit equation (1.89) is solved for the screening radius, which appears as the lower limit of the integral. As we shall see, this can readily be done numerically, but analytic solutions can also be found for certain choices of the density distribution (e.g., for idealised dark matter haloes, as in Arnold et al. (2016)).

The second approach, which we refer to as the "**binary screening condition**", disregards partial screening altogether and classifies objects as either fully screened or fully unscreened by comparing χ to an estimate of Φ_N at the surface of the object. Neglecting the contribution of its environment, an object is classified as screened if $|\Phi_N| > \chi$, and unscreened otherwise. For example, at the level of current constraints in $f(R)$ gravity (Naik et al., 2019; Desmond et al., 2018b,a; Desmond and Ferreira, 2020), objects with deep potentials, e.g. main sequence stars with $|\Phi_N|/c^2 \sim 10^{-6}$, are likely screened, while objects with shallower potentials, e.g. dwarf galaxies with $|\Phi_N|/c^2 \sim 10^{-8}$, can still be unscreened. In the context of galaxies, this approach was suggested by Cabré et al. (2012), who proposed using $\Phi_{\rm vir} = GM_{\rm vir}/r_{\rm vir}$.[1] The same approach was subsequently used in a string of recent papers deriving modified gravity constraints on galactic scales (Desmond et al., 2018c,b,a; Desmond and Ferreira, 2020). However, it is worth noting that these works also included environmental contributions, classifying objects as screened when $(|\Phi_N| + |\Phi_{\rm env.}|) > \chi$, where $|\Phi_{\rm env.}|$ is the environmental contribution to the local gravitational potential.

Implicitly, in the derivation of the critical potential, eq. (1.89), many simplifying assumptions have been required. These assumptions include: the source mass is spherically symmetric; the field reaches its minimum

[1] Using the definitions of $M_{\rm vir}$ and $r_{\rm vir}$ from sec. 1.2.3

value inside the object and this minimum value is negligible; the scalar field can be expressed perturbatively to linear order; the Compton wavelength of the scalar is large compared to the size of the object; and the coupling function $\beta(\phi)$ is constant throughout, adopting its background value $\beta(\bar{\phi})$.

One of the main aims of the present work is to compare the results obtained from these two approximate approaches with more accurate results obtained from exact numerical solutions of the scalar equations of motion. In doing so, we will demonstrate the validity of the previously listed approximations, and visualise where they (and thus the critical potential screening radius approximation) break down.

3.3.3 Chameleon $f(R)$

We now specialise to a specific scalar model, Hu-Sawicki $f(R)$ gravity (Hu and Sawicki, 2007), which exhibits chameleon screening. Chameleon screening is characterised by a density-dependent scalar mass, which leads to the presence of short-range fifth forces in high-density regions. In screened regions the field profile is flat, resulting in a negligible scalar gradient, effectively suppressing the fifth forces.

In the scalar-tensor framework of section 3.3.1, $f(R)$ gravity is captured by the following field theory definition, restated from eq. (1.97),

$$\phi = -\frac{\ln(1+f_R)}{2\beta(\phi)}\,, \qquad V(\phi) = \frac{Rf_R - f(R)}{2(1+f_R)^2} \qquad \text{and} \qquad \beta(\phi) = \frac{1}{\sqrt{6}}\,,$$

where $f_R \equiv \frac{\mathrm{d}f(R)}{\mathrm{d}R}$ is the scalar field of the theory. The model is fully specified by the choice of the function $f(R)$, which we take to be the Hu-Sawicki form (Hu and Sawicki, 2007), eq. (1.103),

$$f(R) = -\frac{am^2}{1+(R/m^2)^{-n}}\,.$$

Choosing $n = 1$ to align with the bulk of the literature, and requiring that $f(R)$ drives the accelerated expansion of the universe, we can express the

model in terms of a single free parameter, the present-day background field value f_{R0},

$$a = -\frac{4\Omega_\Lambda^2}{(\Omega_m + 4\Omega_\Lambda)^2}\frac{1}{f_{R0}} \quad \text{and} \quad m^2 = -\frac{3H_0^2(\Omega_m + 4\Omega_\Lambda)^2}{2\Omega_\Lambda}f_{R0}\,,$$

as in eq. (1.108).

The equation of motion for the scalar field, f_R, is given by eq. (1.101),

$$\nabla^2 f_R = \frac{1}{3}\left(\delta R - 8\pi G\delta\rho\right)\,,$$

where $\delta\rho$ is the density perturbation and δR is the curvature perturbation, given by eq. (1.109),

$$\delta R = R_0\left[\sqrt{\frac{f_{R0}}{f_R}} - 1\right]\,,$$

where R_0 is the background curvature today. The fifth force in $f(R)$ gravity is given by eq. (1.110),

$$\boldsymbol{a}_5 = \frac{1}{2}\boldsymbol{\nabla} f_R\,.$$

Lastly, using our field redefinition eq. (1.97), we can define the critical potential eq. (1.89) in terms of our background scalar field value

$$\chi = -\frac{3}{2}f_{R0}\,, \tag{3.1}$$

where we have assumed $|f_{R0}| \ll 1$.

3.3.4 Symmetron

In this work we also study symmetron screening (Hinterbichler and Khoury, 2010; Hinterbichler et al., 2011), which is characterised by a suppression to the coupling function in dense environments, achieved through a spontaneous symmetry breaking (SSB). The model we adopt is fully described in section 1.3.7; here we provide a brief overview.

Starting with the potential and conformal coupling, restated from equa-

tions (1.112) and (1.113),

$$V(\phi) = \frac{1}{L_{\rm pl}^2}\left[-\frac{1}{2}\left(\frac{\mu}{M_{\rm pl}}\right)^2\phi^2 + \frac{1}{4}\lambda\phi^4\right],$$
$$A(\phi) = 1 + \frac{1}{2}\left(\frac{M_{\rm pl}}{M_{\rm sym}}\right)^2\phi^2,$$

where $M_{\rm sym}$ controls the strength of the coupling to matter, μ is the bare tachyonic mass of the scalar field, and λ governs the scalar self-interactions. This choice results in an effective potential with symmetry breaking properties, given by eq. (1.114),

$$V_{\rm eff}(\phi) = \frac{1}{2L_{\rm c}^2}\left[\frac{1}{2}\left(\frac{\rho}{\rho_{\rm SSB}} - 1\right)\phi^2 + \frac{\lambda}{4}\left(\frac{M_{\rm pl}}{\mu}\right)^2\phi^4\right],$$

where $L_{\rm c}$ and $\rho_{\rm SSB}$ are the background Compton wavelength, eq. (1.115), and SSB density scale, eq. (1.116) respectively, expressed as

$$L_{\rm c}^2 = \frac{1}{2}\left(\frac{M_{\rm pl}}{\mu}\right)^2 L_{\rm pl}^2,$$
$$\rho_{\rm SSB} = \left(\frac{M_{\rm sym}\mu}{M_{\rm pl}^2}\right)^2 \frac{M_{\rm pl}}{L_{\rm pl}^3}.$$

When the symmetry is broken ($\rho < \rho_{\rm SSB}$), the minimum of the effective potential in the background is given by eq. (1.118),

$$\phi = \pm\phi_\infty \equiv \pm\phi_{\rm vev}\sqrt{1 - \frac{\rho}{\rho_{\rm SSB}}},$$

where $\phi_{\rm vev}$ is the vacuum expectation value given by eq. (1.119),

$$\phi_{\rm vev} = \frac{1}{\sqrt{\lambda}}\frac{\mu}{M_{\rm pl}}.$$

Rescaling the scalar field by its vacuum expectation value, $\varphi = \phi/\phi_{\rm vev}$, we can express the symmetron EoM, eq. (1.120), as

$$\nabla^2\varphi = \frac{1}{2L_{\rm c}^2}\left[\left(\frac{\rho}{\rho_{\rm SSB}} - 1\right) + \varphi^2\right]\varphi.$$

The fifth force in symmetron models is given by eq. (1.121),

$$\boldsymbol{a}_5 = -\phi_{\rm vev}^2\left(\frac{M_{\rm pl}}{M_{\rm sym}}\right)^2\varphi\boldsymbol{\nabla}\varphi.$$

Note that the symmetron equation of motion is independent of λ; this parameter only affects the strength of the fifth force via the vacuum expectation value, $\phi_{\rm vev}$.

The critical potential eq. (1.90) for this symmetron model is

$$\chi = \frac{1}{2}\left(\frac{M_{\rm sym}}{M_{\rm pl}}\right)^2 . \tag{3.2}$$

Note that χ depends only on $M_{\rm sym}$. However, as we shall see later, screening is a function of both $M_{\rm sym}$ and $L_{\rm c}$. This discrepancy is a result of the approximations used to derive the general form of χ, eq. (1.89); specifically a combination of assuming the field can be linearised at the screening surface, the background scalar mass is light and thus negligible, and that $\beta(\phi)$ is constant throughout.

The symmetry-breaking nature of the symmetron provides a third possible approximation for the screening surface — in addition to the two described in section 3.3.2 for scalar-tensor theories in general. One can assume that the screening surface universally corresponds to the surface where $\rho(r = r_s) = \rho_{\rm SSB}$, neglecting other relevant factors such as the coupling strength and Compton wavelength of the theory. We will also examine the efficacy of this approximation in section 3.5.

3.4 Numerical Screening Solutions

This section describes the numerical methods we use to obtain isolated galaxy solutions for the scalar field equations of motion under the chameleon $f(R)$, eq. (1.101), and symmetron theories, eq. (1.120). Section 3.4.1 describes our choice of galaxy model, section 3.4.2 then describes our numerical solver for the equations of motion, and section 3.4.3 outlines the conditions we use to identify the screening surface within our scalar field solutions.

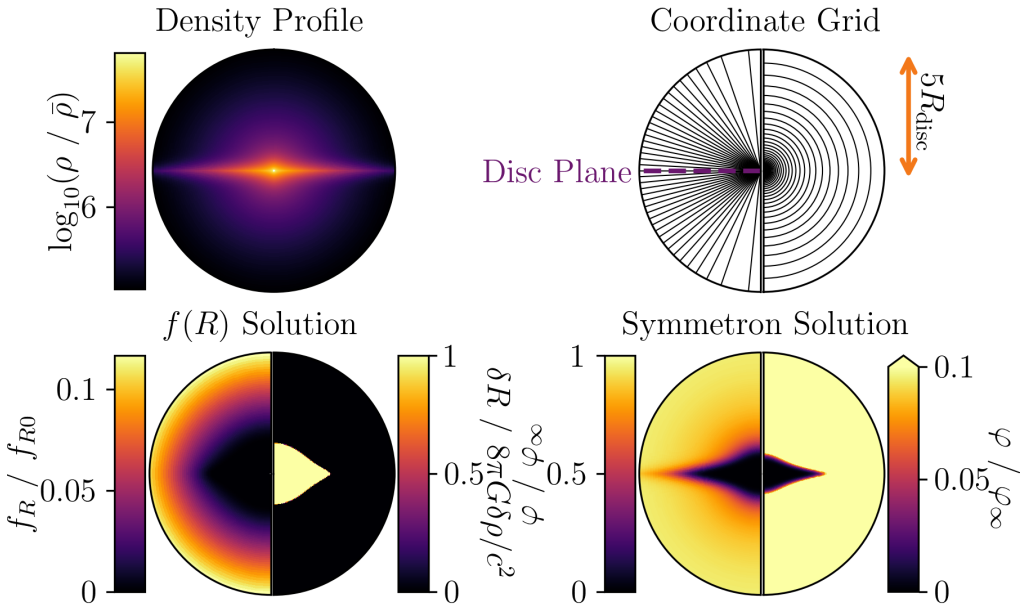


Figure 3.1: Various panels illustrating the different stages of our numerical procedure, as described throughout section 3.4. All plots are zoomed in to $5R_{\rm disc}$, showing only the disc-dominated central region. Top left: input density profile, for an axisymmetric galaxy with $M_{\rm vir} = 10^{11.5}\,M_\odot$, rescaled by the cosmic mean density. Top right: coordinate grid, showing every *fifth* radial and azimuthal angle gridline. Bottom left, left half: f_R field profile rescaled by the background field value, $|f_{R0}| = 10^{-6.4}$. Bottom left, right half: the curvature-density ratio, eq. (3.3a). Bottom right, left half: symmetron field profile rescaled by its background field value, for the input parameters $M_{\rm sym} = 10^{-4.5}\,M_{\rm pl}$ and $L_{\rm c} = 10^{-1}\,$kpc. Bottom right, right half: truncated scalar field profile to illustrate the symmetron screening condition, eq. (3.3b).

Our methods are summarised in figure 3.1, the individual panels of which show a typical density profile under our galaxy model, the coordinate grid of our scalar field solver, the scalar field solutions for the same galaxy, and the screening surfaces identified from the scalar field solutions. These various panels of the figure will be examined in more detail in the corresponding parts of this section.

3.4.1 Galactic Model

Given the $f(R)$ and symmetron EoMs, equations (1.101) and (1.120) respectively, we can solve the scalar field profile given a suitable galactic

density model. Section 1.2.3 contains a full overview of our galactic density profiles. In this work, we use a two-component axisymmetric model comprising a dark matter halo and a galactic disc (note that we are limiting our study to late-type spiral disc galaxies, not elliptical or dwarf spheroidal galaxies). We model the dark matter halo with a Navarro-Frenk-White (NFW) profile (Navarro et al., 1996), as in eq. (1.50), restated here for convenience,

$$\rho(r) = \frac{\rho_{\rm NFW}}{\frac{r}{r_{\rm NFW}}\left(1+\frac{r}{r_{\rm NFW}}\right)^2},$$

As a reminder, r is the spherical radial coordinate, and $\rho_{\rm NFW}$ and $r_{\rm NFW}$ are the characteristic density and length scale. The galactic disc is represented by a simple double exponential profile[2] (Binney and Tremaine, 2008), as in eq. (1.56)

$$\rho(R,z) = \frac{\Sigma_{\rm disc}}{2z_{\rm disc}} e^{-R/R_{\rm disc}} e^{-|z|/z_{\rm disc}},$$

where R represents the cylindrical radial coordinate and z represents the coordinate perpendicular to the galactic disc, and $\Sigma_{\rm disc}$, $R_{\rm disc}$ and $z_{\rm disc}$ are the characteristic density and length scales. In actuality, a more sophisticated galaxy model (e.g. McMillan (2017)) could also include various other components, such as central bulges, stellar haloes, and multiple discs; however, we have chosen to exclude these for the sake of keeping our model as simple as possible while still capturing the key characteristics.

Including these density components will introduce five extra input parameters used to scale the density profiles: $\rho_{\rm NFW}$, $r_{\rm NFW}$, $\Sigma_{\rm disc}$, $R_{\rm disc}$ and $z_{\rm disc}$. Nonetheless, for the remainder of this article, we shall quote our galactic model in terms of one input parameter: the virial mass, $M_{\rm vir}$. This is defined as the mass enclosed within the virial radius, $r_{\rm vir}$, the radius within which the mean density inside is 200 times the cosmological critical density. We reduce the five-dimensional parameter space into a

[2]Using a continuous density profile for a discrete distribution of stars is technically only correct if the Compton wavelength of our theory is larger than the typical separation of stellar objects. This is true for most of the parameters we consider here. In chapter 4 we explore the impact of this approximation.

one-dimensional space by using empirical relations between the various parameters. In doing so, we typically adopt median values on the relations, ignoring any scatter. Thus, for a given $M_{\rm vir}$, the galaxy we model is in some sense a maximally typical one. We describe this process in full detail in section 2.1.1. The top left panel of figure 3.1 shows an example density profile for a galaxy with $M_{\rm vir} = 10^{11.5}\,M_\odot$, corresponding to the following values for the parameters appearing in our density model: $\rho_{\rm NFW} = 5.2 \times 10^6\,M_\odot\,{\rm kpc}^{-3}$, $r_{\rm NFW} = 15\,{\rm kpc}$, $\Sigma_{\rm disc} = 6.4 \times 10^8\,M_\odot\,{\rm kpc}^{-2}$, $R_{\rm disc} = 1.6\,{\rm kpc}$ and $z_{\rm disc} = 0.26\,{\rm kpc}$.

The adoption of the NFW profile for the dark matter halo presents two numerical challenges: the central density singularity and the logarithmically divergent mass. To resolve these issues, we set a constant density within the central 50 pc, and introduce an outer cutoff at $2.2r_{\rm vir}$. Specifically, the inner cutoff coincides with the innermost radial grid point of our numerical solver. Interior to this radius, we apply a Neumann boundary condition, $\frac{{\rm d}\phi}{{\rm d}r}|_{r=0} = 0$, effectively treating the core as a constant density sphere with a flat central field profile. A sharp cutoff at the halo's edge is well motivated astrophysically, e.g. Deason et al. (2020). We tested our analysis for various inner and outer cutoffs. In changing the inner cutoff neither the derived position of the screening surfaces, nor the conclusions we make are altered. We found that increasing the outer cutoff moved the screening surface farther outward, primarily due to the increase in the total mass of the system. However, we find this shift is mirrored in true and approximate solutions, and thus our conclusions remain robust.

In this work, we assume that the galaxy is embedded in a constant-density background equal to the cosmological critical density. Therefore, we do not consider environmental effects, such as inhomogeneities in the matter distribution throughout the Universe, which can manifest as regions of lower density[3] (voids) and higher density (clusters, walls, and filaments),

[3]For an analysis of Chameleon screening in voids see Tamosiunas et al. (2022).

as well as neighbouring galaxies and satellites. This simplification enables us to better investigate other variables that impact screening in galaxies. Overall, higher-density environments tend to enhance screening effects, resulting in more fully screened galaxies and larger screened regions in partially screened galaxies, while the opposite is true for lower-density environments.[4] We comment on where this will impact our results throughout section 3.5, and plan to account for these effects in follow-up work.

3.4.2 Numerical Solver

In section 2.2.1 we fully detail the methodology behind our numerical solver for the $f(R)$ and symmetron equations of motion, eqs. (1.101) and (1.120) respectively. Here we describe the specific implementation used in this work. The solver is designed to handle axisymmetric density distributions, such as the galactic model described in section 3.4.1. We work in spherical polar coordinates, with an implied axisymmetry, (r, θ), where θ is the polar angle measured from the z-axis (perpendicular to the disc plane), and the azimuthal angle is dropped. In the numerical implementation, we perform a coordinate transformation to (u, v) coordinates, defined as $u \equiv \ln(r/[\text{chosen length scale}])$, and $v \equiv \cos\theta$. The logarithmic radial coordinate allows us to capture the large dynamic range in r, yet still ensuring high resolution in the inner region containing the galaxy, while the v coordinate ensures higher clarity in the disc-axis, where the baryonic mass is most concentrated. Throughout this section we use 512 radial (u) cells and 201 angular (v) cells, with boundaries at $r \in [0.05\,\text{kpc}, 10^4\,\text{kpc}]$ and $v \in [-1, 1]$. The quantities of interest (e.g. ϕ, ρ, etc.) are then discretised on this grid structure.

The top right panel of figure 3.1 shows the grid used in our solver, with

[4]Physically, this is because the local background scalar field value, ϕ_{bg}, is inversely related to the environmental density. In high-density environments like clusters, ϕ_{bg} is suppressed, effectively lowering the potential depth required for screening. Conversely, in voids, ϕ_{bg} is larger, making screening harder to achieve.

every fifth radial and angular gridline shown for clarity. Meanwhile, the left-sided semicircles in the bottom row of the figure show the output scalar field profiles for the galaxy density profile shown in the top left panel, with a mass $M_{\rm vir} = 10^{11.5}\,M_\odot$, and theory parameters of $f_{R0} = -10^{-6.4}$ in the $f(R)$ case, $M_{\rm sym} = 10^{-4.5}\,M_{\rm pl}$ and $L_{\rm c} = 10^{-1}\,{\rm kpc}$ in the symmetron case. In all cases, the maximum radius plotted is $5R_{\rm disc}$.

3.4.3 Screening Conditions

This section aims to establish a universal and reliable screening condition to locate the (generally non-spherical) screening surface, $r_s(\theta)$, in a galaxy's scalar field profile. We will find that our conditions to calculate $r_s(\theta)$ are given by

$$\left.\frac{\delta R(r,\theta)}{8\pi G\delta\rho(r,\theta)}\right|_{r=r_s(\theta)} = 0.9\,, \tag{3.3a}$$

$$\left.\frac{\varphi(r,\theta)}{\varphi_\infty}\right|_{r=r_s(\theta)} = 0.1\,, \tag{3.3b}$$

for the $f(R)$ and symmetron models respectively. In other words, for a given angle, the screening surface is the surface at which the $f(R)$ *curvature-density* ratio or the symmetron field value matches a given threshold. The right sides of the bottom row panels in figure 3.1 display the $f(R)$ curvature-density ratio and the symmetron field with a colour map truncated at the threshold. The sharp transition in both of these cases vindicates our chosen threshold. We arrived at the screening conditions presented in this section, after considering a variety of different properties of the scalar field solutions, for example the fifth force profiles. The screening conditions discussed here are the ones that could be most consistently applied across the range of model and galaxy parameters explored in this work.

In the $f(R)$ case, the screening condition, eq. (3.3a), is a threshold on the curvature-density ratio, motivated by the two terms on the right-hand side of the $f(R)$ EoM eq. (1.101). Specifically, inside the screened

region the field is flat and the Laplacian is zero, thus the two terms on the right-hand side of the EoM are approximately equal in magnitude, and the curvature-density ratio is unity. Conversely, in the unscreened regime, the field adopts its background value, causing δR, eq. (1.109), and thus the curvature-density ratio, to become zero. We find that the curvature-density ratio provides a clearer demarcation between the screened and unscreened region than the scalar field, as can be seen in the bottom left plot of figure 3.1. Nevertheless, there are still instances where the transition is more gradual, particularly for smaller values of $|f_{R0}|$. We find that a threshold on the curvature-density of 0.9 correctly separates the screened/unscreened regions and produces universal behaviour across the whole parameter space.

For the symmetron condition, we use a threshold value on the field itself. This is motivated by the coupling function, eq. (1.113), having a first derivative proportional to the scalar field; therefore the density-dependent term in the EoM is then also proportional to the scalar field. Setting this threshold as a ratio of the background scalar field allows for a screening condition that can be universally applied over the whole parameter space. We determine that a threshold value of 10% of the background scalar field value provides consistent results, with the scalar field profile being visually flat, and thus suppressing fifth forces, within a substantial region of r_s.

Figure 3.2 shows the value of the $f(R)$ curvature-density parameter and the symmetron field along the plane of the galactic disc, as well as the magnitude of the fifth forces of both theories. We rescale the radial coordinates by the derived r_s along the disc plane to better visualise the behaviour over the whole parameter space. Taking figures 3.1 and 3.2 together, we are able to justify our choice of thresholds, namely 0.9 for the curvature-density parameter and 0.1 for the symmetron field, finding that this choice allows for consistent results, that suppress the fifth forces inside of the screened region, across our full range of parameters. Quantitatively, these threshold values were found via an iterative process of optimisation.

Adopting 'stricter' thresholds (i.e. higher values for the curvature-density ratio or lower values for the symmetron field) yields smaller screening radii; this misclassifies the transition region (where the fifth force is still physically suppressed) as unscreened, meaning the fifth force would not become noticeable until well outside the calculated r_s. Conversely, 'laxer' thresholds yield larger screening radii, incorrectly classifying regions where the fifth force is already non-negligible as screened.

We classify a galaxy as fully screened if the screening surface determined according to eqs. (3.3) is greater than the extent of the galaxy, or if SSB has not yet occurred in the symmetron case, i.e. $\bar{\rho} > \rho_{\rm SSB}$. Conversely, a galaxy is considered fully unscreened if there is no screened region within the galaxy, i.e., if the conditions given by eq. (3.3) are not satisfied anywhere. However, we also find a small subset of galaxies for which the screening conditions are satisfied somewhere but nonetheless have non-negligible fifth forces in their central regions. To catch these cases, we consider the innermost field value. In the $f(R)$ case, solutions satisfying $f_R(r \approx 0) > 10^{-3} f_{R0}$ are fully unscreened. We find that an analogous threshold on the field central field value can not be used in the symmetron case, as some field solutions yield small central field values but quickly grow away from the centre, giving an unscreened central region. So, for the symmetron, we instead use the Laplacian of the field: solutions satisfying the condition $\nabla^2\varphi(r \approx 0) > 10^{-1}\max\left(\nabla^2\varphi\right)$ are fully unscreened.

The symmetron solutions that avoid the central field threshold condition (i.e. satisfying $\phi(r \approx 0) < 10^{-3}\phi_\infty$) but are correctly classified as fully unscreened by the central Laplacian threshold condition are highlighted in figure 3.2. Here we see that these edge case field profiles grow to be large well within the screening radius, causing a non-zero fifth force in this region, as shown in the bottom panel.

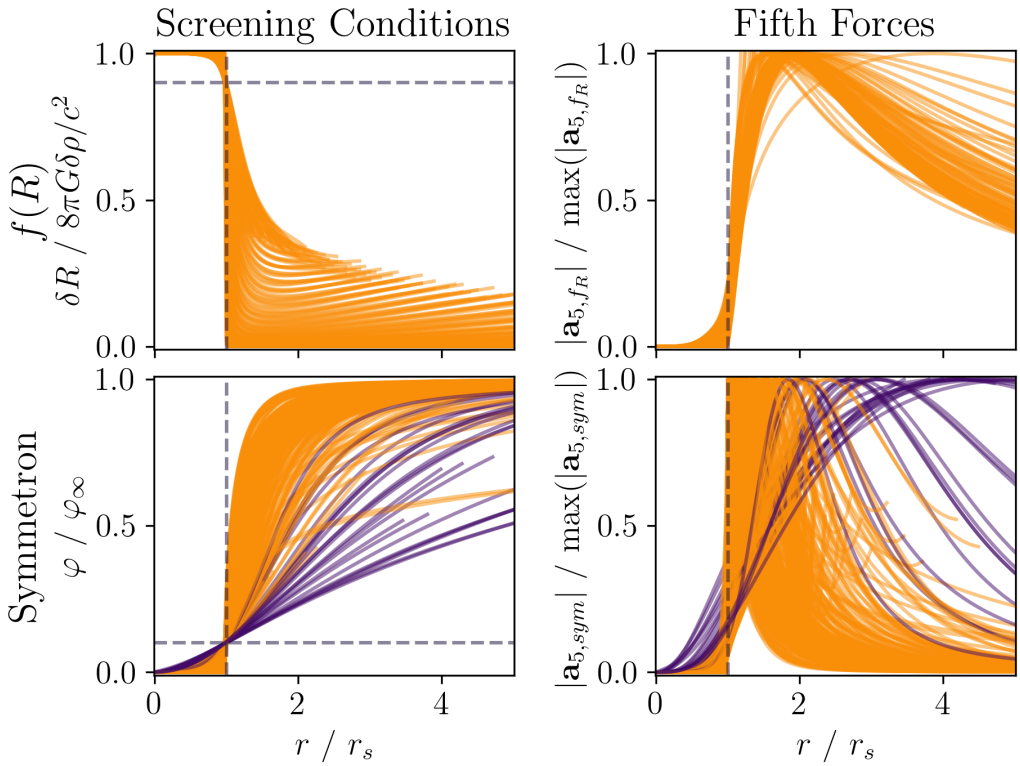


Figure 3.2: Values of the $f(R)$ curvature-density ratio (top left), the $f(R)$ fifth force (top right), the symmetron field (bottom left) and the symmetron fifth force (bottom right), in the plane of the galactic disc, plotted against radial coordinates rescaled by r_s (the radius at which the screening surface meets the disc plane), across a range of theory parameters and galaxy masses. In the $f(R)$ case, $\log(|f_{R0}|) \in [-8, -5]$ and $\log(M_{\rm vir}/M_\odot) \in [10, 13.5]$, both in increments of 0.2. In the symmetron case, $\log(M_{\rm sym}/M_{\rm pl}) \in [-6.5, -3]$, $\log(L_{\rm c}/{\rm kpc}) \in [-3, 3]$ and $\log(M_{\rm vir}/M_\odot) \in [10, 13.5]$, all in increments of 0.5. Profiles are cut off at the extent of the galaxy, $2.2r_{\rm vir}$. Dashed vertical lines represent the location of the screening radius. Dashed horizontal lines correspond to the screening condition threshold. Purple lines on the symmetron plot indicate solutions that evade the fully unscreened central scalar field definition but are properly considered fully unscreened by the central Laplacian definition.

3.5 The Screening of Galaxies

3.5.1 Position and Shape of Screening Surfaces

Figure 3.3 shows an array of solutions for the screening surface (dashed lines), over a range of $f(R)$ and symmetron parameters, for a galaxy with $M_{\rm vir} = 10^{11.5}\,M_\odot$. Generally, decreasing the adopted value of $|f_{R0}|$ or $M_{\rm sym}$, or increasing $L_{\rm c}$, pushes the screening surface further out. We separate these solutions into those for which the screening surfaces lie within the disc-dominated region (left-hand semi-circles) and the halo-dominated region (right-hand semi-circles). The figure shows that screening surfaces that occur in the disc-dominated region are elongated along the galactic disc, whereas larger screening surfaces are spherical and trace the dark matter component.

We also include approximate screening surfaces (dashed-dotted lines) for comparison. In the case of $f(R)$, the approximate screening surface is computed by numerically solving eq. (1.89), where χ is given by the $f(R)$ critical potential, eq. (3.1), and $\delta\rho(r)$ is the galactic density averaged over spherical shells. The approximate symmetron screening surfaces are isodensity contours with a value equal to the symmetry breaking scale, i.e. $\rho(r = r_s(\theta)) = \rho_{\rm SSB}$.

In the $f(R)$ case (top left panel), the true screening surfaces (dashed lines) in the disc-dominated region follow the isodensity contours away from the disc plane, but deviate nearer the disc, where the isodensity contours are flattened to a larger extent. We find that the screening surfaces lie somewhere between the highly flattened isodensity contours of our galactic model and the isopotential contours (not shown), which are visually more spherical than the screening surfaces.

The non-spherical nature of the screening surface in the disc-dominated region of the galaxy (left-hand side of the $f(R)$ plot) indicates that using ap-

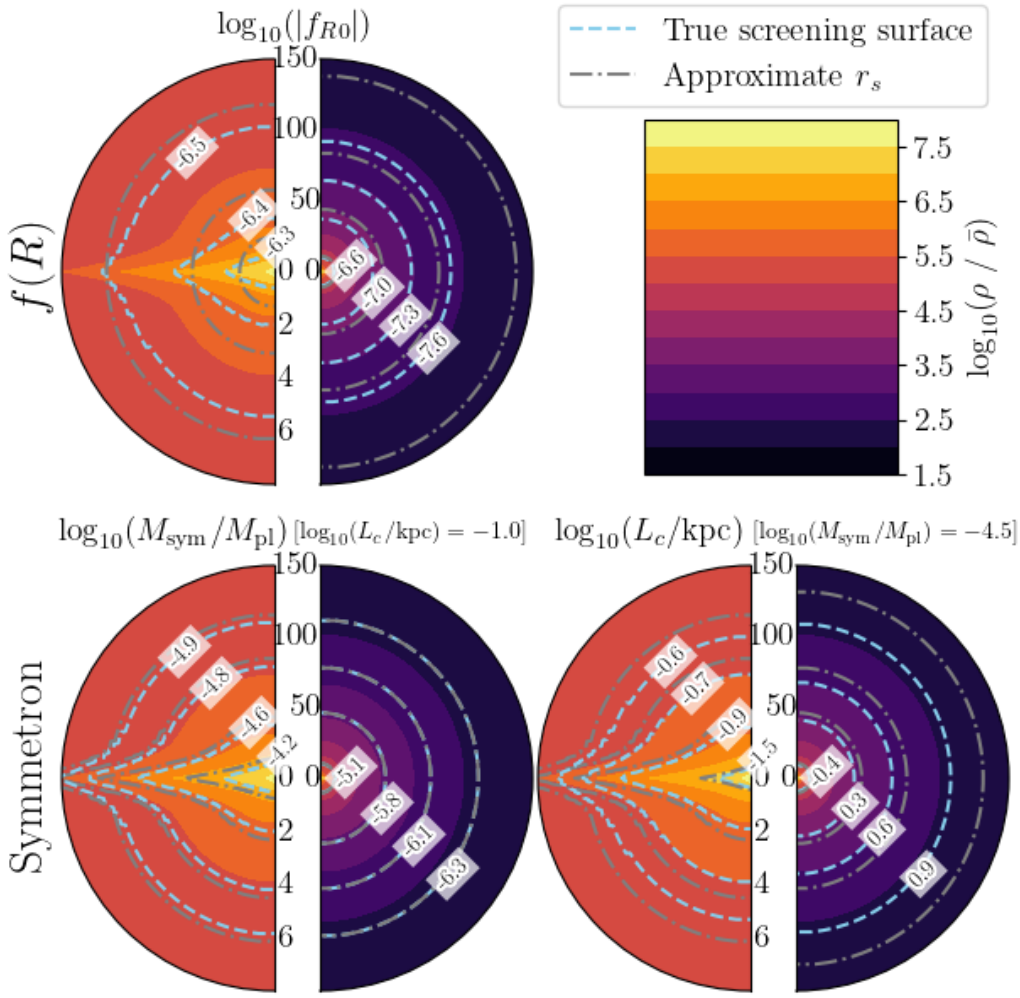


Figure 3.3: Screening surfaces across a range of theory parameters, in a galaxy with mass $M_{\rm vir} = 10^{11.5}\,M_\odot$, for $f(R)$ (top) and symmetron (bottom) models. In the symmetron case, we vary $M_{\rm sym}$ holding $L_{\rm c}$ fixed (bottom left) and vary $L_{\rm c}$ holding $M_{\rm sym}$ fixed (bottom right). Sky blue dashed lines are the calculated screening surfaces with theory parameters labelled. Grey dashed-dotted lines are approximate solutions: numerically integrating the critical potential (1.89) in the $f(R)$ case; isodensity contours equal to $\rho_{\rm SSB}$ in the symmetron case. In each case, the right-hand semi-circle plots the radial range of the galaxy out to $10\,r_{\rm NFW}$ (approximately 150 kpc), while the left-hand semi-circle zooms into the central region, out to $5R_{\rm disc}$ (approximately 8 kpc). The coloured background regions represent the adopted matter density profile, plotted as a fraction of the cosmic mean density.

proximations (dashed-dotted lines) that result in spherical screening radii, such as eq. (1.89), can fail to capture the true nature of the screened region. This is especially relevant when searching for observables along the plane of the disc, where r_s will be underestimated as the spherical screening surface meets the disc plane at a smaller radius than the true, flattened screening surface. As a result, for a given value of the theory parameter, one may expect the presence of fifth force observables at a certain location in the disc plane because it lies outside the assumed spherical screening surface, whereas, in reality, the location lies within the true, flattened, screening surface, and so the fifth force is suppressed. This in turn could lead to exaggerated constraints on the theory parameters.

In the halo-dominated region of the galaxy (right-hand side of the $f(R)$ plot) we see the approximation overestimates the screening radius for smaller values of $|f_{R0}|$ — corresponding to larger values of r_s, and smaller Compton wavelengths. This leads to an overestimation of the amount of dark matter that is screened by this approximation. This behaviour is likely due to a breakdown of the approximations utilised to derive the critical potential at large r_s values, namely that the field can be linearised around the screening surface, and that the scalar mass is negligible in this region. Specifically, when the Compton wavelength is smaller than the extent of the galaxy, not all the mass within the galaxy impacts the field profile, whereas the approximation, which assumes negligible scalar mass and thus infinite Compton wavelength, responds to mass in the extremities of the galaxy. The effect that this overestimation of r_s has on observables is discussed further in section 3.5.2.

By contrast with the $f(R)$ screening surfaces, the screening surfaces under the symmetron theory (bottom plots) follow the isodensity contours very closely. However, this behaviour breaks down in the large $L_{\rm c}$, large $M_{\rm sym}$ regime, as seen with the larger screening radii in the left-sided symmetron plots, where the screening surface fails to trace the finer details of

the isodensity contour, especially near the disc plane. The reasoning for this breakdown is due to the physics associated with each parameter. The Compton wavelength, $L_{\rm c}$, is the characteristic scale on which the field can vary, i.e. the field will not respond to changes on scales much smaller than the Compton wavelength, but in the large $L_{\rm c}$ regime the scale height of the disc profile is much smaller than $L_{\rm c}$. In other words, a larger Compton wavelength responds to mass averaged over a larger distance, causing the field profile to smooth out the finer details of the disc density profile. Meanwhile, for the coupling constant, $M_{\rm sym}$, the coupling function, and thus the density-dependent term in the EoM, eq. (1.120), have an inverse proportionality to $M_{\rm sym}^2$, meaning a large change in density has less impact on the field profile.

The approximation of symmetron screening surfaces as isodensity contours matching $\rho_{\rm SSB}$ is a natural consequence of the highly sensitive relationship between the screened region and the symmetry-breaking scale. These approximate solutions are shown as grey dashed-dotted lines on the symmetron plots of figure 3.3. For the most part, this approximation does a good job of calculating the true value of r_s, especially in the small $M_{\rm sym}$, small $L_{\rm c}$ regime. Outside of this region of parameter space, the approximation always overestimates the value of r_s when compared to the true value. This overestimation is especially prevalent in the large $L_{\rm c}$, large $M_{\rm sym}$ regime.

3.5.2 Amounts of Galactic Mass Screened

One of the main results of our analysis is contained within figure 3.4, where we show the percentage of mass contained within the screening surface over a range of galactic and theory parameters. The left column represents the disc mass and the right column is the halo mass. In the symmetron plots, we vary one parameter with the other parameter fixed. This figure allows us to study how our system transitions from screened to unscreened

across the parameter space, which we can compare with the transition from screened to unscreened given by the binary screening condition, eq. (3.1) in the $f(R)$ case and eq. (3.2) in the symmetron case. As a proxy for the 'true' answer, we include a dashed contour line to show the parameter boundary where 50% of the mass is screened in each case.[5] This line can then be directly compared with the binary screening condition boundary, which we represent with a dotted line in the $f(R)$ and symmetron $M_{\rm sym}$ plots respectively (not included in the $L_{\rm c}$ plot since the symmetron critical potential is a function of $M_{\rm sym}$ only).

All the sub-figures contained in figure 3.4 exhibit some similar behaviours. The galactic disc component transitions sharply from being fully screened to fully unscreened, with the two regimes separated in the parameter space of galaxy and model parameters by only a narrow band in which the disc is partially screened. In contrast, the fraction of screened dark matter varies gradually, due to the significant dynamical range of the halo, which spans several orders of magnitude in density. Another notable feature is the discrepancy between the regions considered fully screened and unscreened by the binary condition and the region where half of the mass is screened. This is explored further throughout this section. In all cases, the r_s approximations (dashed-dotted lines) are closer to the true 50% screened solution than the binary screening condition.

Focusing first on the $f(R)$ case, we see that the $f(R)$ binary screening condition, eq. (3.1), does not correctly characterise the screening of the galactic disc. Specifically, the region of parameter space considered 'fully unscreened' by the binary condition (above the dotted line in the top left panel) includes roughly an order-of-magnitude in which the galactic disc is actually entirely screened. This ultimately means that searching for signatures of screening theories in 'fully unscreened' galaxies may lead to

[5]There is ultimately a degree of arbitrariness in our choice of 50% as a proxy. It intuitively feels the fairest way to divide the spectrum of solutions in two, but one could instead argue for a lower (higher) threshold such that the partially screened solutions are preferentially grouped with the fully screened (unscreened) solutions.

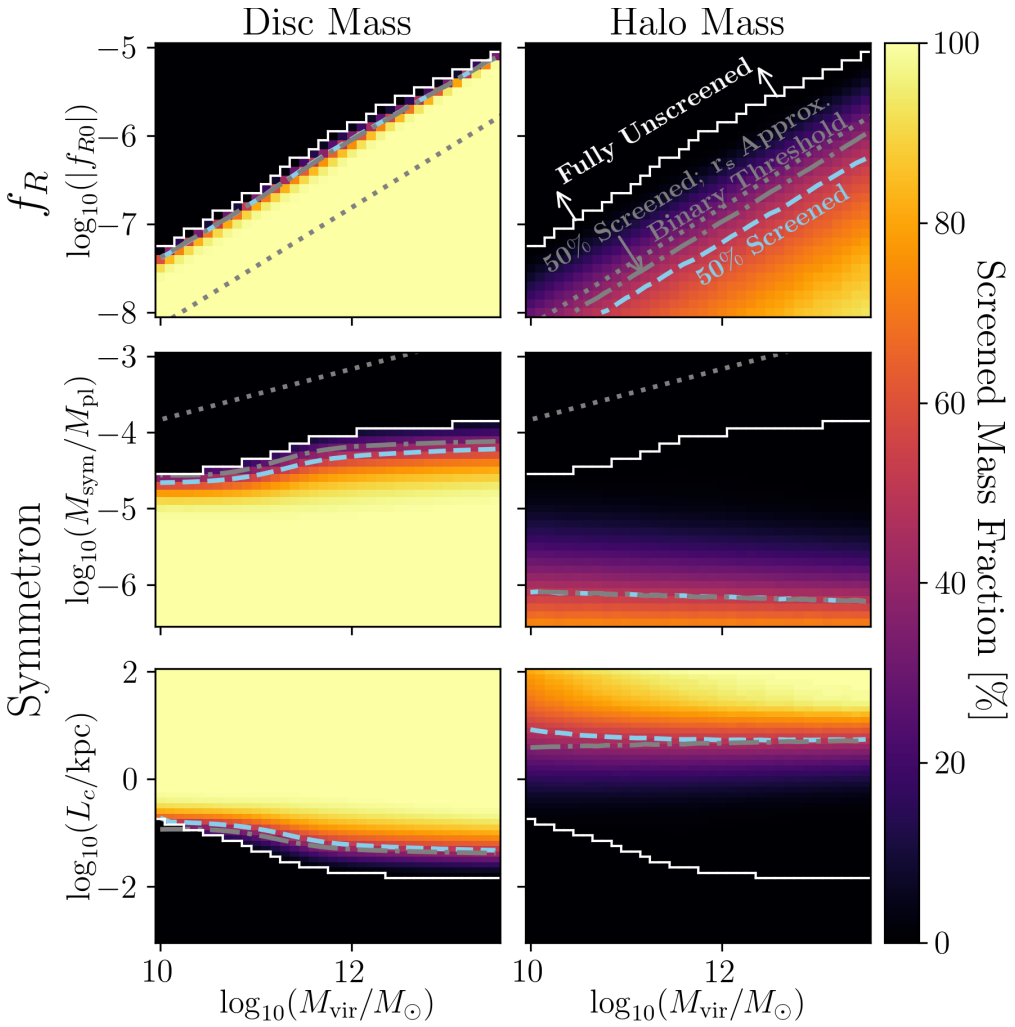


Figure 3.4: Fraction of disc mass (left) and dark matter (right) screened, for a range of $f(R)$ (top) and symmetron parameters, with fixed $L_{\rm c} = 10^{-1}\,{\rm kpc}$ (middle) and with fixed $M_{\rm sym} = 10^{-4.5}\,M_{\rm pl}$ (bottom). Sky blue dashed contours show where 50% of mass is screened. Grey dashed-dotted contours indicate where 50% of mass is screened when r_s is approximated: by numerically integrating eq. (1.89) for the $f(R)$ critical potential, or by finding isodensity contours equal to $\rho_{\rm SSB}$ for the symmetron model. Grey dotted lines correspond to the binary screening condition; solutions below this line would be considered 'fully screened'. Solid white lines separate the fully unscreened and partially screened solutions.

false negative results since the visible stellar and gas components are fully screened. For example, when looking at stellar-gas offsets (Desmond et al., 2018b, 2019a) in this region of parameter space the disc is fully screened and there is therefore no displacement between the stellar and gas components. However, using eq. (3.1) as a binary screening threshold would lead one to assume that the disc is unscreened and thus incorrectly predict the presence of an offset. In practice, this could entail relaxing the current tightest constraints.

By contrast with the disc, for the halo the binary screening condition kicks in at a point where the halo is only partially screened, so there will be haloes (below the dotted line in the top right panel) which will be classed as screened but actually carry a substantial unscreened component in their outskirts, as much as 60-70% of the total halo mass. Similarly, there will be haloes (above the dotted line) which will be classed as unscreened but actually have screened central regions, comprising as much as 30-40% of the total halo mass. This is the fundamental flaw in the binary screening condition: it assumes a step change in a quantity which actually changes gradually over the course of several orders of magnitude in parameter space. In summary, the $f(R)$ binary screening condition underestimates unscreened mass when it classifies an object as screened, and it underestimates screened mass when it classifies an object as unscreened.

The various panels in figure 3.4 also include dashed-dotted lines to indicate when 50% of the mass is screened when r_s is derived by approximate means. In the $f(R)$ case (top row), this is when r_s is derived by numerically integrating eq. (1.89) for a spherically averaged version of our galaxy density profile. This approximation solution yields results closer to the exact solution than the binary screening condition. For the galactic disc (top left panel), this approximation contour is almost identical to the equivalent numerical solution contour, and the difference in the proportion of mass screened between the two calculations is no more than 5% across the

range of parameters we consider. However, as we saw in figure 3.3, the true and approximate solutions for r_s can have vastly different shapes and the spherical nature of the approximate screening surface results in an underestimation of r_s along the galactic disc and an overestimation along the perpendicular axis.

For the dark matter component (top right panel), the approximate value of r_s, and therefore the percentage of mass screened, is very close to the actual value for low values of r_s. However, as r_s becomes larger, the approximate solution begins to overestimate r_s compared to the actual solution, as previously seen in figure 3.3. This overestimation occurs in the limit of large $M_{\rm vir}$ and small f_{R0}, and emerges because, in this regime, the Compton wavelength becomes smaller than the extent of the galaxy. Given that the approximation assumes a negligible scalar mass and thus an infinite Compton wavelength, it considers mass beyond a Compton wavelength (which does not significantly impact the field). The biggest discrepancy between the approximate and true screening surfaces, located in the lower right of the $f(R)$ parameter space of figure 3.4, results in the estimated proportion of screened dark matter being as much as 20% larger than the actual solution. In other words, if the 50% threshold were increased to, e.g., 80%, then the two lines would be further separated. Ultimately this will result in the predicted fifth forces sourced by the galaxy being larger than in the true case, but not to the same extent as the binary screening condition would predict.

For the symmetron model (middle and bottom rows), the binary screening condition is much less accurate. As discussed in section 3.3.4, the condition depends only on $M_{\rm sym}$, but even in the middle row, with varying $M_{\rm sym}$ and fixed $L_{\rm c}$, this estimate of screening disagrees with our solution by several orders of magnitude. Looking at the row with varying $L_{\rm c}$ and fixed $M_{\rm sym}$, it is clear that the location of the screening surface is a strong function of $L_{\rm c}$. Therefore, this simplified version of the symmetron binary

screening condition should be avoided.

Instead, a more useful approximation for screening is obtained by assuming the screening surface is coincident with the surface where the total density equals $\rho_{\rm SSB}$. The parameter space that results in 50% of each mass component being enclosed by this approximate screening surface is shown in the symmetron panels of figure 3.4 as a dashed-dotted contour. As discussed in section 3.5.1, this approximation will never underestimate the value of r_s, and will overestimate r_s for large values of $M_{\rm sym}$ or $L_{\rm c}$. Looking first at the disc mass, in both cases (varying $M_{\rm sym}$ and varying $L_{\rm c}$) the approximation contour follows a similar behaviour to the true contour, but somewhat overestimates the amount of disc mass screened. Notably, the distance in parameter space between the true and approximate 50% screened contours is reduced in the case where $L_{\rm c}$ is smaller (towards the right of the bottom-left panel with varying $L_{\rm c}$ and fixed $M_{\rm sym}$). For the dark matter component, we see that the approximate and true 50% screening lines are indistinguishable in the middle right panel with varying $M_{\rm sym}$ and fixed $L_{\rm c}$. This is due to the fact that $L_{\rm c}$ is fixed at a low value of $10^{-1}\,$kpc, and so to get a large screening radius that screens 50% of the halo we need a small value of $M_{\rm sym}$, thus falling into the regime where this approximation works best (small $M_{\rm sym}$, small $L_{\rm c}$). In the bottom right panel with varying $L_{\rm c}$ and fixed $M_{\rm sym}$, the 50% line is a good match for larger galaxies, but for smaller galaxies the approximation overestimates the amount of mass screened. As length scales get smaller they become comparable with $L_{\rm c}$ and the field can not respond to the density changes quickly enough to screen exactly along the isodensity contour. In summary, the approximation does not account for the full effects of varying $M_{\rm sym}$ and $L_{\rm c}$, so it falters in the regimes in which these effects are strongest.

One noteworthy caveat to this discussion is that we do not consider any environmental effects, e.g., the presence of over-/underdensities within a few Compton wavelengths of our target galaxies. In general, these would

serve to vary the location of the screening surface of a given galaxy from that calculated in isolation. We have done some preliminary tests in this regard, and find the conclusions to this section are robust. We experimented with mimicking overdense environments by embedding our galaxies in large overdense spheres of constant density. As expected, the additional overdensity leads to the galaxies being screened more easily. However, we find that either the true and approximate solutions for the screening surface shift equally or the gulf widens. However, a full reanalysis with proper treatment of environmental effects is required to make a clear, quantitative conclusion.

Finally, we note that the results presented here rely on 'maximally typical' galaxy models derived from the median trend lines of scaling relations. In reality, a population of galaxies exhibit intrinsic scatter around these relations. Propagating this scatter through our analysis to quantify the uncertainty on the screened mass fractions would require a computationally expensive statistical analysis over a large population of galaxy (and scalar field) realisations. While such an analysis would refine the boundaries in figure 3.4, the qualitative conclusions regarding the breakdown of binary screening and spherical approximations remain robust. Furthermore, since the completion of this work, newer constraints have been derived that avoid the need for the approximations benchmarked here (Landim et al., 2024).

3.5.3 Milky Way Observables

Figure 3.5 shows the derived screening radius along the plane of the galactic disc, over the entire model parameter spaces, for a Milky Way-like galaxy with $M_{\rm vir} = 1.5 \times 10^{12} M_\odot$ (McMillan, 2017). The approximate distance from the Milky Way centre to the Solar System (8 kpc) is marked by the dashed lines. The dashed-dotted lines show the screening radius derived via approximate methods, namely, numerically integrating eq. (1.89) given the $f(R)$ critical potential, eq. (3.1), or defining the screening surface as

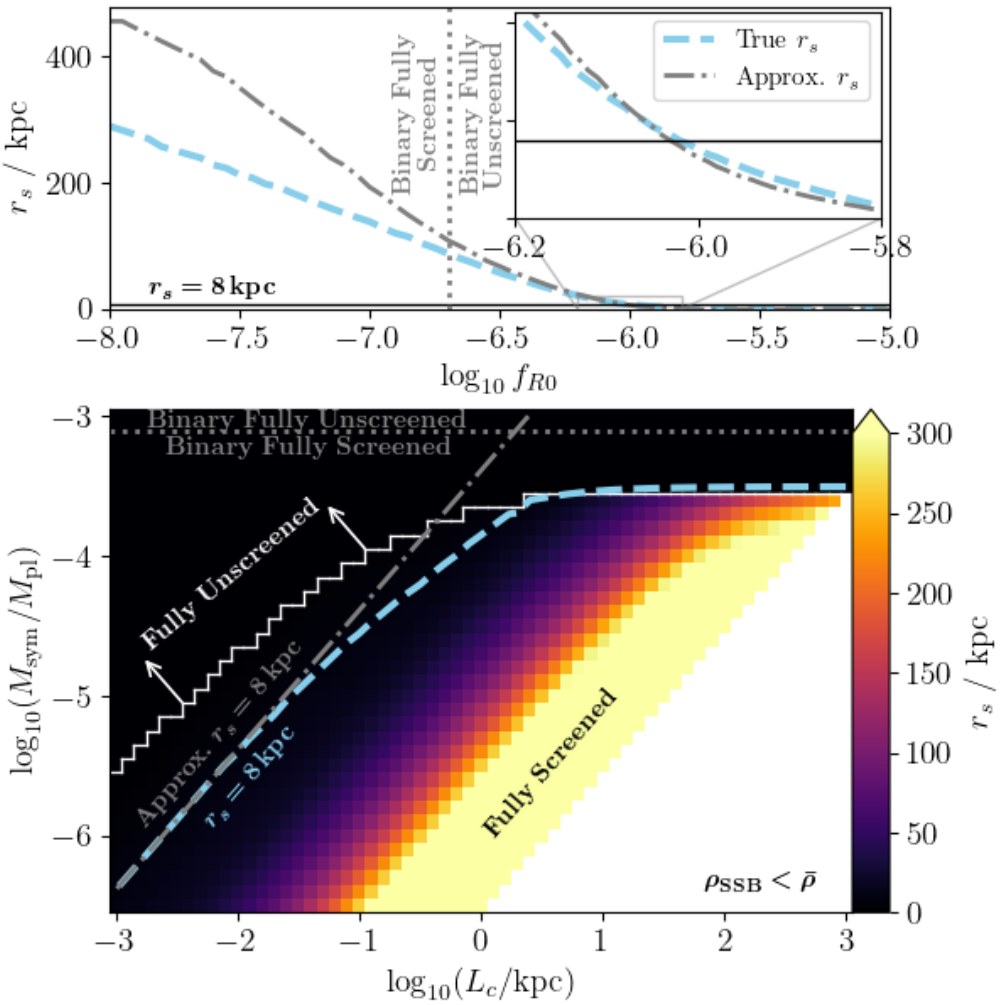


Figure 3.5: Positions where non-spherical screening surface intersects the disc plane of a Milky Way-like galaxy over $f(R)$ (top) and symmetron (bottom) parameter space. In the $f(R)$ plot, the dashed line shows the true r_s value, whereas the dashed-dotted line shows the approximate r_s values, derived by numerically integrating eq. (1.89) for the $f(R)$ critical potential. In the symmetron plots, the colourmap shows the true r_s value, the dashed line indicates where r_s is equal to the Milky Way centre-Solar System separation of 8 kpc, and the dashed-dotted line shows where the approximate r_s, derived by finding isodensity contours equal to ρ_{SSB}, is equal to the Milky Way centre-Solar System separation. Dotted lines indicate the binary screening condition. In the symmetron plot, a solid white line separates the fully unscreened and partially screened solutions, and the white region shows where SSB does not occur, i.e. the cosmic background density, $\bar{\rho}$, is greater than ρ_{SSB}.

the isodensity contour equal to $\rho_{\rm SSB}$ in the symmetron case. The dotted lines represent the binary screening boundary, separating the parameters that cause solutions to be considered 'fully screened' and 'fully unscreened'.

Specifically, all $|f_{R0}|$ values less than $10^{-6.7}$ and all $M_{\rm sym}$ values less than $10^{-3.1}\,M_{\rm pl}$ are considered 'fully screened' by the binary screening conditions. In the $f(R)$ plot, we again see the approximate r_s begins to overestimate the true solutions when the Compton wavelength becomes comparable to the extent of the galaxy, at $|f_{R0}| \lesssim 10^{-7}$.

Stringent constraints based on tests of celestial gravitational dynamics require that the Milky Way screening radius extends to at least 8 kpc, encompassing the entire Solar System (Adelberger et al., 2009). Figure 3.5 allows us to determine the parameter space permitted by such constraints, namely $|f_{R0}| \lesssim 10^{-6.0}$ and the portion of the symmetron parameter space satisfying $M_{\rm sym} \lesssim 10^{-3.6} M_{\rm pl}$ and to the right of the dashed line on the lower panel. There are a few caveats to these constraints. Firstly, they only apply to this particular galaxy model and choice of mass. We do not expect the Milky Way to be a maximally-typical galaxy but for consistency with our previous analysis, we have modelled it as such. In addition, there remains significant empirical uncertainty regarding the total mass of the Milky Way halo (Callingham et al., 2019), which would have a non-negligible effect on the bounds we obtain. We have also neglected any environmental effects, such as the influence of the Local Group and the galaxy's wider cosmographic context.

Given the strict constraint on the minimum value of the Milky Way's screening radius, the question arises as to whether there can still be observable effects in the periphery of the galactic disc. For this galaxy, the disc component becomes subdominant along the disc plane after roughly 14 kpc. Looking at either panel of figure 3.5, between the $r_s = 8$ kpc contour and the parameter space where $r_s = 14$ kpc, there is only a small slice of parameter space in which the Solar System is screened but the bulk of

the galactic disc is not. This means it would require a great deal of fortune to be in a universe adopting these parameter values and allowing us to explain observable effects in the disc via fifth forces.

Nevertheless, there remains several orders of magnitude of unconstrained parameter space in which the screening radius lies between the edge of the galactic disc and the virial radius of $\sim 300\,\mathrm{kpc}$. As such, observable consequences of scalar fields with screening mechanisms located in the Milky Way's dark matter halo, are entirely plausible. For example, the kinematics of halo tracers or the detection of equivalence-principle-violating asymmetries in the leading and trailing tails of stellar streams, from tidally disrupted dwarf galaxies in the dark matter halo, as in Naik et al. (2020); Kesden and Kamionkowski (2006a,b); Keselman et al. (2009).

An additional feature in figure 3.5 worth mentioning is the turn-off in the top right of the symmetron plot. Away from this region, lines of equal screening radius are diagonals across parameter space. These diagonals correspond with lines of equal ρ_{SSB} ($\rho_{\mathrm{SSB}} \propto M_{\mathrm{sym}}/L_{\mathrm{c}}^2$; cf. eq. (1.116)), and as we saw in figure. 3.3, screening surfaces closely match the $\rho = \rho_{\mathrm{SSB}}$ surfaces in the low M_{sym}, low L_{c} regime. The turn-off is another symptom of the breakdown of this behaviour in the large M_{sym}, large L_{c} limit.

3.6 Conclusions

In this work, we have investigated the effects of scalar modifications of gravity on galactic scales, for both chameleon $f(R)$ and symmetron screening theories, with a particular focus on how screening differs between full numerical solutions and common approximations used to derive constraints. To determine the screened region, we solved the quasi-static scalar field EoM numerically, given an input density described by a maximally-typical galaxy consisting of a double-exponential disc profile and a dark matter NFW halo. We developed new and robust screening conditions to com-

pute the position of the screening surface based on the scalar field values, eqs. (3.3).

We examined the shape of our calculated screening surfaces. We find that screening surfaces in the halo-dominated region follow the spherical isodensity contours. In the disc-dominated region, $f(R)$ screening surfaces almost follow the isodensity contours, but are overall more spherical than the disc profile. Symmetron screening surfaces closely follow isodensity contours in the disc-dominated region, except in the large $M_{\rm sym}$, large $L_{\rm c}$ limit where the individual microphysics of each parameter becomes important.

The simplest approximation we explore is the binary screening condition (Cabré et al., 2012) where if a galaxy has a virial potential, $\Phi_{\rm vir} = GM_{\rm vir}/r_{\rm vir}$, greater/smaller than the critical potential then it is classified as fully screened/unscreened, ignoring the effects of partial screening. We note that the symmetron binary screening condition, eq. (3.2), is not suitable as a proxy for screening. This is because the approximations required to derive the critical potential, eq. (1.89), are incompatible with the symmetron theory, namely the assumptions that the field can be linearised, the scalar mass is negligible and $\beta(\phi)$ is constant.

We explored the effectiveness of the binary screening condition as a proxy to $f(R)$ screening, for observables in the visible disc and dark matter halo. We found that the binary screening condition drastically underestimates the amount of parameter space in which the galactic disc is fully screened. In this fully screened region of parameter space, using the binary screening condition would erroneously define the galaxy as 'fully unscreened', i.e. there spans an order-of-magnitude in parameter space where the binary screening condition would lead one to predict an observable signature that would not occur. It follows that constraints set using the binary screening condition in this contested region of parameter space could be up to an order-of-magnitude tighter than if one numerically computed the true screening surface.

We also compare our true solutions against approximate screening surfaces. In the $f(R)$ case, r_s can be approximated by numerically solving the critical potential, eq. (1.89), for a spherically averaged galactic density. In this case, the resulting approximate screening surfaces are spherical. For the symmetron model, it is possible to approximate r_s as the location where the density is equal to the symmetron breaking scale, i.e. $\rho(r = r_s) = \rho_{\rm SSB}$.

For the halo, we found the binary screening condition sits in the region of parameter space where the haloes are partially screened. This means objects classified as "screened" actually have 60-70% unscreened mass, while objects classified as "unscreened" actually have 30-40% screened mass. This is the fundamental flaw of the binary screening condition, the fact that the binary screening condition assumes a discrete step change between fully screened and unscreened, but actually the degree of screening varies gradually over many orders of magnitude in parameter space.

Direct approximation of r_s allows for partial screening solutions and is overall a closer approximation to the true screening solutions than the binary screening condition. In regions where the disc component is not negligible, the spherical approximate screening surface will underestimate r_s along the disc and overestimate r_s perpendicular to the disc. As a result of this, we might expect to see an observable feature at a location along the plane of the disc, but in fact, the location is within the true screening surface and therefore there is no observable feature. In addition, this approximation overestimates r_s for small values of $|f_{R0}|$, corresponding to smaller Compton wavelengths. This is a result of the approximation assuming a negligible scalar mass, and thus being influenced by additional mass that the field does not respond as strongly to. The effect is amplified in the large $M_{\rm vir}$, small f_{R0} limit, where the extent of the galaxy is largest and the Compton wavelength is smallest.

We have shown that defining the symmetron r_s as the radius at which the total density equals $\rho_{\rm SSB}$ is a useful approximation for a large portion

of the parameter space. However, in the large $M_{\rm sym}$, large $L_{\rm c}$ limit, varying the two parameters separately has consequences for the scalar field profile that are not captured purely through a dependence on $\rho_{\rm SSB}$ and the approximation breaks down. In general, the approximate screening surface will never underestimate r_s and the amount of overestimation depends on how large $M_{\rm sym}$ and $L_{\rm c}$ are. In smaller galaxies, the approximation may break down if the galactic scale length becomes comparable to $L_{\rm c}$.

Finally, we explored the possibility of finding observables in a Milky Way-like galaxy. Assuming that the Solar System is screened by the Milky Way, we found that (for our isolated test Milky-Way galaxy) $|f_{R0}|$ must be less than $10^{-6.0}$ and $M_{\rm sym}$ must be less than $10^{-3.6}\,M_{\rm pl}$ with $L_{\rm c}$ being to the right of the dashed line in the bottom panel of figure 3.5. We saw that there is only a small slice of model parameter space in which there could be observable effects in the galactic disc. This suggests we would have to be rather fortunate to exist in a universe where we could detect the modifications to GR considered in this work within our own galactic disc — however, searches for observables in the halo remain promising, thanks in part to the large dynamical range of the halo density.

As cosmological surveys continue to improve the precision of their measurements it is important that theoretical predictions continue to improve in accuracy alongside them. It is in this spirit that we have presented, in this chapter, new definitions of screening for both the $f(R)$ chameleon model and the symmetron model of screening. We have shown that it is important to differentiate between situations where the galactic disc is screened, but much of the dark matter halo is unscreened, and situations where the majority of the total mass of the galaxy is screened. We have shown that some approximations currently used in the literature could lead to order-of-magnitude errors in the constraints placed on model parameters from galactic observations. We intend to present a reanalysis of current constraints in the near future.

Chapter 4

Galactic Compton Wavelengths in $f(R)$ Screening Theories

Declaration: This chapter is based on the published paper: *Galactic Compton Wavelengths in $f(R)$ Screening Theories*, (March et al., 2024). The source code and plotting scripts are publicly available at github.com/Bradley-March/scalar-compton-wavelength.

4.1 Summary

$f(R)$ theories of modified gravity may be compatible with current observations if the deviations from general relativity are sufficiently well screened in dense environments. In recent work (Burrage et al., 2024) we have shown that approximations commonly used to assess whether galaxies are screened, or unscreened, fail to hold in observationally interesting parts of parameter space. One of the assumptions commonly made in these approximations, and more broadly in the study of $f(R)$ models, is that the mass of the scalar mode can be neglected inside a galaxy. In this work we demonstrate that this approximation may fail spectacularly and discuss the implications of this for tests of the theory.

4.2 Introduction

In recent years, the continuing puzzle of the dark sector has motivated the study of scalar-tensor theories of gravity, in which the scalar field mediates gravitational-strength *fifth forces* (Hu and Sawicki, 2007; Joyce et al., 2015; Koyama, 2016; Ishak, 2019; Burrage and Sakstein, 2018; Brax et al., 2022; Saridakis et al., 2021b; Vardanyan and Bartlett, 2023). For such a fifth force to evade detection in stringent Solar System tests of gravity, the theory must possess some *screening mechanism*, such that the force is suppressed in environments resembling the Solar System (i.e., environments of high ambient density or deep gravitational potential). Various screening mechanisms have been proposed along these lines, for example, the Vainshtein and symmetron mechanisms (Hinterbichler and Khoury, 2010; Hinterbichler et al., 2011; Vainshtein, 1972; Babichev and Deffayet, 2013). In this work, we are concerned with the class of theories exhibiting *chameleon* screening (Khoury and Weltman, 2004b,a), in which the mass of the scalar grows large in dense regions. In particular, we focus on the theory of Hu-Sawicki $f(R)$ gravity (Hu and Sawicki, 2007; Brax et al., 2008), which has received especially widespread attention in the literature.

Galactic scales present a particularly interesting area of study in $f(R)$ theories. Baker et al. (2019) showed that galactic scales inhabit a 'desert' in parameter space with comparatively few observable probes. In the years since that work, various studies have sought to explore this desert, with considerable success (Hui et al., 2009; Jain and VanderPlas, 2011; Vikram et al., 2013, 2014; Lombriser and Peñarrubia, 2015; Burrage et al., 2017; Desmond et al., 2018a,b; O'Hare and Burrage, 2018; Naik et al., 2018, 2019, 2020; Bartlett et al., 2021; Pedersen and Stubbs, 2023; Benisty et al., 2023). Indeed, the strongest constraints to date on $f(R)$ gravity were obtained in recent works by Desmond and Ferreira (2020), and Landim et al. (2024) in a search for chameleon-induced equivalence principle violations in a large sample of observed galaxies.

In parallel with these analyses of observable probes, there has been work aiming to improve our theoretical understanding of the interplay between chameleon fifth forces and galaxies. Because galaxies inhabit the deeply non-linear regime of cosmological structure formation, such an understanding can only be obtained by numerical computation, typically with various simplifying approximations. For example, recent work has produced cosmological galaxy formation simulations incorporating a quasi-static chameleon fifth force (Arnold et al., 2019). Another example is our previous work (Burrage et al., 2024) (chapter 3) in which $f(R)$ solvers were applied to static galactic models to solve for the scalar field and accompanying fifth forces. For a review of the approaches and challenges to numerically modelling theories with screened fifth forces see Llinares (2018).

When studying the behaviour of the scalar field within a galaxy, and the resulting screening of the fifth force, the various components of the galaxy (stars, gas and dark matter) are typically treated as continuous fluids of varying density. However, this approximation might not be a very good one in the case of the stellar component, or even the dark matter component if it is composed of compact objects and/or small-scale subhaloes. The goal of the present work is to test the approximation that the distribution of stars in a galaxy can be treated as a smooth density distribution. In particular, we calculate the Compton wavelength of the $f(R)$ scalar field across a series of typical galaxies, assuming a continuous stellar density profile, and compare this length scale with the typical stellar separation. To anticipate our results, we find that in the screened regions of galaxies, the Compton wavelength is often far smaller than the stellar separation, suggesting that the continuous fluid approximation is inadequate.

This work is structured as follows. In section 4.3 we present the Hu-Sawicki $f(R)$ gravity theory, including expressions for the Compton wavelength. Section 4.4 describes our numerical solutions for the scalar field across our galactic model. Section 4.5 describes the results, before conclud-

ing remarks in section 4.6. Throughout this chapter we work in natural units such that $8\pi G = c = \hbar = 1$, except where units are explicitly stated. Note that this differs from the rest of the thesis, where we set $c = \hbar = 1$ but retain $8\pi G$.

4.3 Theory

4.3.1 $f(R)$ Gravity

In this work we focus on $f(R)$ theories of gravity, fully detailed in section 1.3.6. We provide a brief overview of the key equations specific to this work here.[1] In general $f(R)$ theories substitute the Ricci scalar, R, in the Einstein-Hilbert action with the generalised, $R + f(R)$, eq. (1.96)

$$S = \frac{1}{2}\int \mathrm{d}^4x\sqrt{-\tilde{g}}\left[R + f(R)\right] + S_m\left[\tilde{g}_{\mu\nu}, \psi_i^{SM}\right] ,$$

Such an action can be reformulated into the general scalar-tensor framework via the field redefinition (Brax et al., 2008), eq. (1.97)

$$\phi = -\frac{\ln(1+f_R)}{2\beta(\phi)} , \qquad V(\phi) = \frac{Rf_R - f(R)}{2(1+f_R)^2} \qquad \text{and} \qquad \beta(\phi) = \frac{1}{\sqrt{6}} ,$$

where

$$f_R \equiv \frac{\mathrm{d}f(R)}{\mathrm{d}R}$$

serves as the scalar field in the theory.

The theory can exhibit chameleon screening, for certain functional forms of $f(R)$. In this work we adopt the well-known Hu-Sawicki model (Hu and Sawicki, 2007), characterised by the functional form, eq. (1.104),

$$f(R) = -\frac{am^2}{1 + (R/m^2)^{-b}} ,$$

where a and b are positive dimensionless parameters, and m has dimensions of inverse length. For simplicity, and consistency with the majority of

[1] Note that in previous sections the quoted equations have been explicit in $8\pi G$, but in the restated equations here we set $8\pi G = 1$.

literature, we set $b = 1$. The remaining parameters, a and m, can be related by ensuring that in the high curvature limit, $R \gg m^2$, gravity reverts to GR+ΛCDM, i.e. $f(R) \approx -2\Lambda$, where Λ is the cosmological constant. This allows us to express a and m in terms of the cosmological density parameters, and the present-day background field value f_{R0}, eq. (1.108) (Hu and Sawicki, 2007)

$$a = -\frac{4\Omega_\Lambda^2}{(\Omega_m + 4\Omega_\Lambda)^2}\frac{1}{f_{R0}} \quad \text{and} \quad m^2 = -\frac{3H_0^2(\Omega_m + 4\Omega_\Lambda)^2}{2\Omega_\Lambda} f_{R0}\,.$$

The equation of motion for the $f(R)$ field, in the small-field, quasi-static limit, is given by eq. (1.101)

$$\nabla^2 f_R = \frac{1}{3}\left(\delta R - \delta\rho\right)\,,$$

where $\delta\rho$ and δR represent the density perturbation and curvature perturbation, respectively. Within the Hu-Sawicki model the curvature perturbation is defined as

$$\delta R = R_0 \left[\sqrt{\frac{f_{R0}}{f_R}} - 1\right]\,,$$

where R_0 is the background curvature today. Gradients of the scalar field f_R mediate a fifth force, given by eq. (1.110),

$$\boldsymbol{a}_5 = \frac{1}{2}\boldsymbol{\nabla} f_R\,,$$

again assuming $|f_R| \ll 1$.

An examination of the fifth force equation, eq. (1.110), reveals that the effect of the scalar field is minimised when the field is constant and its gradient is approximately zero. This region with $\boldsymbol{\nabla} f_R \approx 0$ is refered to as the screened region. An analytical expression for the field profile can be derived in this limit, by noting that a flat field profile also implies a vanishing Laplacian in the $f(R)$ equation of motion, eq. (1.101). For the right-hand side of this equation to vanish we require

$$\frac{f_R^{\rm scr}}{f_{R0}} = \left(1 + \frac{\delta\rho}{R_0}\right)^{-2}\,, \tag{4.1}$$

where $f_R^{\rm scr}$ represents the analytic approximation to the screened field value. This screened solution corresponds to the curvature tracing the minimum of the effective scalar potential. This method has been utilised in the literature, e.g. Hu and Sawicki (2007).

Outside of a few special simplified cases, for example the screened solution discussed in eq. (4.1), it is not possible to solve the highly non-linear equation of motion for the f_R field analytically. In later sections of this work, where we wish to understand the behaviour of the field in a galaxy, we utilise a two-dimensional, cylindrically symmetric numerical solver, based on MG-GADGET (Puchwein et al., 2013), to solve a discretised version of the equation of motion, eq. (1.101). For a given input f_{R0} and $\delta\rho$, the code performs an iterative Gauss-Seidel method, to generate the field profile f_R. Section 2.2.1 provides in depth details of the numerical solver.

4.3.2 Compton Wavelength

The Compton wavelength of our theory is given by

$$\lambda_{\rm C} \equiv m_\phi^{-1}\,, \tag{4.2}$$

where the scalar mass, m_ϕ, is defined as

$$m_\phi^2 \equiv \frac{{\rm d}^2 V(\phi)}{{\rm d}\phi^2}\,. \tag{4.3}$$

The scalar field, ϕ, and potential, $V(\phi)$, are defined in eq. (1.97). We compute the mass in the field picture (ϕ, not f_R) because it is only in this picture that the scalar degree of freedom is canonically normalised, however, after applying the simplifications described later in this section both forms are equivalent to leading order.

The first derivative of the potential is

$$\frac{{\rm d}V}{{\rm d}\phi} = \frac{{\rm d}R}{{\rm d}\phi}\frac{{\rm d}V}{{\rm d}R} = -\beta\frac{R + 2f(R) - Rf_R}{(1+f_R)^2}\,, \tag{4.4}$$

where we have used

$$\frac{\mathrm{d}R}{\mathrm{d}\phi} = \left(\frac{\mathrm{d}\phi}{\mathrm{d}R}\right)^{-1} = -\frac{2\beta(1+f_R)}{f_{RR}}\,, \tag{4.5}$$

given $f_{RR} \equiv \frac{\mathrm{d}f_R}{\mathrm{d}R}$. The second derivative, resulting in the scalar mass, is

$$m_\phi^2 = \frac{\mathrm{d}^2V(\phi)}{\mathrm{d}\phi^2} = \frac{2\beta^2}{(1+f_R)^2 f_{RR}}\left[(1+f_R)^2 - f_{RR}\left((3-f_R)R + 4f(R)\right)\right]\,. \tag{4.6}$$

We can simplify this scalar mass using the functional form of $f(R)$, eq. (1.104), and its derivatives

$$f(R) = -\frac{am^2R}{R+m^2}\,, \tag{4.7}$$

$$f_R = -\frac{am^4}{(R+m^2)^2}\,, \tag{4.8}$$

$$f_{RR} = \frac{2am^4}{(R+m^2)^3}\,. \tag{4.9}$$

In the high curvature regime, $R \gg m^2$, these expressions are well approximated as

$$f(R) \approx -am^2\,, \tag{4.10}$$

$$f_R \approx -\frac{am^4}{R^2}\,, \tag{4.11}$$

$$f_{RR} \approx \frac{2am^4}{R^3}\,. \tag{4.12}$$

Eliminating R between equations (4.11) and eq. (4.12) gives

$$f_{RR} \approx \frac{2}{m^2}\sqrt{\frac{(-f_R)^3}{a}}\,. \tag{4.13}$$

Substituting these expressions into the scalar mass, eq. (4.6), and assuming $|f_R| \ll 1$, we obtain

$$\frac{m_\phi^2}{2\beta^2m^2} \approx \frac{\sqrt{a}}{2}(-f_R)^{-3/2} - 3\sqrt{a}(-f_R)^{-1/2} - a\,. \tag{4.14}$$

Eq. (1.108) shows that $a \sim |f_{R0}|^{-1}$. Therefore, given that $|f_R| \ll 1$, the latter two terms in this equation are subdominant to the first, leaving us

with the rather simple

$$m_\phi^2 \approx \beta^2 \sqrt{a} m^2 (-f_R)^{-3/2} \,. \tag{4.15}$$

This expression is equivalent to the previously obtained result (equation (48) in Hu and Sawicki (2007)), albeit we have expanded the f_{RR} term.

Using this simplified scalar mass, we determine the Compton wavelength of our theory to be

$$\lambda_{\rm C} \approx \left(\frac{(-f_R)^3}{a m^4 \beta^4} \right)^{1/4} \,. \tag{4.16}$$

By substituting the values for β and the model parameters a and m (eqs. (1.97) and (1.108) respectively), we arrive at the final expression

$$\lambda_{\rm C} \approx \frac{1}{H_0} \sqrt{\frac{2}{\Omega_m + 4\Omega_\Lambda}} \left(\frac{f_R^3}{f_{R0}} \right)^{1/4} \,. \tag{4.17}$$

In the cosmological background, $f_R \to f_{R0}$, the Compton wavelength reduces to

$$\bar{\lambda}_{\rm C} \approx \frac{1}{H_0} \sqrt{\frac{2|f_{R0}|}{\Omega_m + 4\Omega_\Lambda}}. \tag{4.18}$$

In previous work, e.g. Cabré et al. (2012), this equation is often quoted as $\bar{\lambda}_{\rm C} \approx 32 \sqrt{\frac{|f_{R0}|}{10^{-4}}}$ Mpc, where the prefactor of 32 requires adopting cosmological parameters of $h = 0.73$, $\Omega_m = 0.24$ and $\Omega_\Lambda = 0.76$.

4.4 Galaxy Model

4.4.1 Galactic Density Model

To represent the galactic density profile we employ a two-component model, comprising a dark matter and stellar disc component. This model is detailed fully in section 1.2.3, and restated here for convenience. The dark matter is represented by the standard NFW profile (Navarro et al., 1996),

eq. (1.50),

$$\rho_{\rm DM}(r) = \frac{\rho_{\rm NFW}}{\frac{r}{r_{\rm NFW}}\left(1+\frac{r}{r_{\rm NFW}}\right)^2},$$

where r is the spherical radial coordinate, and $\rho_{\rm NFW}$ and $r_{\rm NFW}$ are the characteristic density and length scales. The stellar disc is represented by a double exponential profile, eq. (1.56),

$$\rho_{\rm SD}(R,z) = \frac{\Sigma_{\rm disc}}{2z_{\rm disc}} \mathrm{e}^{-R/R_{\rm disc}} \mathrm{e}^{-|z|/z_{\rm disc}},$$

where R represents the cylindrical radial coordinate, z represents the coordinate perpendicular to the galactic disc, and $\Sigma_{\rm disc}$, $R_{\rm disc}$ and $z_{\rm disc}$ are the characteristic density and length scales.

In order to maintain the simplicity of our model and reduce the number of input parameters, we utilise several empirical relations to relate the various density profile scales to a single input parameter, the virial mass of the dark matter halo, $M_{\rm vir}$. In the empirical relations with scatter, we assume the median value; as such for any given $M_{\rm vir}$ we produce a maximally typical galaxy. The methodology employed to achieve this is outlined in section 2.1.

4.4.2 Separation Between Stars

In section 4.5 we will discuss how the Compton wavelength of the f_R field compares to the spatial separation between stars. Under the simplifying assumption of a single universal stellar mass M_* and neglecting binary or multiple systems, the separation between stars is approximately given by

$$S = \left(\frac{\rho_{\rm SD}}{M_*}\right)^{-\frac{1}{3}}, \tag{4.19}$$

where $\rho_{\rm SD}$ is the stellar density profile. In the rest of this work we assume $M_* = M_\odot$ in this estimate. For a Milky-Way-like galaxy, we would estimate the typical stellar separation at a galactic radius of 8 kpc is 2.5 pc, which is of similar order to the Solar System-α Centauri separation of 1.3 pc.

We acknowledge that this choice of $M_* = M_\odot$ as a single universal stellar mass is a simplification. The true stellar initial mass function is dominated by low-mass stars ($M < 0.5M_\odot$), which would suggest a lower average mass and thus a smaller average separation $S \propto M_*^{1/3}$. However, this effect is partially offset by the high fraction of stars in binary or multiple systems (estimated at $\gtrsim 50\%$ for solar-type stars), effectively increasing the mass of each discrete "source". Ultimately, these factors introduce uncertainties of order unity. As we will show, the discrepancies between the Compton wavelength and stellar separation in the screened regime span orders of magnitude, rendering our conclusions insensitive to the precise choice of average stellar mass.

4.5 Results

4.5.1 Compton Wavelength in Galaxies

Figure 4.1 provides an example of the field profile, with a background value of $f_{R0} = -10^{-6}$, and related quantities that we can compute in a Milky-Way-like galaxy; specifically: the numerically calculated field profile, treating the stars as a continuous fluid, f_R, (top left); the Compton wavelength calculated from this field profile, eq. (4.17), $\lambda_{\rm C}$, (top right); the analytic screened field value, $f_R^{\rm scr}$, eq. (4.1) (bottom left); and the galactic density profile, $\delta\rho$, eqs. (1.50) and (1.56) (bottom right). The sharp transition in f_R values shown in figure 4.1 corresponds to the position of the screening surface, r_s. Inside this surface fifth forces are suppressed and the field is small; outside, the field increases towards the background value of f_{R0} and fifth forces are unsuppressed. For the parameters chosen in this figure, the galaxy is partially screened, with a screening surface located within the stellar disc.

Figure 4.1 also illustrates a number of relationships between parameters we have previously discussed. That $\lambda_{\rm C} \propto |f_R|^{3/4}$, eq. (4.17), can be

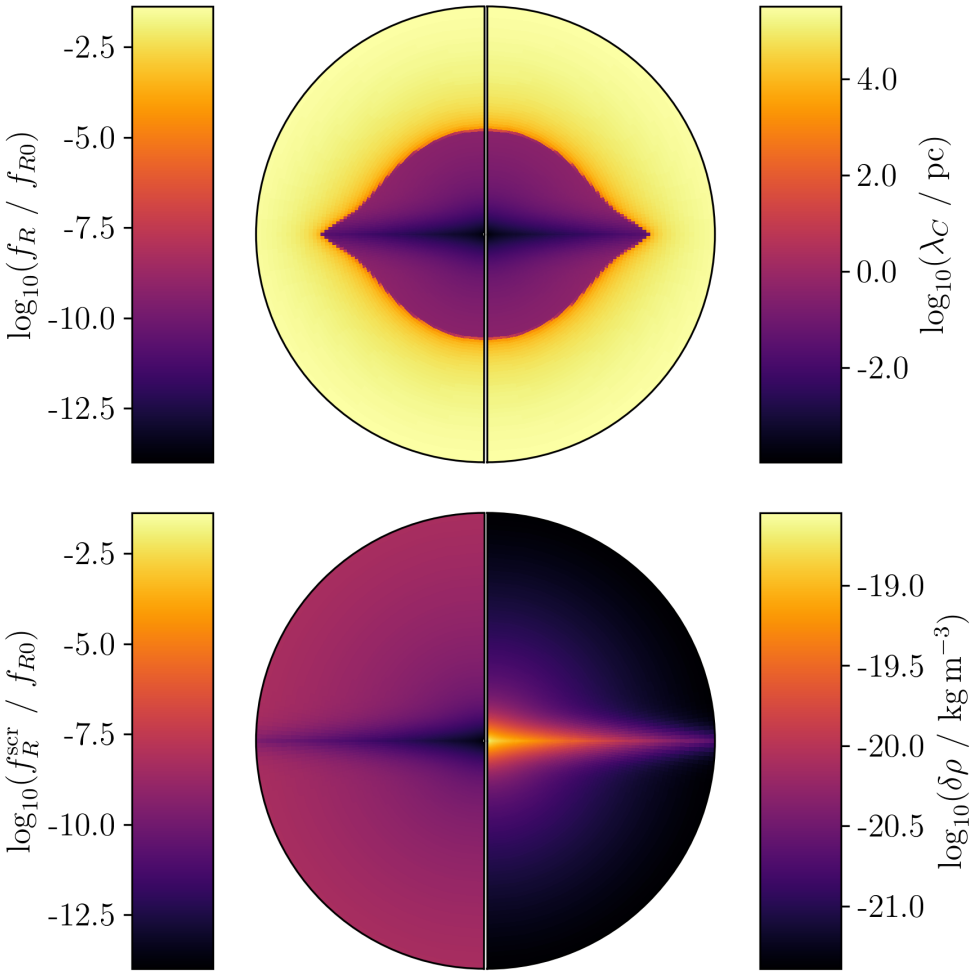


Figure 4.1: An example solution for a Milky-Way-like galaxy with $M_{\mathrm{vir}} = 1.5 \times 10^{12} M_\odot$, and $f_{R0} = -10^{-6}$, plotted to a maximum radius of 10 kpc. Top left shows the field solution obtained from the numerical solver. Top right is the Compton wavelength, eq. (4.17). Bottom left shows the screened field value, eq. (4.1). Bottom right is the galactic density profile. This example illustrates a partially screened case, where the scalar field (and Compton wavelength) change dramatically at the screening surface, which is located within the stellar disc.

seen from the similarity of the profiles of the field (top left) and Compton wavelength (top right). We find that in the screened region the numerically calculated field (interior of the top left plot) is well approximated by the analytically derived screened field value (bottom left), i.e. $f_R(r < r_s) \approx f_R^{\rm scr}$. We also see the relationship of eq. (4.1) in the similarity between the density profile (bottom right) and the screened field (bottom left).

Considering the magnitude of the Compton wavelength in the top right panel of figure 4.1, we notice that outside the screened region the Compton wavelength is large, reaching values $\mathcal{O}$(Mpc). However, inside the screened region the value of the Compton wavelength plummets to sub-parsec scales, significantly smaller than the typical separation of stars, eq. (4.19).

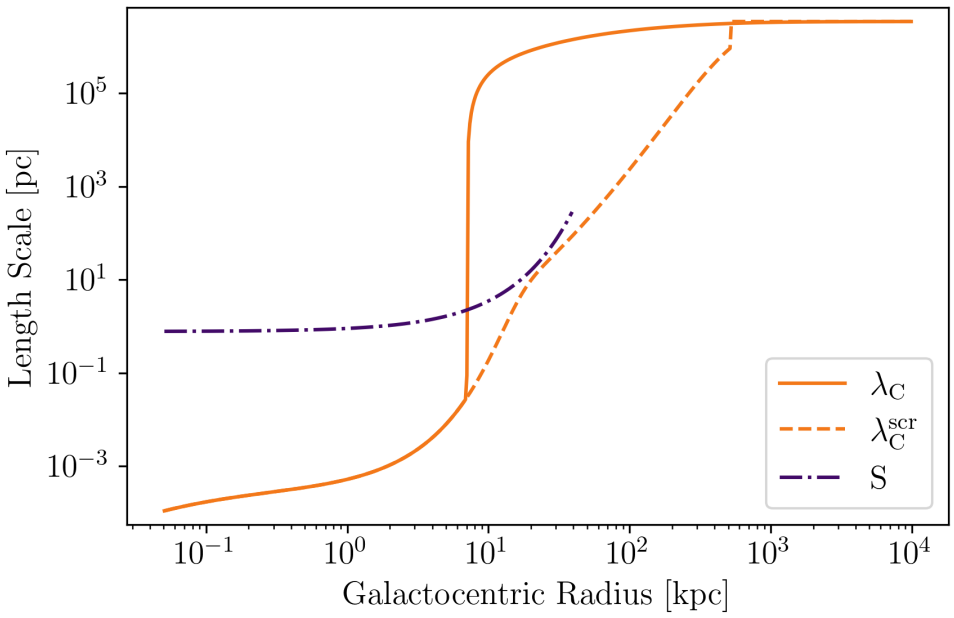


Figure 4.2: Comparison between average stellar separation (purple) and Compton wavelength (orange) as a function of galactocentric radius, in a Milky-Way-like galaxy with $M_{\rm vir} = 1.5 \times 10^{12} M_\odot$ and $f_{R0} = -10^{-6}$. Two curves are shown for the Compton wavelength: the numerical solution extracted from our solver (solid) and the analytic solution in the screened regime (eq. (4.1); dashed). The curve representing the stellar separation has been truncated at the point where the stellar density is subdominant to the cosmic mean density. The figure shows that the Compton wavelength is orders of magnitude smaller(larger) than the stellar separation in the screened(unscreened) regime.

We expand on this visualisation in figure 4.2 by comparing the lengths of the Compton wavelength and the stellar separation, eq. (4.19), along the radial axis of the galactic disc, using the same parameters as in the previous figure. It is now evident that the Compton wavelength is orders of magnitude smaller than the stellar separation inside the screened portion of the galaxy, but rapidly grows to be much larger in the unscreened region of the galaxy.

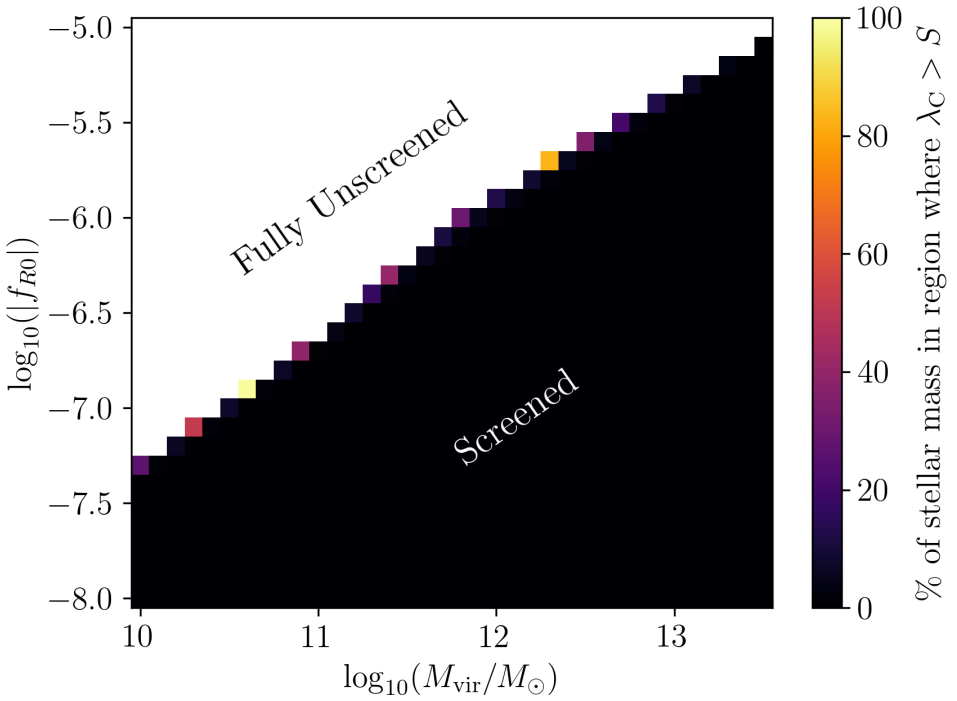


Figure 4.3: Proportion (in percent) of the stellar mass within the region where the Compton wavelength (calculated numerically, assuming a smooth stellar profile) is larger than the stellar separation, across a range of f_{R0} and $M_{\rm vir}$ values. The top-left white region corresponds to fully unscreened solutions. This figure shows that the majority of galaxies that are not fully screened have stellar profiles with separations less than the Compton wavelength.

The parameters in figures 4.1 and 4.2 were specifically chosen to simulate a galaxy with partial screening, where the screening radius lies within the stellar disc. In general, varying $M_{\rm vir}$ and f_{R0}, we find that most locations in parameter space result in a fully screened or fully unscreened stellar disc. Figure 4.3 shows the proportion of stellar mass located in a

region of the galaxy where $\lambda_{\rm C} > S$, for a range of $M_{\rm vir}$ and f_{R0} parameters. In the top left of the plot, where the galaxies are fully unscreened, we find $f_R \approx f_{R0}$ everywhere, and thus $\lambda_{\rm C} \approx \bar{\lambda}_{\rm C} \gg S$. In the lower right region, the galaxies have fully screened stellar discs, resulting in $\lambda_{\rm C} \approx \lambda_{\rm C}^{\rm scr} \ll S$, as illustrated by the example in figure 4.2. In the following section, we will further discuss the implications of the partially screened solutions, represented by the coloured (not black and white) points in figure 4.3.

4.5.2 Scalar Field Values in the Interstellar Medium

At a given point in space, the scalar field is sourced primarily by mass within a few Compton wavelengths; the contributions of more distant matter are exponentially suppressed. Where the Compton wavelength is larger than the typical separation between objects, the field profile evolves as if the density profile of the individual sources had been smoothed, with a smoothing scale of order the Compton wavelength. When the Compton wavelength is less than the typical separation between objects, there is no smoothing effect, and the field responds to the objects individually. When studying the behaviour of the $f(R)$ field within a galaxy it is common to treat the stellar component as a fluid with a smooth density profile (for example, Arnold et al. (2019); Desmond and Ferreira (2020)). As we have seen, this approximation is not valid in much of the interesting parameter space. In this section we consider how the field might behave in the absence of the smoothing of the stellar density profile.

In the small Compton wavelength regime, it becomes invalid to consider the stellar density profile as a continuous distribution. As a result, we expect the scalar field to take differing field values near to stars, and deep in the interstellar medium. This is impossible to study analytically and will be challenging to solve numerically given the dynamical range of the problem. However, we can suggest some behaviour of the field in this regime. We expect that, in between the stars, the field will relax to the

dark-matter-only solution, $f_R^{\rm DM}$, with pockets around the now-discrete stars where the field becomes orders of magnitude smaller. Therefore, except in the neighbourhood of the stars, the field evolves as if the stellar component of the galaxy was absent.

There is also a rare, more complex case where, if we include the smoothed stellar mass in the galactic density profile, the Compton wavelength is smaller than the stellar separation, but removing the stellar contribution from the density profile, the dark-matter-only solution results in a Compton wavelength larger than the stellar separation (i.e. $\lambda_{\rm C}^{\rm DM+SD} < S < \lambda_{\rm C}^{\rm DM}$). In this highly non-linear regime, we suggest that the field in the inter-stellar medium relaxes to larger values causing an increase in the Compton wavelength until the Compton wavelength becomes large enough to be comparable to the stellar separation. A similar situation to this, although on very different scales, was considered in Brax et al. (2013). In this situation, we suggest that the typical field value will be that which gives a Compton wavelength of order the stellar separation. However, further numerical study would be needed to understand this case in detail.

If it is the case that treating the stellar population as a discrete distribution would result in the field decreasing from $f_R^{\rm DM+SD}$ to $f_R^{\rm DM}$, then there would be a knock-on effect on the position of the screening surface, r_s. In figure 4.4 we compare the screening radii derived in the two cases: by assuming the stellar profile is a continuous distribution that contributes to the field profile, $f_R^{\rm DM+SD}$; and by neglecting the contribution of the stellar density profile, i.e. a dark matter only solution, $f_R^{\rm DM}$. In both cases we calculate the screening radius using the curvature-to-density parameter derived in the previous chapter, eq. (3.3a), (Burrage et al., 2024).

Figure 4.4 shows that if r_s is situated within the stellar disc, and $\lambda_{\rm C} < S$, then the decrease in the field values would act to shift r_s towards the centre of the galaxy. Overall this would lead to less of the galaxy being screened, in this narrow diagonal band of parameter space. Although this only affects

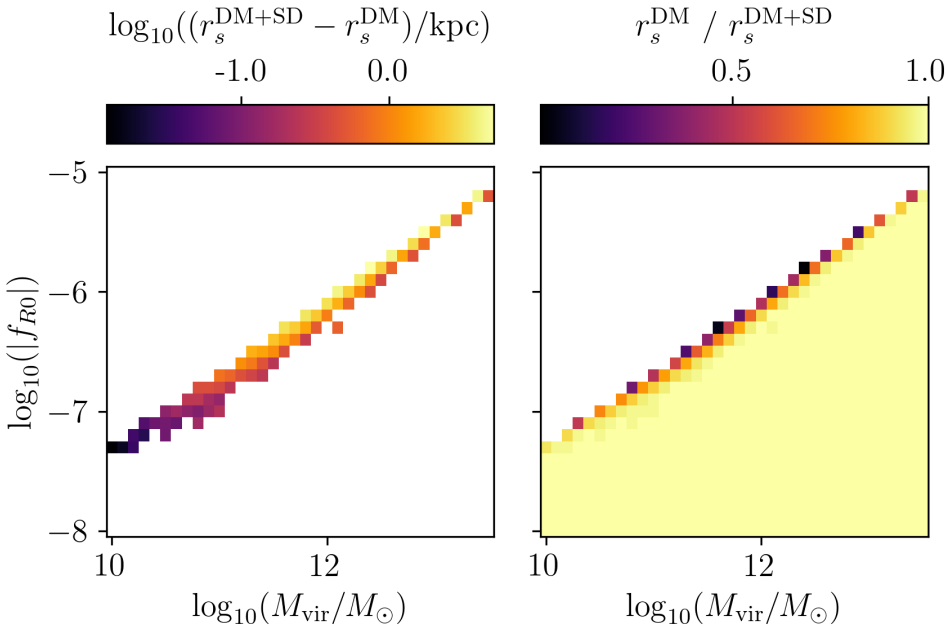


Figure 4.4: Comparisons of the screening radius assuming no stellar contribution to the galactic density ($r_s^{\rm DM}$) and assuming a smooth stellar density profile ($r_s^{\rm DM+SD}$). Left shows the absolute distance between the two r_s solutions, and right shows the ratio between them. In both cases, the upper-left white region corresponds to fully unscreened solutions. In the lower-right regions, the screening radii are larger than the extent of the stellar profile and thus are unchanged by ignoring the stellar contribution. In the right plot these correspond to ratios of 1, in the left we have masked these values. Assuming no stellar contribution has the largest impact on solutions where the screening radius is within the stellar disc, corresponding to the thin diagonal highlighted in the left plot, or the ratios with a value less than one in the right plot.

a small part of the parameter space, it remains relevant for current constraints, since many contemporary tests rely on partially screened stellar populations as observable tracers of equivalence principle violations.

4.5.3 Fifth Forces Around Stars

Compton wavelengths that are shorter than the interstellar separation, mean that there can be significant variation in the value of the field in the space between the stars. Here we provide an estimate of whether this can lead to observable fifth forces in the Solar System.

We approximate the Sun as a sphere of constant density, embedded in a background in which the field is screened, $f_R = f_R^{\rm scr}$. The star is screened as long as $|f_R| \lesssim \Phi_N(R_*)$ where $\Phi_N(R_*)$ is the Newtonian potential evaluated at the surface of the star. As $|f_R^{\rm scr}| \ll |f_{R0}|$, this is a weaker condition than that normally applied, which states that a star is screened if $|f_{R0}| \lesssim \Phi_N(R_*)$. At the position of the Sun, $f_R^{\rm scr} \sim 4\times10^{-11} f_{R0}$, and $\lambda_{\rm C} \sim 10^{18} f_{R0}^{1/2}\,{\rm m}$. The fifth force, in this approximation of the Solar System, is

$$\frac{F_5}{F_N} \approx \left(\frac{|f_R|}{5\times10^{-6}}\right)\left(\frac{R_\odot}{r}\right)^2 e^{-r/\lambda_{\rm C}}\,, \tag{4.20}$$

which is extremely small, and well beyond the sensitivity of current probes.

4.6 Conclusions

Scalar fields react to matter on scales equivalent to the Compton wavelength of the field. When modelling populations of discrete objects, it is common practice to treat the profiles as continuous distributions, assuming that many discrete objects are contained within a Compton wavelength, acting to smooth out the scalar field profile.

In the context of chameleon $f(R)$ gravity in galactic environments, surveys are beginning to probe the regime where the screening radius may lie

within the galactic disc and where the Compton wavelength can become significantly smaller than the typical separation of stars within the galaxy. As such, it is important to exercise caution when assuming a continuous stellar density profile.

A proper treatment of the stars as individual discrete objects may result in a heterogeneous field profile, in which the mass of the stars is inconsequential to the field in the interstellar medium, allowing the interstellar field to relax to a larger field value permitted by the dark matter density only solution. In regions closer to the high-density stars, the scalar field will become further screened, adopting smaller, more screened field values. Such a situation could cause galaxies with partially screened stellar discs to become less screened, as neglecting the stellar mass profile pushes the screening surfaces towards the centre of the galaxy. In this case, there is the possibility that modified gravity tracers that rely on the galaxy being unscreened could become observable once more.

In conclusion, we should always be careful to check that the assumptions we are making actually hold in the environments we study, and as the accuracy of observations improves we should also improve the accuracy of our theoretical predictions.

Chapter 5

Lensing in Modified Gravity Theories

Declaration: This chapter is a write-up of unpublished work done in collaboration with Prof. Clare Burrage and Prof. Ed Copeland, who provided guidance and feedback throughout the project. In the near future we plan to further investigate the details of this project and submit our findings to a peer-reviewed journal.

5.1 Summary

Recent observations of the radial acceleration relation using weak gravitational lensing have extended the relation to unprecedentedly low accelerations, reaching $g_{\rm bar} \approx 10^{-15}\,{\rm ms}^{-2}$ (Brouwer et al., 2021; Mistele et al., 2024b). These measurements provide a powerful test of modified gravity theories, which often predict specific correlations between baryonic and observed accelerations. In this chapter, we explore how scalar-tensor modifications to general relativity might manifest in weak lensing observations of the RAR, focusing on the symmetron mechanism as a representative screened modified gravity theory. We first demonstrate how the classical symmetron would manifest in the RAR, assuming one could track the motion of visible tracers within galactic haloes. However, since the recent RAR

results are based on photon propagation rather than massive tracer dynamics, we extend the symmetron framework to include modifications that specifically affect photon geodesics by introducing a small photon mass. We consider both a fixed mass model and a scalar-dependent mass model for the photon. We develop a novel framework for predicting lensing signatures of general conformally coupled scalar field models and compare these predictions with recent observational data. Our analysis reveals that fifth-force-like enhancements to lensing observations are possible within this new framework. However, we find that the symmetron model struggles to reproduce the observed RAR across all acceleration scales without requiring photon masses that conflict with current observational constraints.

5.2 Introduction

For nearly a century, observations of galactic dynamics have revealed a persistent puzzle: the outer regions of galaxies rotate significantly faster than expected from their visible matter alone (Kapteyn, 1922; Oort, 1932; Babcock, 1939; Bosma, 1981; Rubin, 1983). The traditional resolution invokes dark matter, which has been highly successful at explaining many cosmic phenomena, from the cosmic microwave background to large-scale structure formation (Planck Collaboration et al., 2020; Springel et al., 2006). However, despite intensive searches, the elusive DM particle remains undetected, leaving room for alternative explanations.

Time and again, galactic observations have exhibited remarkable regularities, despite the underlying processes governing them being highly nonlinear. These regularities include the Baryonic Tully-Fisher Relation (McGaugh et al., 2000; McGaugh, 2012), which links galactic baryonic mass to rotation velocity, and the Central Density Relation (Donato et al., 2009), which connects central baryonic surface density to rotation curve steepness.

The most fundamental of these correlations is the Radial Accelera-

tion Relation (RAR), which compares the observed centripetal acceleration $g_{\rm obs} = v_{\rm rot}^2/r$ (where $v_{\rm rot}$ is the observed rotational velocity) with the baryonic acceleration $g_{\rm bar}$, coming from the gravitational pull of visible matter within the galaxy (e.g., stars and gas). Using data from the Spitzer Photometry and Accurate Rotation Curves (SPARC) sample, McGaugh et al. (2016) demonstrated universality across a wide array of galaxies, tightly following a fitting function that transitions from $g_{\rm obs} \approx g_{\rm bar}$ at high accelerations to $g_{\rm obs} \propto \sqrt{g_{\rm bar}}$ at low accelerations.

However, kinematic studies using visible tracers, such as the SPARC RAR result, are limited to the inner regions of galaxies, typically extending to $\sim 30\,$kpc where stellar and gas dynamics can be reliably measured. Weak gravitational lensing provides the necessary tools to probe beyond this range. By measuring statistical distortions of background galaxy shapes caused by foreground lenses, lensing observations can map gravitational fields to unprecedented distances, reaching hundreds of kiloparsecs from galaxy centres (Brouwer et al., 2021; Mistele et al., 2024b). This extension to galactic outskirts opens new opportunities for testing theories of gravity and galactic physics.

Modified gravity theories naturally predict correlations between $g_{\rm bar}$ and $g_{\rm obs}$ by altering gravitational physics, e.g. Burrage et al. (2017). To explain these weak lensing results through modified gravity theories, we must first understand how such theories alter the relationship between baryonic and observed accelerations.

The use of weak lensing observations as a test of gravity, particularly as a probe of modified gravity theories, has a well-established history. Such observations can be used in a model-independent way, for example to determine the distance-redshift relation and density contrast growth factor (Knox et al., 2006), by measuring the growth of structures (Bertschinger, 2006; Song, 2006) or through GR consistency relations (Song and Koyama, 2009; Koyama et al., 2009). Signatures of specific models have also been

studied, including those proposed to explain dark energy including $f(R)$ (Carroll et al., 2004, 2005) and DGP (Dvali et al., 2000; Deffayet, 2001), as well as models of modified gravity as an alternative to dark matter (Bekenstein, 2004; Schmidt, 2008; Tsujikawa and Tatekawa, 2008; Thomas et al., 2009; Harnois-Déraps et al., 2015; Liu et al., 2016; Davies et al., 2024). Weak lensing can also be used to directly constrain the fraction of dark energy in our universe and its equation of state (Hu and Jain, 2004) in addition to its evolution with time (Jain and Taylor, 2003). Weak lensing is particularly useful for such theories as it depends on both the background geometry (angular diameter distances) and the growth of structure (linear perturbations). Although the lensing signal itself measures only the gravitational potential perturbations along the line of sight, this dual dependence helps break degeneracies between expansion history and structure growth. A number of proposals have focused on parameterising how dark energy models can affect weak lensing through the growth factor, anisotropic stress and modifications to the Poisson equation (Caldwell et al., 2007; Amendola et al., 2008; Jain and Zhang, 2008; Thomas et al., 2011). Progress in making accurate predictions for weak lensing observables has been aided by advances in numerical simulations such as COLA (Hoyland et al., 2025) and MGLenS (Harnois-Déraps et al., 2023).

In this chapter, we investigate how scalar-tensor modifications to general relativity might manifest in weak lensing observations of the RAR, focusing on the symmetron mechanism as a representative screened modified gravity theory. In section 5.3, we review recent measurements of the RAR using weak lensing data. In section 5.4, we introduce our scalar coupling model, which extends the symmetron framework to include modifications that specifically affect photon geodesics through the introduction of a small photon mass. In section 5.5, we detail the numerical and statistical modelling methods employed to generate a statistically-relevant mock-galaxy sample and solve the symmetron equation of motion for individual galaxies within this sample. In section 5.6, we demonstrate the impact of classical

fifth forces on the RAR, considering the scenario where one could track the motion of visible tracers within galactic haloes. In section 5.7, we present our main results: first developing a novel theoretical framework to relate the impact of conformally coupled scalars to lensing observations, and subsequently applying this framework to our mock-galaxy sample to derive a scalar-enhanced RAR. Finally, in section 5.8, we discuss our findings and their implications.

5.3 Measurements of the RAR

Using data from the SPARC galaxy sample (Lelli et al., 2016), the work of McGaugh et al. (2016) demonstrated a tight relation between the baryonic acceleration, $g_{\rm bar}$, and the observed acceleration, $g_{\rm obs}$, in 153 late-type galaxies. This relationship can be best expressed by the simple one-parameter fitting function given in eq. 4 of McGaugh et al. (2016):

$$g_{\rm fit} = \frac{g_{\rm bar}}{1 - {\rm e}^{-\sqrt{g_{\rm bar}/g_\dagger}}}\,, \tag{5.1}$$

where $g_\dagger = 1.20 \times 10^{-10}\,{\rm ms}^{-2}$. This relation captures the essential features of the RAR and provides a convenient estimate of the observed accelerations for (relatively) large baryonic accelerations ($10^{-12} \lesssim g_{\rm bar} \lesssim 10^{-9}\,{\rm ms}^{-2}$) — equivalent to small radii within the visible portion of the galactic disc ($r \lesssim 30\,{\rm kpc}$).

The results of McGaugh et al. (2016) suggest that an external force is acting to prop up the velocity curves of baryonic matter, a well-understood motivation for DM haloes. Nevertheless, many previous works have attempted to explain this additional force through different mechanisms, including modified gravity theories such as MOND (Milgrom, 2016), TeVeS (Skordis, 2009), symmetron (Burrage et al., 2017), and generally covariant formulations of modified gravity (Moffat, 2016). Whilst these attempts go some way towards explaining the results in McGaugh et al. (2016), they

typically struggle when attempting to explain other DM-related phenomena, including CMB observations, large-scale structure formation, galaxy cluster dynamics, and, relevantly, weak lensing observations. Due to this extensive body of evidence, DM has become the de facto standard to explain the magnitude of the RAR in this baryonic regime. Yet still, ΛCDM simulations are unable to account for the tight correlation (small scatter) between observations of $g_{\rm bar}$ and $g_{\rm obs}$.[1]

With the advent of enormous galactic surveys in recent years, researchers have sought to use new data to extend the RAR to smaller acceleration values (larger galactic radii) and determine whether this intriguing relation is truly fundamental. One such attempt is the work of the Kilo-Degree Survey (KiDS) collaboration (Brouwer et al., 2021), who utilised weak lensing data from over 250,000 isolated galaxies to extend the RAR out to $g_{\rm bar} \approx 10^{-15}\,{\rm ms}^{-2}$, equivalent to physical radii of $r \approx 3\,{\rm Mpc}$. This work was itself a follow-up to a previous KiDS paper (Brouwer et al., 2017), which used an overlap of the GAMA spectroscopic survey and the KiDS photometric survey to measure the Excess Surface Density (ESD) around isolated galaxies. The results in (Brouwer et al., 2021) were found to be in agreement with Emergent Gravity (Verlinde, 2017) and MOND (Milgrom and Sanders, 2008) theories; both of which adopt functional forms almost identical to the fitting function described earlier, eq. (5.1).

In Brouwer et al. (2021), several steps are taken before arriving at the RAR. The authors estimated the gravitational acceleration around galaxies using galaxy-galaxy lensing, which statistically measures the weak lensing-induced tangential shear $\gamma_t(R)$ by averaging the projected ellipticity of background sources in annuli around foreground lenses. Because the lensing image distortions are extremely small, this process is only possible statistically, requiring averaging and binning of the results. The shear profile was binned according to the predicted baryonic acceleration $g_{\rm bar}$ into

[1] Certain ΛCDM simulations claim to reproduce the low scatter in specific cases with more complex baryonic physics, e.g. Keller and Wadsley (2017); Ludlow et al. (2017).

15 logarithmically spaced bins between $10^{-15}\,\mathrm{ms}^{-2}$ and $10^{-12}\,\mathrm{ms}^{-2}$, roughly equivalent to $30\,\mathrm{kpc} \lesssim r \lesssim 3\,\mathrm{Mpc}$. The lensing shear profile is then related to an ESD, which is subsequently converted into the final observed acceleration — assuming a Singular Isothermal Sphere (SIS) density profile to more easily relate these two quantities.

To determine whether a lens galaxy is isolated (i.e., satellite masses within 3 Mpc comprise less than 10% of the lens galaxy's stellar mass) and to correctly calculate the mass of the visible matter (and therefore g_{bar}) from luminosity measurements, one must utilise the redshift measurement of the galaxy. In principle the GAMA survey would be ideal for this purpose, as it provides accurate spectroscopic redshift measurements. However, the GAMA survey has a much smaller sample size compared to the KiDS survey. As such, the photometric galaxies from KiDS are chosen. To help increase the precision of the lens galaxy redshifts, the KiDS collaboration utilises an Artificial Neural Network (ANNz2) trained on the overlap between the GAMA and KiDS surveys to improve the photometric redshift estimates. While this process can help improve results, it is not without its own limitations and uncertainties, and one should be cautious when assuming a galaxy is isolated if the estimated error on photometric redshift measurements is larger than the isolation criteria. Because of these implied uncertainties on the isolation criteria, the results in Brouwer et al. (2021) are only reliable down to $g_{\mathrm{bar}} \approx 10^{-13}\,\mathrm{ms}^{-2}$.

Significant uncertainty also exists when estimating stellar masses and the overall baryonic mass, inclusive of intragalactic gas and dust. The accuracy of the baryonic mass estimates is limited by uncertainties in the stellar mass estimates, and the magnitude of contributions from invisible gas and dust is not well understood. As such, the derived RAR has some flexibility, as a shift in the baryonic mass (and therefore acceleration) can shift the observed accelerations to be below, above, or on the expected fitting relation. In fact, the accuracy of g_{obs} measurements now exceeds

that of $g_{\rm bar}$, with systematic uncertainties in baryonic mass (especially hot gas) limiting model discrimination.

Despite these potential drawbacks, the results in Brouwer et al. (2021) prove to be of considerable interest. Key findings from this work include:

- Rotation curves are consistent with SPARC but also remain approximately flat well beyond the visible disc.
- At low accelerations, the lensing RAR follows $g_{\rm obs} \propto \sqrt{g_{\rm bar}}$, consistent with the shape of the fitting relation from the SPARC dataset, eq. (5.1).
- Splitting galaxies by type (Sérsic index or colour) reveals a significant offset in the RAR, which is challenging for MG models that predict a fixed baryonic-gravitational relation.[2]
- The RAR for galaxies split by stellar mass shows a slight upward trend with increasing stellar mass (M_*), possibly due to missed satellites or uncertainties in isolation.
- No significant difference is found in the RAR for isolated dwarf galaxies compared to the full sample.
- The observed flatness of lensing rotation curves at large radii is difficult to reconcile with simple NFW-like DM haloes.
- Additional lensing power at large radii may be due to large-scale structure along the line of sight, highlighting the need for accurate isolation criteria and comprehensive simulations.
- Inclusion of undetected hot gas would act to increase the baryonic acceleration, shifting the RAR and steepening its slope at low accelerations, moving results towards DM predictions and away from MG expectations.

[2]This offset is likely due to systematic differences in stellar mass estimates between early- and late-type galaxies, as discussed in Mistele et al. (2024b), and later in this section.

Overall, the lensing RAR provides a powerful test for MG and DM models, but future progress depends critically on improved measurements of baryonic mass distributions and reduction of systematic uncertainties in stellar and gas mass estimates.

In follow-up work, Mistele et al. (2024a,b) developed the results of the KiDS collaboration, reprocessing the lensing data with several new techniques to improve the accuracy and precision of the measurements. The first major change is that they calculate $g_{\rm obs}$ in a density-independent way, side-stepping the assumption of an SIS density profile to relate the ESD to the observed acceleration. In particular, they use a more general relation between the ESD and the observed acceleration, accounting for the contribution from all radii at each spherical shell (see eq. 2.3 within Mistele et al. (2024b)). Besides being more generally applicable, this calculation also reduces the errors on $g_{\rm obs}$ and results in a smoother RAR.

The second implemented change is a much stricter cutoff on the isolation condition, requiring the galaxy to be isolated out to 4 Mpc, instead of the previous 3 Mpc. This reduces the number of galaxies in the lens sample from over 250,000 to around 100,000. The decrease in sample size increases the statistical uncertainties; however, the overall total errors are roughly the same due to the decreased uncertainty in the ESD-$g_{\rm obs}$ calculation. Additionally, the systematic uncertainties are improved by this stricter isolation criterion. Figure 4 in Mistele et al. (2024b) shows the impact of increasing the isolation radius on early- and late-type galaxies. Early-type galaxies (ETGs) are more susceptible to contamination from satellite galaxies, as expected from galaxy-morphology density studies (Dressler, 1980), which show that ETGs are typically more clustered. Meanwhile, thanks to this stricter consideration of isolated galaxies, late-type galaxies (LTGs) are now reliably isolated down to $g_{\rm bar} \approx 10^{-14}\,{\rm ms}^{-2}$, allowing for conclusions to be drawn with more confidence in the low-acceleration region of the RAR.

The remaining major changes relate to stellar and baryonic mass estimations. To ensure consistency between kinematic (SPARC) and lensing (KiDS) data, Mistele et al. (2024b) reanalyse the KiDS lensing sample using the same stellar population synthesis model as for the kinematic data. Stellar masses are not measured directly but inferred from luminosity via mass-to-light ratios, which depend on the assumed stellar population model and observed colours. To address the difference between ETG and LTG accelerations, the authors apply a uniform scaling factor Q to the KiDS stellar masses: $Q_{\rm LTG} = 1.0$ for LTGs and $Q_{\rm ETG} = 1.4$ for ETGs, reflecting a modest offset for ETGs compared to previous work. This correction ensures a consistent stellar mass scale across both samples. For baryonic mass estimates, the authors add gas contributions using scaling relations: hot gas for ETGs (eq. 4.1 of Mistele et al. (2024b)) and cold gas for LTGs (eqs. 4.2–4.3 of Mistele et al. (2024b)), closely matching previous approaches for LTGs but yielding higher baryonic masses for ETGs (on average by a factor of $\sim$1.7). These adaptations to the modelling of the baryonic mass alleviate the tension between the RAR curves of early- and late-type galaxies found in Brouwer et al. (2021).

Due to the improved isolation criteria and mass estimations, the results in Mistele et al. (2024b) provide a more robust framework for testing modified gravity models against observational data. In both Brouwer et al. (2021) and Mistele et al. (2024b), the results are more robust for late-type galaxies, allowing us to reliably probe smaller accelerations in LTGs. Additionally, the kinematic accelerations in McGaugh et al. (2016) are also derived from late-type galaxies. In our analysis in this chapter we work in a type-independent manner. In future work, to better align with the results of Mistele et al. (2024b), we plan to adjust our methods and focus only on late-type galaxies, as they provide the most reliable results.

5.4 Scalar Coupling Model

In this chapter, we utilise the RAR results explained in the previous section as a test of gravity. We adopt a scalar model described by our symmetron theory in section 1.3.7. The equation of motion for the symmetron field is given in eq. (1.120),

$$\nabla^2\varphi = \frac{1}{2L_{\rm c}^2}\left[\left(\frac{\rho}{\rho_{\rm SSB}} - 1\right) + \varphi^2\right]\varphi\,.$$

where $L_{\rm c}$ and $\rho_{\rm SSB}$ are the background Compton wavelength and SSB density scale, respectively, as in eq. (1.115) and eq. (1.116):

$$L_{\rm c}^2 = \frac{1}{2}\left(\frac{M_{\rm pl}}{\mu}\right)^2 L_{\rm pl}^2\,,$$
$$\rho_{\rm SSB} = \left(\frac{M_{\rm sym}\mu}{M_{\rm pl}^2}\right)^2 \frac{M_{\rm pl}}{L_{\rm pl}^3}\,.$$

with the usual symmetron parameters ($M_{\rm sym}$, μ, and λ) outlined and explored in previous chapters. Additionally, the field in this equation of motion has been normalised to its vacuum expectation value, $\varphi = \phi/\phi_{\rm vev}$, where $\phi_{\rm vev} = \frac{1}{\sqrt{\lambda}}\frac{\mu}{M_{\rm pl}}$, as in eq. (1.119). The conformal coupling to matter is given by eq. (1.113),

$$A(\phi) = 1 + \frac{1}{2}\left(\frac{M_{\rm pl}}{M_{\rm sym}}\right)^2 \phi^2\,.$$

It is assumed that $\phi/M_{\rm sym} \ll M_{\rm pl}$, such that the higher order terms in the perturbative expansion of $A(\phi)$ can be neglected. The density-dependent effective potential of this theory causes the field, and therefore the coupling function, to be suppressed in dense environments, returning the standard GR results in such regions. This behaviour is vital in understanding any modifications to outer regions of galaxies, such as those observed in the recent weak-lensing results, without contradicting the precision of the results in the inner galactic regions.

Previous work has been conducted to describe galactic rotation curves,

or equivalently radial accelerations, using the symmetron framework, e.g. Burrage et al. (2017). However, this work mainly focused on the baryonic component, aiming to replace dark matter as the force propping up the acceleration of visible galactic matter. In follow-up work, it was shown that the standard symmetron model could not fully replace dark matter by reproducing gravitational lensing results (Burrage et al., 2019). Given that the more recent results of Brouwer et al. (2021) and Mistele et al. (2024b) extend the RAR well past any visible tracers (using photon-based lensing methods), it is apparent that any scalar modifications designed to explain these new results must act directly on the photons, not on the visible tracers.

The reliance on photons as observational probes causes complications for the usual symmetron model. In these models scalar modifications arise due to a coupling with the trace of the energy-momentum tensor. Given that photons possess a traceless energy-momentum tensor, one would expect no modification to photon geodesics in the presence of a canonical scalar field. In order to navigate these challenges, we must extend the symmetron framework to include modifications that specifically affect photon propagation. This can be readily achieved by introducing a (necessarily small) mass to the photon field.[3] We discuss the allowed bounds of the photon mass at the end of this section.

The motion of a particle with mass m can be derived from the action

$$S = -m \int \mathrm{d}\tau = -m \int \sqrt{-\tilde{g}^2_{\mu\nu} \frac{\mathrm{d}x^\mu}{\mathrm{d}t} \frac{\mathrm{d}x^\nu}{\mathrm{d}t}}\, \mathrm{d}t\,. \tag{5.2}$$

In models with a small fixed photon mass ($m = m_\gamma$), the above equation is sufficient for describing the modification to photon geodesics — the massive photon is now impacted by the scalar field through the conformal coupling within $\tilde{g}_{\mu\nu}$.

[3]There also exists work on generalised symmetrons with fifth forces arising from a disformal coupling, e.g. Käding (2023). However, Burrage et al. (2019) demonstrate that the energy scale required to produce such lensing corrections is orders of magnitude larger than the limits imposed by terrestrial constraints on disformal couplings.

In a more sophisticated treatment, if we give the photon a mass $m_\gamma \propto \alpha(\phi)$ which depends on the symmetron scalar field, such that the interaction Lagrangian is given by

$$\mathcal{L} \supset \alpha(\phi) A_\mu A^\mu \,, \tag{5.3}$$

where A_μ is the electromagnetic four-potential, then the geodesic action becomes

$$S = -v \int \alpha(\phi)\, \mathrm{d}\tau = -v \int \sqrt{-\alpha^2(\phi) \tilde{g}^2_{\mu\nu} \frac{\mathrm{d}x^\mu}{\mathrm{d}t} \frac{\mathrm{d}x^\nu}{\mathrm{d}t}}\, \mathrm{d}t \,, \tag{5.4}$$

where v is a dimensionful scale, related to the vacuum photon mass. With this, we see the impact of a scalar-dependent mass on the geodesics of photons is equivalent to a conformal coupling. In this model, we take $\alpha(\phi) = \phi/\phi_{\rm vev}$, which will set $v = \phi_{\rm vev} M_{\rm pl}$, so that $m_\gamma(\phi) = \phi M_{\rm pl}$. The quantity $\alpha(\phi)$ effectively parameterises the impact of the symmetron field on the photon geodesic. When the field is screened, $\alpha = 0$ and the geodesic modifications are all zero; when the field is fully unscreened, reaching its background value, $\alpha = 1$, and the symmetron conformal coupling, $A(\phi)$, fully impacts the photon geodesic, as in the fixed mass scenario.

As a summary, we adopt two models: one with a fixed photon mass, and one with a scalar-dependent photon mass. In both cases, the modification can be described by a conformal factor on the metric

$$\mathcal{A}(\phi) = \alpha(\phi) A(\phi) \,, \tag{5.5}$$

where $\alpha = 1$ for the fixed mass model, and $\alpha = \phi/\phi_{\rm vev}$ in the scalar-dependent mass model. In both cases the field profile is determined by the symmetron equation of motion, for a given source density ($\delta\rho$) and set of parameters ($M_{\rm sym}$ and $L_{\rm c}$).

5.4.1 Constraints on the Photon Mass

The photon mass, m_γ, is a heavily constrained parameter. In particle theory, the photon is assumed to have zero mass. Theories such as quantum electrodynamics necessitate it to be massless for gauge invariance, renormalisation, and charge conservation. Yet many alternative photon theories contain mass terms that result in non-zero photon rest masses. From an experimental standpoint, it is near impossible to definitively show that the photon is massless — at best, upper limits can be placed on its mass. A wide array of experiments exists to constrain the photon mass; for a non-comprehensive overview, see e.g. (Tu et al., 2005; Goldhaber and Nieto, 2010).

Some recent photon mass constraints come from tests of the Jovian magnetic field (Yan et al., 2024), which place a limit of $m_\gamma \lesssim 10^{-18}\,\mathrm{eV}$, and tests of fast radio bursts (Wang et al., 2023), which place a limit of $m_\gamma \lesssim 10^{-15}\,\mathrm{eV}$. The most stringent constraint comes from tests of the galactic magnetic field (Chibisov, 1976), which place a limit of $m_\gamma \lesssim 10^{-27}\,\mathrm{eV}$.

It should be noted that these constraints assume a fixed photon mass. In the case of a screened scalar-dependent photon mass, the constraints may be relaxed, as the effective mass can vary with the scalar field configuration. In fact, any laboratory- or solar system-based constraints would be entirely evaded due to the scalar suppression required in these high-density regions. Nevertheless, tests involving extragalactic measurements, such as fast radio bursts (Wang et al., 2023) or multimessenger astronomy[4] (Baker et al., 2017), would still provide stringent constraints for the allowed vacuum value of the photon mass.

[4]It should be noted this method can only measure the difference in the photon and graviton mass given the multimessenger time delay. They could both have similar non-zero masses and arrive at roughly the same time.

5.5 Numerical and Statistical Modelling

In this section we review the numerical methods we use to generate a statistically relevant mock-galaxy sample, and solve the symmetron equation of motion for individual galaxies within this sample. We adopt similar methods to previous chapters; however, we are able to make a useful simplification by treating the baryonic component of the galaxy as a point mass. We are able to do this since the aim of this chapter is to reproduce the lensing-based RAR results of Brouwer et al. (2021) and Mistele et al. (2024b), which focus on large radii, well outside the baryonic disc. Since we are not concerned with the inner galactic regions, we do not need to model the baryonic density profile in detail, a point mass model is sufficient. This simplification allows us to simplify our galactic parameter estimation process, as we only need to estimate the stellar mass, rather than the full set of parameters required to model a baryonic density profile. Additionally, we are able to reduce the dimensionality of our numerical field solver from two-dimensional with axisymmetry to one-dimensional with spherical symmetry, significantly reducing the computational cost. We detail these methods in the subsections below.

5.5.1 Galactic Model

As mentioned in section 5.3, previous weak lensing literature, including the recent work of Brouwer et al. (2021), assumes the dark matter density profile is described by a Singular Isothermal Sphere (SIS) model, given in eq. (1.54):

$$\rho(r) = \frac{\sigma_v^2}{2\pi G r^2}\,, \tag{5.6}$$

where σ_v represents the total dark matter velocity dispersion. This model provides a simple description of the dark matter halo, representing an ideal gas of dark matter particles with a Gaussian velocity distribution.

In addition to the SIS model, we will also test the robustness of our

results against the more complex and commonly used NFW profile (Navarro et al., 1996), given in eq. (1.50):

$$\rho(r) = \frac{\rho_{\rm NFW}}{\dfrac{r}{r_{\rm NFW}}\left(1+\dfrac{r}{r_{\rm NFW}}\right)^2}\,, \tag{5.7}$$

where $\rho_{\rm NFW}$ is the characteristic density and $r_{\rm NFW}$ is the scale radius. This model allows for a more realistic description of the dark matter halo, consistent with contemporary cosmological simulations, but does introduce an additional free parameter compared to the SIS profile.

Both models possess a central density singularity and a divergent total mass. We fix the first issue by assuming a constant density in the central 50 pc. The second issue is addressed by truncating the density profile at the splashback radius, $r_{\rm SB}$. Deason et al. (2020) find the splashback radius to be approximately $r_{\rm SB} \approx 2.2 r_{\rm vir}$,[5] where $r_{\rm vir} \equiv r_{200c}$ is the virial radius, as defined in section 1.2.3.

The baryonic disc component is modelled as a point mass, with mass M_*, located at the centre of the galaxy. This simplification is valid since we are only concerned with results well outside the baryonic disc ($r \gtrsim 30\,\mathrm{kpc}$), where the impact of an extended baryonic density profile is negligible.

5.5.2 Mock Galaxy Sample

Our goal for this subsection is to generate a statistically relevant sample of mock-galaxy density profiles, with which we can calculate the RAR and compare against the lensing data. To achieve this, we will use the MCMC sampling techniques outlined in section 2.1.2. The main difference is that we are no longer required to sample a full set of baryonic density parameters; sampling only the stellar mass, M_*, will suffice for our point mass model. Additionally, in this chapter we have adopted two different DM

[5] In this work, the splashback radius is stated in terms of r_{200m}, as $r_{\rm SB} \approx 1.4 r_{200m}$, but they also provide the conversion $r_{200m} \approx 1.6 r_{200c}$, resulting in our quoted figure.

density profiles. The NFW pipeline is already detailed in section 2.1.2, and we will give an overview of how we derive the SIS parameters here. The work in this section is agnostic to the galaxy type (ETG or LTG), however, as mentioned in section 5.3, we plan to adapt our methods in future work to focus exclusively on late-type galaxies. An overview of the required adaptations is given at the end of the section.

The starting point for our pipeline is the stellar mass function (SMF), which describes the number density of galaxies as a function of their stellar mass. While the general galaxy population is typically well-described by a canonical Schechter function, the specific samples used in Brouwer et al. (2021) and Mistele et al. (2024b) are subject to strict isolation criteria (e.g., no neighbours within $3-4\,\mathrm{Mpc}$). These criteria introduce significant selection effects: since galaxy clustering is mass-dependent, this filtering distorts the underlying mass function, resulting in a distribution that deviates from the Schechter form. Consequently, using a standard SMF would generate a sample unrepresentative of the actual galaxies used in the lensing analysis.

To ensure our mock sample matches the observational dataset, we instead construct an effective SMF designed to reproduce the post-selection distribution shown in Brouwer et al. (2021) (figure 7). We model this SMF as a log-normal distribution with mean $\mu_{\log M_*} = 10.6$ and standard deviation $\sigma_{\log M_*} = 0.35$, as well as a sharp cutoff at $M_* = 10^{11} M_\odot$. By matching the final stellar mass distribution directly, we implicitly assume that the isolation criteria do not introduce strong secondary biases in the halo properties (e.g., concentration) beyond the intrinsic scatter already captured by the scaling relations employed in the subsequent steps of our pipeline. Sampling from the SMF gives us a stellar mass for each galaxy in our sample. On the baryonic side of our pipeline, this is all we require to fully describe the point mass model we adopt.

We then correlate the stellar mass to the halo mass via the Stellar-Halo Mass Relation (SHMR). As detailed in section 2.1.2, simply sampling a halo

mass from a stellar mass using the forward relation introduces Eddington bias. Therefore, we invert the relation numerically, determining the halo mass $M_{\rm vir}$ such that it is consistent with the Moster et al. (2013) relation and its intrinsic scatter (mapped to the virial mass as $\sigma_{\log M_{\rm vir}} \approx 0.15\,\mathrm{dex}$). This gives us the virial mass, $M_{\rm vir}$, which we can use to derive the parameters for our DM density profiles. For the NFW model, we also require the concentration parameter, $c_{\rm vir}$, which we sample using the concentration-mass relation from Dutton and Macciò (2014), with a log-normal intrinsic scatter of 0.11 dex. With this, we can relate $M_{\rm vir}$ and $c_{\rm vir}$ to the NFW density parameters $r_{\rm NFW}$ and $\rho_{\rm NFW}$, as described in section 2.1.1.

The process for the SIS model is much simpler since we only require a single parameter: the velocity dispersion σ_v, which we can directly relate to the virial mass, $M_{\rm vir}$, as follows. First, the interior mass function is given by eq. (1.55):

$$m(r) = \frac{2\sigma_v^2 r}{G}\,.$$

Evaluating this at the virial radius results in an expression for σ_v in terms of $M_{\rm vir}$ and $r_{\rm vir}$. Simultaneously solving this with the definition of the virial radius, eq. (1.46), and the virial mass, eq. (1.47), gives us an expression for σ_v in terms of $M_{\rm vir}$ only,

$$\sigma_v^6 = \frac{200\rho_c \pi G^3 M_{\rm vir}^2}{6}\,. \tag{5.8}$$

Following the procedure laid out in this section and the MCMC sampling techniques from section 2.1.2, we generate two samples of 1000 galaxies each: one using the SIS model and the other using the NFW model. We calculate the RAR for each galaxy in our sample, which we can compare against the lensing RAR data points, as shown in figure 5.1. This figure is a recreation of figure 2 of Mistele et al. (2024b), using the data from table 1 of the same work. We plot our Newtonian accelerations, evaluated at the given $g_{\rm bar}$ values, on top of this figure, shown as green error bars.

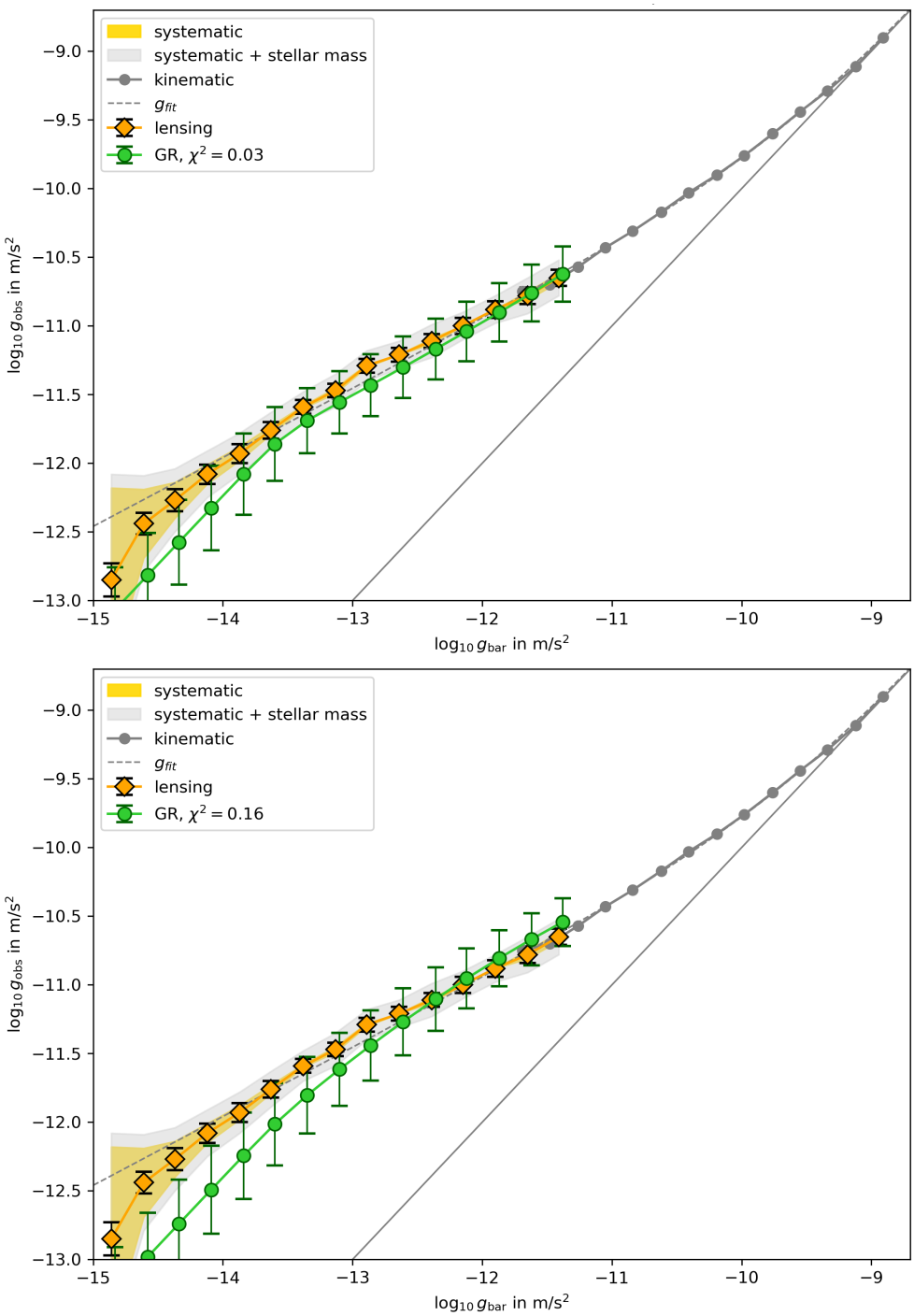


Figure 5.1: RAR of a statistical sample of 1000 galaxies, using the SIS (top) and NFW (bottom) models, plotted on top of the kinematic (SPARC) and lensing (Mistele) data points. Each green data point represents the mean acceleration values ($\pm 1\sigma$), evaluated at the corresponding $g_{\rm bar}$. In the data points from Mistele et al. (2024b) the error bars represent the 1σ statistical uncertainty on the mean in each bin; the yellow band represents the systematic uncertainties from interpolating between bins; and the grey band represents the additional systematic uncertainties from stellar mass estimates. The reduced chi-squared values in the legend represent the goodness of fit for each model to the lensing data points.

In figure 5.1, we observe that the Newtonian RAR for our two samples of galaxies provides a relatively good fit to the lensing data points; however, there is an underestimation of the acceleration for small $g_{\rm bar}$ values and an overestimation for large $g_{\rm bar}$ values (in the SIS case this effect is minimal). Any discrepancy at large acceleration values suggests that the baryonic contribution to the gravitational potential is not fully captured by our models. A full treatment including the SPARC kinematic data as a constraining tool for large accelerations should ideally be performed, but this is left for future work. Fitting to the kinematic data would likely shift the curves below the lensing data points. This should alleviate the tension at high accelerations, but may increase the tension in the low-acceleration regime.[6]

In the legend of figure 5.1, we provide a reduced chi-squared value describing the goodness of fit for each model to the lensing data points. This is calculated using the following formula:

$$\chi^2_{\rm red} = \frac{1}{N_{\rm dof}} \sum_i \frac{(g_{\rm obs} - g_{\rm model})^2}{(\sigma^2_{\rm obs} + \sigma^2_{\rm model})}\,, \tag{5.9}$$

where $N_{\rm dof}$ is the number of degrees of freedom, $g_{\rm obs}$ are the lensing data points, $g_{\rm model}$ are the model predictions, and $\sigma_{\rm obs}$ and $\sigma_{\rm model}$ are the uncertainties in the lensing data and model predictions, respectively. The observational uncertainties are inclusive of the statistical and systematic uncertainties. In this case, $N_{\rm dof}$ is the number of data points minus the number of free parameters in the model ($15 - 0$ in this case). The observed uncertainties for this dataset can be found in Table 1 of Mistele et al. (2024b).

From the reduced chi-squared values, we see that the SIS model provides a slightly better fit to the lensing data points than the NFW model. This is likely due to the SIS model's ability to maintain a flat rotation curve out to large radii, consistent with the lensing data points, whereas the NFW

[6]Fortunately for us, this would provide more room for scalar enhancements to the RAR at low accelerations, without overestimating the observed accelerations.

model predicts a declining rotation curve at large radii. However, it is important to note that neither model provides a perfect fit to the data, and there is still room for improvement. The discrepancies at both high and low accelerations suggest that additional physics may be required to fully capture the behaviour of the RAR. Additionally, at low accelerations, the RAR of both models falls off as $g_{\rm obs} \propto g_{\rm bar}$, whereas the lensing data points follow $g_{\rm obs} \propto \sqrt{g_{\rm bar}}$. This is a direct result of the truncation of the density profiles at the splashback radius.

In future work, we plan to adapt the pipeline in this section to better align with the results of Mistele et al. (2024b) by focusing exclusively on late-type galaxies. This will involve updating the SMF to match the LTG-specific SMF in Mistele et al. (2024b) (see figure 1 in the cited work); including a cold gas component to the baryonic matter, as in eqs. (4.2) and (4.3) of Mistele et al. (2024b); and adopting a SHMR that derives from the KiDS survey galaxy populations (and is specific to late-type galaxies), such as eq. 7 in Bilicki et al. (2021). These adaptations should better align our mock-galaxy sample and thus improve the accuracy and reliability of our results when compared to Mistele et al. (2024b).

5.5.3 Numerical Scalar Field Solver

Now that we have fully defined our density models, we can use them to determine the scalar field profile using a numerical scalar field solver. The solver we use is the same as that described in section 2.2. However, since we are now working with one-dimensional, spherically symmetric sources, we are able to drop the angular terms in the solver (i.e., terms including v). This significantly reduces the computational cost of the simulation.

The solver discretises the scalar field over a grid of 512 radial coordinates. The grid coordinates are equidistant in log-space, with the first point at $r = 50\,\mathrm{pc}$ and the last point at $r = 1000\,\mathrm{kpc}$. This covers the

full range of interest in the RAR for the entire sample of galaxies. The innermost coordinate acts as an inner cutoff, preventing the solver from being affected by the density singularity at the centre of the galaxy. The outermost coordinate is sufficiently large that the field is able to fully relax to its background value, $\varphi = 1$, at the boundary.

Since our field and density profiles are defined on a radial coordinate grid, but the RAR data points are defined in terms of $g_{\rm bar}$, which differs for each galaxy, we must use an interpolator to assess values of interest at the correct coordinates. For this, we use the `scipy.interpolate` package, specifically the `CubicSpline` function (Virtanen et al., 2020). We have found this to be a robust interpolator for our purposes, and any discrepancies in the RAR are negligible compared to the statistical noise from other sources.

An example plot of the field profiles for 1000 NFW galaxies is shown in figure 5.2. Here, we choose symmetron parameters of $M_{\rm sym} = 10^{-3.5}\, M_{\rm pl}$ and $L_{\rm c} = 10^2\,{\rm Mpc}$. This choice of parameters results in scalar fields that are screened at small radii and large accelerations, but allows scalar enhancements at lower acceleration values.

5.6 Fifth Force Contributions to the RAR

Before progressing to the various photon mass models, we first quantify the modifications to the RAR that arise from classical fifth forces. These modifications represent the type that one would observe when measuring visible tracers within the galaxy, such as gas or stars. These observables typically exist within the galactic disc component, extending out to approximately 30 kpc. Nevertheless, objects such as orphan stars and intracluster light (Martínez-Lombilla et al., 2023; Butler et al., 2025; Mondelin et al., 2025) in the outskirts of galactic haloes could prove useful for future observations.

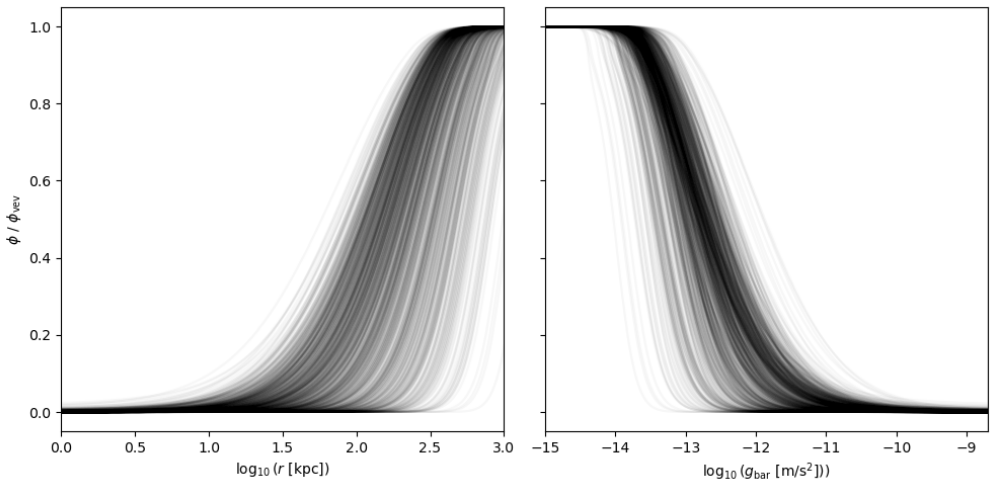


Figure 5.2: Scalar field profiles for a statistical sample of 1000 NFW galaxies, for the symmetron parameters $M_{\mathrm{sym}} = 10^{-3.5}\, M_{\mathrm{pl}}$ and $L_{\mathrm{c}} = 10^2\,\mathrm{Mpc}$. Each line represents the scalar field value as a function of radius (left) and g_{bar} (right), illustrating the variation in field strength across different galaxies.

For simplicity, we consider a static, spherically symmetric galaxy. This constitutes a reasonable assumption for the observational range of interest ($r \gtrsim 30\,\mathrm{kpc}$), where the disc-like baryonic component is subdominant to the roughly spherical dark matter halo and can therefore be effectively treated as a point mass. For such a system, the radial acceleration of a massive test particle can be calculated through the geodesic equation (as detailed in appendix B) to yield eq. (B.24) in the weak-field, non-relativistic limit, restated here for convenience,

$$\frac{\mathrm{d}^2 r}{\mathrm{d}t^2} \approx -\frac{Gm}{r^2} - \frac{1}{2}\partial_r A^2\,.$$

Here m is the enclosed mass at radius r, and $A(\phi)$ is the conformal coupling function.

The above equation is well established, with the first term representing the usual Newtonian acceleration and the second term representing the classical fifth force contribution, g_5. In the symmetron model under consideration, with a conformal coupling given by eq. (1.113), this fifth force

acceleration becomes a function of the field gradient

$$g_5 = -\phi_{\rm vev}^2 \left(\frac{M_{\rm pl}}{M_{\rm sym}}\right)^2 \varphi \nabla \varphi \,, \tag{5.10}$$

where $\varphi \in [0, 1]$ is the rescaled version of the scalar field, defined as $\varphi = \phi/\phi_{\rm vev}$, and $\phi_{\rm vev}$ is the vacuum expectation value of the scalar field, eq. (1.119), restated here in terms of $L_{\rm c}$,

$$\phi_{\rm vev} = \frac{1}{\sqrt{2\lambda}} \frac{L_{\rm pl}}{L_{\rm c}} \,. \tag{5.11}$$

The symmetron model contains three parameters ($M_{\rm sym}$, $L_{\rm c}$, and λ), each contributing to the shape of the RAR in unique ways. All three parameters are inversely proportional to the fifth force, eq. (5.10). The simplest parameter to explain is λ, which appears only in the fifth force equation and thus primarily controls the strength of the fifth force (smaller values of λ result in larger values of g_5). In this chapter, we parameterise λ through $\phi_{\rm vev}$ using eq. (5.11) to match later sections where $\phi_{\rm vev}$ will be more relevant (due to its relation to the scalar photon mass).

The parameters $M_{\rm sym}$ and $L_{\rm c}$ also appear in the symmetron equation of motion and therefore determine the overall shape of the field profile (and thus the form of g_5). In particular, the combination $(M_{\rm sym}/L_{\rm c})^2$ controls the symmetry-breaking scale, $\rho_{\rm SSB}$, eq. (1.116). We demonstrated in chapter 3 that $\rho(r_s) = \rho_{\rm SSB}$ approximately describes the screening radius, i.e. where the scalar field begins to become non-zero and therefore where the fifth force "turns on". Additionally, $L_{\rm c}$ represents the Compton wavelength of the scalar field and controls the 'width' of the fifth force; large values of $L_{\rm c}$ result in a smoother transition from a screened to unscreened field across a larger region, whilst small values of $L_{\rm c}$ result in a more localised fifth force.

To best match the observed RAR found in Mistele et al. (2024b), we require the fifth force to provide a sustained enhancement to the Newtonian force at the outskirts of the galaxy. This necessitates a small value of $\rho_{\rm SSB}$ to correspond to the low density at the galactic outskirts, and a large $L_{\rm c}$

to sustain the modification across a large domain in $g_{\rm bar}$. The value of $\phi_{\rm vev}$ (or equivalently λ) can then be set to best match the observed amount of additional acceleration required.

For this model, we plot the resulting RAR for a single set of parameters (the same ones used to derive the scalar profiles in figure 5.2) across the full sample of 1000 galaxies (as shown in figure 5.1). The resulting fifth-force RARs are presented in figure 5.3. Here we observe the fifth force accelerations (pink) rising above the Newtonian accelerations (green) at low accelerations, where the scalar effects become significant. The choice of parameters ($M_{\rm sym} = 10^{-3.5}\,M_{\rm pl}$, $L_{\rm c} = 10^2\,{\rm Mpc}$, and $\phi_{\rm vev} = 2 \times 10^{-7}$) are chosen to illustrate the effects of the fifth force, rather than to provide a best fit to the data. In particular, the magnitude of the fifth force is overstated for visual clarity — a smaller value of $\phi_{\rm vev}$ would better fit the data. In future work, a comprehensive parameter search using more sophisticated methods (e.g., Bayesian parameter inference, section 2.1.2) would yield a more suitable set of values for the symmetron parameters, and could additionally be used as a tool to rule out obviously unphysical regions of parameter space.

Notably, for the chosen values of $M_{\rm sym}$ and $L_{\rm c}$, we find that the fifth force effects are significant at the outskirts of galaxies, where the baryonic density is low, whilst none of the larger acceleration values are altered. This behaviour is consistent with the observed RAR, which requires a deviation from Newtonian predictions in low-acceleration regions only. However, the scalar fifth force does not extend deep into the low-acceleration regime, instead falling off quickly at the splashback radius where the density profile is cut off. This is unfortunate, but acceptable given the systematic uncertainties present in this region (i.e., one should only trust the comparison to the observed data for $g_{\rm bar} \gtrsim 10^{-14}\,{\rm ms}^{-2}$ where the galaxies are reliably isolated). In future work one could consider the effect of increasing the density cutoff, $r_{\rm SB}$, to provide a more sustained enhancement in this

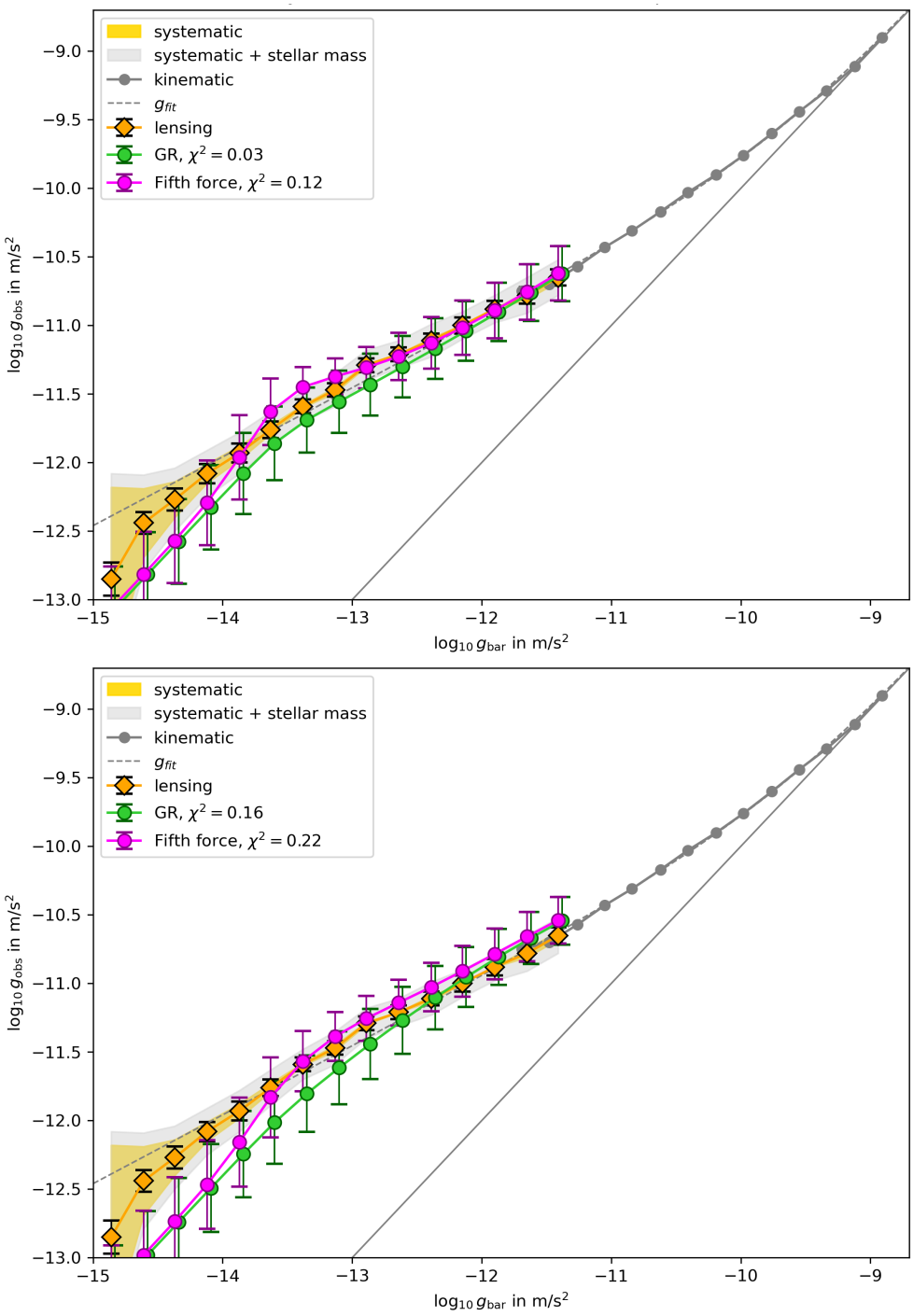


Figure 5.3: RAR of a statistical sample of 1000 galaxies, using the SIS (top) and NFW (bottom) models, plotted on top of the kinematic (SPARC) and lensing (Mistele) data points. Each pink data point represents the mean fifth force acceleration, eq. (B.24), evaluated at the corresponding $g_{\rm bar}$, for symmetron parameters $M_{\rm sym} = 10^{-3.5}\, M_{\rm pl}$, $L_{\rm c} = 10^2\,$Mpc, and $\phi_{\rm vev} = 2 \times 10^{-7}$. Other data points are explained in figure 5.1.

domain.

5.7 Scalar Modifications to RAR Observations

So far, we have determined the radial acceleration of a visible, massive test particle. However, a key objective of this chapter is to understand the impact of modified gravity theories on the lensing of light in areas of galaxies devoid of visual tracers. As such, we must develop a method to quantify lensing in classical and scalar-modified cases — comparing implied accelerations (or mass profiles) in each cases.

As previously discussed, the classical fifth force only presents itself through its impact on massive (visible) tracers within the galactic environment. This is at odds with the acquisition of the data in Brouwer et al. (2021) and Mistele et al. (2024b), which rely on lensing measurements from photon-based observations. In fact, for the scalar model to impact the lensing data collected, we are required to introduce a (small) mass to the photon, m_γ. We achieve this using two models: a fixed photon mass and a scalar-dependent photon mass, both described in section 5.4. Adopting either of these models results in a modification to the photon geodesic, which will impact the observational results of Brouwer et al. (2021) and Mistele et al. (2024b).

In section 5.7.1, we derive a novel method to relate the radial acceleration found by lensing measurements, to the radial acceleration one would anticipate in a universe where (massive) photon geodesics are modified in the presence of a conformally coupled scalar field. This method is general and can be applied to any metric theory of gravity with a conformal coupling. In section 5.7.2, we apply this method to the symmetron model with a fixed photon mass, and a scalar-dependent photon mass, and show how these models would impact the RAR.

5.7.1 Scalar Impact on Lensing

In section 1.4, we outlined the classical GR calculation of the lensing deflection angle, $\Delta\theta$, for a photon travelling through a static, spherically symmetric spacetime, described by an exterior Schwarzschild metric. While performing this calculation, we found that the photon trajectory, and thus the deflection angle, could be described by the angular acceleration, $\frac{\mathrm{d}^2u}{\mathrm{d}\theta^2}$, where $u = 1/r$ is the inverse radial distance of the photon. This quantity can be calculated for any metric theory of gravity and thus provides a useful tool to compare the lensing effects of different theories. In this section, we derive the general expression for the angular acceleration, $\frac{\mathrm{d}^2u}{\mathrm{d}\theta^2}$, for a particle travelling through a static, spherically symmetric spacetime, described by the Jordan frame metric, $\tilde{g}_{\alpha\beta} = A^2(\phi)g_{\alpha\beta}$. This expression can then be applied to any specific metric theory of gravity with a conformal coupling, such as the symmetron model with a fixed or scalar-dependent photon mass, described in section 5.4.

We begin with the line element for a static, spherically symmetric spacetime, given by

$$\tilde{g}_{tt}\left(\frac{\mathrm{d}t}{\mathrm{d}\tau}\right)^2 + \tilde{g}_{rr}\left(\frac{\mathrm{d}r}{\mathrm{d}\tau}\right)^2 + \tilde{g}_{\theta\theta}\left(\frac{\mathrm{d}\theta}{\mathrm{d}\tau}\right)^2 = q\,, \tag{5.12}$$

where τ is the proper time along the geodesic, and $q = 0$ for a massless particle and $q = -1$ for a massive particle. It is implicit in this line element that we have restricted the motion to the equatorial plane, $\vartheta = \pi/2$, without loss of generality. The metric components $\tilde{g}_{\alpha\beta}$ are functions of the radial coordinate r only. Given the symmetries of the spacetime, we can identify two conserved quantities, given by

$$E = \tilde{g}_{tt}\frac{\mathrm{d}t}{\mathrm{d}\tau} \quad \text{and} \quad h = \tilde{g}_{\theta\theta}\frac{\mathrm{d}\theta}{\mathrm{d}\tau}\,. \tag{5.13}$$

These represent the particles energy per unit mass and angular momentum per unit mass, respectively. Using these conserved quantities, we rearrange

the line element to find

$$\left(\frac{\mathrm{d}r}{\mathrm{d}\tau}\right)^2 = \frac{q}{\tilde{g}_{rr}} - \frac{E^2}{\tilde{g}_{tt}\tilde{g}_{rr}} - \frac{h^2}{\tilde{g}_{rr}\tilde{g}_{\theta\theta}}\,.$$

Our next step is to rewrite the radial component in terms of the inverse radial distance, $u = 1/r$, as follows

$$\frac{\mathrm{d}r}{\mathrm{d}\tau} = \frac{\mathrm{d}r}{\mathrm{d}u}\frac{\mathrm{d}u}{\mathrm{d}\tau} = -\frac{1}{u^2}\frac{\mathrm{d}u}{\mathrm{d}\tau}\,. \tag{5.14}$$

In a similar vein, the angular component can be rewritten as

$$\frac{\mathrm{d}u}{\mathrm{d}\tau} = \frac{\mathrm{d}u}{\mathrm{d}\theta}\frac{\mathrm{d}\theta}{\mathrm{d}\tau} = \frac{h}{\tilde{g}_{\theta\theta}}\frac{\mathrm{d}\theta}{\mathrm{d}\tau}\,, \tag{5.15}$$

where we have used the angular constant of motion, eq. (5.13). Putting these together, we arrive at

$$\left(\frac{\mathrm{d}u}{\mathrm{d}\theta}\right)^2 = \frac{qu^4\tilde{g}_{\theta\theta}^2}{h^2\tilde{g}_{rr}} - \frac{E^2u^4\tilde{g}_{\theta\theta}^2}{h^2\tilde{g}_{tt}\tilde{g}_{rr}} - \frac{u^4\tilde{g}_{\theta\theta}}{\tilde{g}_{rr}}\,. \tag{5.16}$$

For every metric we will consider, $\tilde{g}_{\alpha\beta} = A^2(\phi)g_{\alpha\beta}$ and $g_{\theta\theta} = r^2$; as such, we can simplify the above equation to

$$\left(\frac{\mathrm{d}u}{\mathrm{d}\theta}\right)^2 = -\frac{u^2}{g_{rr}} - \frac{E^2}{h^2g_{tt}g_{rr}} + \frac{qA^2}{h^2g_{rr}}\,. \tag{5.17}$$

In order to relate more directly to observables, we calculate the angular acceleration,

$$\begin{aligned}\frac{\mathrm{d}^2u}{\mathrm{d}\theta^2} &= \frac{1}{2}\frac{\mathrm{d}}{\mathrm{d}u}\left(\left(\frac{\mathrm{d}u}{\mathrm{d}\theta}\right)^2\right)\\ &= -\frac{u}{g_{rr}} + \frac{u^2}{2g_{rr}^2}\frac{\mathrm{d}g_{rr}}{\mathrm{d}u} + \frac{E^2}{2h^2g_{tt}^2g_{rr}^2}\left(g_{rr}\frac{\mathrm{d}g_{tt}}{\mathrm{d}u} + g_{tt}\frac{\mathrm{d}g_{rr}}{\mathrm{d}u}\right)\\ &\quad - \frac{qA^2}{2h^2g_{rr}^2}\frac{\mathrm{d}g_{rr}}{\mathrm{d}u} + \frac{q}{2h^2g_{rr}}\frac{\mathrm{d}A^2}{\mathrm{d}u}\,.\end{aligned} \tag{5.18}$$

It is possible to equate this to the usual GR case by setting $q = 0$ and $A = 1$, which recovers eq. (1.127), for an exterior Schwarzschild metric in the weak field limit. For later convenience, we convert the right-hand side

of eq. (5.18) back to radial coordinates, $r = 1/u$, giving us

$$\begin{aligned}\frac{\mathrm{d}^2u}{\mathrm{d}\theta^2} =& -\frac{1}{rg_{rr}} - \frac{1}{2g_{rr}^2}\frac{\mathrm{d}g_{rr}}{\mathrm{d}r} - \frac{E^2r^2}{2h^2g_{tt}^2g_{rr}^2}\left(g_{rr}\frac{\mathrm{d}g_{tt}}{\mathrm{d}r} + g_{tt}\frac{\mathrm{d}g_{rr}}{\mathrm{d}r}\right) \\ &+ \frac{qA^2r^2}{2h^2g_{rr}}\left(\frac{1}{g_{rr}}\frac{\mathrm{d}g_{rr}}{\mathrm{d}r} - \frac{1}{A^2}\frac{\mathrm{d}A^2}{\mathrm{d}r}\right).\end{aligned} \tag{5.19}$$

This is the general metric expression for the angular acceleration. It should be noted that scalar modifications arising through $A(\phi)$ come alongside the parameters q. As such, these modifications will only be present for massive particles ($q = -1$) and will vanish for massless particles ($q = 0$), as one would expect.

We propose that the quantity $\frac{\mathrm{d}^2u}{\mathrm{d}\theta^2}$ can be used as a proxy to quantify the observable amount of lensing experienced by a photon in a given spacetime geometry. As such, comparing the angular acceleration in GR (with $q = 0$ and $A = 1$) to that in an MG model (with $q = -1$ and $A = A(\phi)$) will allow us to determine the impact of the scalar field on the mass/acceleration profiles hiding within the metric components.

To exemplify this concept, we will calculate the angular acceleration for a photon (in both GR and MG) for a metric describing an NFW mass source, derived in appendix A.2. The metric for an NFW profile is given by eq. (A.28), restated here for convenience:

$$\begin{aligned}\mathrm{d}s^2 \approx& \left(1 - \frac{2Gm(r)}{r} - f_{\mathrm{NFW}}(r)\right)\mathrm{d}t^2 \\ &+ \left(1 + \frac{2Gm(r)}{r}\right)\mathrm{d}r^2 + r^2\mathrm{d}\Omega^2,\end{aligned}$$

where $m(r)$ is the enclosed mass function for the NFW profile, eq. (1.52). Additionally, for brevity we have defined the correction term, eq. (A.29), as

$$f_{\mathrm{NFW}} = 8\pi G\rho_{\mathrm{NFW}}r_{\mathrm{NFW}}^2\left[\frac{1}{1 + r/r_{\mathrm{NFW}}} - \frac{1}{1 + R/r_{\mathrm{NFW}}}\right],$$

where r_{NFW} and ρ_{NFW} are the usual NFW density profile parameters, and R is the 'surface' of the object, or more precisely the splashback radius, r_{SB}.

Using the NFW metric in eq. (5.19), we find the angular acceleration for a particle travelling through an NFW spacetime is given by

$$\begin{aligned}\frac{\mathrm{d}^2u}{\mathrm{d}\theta^2} =& -\frac{1}{r}\left(1+\frac{2Gm}{r}\right)^{-1} - \frac{1}{2}\left(1+\frac{2Gm}{r}\right)^{-2}\left(-\frac{2Gm}{r^2}+\frac{2Gm'}{r}\right)\\ &+\frac{E^2r^2}{2h^2}\left(1-\frac{2Gm}{r}-f_{\mathrm{NFW}}(r)\right)^{-1}\left(1+\frac{2Gm}{r}\right)^{-1}\\ &\quad\times\left[\frac{2Gm}{r^2}\left(1-\frac{2Gm}{r}-f_{\mathrm{NFW}}(r)\right)^{-1}\right.\\ &\qquad\left.+\left(-\frac{2Gm}{r^2}\frac{2Gm'}{r}\right)\left(1+\frac{2Gm}{r}\right)^{-1}\right]\\ &+\frac{qA^2r^2}{2h^2}\left(1+\frac{2Gm}{r}\right)^{-2}\left(-\frac{2Gm}{r^2}+\frac{2Gm'}{r}\right)^{-1}\\ &-\frac{qr^2}{2h^2}\left(1+\frac{2Gm}{r}\right)^{-1}\frac{\mathrm{d}A^2}{\mathrm{d}r}\,,\end{aligned} \tag{5.20}$$

where $m' = \frac{\mathrm{d}m}{\mathrm{d}r}$ is the radial derivative of the enclosed mass function. Taking the weak-field limit (ignoring terms that are sub-leading order in Gm/r, Gm'/r, f_{NFW} and $\partial_r A^2$) and rearranging, we find the much more managable expression

$$\begin{aligned}\frac{\mathrm{d}^2u}{\mathrm{d}\theta^2} \approx& -\frac{1}{r}+\frac{Gm}{r^2}\left(3-\frac{qA^2r^2}{h^2}\right)\\ &-\frac{Gm'}{r}\left(1-\frac{E^2r^2}{h^2}-\frac{qA^2r^2}{h^2}\right)-\frac{qr^2}{2h^2}\frac{\mathrm{d}A^2}{\mathrm{d}r}\,.\end{aligned} \tag{5.21}$$

Now we are able to compute the inferred mass/acceleration profiles observed in lensing observations by equating the predicted lensing impact in GR (with $q = 0$ and $A = 1$) and MG (with $q = -1$ and $A = A(\phi)$), i.e.

$$\left.\frac{\mathrm{d}^2u}{\mathrm{d}\theta^2}\right|_{\mathrm{GR}} = \left.\frac{\mathrm{d}^2u}{\mathrm{d}\theta^2}\right|_{\mathrm{MG}}\,. \tag{5.22}$$

In essence, we are saying here that whatever lensing effect is observed and ascribed to GR can instead be described by the MG model. So an observed mass profile derived from lensing observations assuming a GR model, m_{GR}, could instead be the result of an MG model with a different mass profile, m_{MG}, and additional scalar modifications. Using eq. (5.21) in the above

expression (and setting $q = 0$, $A = 1$ for the GR case), we find

$$\frac{Gm_{\rm GR}}{r^2}(3) - \frac{Gm'_{\rm GR}}{r}\left(1 - \frac{E^2r^2}{h^2}\right) = \tag{5.23}$$
$$\frac{Gm_{\rm MG}}{r^2}\left(3 - \frac{qA^2r^2}{h^2}\right) - \frac{Gm'_{\rm MG}}{r}\left(1 - \frac{E^2r^2}{h^2} - \frac{qA^2r^2}{h^2}\right) - \frac{qr^2}{2h^2}\frac{{\rm d}A^2}{{\rm d}r}\,.$$

This equation contains mass derivative terms that do not vanish in the GR case, which make the GR-MG comparison complicated at best.

Thankfully, we can simplify this expression by relating the conserved parameters, h and E, through the turning point of the photon trajectory (i.e., $\frac{{\rm d}u}{{\rm d}\theta}\big|_{r=b} = 0$, where b is the impact parameter) to find $h \approx bE$, as is standard in weak lensing calculations (see eq. (1.126)). In our case, we are measuring lensing at a range of impact parameters, quantified by our radial coordinate, i.e., $b = r$. As such we have the relation

$$h = rE\,. \tag{5.24}$$

Plugging eq. (5.24) into eq. (5.23) causes the mass derivative term on the GR side to vanish and results in our final expression for the implied radial acceleration in an NFW spacetime:

$$\frac{Gm_{\rm GR}}{r^2} = \frac{Gm_{\rm MG}}{r^2}\left(1 - \frac{qA^2}{3E^2}\right) + \frac{qA^2}{3E^2}\frac{Gm'_{\rm MG}}{r} - \frac{q}{6E^2}\frac{{\rm d}A^2}{{\rm d}r}\,. \tag{5.25}$$

Here, the term on the left is the radial acceleration profile that would be inferred from lensing observations assuming GR, and the terms on the right are the acceleration-like terms arising from the true mass profile[7] in the MG model, $m_{\rm MG}$, with further enhancements arising from the scalar field through the conformal coupling function $A(\phi)$. Note here that for any conformally coupled MG model with a massless photon ($q = 0$), the implied lensing acceleration trivially reduces to the classical GR case, i.e., $m_{\rm GR} = m_{\rm MG}$, as one would expect.

The expression we have derived in eq. (5.25) is general and can be

[7]In this work the true mass profile is assumed to be the usual SIS/NFW DM profile.

applied to any metric theory of gravity with a conformal coupling. We also derive equivalent expressions for an exterior Schwarzchild metric, and an SIS metric, in appendix C. The results of both of these calculations can be thought of as special cases of the above expression. Specifically, the exterior Schwarzschild metric result is identical to eq. (5.25), with $m(r) = M$ (where M is a point mass) and $m'(r) = 0$, i.e., eq. (C.5)

$$\frac{GM_{\rm GR}}{r^2} = \frac{GM_{\rm MG}}{r^2}\left(1 - \frac{qA^2}{3E^2}\right) - \frac{q}{6E^2}\frac{{\rm d}A^2}{{\rm d}r}\,.$$

Here, we see this is equivalent to the NFW case but without the term containing the mass derivative.

The SIS metric result is a special case because its mass profile (eq. 1.55) has a linear dependence on radius ($m \propto r$), and therefore the mass derivative term exactly cancels the scalar term modifying the Newtonian acceleration, i.e., eq. (C.10):

$$\frac{Gm_{\rm GR}}{r^2} = \frac{Gm_{\rm MG}}{r^2} - \frac{q}{6E^2}\frac{{\rm d}A^2}{{\rm d}r}\,.$$

As such, for the SIS density profile, the scalar enhancement to lensing observations behaves identically to a classical fifth force enhancement, eq. (1.63), now with a constant prefactor of $1/(3E^2)$ on the term containing derivatives of A^2. For an NFW density profile, this cancellation does not occur, although as we shall see, the overall behaviour is very similar to the classical fifth force enhancement.

5.7.2 Scalar Lensing RAR Results

In this section, we will use the implied radial acceleration, eq. (5.25), to determine the impact of the symmetron model on lensing-based RAR measurements for both a fixed and a scalar-dependent photon mass model. As a reminder, for a given true mass profile $m_{\rm MG}$, the implied lensing acceleration (i.e., the acceleration that would be inferred from lensing observations assuming GR) is given by the left-hand side of eq. (5.25). This allows us

to calculate the expected RAR ($g_{\rm obs} = Gm_{\rm GR}/r^2$) for our modified gravity theory, given the true mass profile ($m_{\rm MG}$) and the scalar field profile (through $A(\phi)$).

Before we calculate the observed radial acceleration, we must define the remaining conserved quantity in eq. (5.25), E. In classical GR geodesic calculations, the provocatively labeled constant of motion, E, represents the energy per unit rest mass of a particle in orbit around a gravitational source. As such, in our photon mass models, the adopted values of this constant are $E = \nu/m_\gamma$ in the fixed mass case and equivalently, but with $m_\gamma = M_{\rm pl}\phi_{\rm vev}$ in the scalar-dependent mass case.

Given that the typical photon frequency for observable light is $\sim$ eV, and the photon mass is measured to be small ($m_\gamma \lesssim 10^{-15}\,$eV from fast radio bursts), the constant parameter E is required to be very large. This means that the modifications to the implied acceleration are suppressed by the factor of $1/E^2$. This is unfortunate, as it means that the scalar modifications to the RAR are negligible for most (if not all) of the viable parameter space. Nevertheless, we shall proceed to show how the RAR would appear in such models.

For a fixed photon mass, with $E = \nu/m_\gamma$, the conformal coupling factor is given by the usual symmetron coupling, $A(\phi)$, eq. (1.113).[8] Substituting these into the implied acceleration equation, eq. (5.25), we are able to calculate the observed accelerations, which we plot in figure 5.4. Instead of specifying a λ or $\phi_{\rm vev}$, we set these values to be as high as possibly allowed whilst retaining the perturbative nature of the coupling function, i.e., $\delta A(\phi_{\rm vev}) = 0.1$, where $A(\phi_{\rm vev}) = 1 + \delta A(\phi_{\rm vev})$. Even with this relatively large value for the vacuum expectation value, we must adopt an unphysically large value on the photon mass of $m_{\rm photon} = 0.2\,$eV to see any significant effects. Despite this obvious drawback, we demonstrate that the

[8]This conformal coupling now acts on the massive photon, which no longer possesses a traceless energy-momentum tensor.

same behaviour seen in classical symmetron enhancements (cf. figure 5.3) can also be found using this lensing methodology with a massive photon model.

In the variable photon mass model, $E = \nu/(M_{\rm pl}\phi_{\rm vev})$, and the conformal coupling function picks up a correction from the photon mass factor $\alpha = \phi/\phi_{\rm vev}$. Overall, the conformal factor now behaves as $\mathcal{A} = \alpha A$, where A is the usual symmetron coupling function (eq. (1.113)). Note that now the vacuum expectation value for the field is set by the value of the photon mass via $m_\gamma = M_{\rm pl}\phi_{\rm vev}$. Plotting the RAR for this model yields figure 5.5. Again, the same behaviours as in the classical symmetron RAR can be found for this new method, but the photon mass is required to be unphysically large — this time $m_\gamma \approx 10^{-3}\,\text{eV}$ to produce any noticeable effects.

5.8 Conclusions

In this work, we have explored the implications of scalar enhancements to radial accelerations and related these results to recent findings from weak lensing observations. We tested the impact of scalar symmetron fifth forces in three scenarios: the motion of a visible test particle, a fixed mass photon, and a photon with scalar-dependent mass. In each case, we found that the symmetron mechanism can produce significant modifications to the expected acceleration profiles, potentially providing a new avenue for understanding galactic dynamics and the nature of dark matter.

For certain model parameters, accelerations with scalar enhancements can improve the fit to recent RAR data. However, our models that most directly relate to the new lensing-based RARs require a large photon mass to obtain noticeable effects. This is at odds with current constraints on the photon mass, which require values orders of magnitude smaller than those used here.

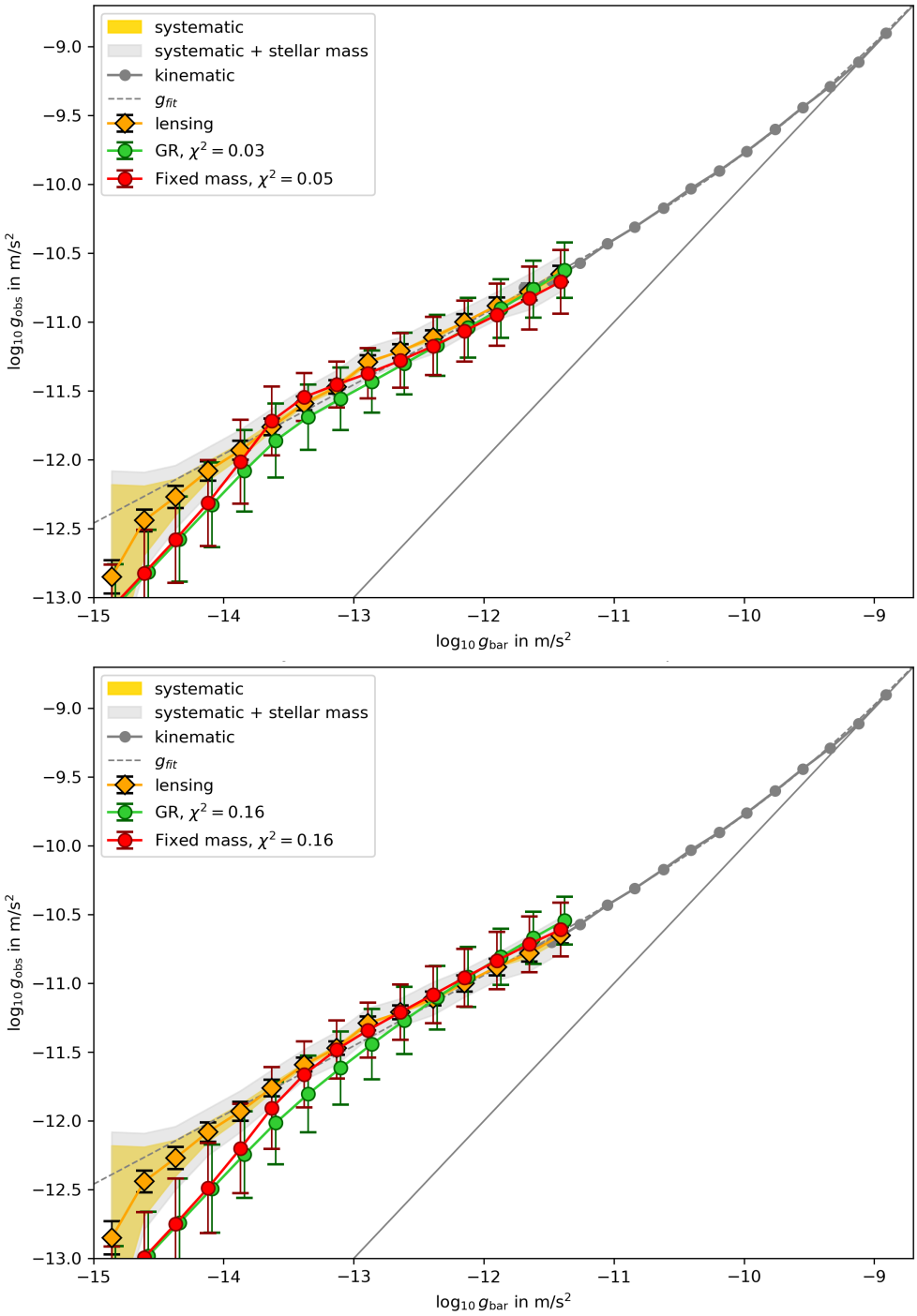


Figure 5.4: RAR of a statistical sample of 1000 galaxies, using the SIS (top) and NFW (bottom) models, plotted on top of the kinematic (SPARC) and lensing (Mistele) data points. Each red data point represents the mean fixed photon mass acceleration values ($\pm 1\sigma$), evaluated at the corresponding g_{bar} for symmetron parameters $M_{\mathrm{sym}} = 10^{-3.5}\, M_{\mathrm{pl}}$, $L_{\mathrm{c}} = 10^2\,\mathrm{Mpc}$, and $\delta A = 0.1$, with a photon mass $m_\gamma = 0.2\,\mathrm{eV}$. Other data points are explained in figure 5.1. Note, parameters are not necessarily best-fit parameters, but chosen to show the effects of the model.

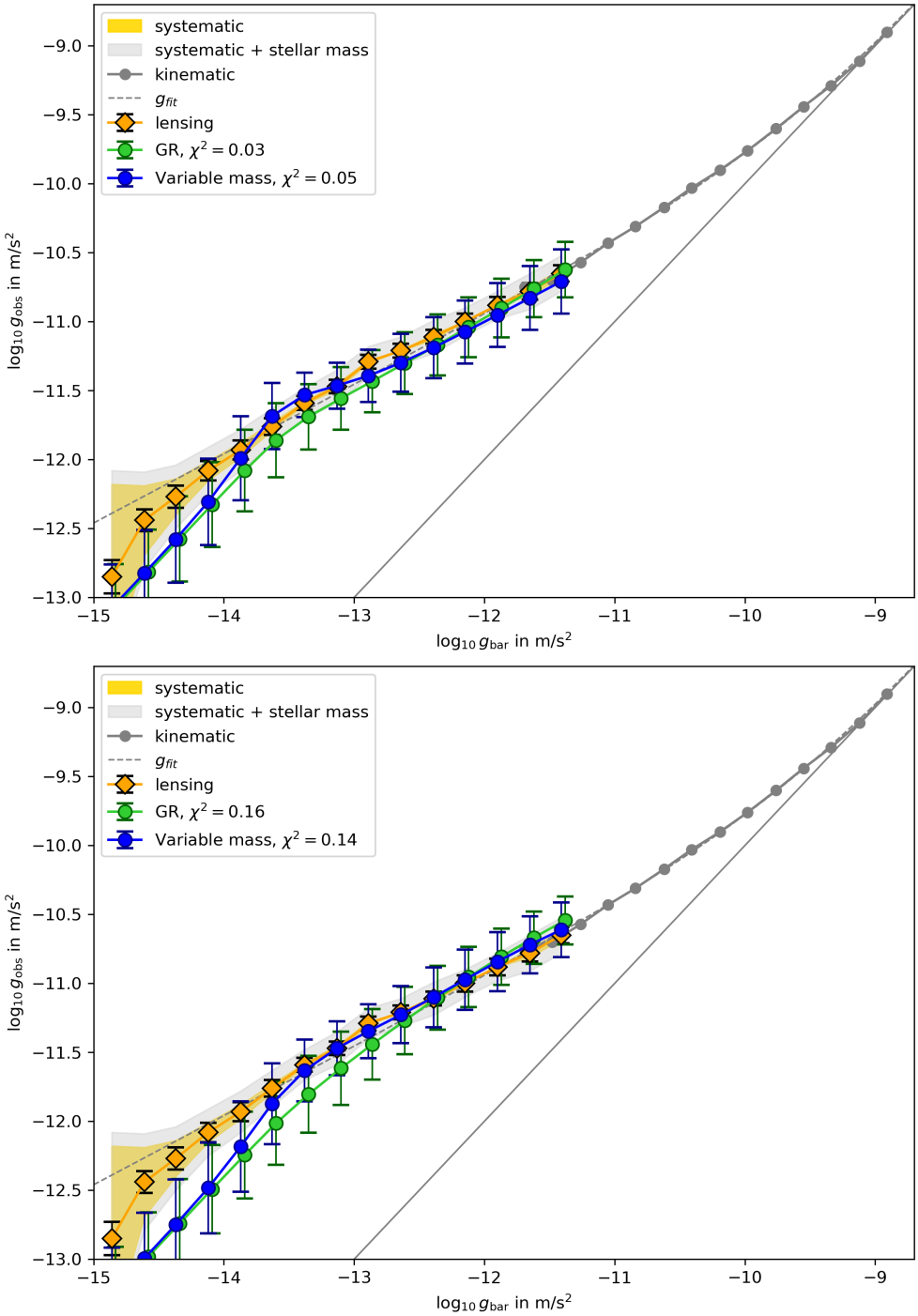


Figure 5.5: RAR of a statistical sample of 1000 galaxies, using the SIS (top) and NFW (bottom) models, plotted on top of the kinematic (SPARC) and lensing (Mistele) data points. Each blue data point represents the mean fixed photon mass acceleration values ($\pm 1\sigma$), evaluated at the corresponding $g_{\rm bar}$ for symmetron parameters $M_{\rm sym} = 10^{-3.5}\, M_{\rm pl}$, $L_{\rm c} = 10^2\,$Mpc. Here the photon mass is scalar dependent, with a vacuum expectation value given by $m_\gamma = M_{\rm pl}\phi_{\rm vev} = 2 \times 10^{-3}\,$eV. Other data points are explained in figure 5.1. Note, parameters are not necessarily best-fit parameters, but chosen to show the effects of the model.

Nevertheless, we have developed novel tests for scalar modifications to gravity using lensing data, which can be further refined and expanded in future work. In the context of symmetron scalar fields, the lensing RAR observations may exhibit a characteristic turn-on feature corresponding to the screening radius, distinct from the smoother transitions typically predicted by dark matter or MOND models. Future investigations could explore a wider range of scalar field models, including those with different coupling functions or potential forms. Additionally, more sophisticated statistical methods could be employed to better constrain the model parameters and assess the goodness of fit to observational data. Furthermore, we have demonstrated that the symmetron mechanism can produce significant modifications to the expected acceleration profiles, which could be utilised in future observations involving visible tracers in the outskirts of galaxies, without requiring any modification to the photon mass.

Chapter 6

Conclusions

With the ongoing discourse in the scientific community regarding the nature of dark matter and dark energy, and the persistent challenges in reconciling observations with theoretical models, scalar-tensor theories of gravity present a promising avenue for exploration. Such theories provide a natural framework for extending General Relativity whilst preserving the theory's elegant geometric foundation, and offer potential explanations for cosmic phenomena that remain elusive under the standard cosmological paradigm. These fields couple to matter through conformal factors, leading to fifth forces that modify gravitational interactions. However, such modifications must be carefully constructed to avoid conflict with stringent Solar System constraints on deviations from General Relativity. This requirement has led to the development of screening mechanisms that suppress fifth forces in well-studied high-density environments, while permitting them to operate in low-density regions — remaining cosmologically relevant and phenomenologically interesting.

The implementation of scalar-tensor theories in realistic galactic environments requires sophisticated numerical and statistical methodologies. To address this challenge, in chapter 2 we developed a mock-galaxy generation pipeline that transforms observable galactic properties into the detailed density profiles required for scalar field calculations. This pipeline incorporates empirical scaling relations connecting stellar masses, halo masses,

galaxy sizes, and structural parameters. We utilised this pipeline with two distinct approaches: first, to generate deterministic galactic parameters for a given input mass, assuming each empirical scaling relation adopts its mean expected value, and thus creating 'maximally typical' galaxies; and second, by employing Markov Chain Monte Carlo methods to generate statistically representative samples of galaxies that account for the intrinsic scatter observed in real galaxy populations, thereby enabling robust comparisons with observational data.

Using these mock galaxies as scalar field sources, we numerically solved the scalar field equations of motion with a robust numerical solver adapted from the work of Naik et al. (2018). The solver employs a two-dimensional (axisymmetric) spherical coordinate system with grid discretisation equally spaced in $u = \ln r$ and $v = \cos\theta$, providing enhanced resolution in regions of interest, while capturing the full dynamical range of galaxies and allowing the field to properly relax to its background value at the boundaries. The solver uses an iterative Gauss-Seidel method with Newton-Raphson updates to achieve convergence on the scalar field profiles, upon which our studies were founded.

Key Findings

The research presented in this thesis has provided important insights into the behaviour of scalar fields, assessed the accuracy of commonly used approximations, and developed novel methods to test scalar-tensor theories. The key findings from each of the three main investigations are summarised below.

Screening Approximations and Their Limitations: In chapter 3, we investigated the accuracy of screening approximations commonly used to constrain chameleon $f(R)$ and symmetron theories. Through precise

numerical solutions and the development of novel methods to accurately determine the location of screened regions within galaxies, we revealed significant discrepancies between approximate and true screening surfaces.

The widely used binary screening condition, which classifies galaxies as either fully screened or fully unscreened based on their virial potential, was found to drastically underestimate the parameter space where galactic discs are screened. This leads to erroneously tight constraints on theory parameters, as the approximation predicts observable signatures in regions where a full analysis reveals screening suppresses all scalar modifications.

More sophisticated approximations that account for partial screening perform better but still exhibit systematic errors. Spherically symmetric approximations underestimate screening radii in galactic discs whilst overestimating them perpendicular to the disc plane. For symmetron models, the approximation $\rho(r_s) = \rho_{\rm SSB}$ provides reasonable accuracy across much of parameter space but breaks down when the Compton wavelength becomes comparable to galactic scales. These findings demonstrate that observational constraints derived using approximate screening methods may be unreliable, potentially ruling out regions of parameter space where modifications would actually be screened and unobservable.

Discrete Versus Continuous Matter Distributions: The second investigation, detailed in chapter 4, explored whether the common assumption of continuous stellar density profiles remains valid for $f(R)$ theories. This work demonstrated that the Compton wavelength of the theory becomes comparable to or smaller than typical stellar separations, particularly in the screened regions of galaxies. In such cases, the discrete nature of stars can significantly affect scalar field profiles. We posit that in this regime, the scalar field in the interstellar medium may relax to values determined primarily by the smooth dark matter distribution, whilst becoming more strongly screened only in the immediate vicinity of individual stars.

This heterogeneous field behaviour can shift screening surfaces toward galactic centres, effectively reducing the screened mass fraction and potentially making previously screened modifications observable. These effects become increasingly important as $f(R)$ theories approach the boundaries of current observational constraints, where Compton wavelengths naturally decrease. The findings suggest that future probes of $f(R)$ in galaxies must account for stellar discreteness to maintain accuracy as observational constraints tighten.

Novel Tests Using Weak Gravitational Lensing: The third investigation, presented in chapter 5, developed a novel theoretical framework to test scalar modifications through weak gravitational lensing observations, motivated by recent measurements of the radial acceleration relation (Brouwer et al., 2021; Mistele et al., 2024b). Most scalar-tensor theories couple to the trace of the energy-momentum tensor, which vanishes for photons, rendering standard lensing observations insensitive to scalar modifications. Introducing a small photon mass — either fixed or scalar-dependent — enables photons to couple to scalar fields through conformal factors, and pick up fifth-force-like accelerations.

We derived general expressions able to determine the implied radial acceleration of massive photons in observed lensing results, providing a novel method for constraining conformally coupled scalar field theories. Application to symmetron models in an attempt to reproduce weak-lensing-based observations of the radial acceleration relation revealed that whilst scalar enhancements to lensing observations are theoretically possible, they require photon masses many orders of magnitude larger than current observational limits. Nevertheless, the theoretical framework established provides a foundation for future investigations exploring alternative conformally coupled scalar models.

Broader Implications and Future Directions

The findings of this thesis have several broader implications for modified gravity research and observational astronomy. The demonstrated inaccuracies in commonly used screening approximations suggest that many existing constraints on chameleon and symmetron theories may require reassessment. Future analyses should employ sophisticated numerical and theoretical methods to ensure reliable constraints, particularly in parameter regimes where partial screening effects are important.

The identification of the discrete nature of galactic matter profiles highlights the need for more detailed theoretical treatments as observational precision improves. The development of efficient computational methods to handle stellar discreteness represents an important avenue for future research. This is particularly relevant for upcoming surveys that will probe galactic dynamics with unprecedented accuracy. Specifically, as surveys constrain smaller scales, the relevant Compton wavelengths approach the typical separation between stars, causing the smooth-fluid approximation used in standard modelling to break down.

The novel lensing methodology, whilst currently limited by photon mass constraints, opens new theoretical directions for testing modified gravity. Future work might explore alternative coupling mechanisms that could produce observable lensing signatures without requiring large photon masses. Additionally, the framework could be extended to other scalar-tensor theories beyond the symmetron model investigated here.

More broadly, this thesis demonstrates the critical importance of precision in modified gravity theory. As observational constraints continue to tighten, theoretical predictions must achieve corresponding levels of accuracy through sophisticated numerical methods and careful attention to the physical assumptions underlying theoretical approximations. The interplay between theory and observation remains central to progress in this

field, and as next-generation surveys provide increasingly detailed maps of galactic structure and dynamics, the theoretical framework developed in this thesis will prove essential for extracting reliable constraints on modified gravity theories and determining their viability as alternatives to standard explanations for the cosmological dark sector.

— Assumptions are just that; as the Universe speaks to us in ever-clearer data, the grammar of our theories must evolve to comprehend its language.

Bibliography

Abbott, T. M. C., Abdalla, F. B., Alarcon, A., Aleksić, J., Allam, S., Allen, S., Amara, A., Annis, J., Asorey, J., Avila, S., Bacon, D., Balbinot, E., Banerji, M., Banik, N., Barkhouse, W., Baumer, M., Baxter, E., Bechtol, K., Becker, M. R., Benoit-Lévy, A., Benson, B. A., Bernstein, G. M., Bertin, E., Blazek, J., Bridle, S. L., Brooks, D., Brout, D., Buckley-Geer, E., Burke, D. L., Busha, M. T., Campos, A., Capozzi, D., Carnero Rosell, A., Carrasco Kind, M., Carretero, J., Castander, F. J., Cawthon, R., Chang, C., Chen, N., Childress, M., Choi, A., Conselice, C., Crittenden, R., Crocce, M., Cunha, C. E., D'Andrea, C. B., da Costa, L. N., Das, R., Davis, T. M., Davis, C., De Vicente, J., DePoy, D. L., DeRose, J., Desai, S., Diehl, H. T., Dietrich, J. P., Dodelson, S., Doel, P., Drlica-Wagner, A., Eifler, T. F., Elliott, A. E., Elsner, F., Elvin-Poole, J., Estrada, J., Evrard, A. E., Fang, Y., Fernandez, E., Ferté, A., Finley, D. A., Flaugher, B., Fosalba, P., Friedrich, O., Frieman, J., García-Bellido, J., Garcia-Fernandez, M., Gatti, M., Gaztanaga, E., Gerdes, D. W., Giannantonio, T., Gill, M. S. S., Glazebrook, K., Goldstein, D. A., Gruen, D., Gruendl, R. A., Gschwend, J., Gutierrez, G., Hamilton, S., Hartley, W. G., Hinton, S. R., Honscheid, K., Hoyle, B., Huterer, D., Jain, B., James, D. J., Jarvis, M., Jeltema, T., Johnson, M. D., Johnson, M. W. G., Kacprzak, T., Kent, S., Kim, A. G., King, A., Kirk, D., Kokron, N., Kovacs, A., Krause, E., Krawiec, C., Kremin, A., Kuehn, K., Kuhlmann, S., Kuropatkin, N., Lacasa, F., Lahav, O., Li, T. S., Liddle, A. R., Lidman, C., Lima, M., Lin, H., MacCrann, N., Maia, M. A. G., Makler, M., Manera,

M., March, M., Marshall, J. L., Martini, P., McMahon, R. G., Melchior, P., Menanteau, F., Miquel, R., Miranda, V., Mudd, D., Muir, J., Möller, A., Neilsen, E., Nichol, R. C., Nord, B., Nugent, P., Ogando, R. L. C., Palmese, A., Peacock, J., Peiris, H. V., Peoples, J., Percival, W. J., Petravick, D., Plazas, A. A., Porredon, A., Prat, J., Pujol, A., Rau, M. M., Refregier, A., Ricker, P. M., Roe, N., Rollins, R. P., Romer, A. K., Roodman, A., Rosenfeld, R., Ross, A. J., Rozo, E., Rykoff, E. S., Sako, M., Salvador, A. I., Samuroff, S., Sánchez, C., Sanchez, E., Santiago, B., Scarpine, V., Schindler, R., Scolnic, D., Secco, L. F., Serrano, S., Sevilla-Noarbe, I., Sheldon, E., Smith, R. C., Smith, M., Smith, J., Soares-Santos, M., Sobreira, F., Suchyta, E., Tarle, G., Thomas, D., Troxel, M. A., Tucker, D. L., Tucker, B. E., Uddin, S. A., Varga, T. N., Vielzeuf, P., Vikram, V., Vivas, A. K., Walker, A. R., Wang, M., Wechsler, R. H., Weller, J., Wester, W., Wolf, R. C., Yanny, B., Yuan, F., Zenteno, A., Zhang, B., Zhang, Y., and Zuntz, J. (2018). Dark Energy Survey year 1 results: Cosmological constraints from galaxy clustering and weak lensing. *Phys. Rev. D*, 98(4):043526.

Abdalla, E., Abellán, G. F., Aboubrahim, A., Agnello, A., Akarsu, Ö., Akrami, Y., Alestas, G., Aloni, D., Amendola, L., Anchordoqui, L. A., Anderson, R. I., Arendse, N., Asgari, M., Ballardini, M., Barger, V., Basilakos, S., Batista, R. C., Battistelli, E. S., Battye, R., Benetti, M., Benisty, D., Berlin, A., de Bernardis, P., Berti, E., Bidenko, B., Birrer, S., Blakeslee, J. P., Boddy, K. K., Bom, C. R., Bonilla, A., Borghi, N., Bouchet, F. R., Braglia, M., Buchert, T., Buckley-Geer, E., Calabrese, E., Caldwell, R. R., Camarena, D., Capozziello, S., Casertano, S., Chen, G. C. F., Chluba, J., Chen, A., Chen, H.-Y., Chudaykin, A., Cicoli, M., Copi, C. J., Courbin, F., Cyr-Racine, F.-Y., Czerny, B., Dainotti, M., D'Amico, G., Davis, A.-C., de Cruz Pérez, J., de Haro, J., Delabrouille, J., Denton, P. B., Dhawan, S., Dienes, K. R., Di Valentino, E., Du, P., Eckert, D., Escamilla-Rivera,

C., Ferté, A., Finelli, F., Fosalba, P., Freedman, W. L., Frusciante, N., Gaztañaga, E., Giarè, W., Giusarma, E., Gómez-Valent, A., Handley, W., Harrison, I., Hart, L., Hazra, D. K., Heavens, A., Heinesen, A., Hildebrandt, H., Hill, J. C., Hogg, N. B., Holz, D. E., Hooper, D. C., Hosseininejad, N., Huterer, D., Ishak, M., Ivanov, M. M., Jaffe, A. H., Jang, I. S., Jedamzik, K., Jimenez, R., Joseph, M., Joudaki, S., Kamionkowski, M., Karwal, T., Kazantzidis, L., Keeley, R. E., Klasen, M., Komatsu, E., Koopmans, L. V. E., Kumar, S., Lamagna, L., Lazkoz, R., Lee, C.-C., Lesgourgues, J., Levi Said, J., Lewis, T. R., L'Huillier, B., Lucca, M., Maartens, R., Macri, L. M., Marfatia, D., Marra, V., Martins, C. J. A. P., Masi, S., Matarrese, S., Mazumdar, A., Melchiorri, A., Mena, O., Mersini-Houghton, L., Mertens, J., Milaković, D., Minami, Y., Miranda, V., Moreno-Pulido, C., Moresco, M., Mota, D. F., Mottola, E., Mozzon, S., Muir, J., Mukherjee, A., Mukherjee, S., Naselsky, P., Nath, P., Nesseris, S., Niedermann, F., Notari, A., Nunes, R. C., Ó Colgáin, E., Owens, K. A., Özülker, E., Pace, F., Paliathanasis, A., Palmese, A., Pan, S., Paoletti, D., Perez Bergliaffa, S. E., Perivolaropoulos, L., Pesce, D. W., Pettorino, V., Philcox, O. H. E., Pogosian, L., Poulin, V., Poulot, G., Raveri, M., Reid, M. J., Renzi, F., Riess, A. G., Sabla, V. I., Salucci, P., Salzano, V., Saridakis, E. N., Sathyaprakash, B. S., Schmaltz, M., Schöneberg, N., Scolnic, D., Sen, A. A., Sehgal, N., Shafieloo, A., Sheikh-Jabbari, M. M., Silk, J., Silvestri, A., Skara, F., Sloth, M. S., Soares-Santos, M., Solà Peracaula, J., Songsheng, Y.-Y., Soriano, J. F., Staicova, D., Starkman, G. D., Szapudi, I., Teixeira, E. M., Thomas, B., Treu, T., Trott, E., van de Bruck, C., Vazquez, J. A., Verde, L., Visinelli, L., Wang, D., Wang, J.-M., Wang, S.-J., Watkins, R., Watson, S., Webb, J. K., Weiner, N., Weltman, A., Witte, S. J., Wojtak, R., and Yadav, A. K. (2022). Cosmology intertwined: A review of the particle physics, astrophysics, and cosmology associated with the cosmological tensions and anomalies. *Journal of High Energy Astrophysics*, 34:49–211.

Adame, A. G., Aguilar, J., Ahlen, S., Alam, S., Alexander, D. M., Alvarez, M., Alves, O., Anand, A., Andrade, U., Armengaud, E., Avila, S., Aviles, A., Awan, H., Bahr-Kalus, B., Bailey, S., Baltay, C., Bault, A., Behera, J., BenZvi, S., Bera, A., Beutler, F., Bianchi, D., Blake, C., Blum, R., Brieden, S., Brodzeller, A., Brooks, D., Buckley-Geer, E., Burtin, E., Calderon, R., Canning, R., Carnero Rosell, A., Cereskaite, R., Cervantes-Cota, J. L., Chabanier, S., Chaussidon, E., Chaves-Montero, J., Chen, S., Chen, X., Claybaugh, T., Cole, S., Cuceu, A., Davis, T. M., Dawson, K., de la Macorra, A., de Mattia, A., Deiosso, N., Dey, A., Dey, B., Ding, Z., Doel, P., Edelstein, J., Eftekharzadeh, S., Eisenstein, D. J., Elliott, A., Fagrelius, P., Fanning, K., Ferraro, S., Ereza, J., Findlay, N., Flaugher, B., Font-Ribera, A., Forero-Sánchez, D., Forero-Romero, J. E., Frenk, C. S., Garcia-Quintero, C., Gaztañaga, E., Gil-Marín, H., Gontcho a Gontcho, S., Gonzalez-Morales, A. X., Gonzalez-Perez, V., Gordon, C., Green, D., Gruen, D., Gsponer, R., Gutierrez, G., Guy, J., Hadzhiyska, B., Hahn, C., Hanif, M. M. S., Herrera-Alcantar, H. K., Honscheid, K., Howlett, C., Huterer, D., Iršič, V., Ishak, M., Juneau, S., Karaçaylı, N. G., Kehoe, R., Kent, S., Kirkby, D., Kremin, A., Krolewski, A., Lai, Y., Lan, T. W., Landriau, M., Lang, D., Lasker, J., Le Goff, J. M., Le Guillou, L., Leauthaud, A., Levi, M. E., Li, T. S., Linder, E., Lodha, K., Magneville, C., Manera, M., Margala, D., Martini, P., Maus, M., McDonald, P., Medina-Varela, L., Meisner, A., Mena-Fernández, J., Miquel, R., Moon, J., Moore, S., Moustakas, J., Mueller, E., Muñoz-Gutiérrez, A., Myers, A. D., Nadathur, S., Napolitano, L., Neveux, R., Newman, J. A., Nguyen, N. M., Nie, J., Niz, G., Noriega, H. E., Padmanabhan, N., Paillas, E., Palanque-Delabrouille, N., Pan, J., Penmetsa, S., Percival, W. J., Pieri, M. M., Pinon, M., Poppett, C., Porredon, A., Prada, F., Pérez-Fernández, A., Pérez-Ràfols, I., Rabinowitz, D., Raichoor, A., Ramírez-Pérez, C., Ramirez-Solano, S., Rashkovetskyi, M., Ravoux, C., Rezaie, M., Rich, J., Rocher, A., Rockosi, C., Roe, N. A.,

Rosado-Marin, A., Ross, A. J., Rossi, G., Ruggeri, R., Ruhlmann-Kleider, V., Samushia, L., Sanchez, E., Saulder, C., Schlafly, E. F., Schlegel, D., Schubnell, M., Seo, H., Shafieloo, A., Sharples, R., Silber, J., Slosar, A., Smith, A., Sprayberry, D., Tan, T., Tarlé, G., Taylor, P., Trusov, S., Ureña-López, L. A., Vaisakh, R., Valcin, D., Valdes, F., Vargas-Magaña, M., Verde, L., Walther, M., Wang, B., Wang, M. S., Weaver, B. A., Weaverdyck, N., Wechsler, R. H., Weinberg, D. H., White, M., Yu, J., Yu, Y., Yuan, S., Yèche, C., Zaborowski, E. A., Zarrouk, P., Zhang, H., Zhao, C., Zhao, R., Zhou, R., and Zhuang, T. (2025). DESI 2024 VI: cosmological constraints from the measurements of baryon acoustic oscillations. *JCAP*, 2025(2):021.

Adelberger, E. G., Gundlach, J. H., Heckel, B. R., Hoedl, S., and Schlamminger, S. (2009). Torsion balance experiments: A low-energy frontier of particle physics. *Prog. Part. Nucl. Phys.*, 62:102–134.

Adelberger, E. G., Heckel, B. R., and Nelson, A. E. (2003). Tests of the Gravitational Inverse-Square Law. *Annual Review of Nuclear and Particle Science*, 53:77–121.

Akerib, D. S., Alsum, S., Araújo, H. M., Bai, X., Bailey, A. J., Balajthy, J., Beltrame, P., Bernard, E. P., Bernstein, A., Biesiadzinski, T. P., Boulton, E. M., Bramante, R., Brás, P., Byram, D., Cahn, S. B., Carmona-Benitez, M. C., Chan, C., Chiller, A. A., Chiller, C., Currie, A., Cutter, J. E., Davison, T. J. R., Dobi, A., Dobson, J. E. Y., Druszkiewicz, E., Edwards, B. N., Faham, C. H., Fiorucci, S., Gaitskell, R. J., Gehman, V. M., Ghag, C., Gibson, K. R., Gilchriese, M. G. D., Hall, C. R., Hanhardt, M., Haselschwardt, S. J., Hertel, S. A., Hogan, D. P., Horn, M., Huang, D. Q., Ignarra, C. M., Ihm, M., Jacobsen, R. G., Ji, W., Kamdin, K., Kazkaz, K., Khaitan, D., Knoche, R., Larsen, N. A., Lee, C., Lenardo, B. G., Lesko, K. T., Lindote, A., Lopes, M. I., Manalaysay, A., Mannino, R. L., Marzioni, M. F., McKinsey, D. N., Mei, D. M., Mock, J., Moongweluwan, M., Morad, J. A., Murphy, A. S. J.,

Nehrkorn, C., Nelson, H. N., Neves, F., O'Sullivan, K., Oliver-Mallory, K. C., Palladino, K. J., Pease, E. K., Phelps, P., Reichhart, L., Rhyne, C., Shaw, S., Shutt, T. A., Silva, C., Solmaz, M., Solovov, V. N., Sorensen, P., Stephenson, S., Sumner, T. J., Szydagis, M., Taylor, D. J., Taylor, W. C., Tennyson, B. P., Terman, P. A., Tiedt, D. R., To, W. H., Tripathi, M., Tvrznikova, L., Uvarov, S., Verbus, J. R., Webb, R. C., White, J. T., Whitis, T. J., Witherell, M. S., Wolfs, F. L. H., Xu, J., Yazdani, K., Young, S. K., Zhang, C., and LUX Collaboration (2017). Results from a Search for Dark Matter in the Complete LUX Exposure. *Phys. Rev. Lett.*, 118(2):021303.

Almasi, A., Brax, P., Iannuzzi, D., and Sedmik, R. I. P. (2015). Force sensor for chameleon and Casimir force experiments with parallel-plate configuration. *Phys. Rev. D*, 91(10):102002.

Almeida, A., Anderson, S. F., Argudo-Fernández, M., Badenes, C., Barger, K., Barrera-Ballesteros, J. K., Bender, C. F., Benitez, E., Besser, F., Bird, J. C., Bizyaev, D., Blanton, M. R., Bochanski, J., Bovy, J., Brandt, W. N., Brownstein, J. R., Buchner, J., Bulbul, E., Burchett, J. N., Cano Díaz, M., Carlberg, J. K., Casey, A. R., Chandra, V., Cherinka, B., Chiappini, C., Coker, A. A., Comparat, J., Conroy, C., Contardo, G., Cortes, A., Covey, K., Crane, J. D., Cunha, K., Dabbieri, C., Davidson, J. W., Davis, M. C., de Andrade Queiroz, A. B., De Lee, N., Méndez Delgado, J. E., Demasi, S., Di Mille, F., Donor, J., Dow, P., Dwelly, T., Eracleous, M., Eriksen, J., Fan, X., Farr, E., Frederick, S., Fries, L., Frinchaboy, P., Gänsicke, B. T., Ge, J., González Ávila, C., Grabowski, K., Grier, C., Guiglion, G., Gupta, P., Hall, P., Hawkins, K., Hayes, C. R., Hermes, J. J., Hernández-García, L., Hogg, D. W., Holtzman, J. A., Ibarra-Medel, H. J., Ji, A., Jofre, P., Johnson, J. A., Jones, A. M., Kinemuchi, K., Kluge, M., Koekemoer, A., Kollmeier, J. A., Kounkel, M., Krishnarao, D., Krumpe, M., Lacerna, I., Lago, P. J. A., Laporte, C., Liu, C., Liu, A., Liu, X., Lopes, A. R., Macktoobian, M., Majewski, S. R., Malanushenko, V.,

Maoz, D., Masseron, T., Masters, K. L., Matijevic, G., McBride, A., Medan, I., Merloni, A., Morrison, S., Myers, N., Mészáros, S., Negrete, C. A., Nidever, D. L., Nitschelm, C., Oravetz, D., Oravetz, A., Pan, K., Peng, Y., Pinsonneault, M. H., Pogge, R., Qiu, D., Ramirez, S. V., Rix, H.-W., Fernández Rosso, D., Runnoe, J., Salvato, M., Sanchez, S. F., Santana, F. A., Saydjari, A., Sayres, C., Schlaufman, K. C., Schneider, D. P., Schwope, A., Serna, J., Shen, Y., Sobeck, J., Song, Y.-Y., Souto, D., Spoo, T., Stassun, K. G., Steinmetz, M., Straumit, I., Stringfellow, G., Sánchez-Gallego, J., Taghizadeh-Popp, M., Tayar, J., Thakar, A., Tissera, P. B., Tkachenko, A., Hernandez Toledo, H., Trakhtenbrot, B., Fernández-Trincado, J. G., Troup, N., Trump, J. R., Tuttle, S., Ulloa, N., Vazquez-Mata, J. A., Vera Alfaro, P., Villanova, S., Wachter, S., Weijmans, A.-M., Wheeler, A., Wilson, J., Wojno, L., Wolf, J., Xue, X.-X., Ybarra, J. E., Zari, E., and Zasowski, G. (2023). The Eighteenth Data Release of the Sloan Digital Sky Surveys: Targeting and First Spectra from SDSS-V. *Astrophys. J. Suppl.*, 267(2):44.

Amendola, L., Kunz, M., and Sapone, D. (2008). Measuring the dark side (with weak lensing). *JCAP*, 04:013.

Aprile, E., Aalbers, J., Agostini, F., Alfonsi, M., Althueser, L., Amaro, F. D., Anthony, M., Arneodo, F., Baudis, L., Bauermeister, B., Benabderrahmane, M. L., Berger, T., Breur, P. A., Brown, A., Brown, A., Brown, E., Bruenner, S., Bruno, G., Budnik, R., Capelli, C., Cardoso, J. M. R., Cichon, D., Coderre, D., Colijn, A. P., Conrad, J., Cussonneau, J. P., Decowski, M. P., de Perio, P., di Gangi, P., di Giovanni, A., Diglio, S., Elykov, A., Eurin, G., Fei, J., Ferella, A. D., Fieguth, A., Fulgione, W., Gallo Rosso, A., Galloway, M., Gao, F., Garbini, M., Geis, C., Grandi, L., Greene, Z., Qiu, H., Hasterok, C., Hogenbirk, E., Howlett, J., Itay, R., Joerg, F., Kaminsky, B., Kazama, S., Kish, A., Koltman, G., Landsman, H., Lang, R. F., Levinson, L., Lin, Q., Lindemann, S., Lindner, M., Lombardi, F., Lopes, J. A. M.,

Mahlstedt, J., Manfredini, A., Marrodán Undagoitia, T., Masbou, J., Masson, D., Messina, M., Micheneau, K., Miller, K., Molinario, A., Morâ, K., Murra, M., Naganoma, J., Ni, K., Oberlack, U., Pelssers, B., Piastra, F., Pienaar, J., Pizzella, V., Plante, G., Podviianiuk, R., Priel, N., Ramírez García, D., Rauch, L., Reichard, S., Reuter, C., Riedel, B., Rizzo, A., Rocchetti, A., Rupp, N., Dos Santos, J. M. F., Sartorelli, G., Scheibelhut, M., Schindler, S., Schreiner, J., Schulte, D., Schumann, M., Scotto Lavina, L., Selvi, M., Shagin, P., Shockley, E., Silva, M., Simgen, H., Thers, D., Toschi, F., Trinchero, G., Tunnell, C., Upole, N., Vargas, M., Wack, O., Wang, H., Wang, Z., Wei, Y., Weinheimer, C., Wittweg, C., Wulf, J., Ye, J., Zhang, Y., Zhu, T., and Xenon Collaboration (2018). Dark Matter Search Results from a One Ton-Year Exposure of XENON1T. *Phys. Rev. Lett.*, 121(11):111302.

Armendariz-Picon, C., Mukhanov, V., and Steinhardt, P. J. (2001). Essentials of k-essence. *Phys. Rev. D*, 63(10):103510.

Arnold, C., Leo, M., and Li, B. (2019). Realistic simulations of galaxy formation in f(R) modified gravity. *Nature Astronomy*, 3:945–954.

Arnold, C., Li, B., Giblin, B., Harnois-Déraps, J., and Cai, Y.-C. (2022). FORGE: the f(R)-gravity cosmic emulator project - I. Introduction and matter power spectrum emulator. *Mon. Not. Royal Astron. Soc.*, 515(3):4161–4175.

Arnold, C., Springel, V., and Puchwein, E. (2016). Zoomed cosmological simulations of Milky Way-sized haloes in f(R) gravity. *Mon. Not. Royal Astron. Soc.*, 462(2):1530–1541.

Babcock, H. W. (1939). The rotation of the Andromeda Nebula. *Lick Observatory Bulletin*, 498:41–51.

Babichev, E. and Deffayet, C. (2013). An introduction to the Vainshtein mechanism. *Class. Quant. Grav.*, 30:184001.

Bai, J. and Xia, J.-Q. (2024). FREmu: Power Spectrum Emulator for f(R) Gravity. *Astrophys. J.*, 971(1):11.

Baker, T., Barreira, A., Desmond, H., Ferreira, P., Jain, B., Koyama, K., Li, B., Lombriser, L., Nicola, A., Sakstein, J., and Schmidt, F. (2019). The Novel Probes Project – Tests of Gravity on Astrophysical Scales. *arXiv e-prints*, page arXiv:1908.03430.

Baker, T., Bellini, E., Ferreira, P. G., Lagos, M., Noller, J., and Sawicki, I. (2017). Strong Constraints on Cosmological Gravity from GW170817 and GRB 170817A. *Phys. Rev. Lett.*, 119(25):251301.

Baldry, I. K., Driver, S. P., Loveday, J., Taylor, E. N., Kelvin, L. S., Liske, J., Norberg, P., Robotham, A. S. G., Brough, S., Hopkins, A. M., Bamford, S. P., Peacock, J. A., Bland-Hawthorn, J., Conselice, C. J., Croom, S. M., Jones, D. H., Parkinson, H. R., Popescu, C. C., Prescott, M., Sharp, R. G., and Tuffs, R. J. (2012). Galaxy And Mass Assembly (GAMA): the galaxy stellar mass function at z ¡ 0.06. *Mon. Not. Royal Astron. Soc.*, 421(1):621–634.

Baldry, I. K., Glazebrook, K., and Driver, S. P. (2008). On the galaxy stellar mass function, the mass-metallicity relation and the implied baryonic mass function. *Mon. Not. Royal Astron. Soc.*, 388(3):945–959.

Bartelmann, M. and Schneider, P. (2001a). Weak gravitational lensing. *Phys. Rep.*, 340(4-5):291–472.

Bartelmann, M. and Schneider, P. (2001b). Weak gravitational lensing. *Phys. Rep.*, 340(4-5):291–472.

Bartlett, D. J., Desmond, H., and Ferreira, P. G. (2021). Calibrating galaxy formation effects in galactic tests of fundamental physics. *Phys. Rev. D*, 103(12):123502.

Baumann, D. (2022). *Cosmology*. Cambridge University Press.

Bekenstein, J. D. (2004). Relativistic gravitation theory for the MOND paradigm. *Phys. Rev. D*, 70:083509. [Erratum: Phys.Rev.D 71, 069901 (2005)].

Benisty, D., Mifsud, J., Levi Said, J., and Staicova, D. (2023). Strengthening extended gravity constraints with combined systems: f(R) bounds from cosmology and the galactic center. *Phys. Dark Univ.*, 42:101344.

Bennett, C. L., Larson, D., Weiland, J. L., Jarosik, N., Hinshaw, G., Odegard, N., Smith, K. M., Hill, R. S., Gold, B., Halpern, M., Komatsu, E., Nolta, M. R., Page, L., Spergel, D. N., Wollack, E., Dunkley, J., Kogut, A., Limon, M., Meyer, S. S., Tucker, G. S., and Wright, E. L. (2013). Nine-year Wilkinson Microwave Anisotropy Probe (WMAP) Observations: Final Maps and Results. *Astrophys. J. Suppl.*, 208(2):20.

Benson, A. J., Bower, R. G., Frenk, C. S., Lacey, C. G., Baugh, C. M., and Cole, S. (2003). What Shapes the Luminosity Function of Galaxies? *Astrophys. J.*, 599(1):38–49.

Bershady, M. A., Verheijen, M. A. W., Westfall, K. B., Andersen, D. R., Swaters, R. A., and Martinsson, T. (2010). The DiskMass Survey. II. Error Budget. *Astrophys. J.*, 716(1):234–268.

Bertoldi, A., Bongs, K., Bouyer, P., Buchmueller, O., Canuel, B., Caramete, L.-I., Chiofalo, M. L., Coleman, J., De Roeck, A., Ellis, J., Graham, P. W., Haehnelt, M. G., Hees, A., Hogan, J., von Klitzing, W., Krutzik, M., Lewicki, M., McCabe, C., Peters, A., Rasel, E., Roura, A., Sabulsky, D., Schiller, S., Schubert, C., Signorini, C., Sorrentino, F., Singh, Y., Tino, G. M., Vaskonen, V., and Zhan, M.-S. (2021). AEDGE: Atomic experiment for dark matter and gravity exploration in space. *Experimental Astronomy*, 51(3):1417–1426.

Bertotti, B., Iess, L., and Tortora, P. (2003). A test of general relativity

using radio links with the Cassini spacecraft. *Nature*, 425(6956):374–376.

Bertschinger, E. (2006). On the Growth of Perturbations as a Test of Dark Energy. *Astrophys. J.*, 648:797–806.

Beutler, F., Blake, C., Colless, M., Jones, D. H., Staveley-Smith, L., Campbell, L., Parker, Q., Saunders, W., and Watson, F. (2011). The 6dF Galaxy Survey: baryon acoustic oscillations and the local Hubble constant. *Mon. Not. Royal Astron. Soc.*, 416(4):3017–3032.

Bilicki, M., Dvornik, A., Hoekstra, H., Wright, A. H., Chisari, N. E., Vakili, M., Asgari, M., Giblin, B., Heymans, C., Hildebrandt, H., Holwerda, B. W., Hopkins, A., Johnston, H., Kannawadi, A., Kuijken, K., Nakoneczny, S. J., Shan, H. Y., Sonnenfeld, A., and Valentijn, E. (2021). Bright galaxy sample in the Kilo-Degree Survey Data Release 4. Selection, photometric redshifts, and physical properties. *Astron. & Astrophys.*, 653:A82.

Binney, J. and Tremaine, S. (2008). *Galactic Dynamics: Second Edition*. Princeton University Press, Princeton, NJ USA.

Bissantz, N. and Gerhard, O. (2002). Spiral arms, bar shape and bulge microlensing in the Milky Way. *Mon. Not. Royal Astron. Soc.*, 330(3):591–608.

Blanton, M. R., Dalcanton, J., Eisenstein, D., Loveday, J., Strauss, M. A., SubbaRao, M., Weinberg, D. H., Anderson, Jr., J. E., Annis, J., Bahcall, N. A., Bernardi, M., Brinkmann, J., Brunner, R. J., Burles, S., Carey, L., Castander, F. J., Connolly, A. J., Csabai, I., Doi, M., Finkbeiner, D., Friedman, S., Frieman, J. A., Fukugita, M., Gunn, J. E., Hennessy, G. S., Hindsley, R. B., Hogg, D. W., Ichikawa, T., Ivezić, Ž., Kent, S., Knapp, G. R., Lamb, D. Q., Leger, R. F., Long, D. C., Lupton, R. H., McKay, T. A., Meiksin, A., Merelli, A., Munn, J. A., Narayanan, V., Newcomb, M., Nichol, R. C., Okamura, S.,

Owen, R., Pier, J. R., Pope, A., Postman, M., Quinn, T., Rockosi, C. M., Schlegel, D. J., Schneider, D. P., Shimasaku, K., Siegmund, W. A., Smee, S., Snir, Y., Stoughton, C., Stubbs, C., Szalay, A. S., Szokoly, G. P., Thakar, A. R., Tremonti, C., Tucker, D. L., Uomoto, A., Vanden Berk, D., Vogeley, M. S., Waddell, P., Yanny, B., Yasuda, N., and York, D. G. (2001). The Luminosity Function of Galaxies in SDSS Commissioning Data. *Astron. J.*, 121(5):2358–2380.

Blumenthal, G. R., Faber, S. M., Primack, J. R., and Rees, M. J. (1984). Formation of galaxies and large-scale structure with cold dark matter. *Nature*, 311:517–525.

Bose, S., Li, B., Barreira, A., He, J.-h., Hellwing, W. A., Koyama, K., Llinares, C., and Zhao, G.-B. (2017). Speeding up N-body simulations of modified gravity: chameleon screening models. *JCAP*, 2017(2):050.

Bosma, A. (1981). 21-cm line studies of spiral galaxies. I. Observations of the galaxies NGC 5033, 3198, 5055, 2841, and 7331. *Astron. J.*, 86:1791–1824.

Boughn, S. and Crittenden, R. (2004). A correlation between the cosmic microwave background and large-scale structure in the Universe. *Nature*, 427(6969):45–47.

Brax, P. and Burrage, C. (2011). Atomic precision tests and light scalar couplings. *Phys. Rev. D*, 83(3):035020.

Brax, P., Davis, A.-C., and Elder, B. (2022). $(\mathrm{g}\text{-}2)_\mu$ and screened modified gravity. *Phys. Rev. D*, 106(4):044040.

Brax, P. and Pignol, G. (2011). Strongly Coupled Chameleons and the Neutronic Quantum Bouncer. *Phys. Rev. Lett.*, 107(11):111301.

Brax, P., Pignol, G., and Roulier, D. (2013). Probing Strongly Coupled Chameleons with Slow Neutrons. *Phys. Rev. D*, 88:083004.

Brax, P., van de Bruck, C., Davis, A.-C., Mota, D. F., and Shaw, D. (2007). Detecting chameleons through casimir force measurements. *Phys. Rev. D*, 76:124034.

Brax, P., van de Bruck, C., Davis, A.-C., and Shaw, D. J. (2008). f(R) gravity and chameleon theories. *Phys. Rev. D*, 78(10):104021.

Brax, P., van de Bruck, C., Davis, A. C., Shaw, D. J., and Iannuzzi, D. (2010). Tuning the Mass of Chameleon Fields in Casimir Force Experiments. *Phys. Rev. Lett.*, 104(24):241101.

Briddon, C., Burrage, C., Moss, A., and Tamosiunas, A. (2021). SELCIE: a tool for investigating the chameleon field of arbitrary sources. *JCAP*, 2021(12):043.

Brouwer, M. M., Oman, K. A., Valentijn, E. A., Bilicki, M., Heymans, C., Hoekstra, H., Napolitano, N. R., Roy, N., Tortora, C., Wright, A. H., Asgari, M., van den Busch, J. L., Dvornik, A., Erben, T., Giblin, B., Graham, A. W., Hildebrandt, H., Hopkins, A. M., Kannawadi, A., Kuijken, K., Liske, J., Shan, H., Tröster, T., Verlinde, E., and Visser, M. (2021). The weak lensing radial acceleration relation: Constraining modified gravity and cold dark matter theories with KiDS-1000. *Astron. & Astrophys.*, 650:A113.

Brouwer, M. M., Visser, M. R., Dvornik, A., Hoekstra, H., Kuijken, K., Valentijn, E. A., Bilicki, M., Blake, C., Brough, S., Buddelmeijer, H., Erben, T., Heymans, C., Hildebrandt, H., Holwerda, B. W., Hopkins, A. M., Klaes, D., Liske, J., Loveday, J., McFarland, J., Nakajima, R., Sifón, C., and Taylor, E. N. (2017). First test of Verlinde's theory of emergent gravity using weak gravitational lensing measurements. *Mon. Not. Royal Astron. Soc.*, 466(3):2547–2559.

Bryan, G. L. and Norman, M. L. (1998). Statistical Properties of X-Ray Clusters: Analytic and Numerical Comparisons. *Astrophys. J.*, 495(1):80–99.

Bundy, K., Bershady, M. A., Law, D. R., Yan, R., Drory, N., MacDonald, N., Wake, D. A., Cherinka, B., Sánchez-Gallego, J. R., Weijmans, A.-M., Thomas, D., Tremonti, C., Masters, K., Coccato, L., Diamond-Stanic, A. M., Aragón-Salamanca, A., Avila-Reese, V., Badenes, C., Falcón-Barroso, J., Belfiore, F., Bizyaev, D., Blanc, G. A., Bland-Hawthorn, J., Blanton, M. R., Brownstein, J. R., Byler, N., Cappellari, M., Conroy, C., Dutton, A. A., Emsellem, E., Etherington, J., Frinchaboy, P. M., Fu, H., Gunn, J. E., Harding, P., Johnston, E. J., Kauffmann, G., Kinemuchi, K., Klaene, M. A., Knapen, J. H., Leauthaud, A., Li, C., Lin, L., Maiolino, R., Malanushenko, V., Malanushenko, E., Mao, S., Maraston, C., McDermid, R. M., Merrifield, M. R., Nichol, R. C., Oravetz, D., Pan, K., Parejko, J. K., Sanchez, S. F., Schlegel, D., Simmons, A., Steele, O., Steinmetz, M., Thanjavur, K., Thompson, B. A., Tinker, J. L., van den Bosch, R. C. E., Westfall, K. B., Wilkinson, D., Wright, S., Xiao, T., and Zhang, K. (2015). Overview of the SDSS-IV MaNGA Survey: Mapping nearby Galaxies at Apache Point Observatory. *Astrophys. J.*, 798(1):7.

Burkert, A. (1995). The Structure of Dark Matter Halos in Dwarf Galaxies. *Astrophys. J. Lett.*, 447:L25–L28.

Burrage, C. and Copeland, E. J. (2016). Using atom interferometry to detect dark energy. *Contemporary Physics*, 57(2):164–176.

Burrage, C., Copeland, E. J., and Hinds, E. A. (2015a). Probing dark energy with atom interferometry. *JCAP*, 2015(3):042–042.

Burrage, C., Copeland, E. J., Käding, C., and Millington, P. (2019). Symmetron scalar fields: Modified gravity, dark matter, or both? *Phys. Rev. D*, 99(4):043539.

Burrage, C., Copeland, E. J., and Millington, P. (2017). Radial acceleration relation from symmetron fifth forces. *Phys. Rev. D*, 95(6):064050.

Burrage, C., Copeland, E. J., and Stevenson, J. A. (2015b). Ellipticity weakens chameleon screening. *Phys. Rev. D*, 91(6):065030.

Burrage, C., Kuribayashi-Coleman, A., Stevenson, J., and Thrussell, B. (2016). Constraining symmetron fields with atom interferometry. *JCAP*, 2016(12):041.

Burrage, C., March, B., and Naik, A. P. (2024). Accurate computation of the screening of scalar fifth forces in galaxies. *JCAP*, 2024(4):004.

Burrage, C. and Sakstein, J. (2016). A compendium of chameleon constraints. *JCAP*, 2016(11):045.

Burrage, C. and Sakstein, J. (2018). Tests of chameleon gravity. *Living Reviews in Relativity*, 21(1):1.

Butler, J., Martin, G., Hatch, N. A., Pearce, F., Brough, S., and Dubois, Y. (2025). Intracluster light is a biased tracer of the dark matter distribution in clusters. *Mon. Not. Royal Astron. Soc.*, 539(3):2279–2291.

Cabré, A., Vikram, V., Zhao, G.-B., Jain, B., and Koyama, K. (2012). Astrophysical tests of gravity: a screening map of the nearby universe. *JCAP*, 2012(7):034.

Caldwell, R., Cooray, A., and Melchiorri, A. (2007). Constraints on a New Post-General Relativity Cosmological Parameter. *Phys. Rev. D*, 76:023507.

Caldwell, R. R. (2002). A phantom menace? Cosmological consequences of a dark energy component with super-negative equation of state. *Physics Letters B*, 545(1-2):23–29.

Caldwell, R. R., Dave, R., and Steinhardt, P. J. (1998). Cosmological Imprint of an Energy Component with General Equation of State. *Phys. Rev. Lett.*, 80(8):1582–1585.

Callingham, T. M., Cautun, M., Deason, A. J., Frenk, C. S., Wang, W., Gómez, F. A., Grand, R. J. J., Marinacci, F., and Pakmor, R. (2019). The mass of the Milky Way from satellite dynamics. *Mon. Not. Royal Astron. Soc.*, 484(4):5453–5467.

Capozziello, S. and Fang, L. Z. (2002). Curvature Quintessence. *International Journal of Modern Physics D*, 11(4):483–491.

Cardone, V. F., Piedipalumbo, E., and Tortora, C. (2005). Spherical galaxy models with power-law logarithmic slope. *Mon. Not. Royal Astron. Soc.*, 358(4):1325–1336.

Carroll, S. M. (2001). The Cosmological Constant. *Living Reviews in Relativity*, 4(1):1.

Carroll, S. M. (2004). *Spacetime and geometry. An introduction to general relativity.* Addison Wesley.

Carroll, S. M., De Felice, A., Duvvuri, V., Easson, D. A., Trodden, M., and Turner, M. S. (2005). The Cosmology of generalized modified gravity models. *Phys. Rev. D*, 71:063513.

Carroll, S. M., Duvvuri, V., Trodden, M., and Turner, M. S. (2004). Is cosmic speed-up due to new gravitational physics? *Phys. Rev. D*, 70(4):043528.

Carroll, S. M., Duvvuri, V., Trodden, M., and Turner, M. S. (2004). Is Cosmic Speed-Up Due to New Gravitational Physics? *Phys. Rev. D*, 70:043528.

Cataldi, P., Pedrosa, S., Padilla, N., Landau, S., Arnold, C., and Li, B. (2022). Fingerprints of modified gravity on galaxies in voids. *Mon. Not. Royal Astron. Soc.*, 515(4):5358–5374.

Chibisov, G. V. (1976). Astrophysical upper limits on the photon rest mass. *Sov. Phys. Usp.*, 19:624–626.

Christiansen, Ø., Hassani, F., and Mota, D. F. (2024). Asimulation: Domain formation and impact on observables in resolved cosmological simulations of the (a)symmetron. *Astron. & Astrophys.*, 689:A6.

Code, A. D., Houck, T. E., McNall, J. F., Bless, R. C., and Lillie, C. F. (1970). Ultraviolet Photometry from the Orbiting Astronomical Observatory. I. Instrumentation and Operation. *Astrophys. J.*, 161:377.

Cole, S., Percival, W. J., Peacock, J. A., Norberg, P., Baugh, C. M., Frenk, C. S., Baldry, I., Bland-Hawthorn, J., Bridges, T., Cannon, R., Colless, M., Collins, C., Couch, W., Cross, N. J. G., Dalton, G., Eke, V. R., De Propris, R., Driver, S. P., Efstathiou, G., Ellis, R. S., Glazebrook, K., Jackson, C., Jenkins, A., Lahav, O., Lewis, I., Lumsden, S., Maddox, S., Madgwick, D., Peterson, B. A., Sutherland, W., and Taylor, K. (2005). The 2dF Galaxy Redshift Survey: power-spectrum analysis of the final data set and cosmological implications. *Mon. Not. Royal Astron. Soc.*, 362(2):505–534.

Colless, M., Dalton, G., Maddox, S., Sutherland, W., Norberg, P., Cole, S., Bland-Hawthorn, J., Bridges, T., Cannon, R., Collins, C., Couch, W., Cross, N., Deeley, K., De Propris, R., Driver, S. P., Efstathiou, G., Ellis, R. S., Frenk, C. S., Glazebrook, K., Jackson, C., Lahav, O., Lewis, I., Lumsden, S., Madgwick, D., Peacock, J. A., Peterson, B. A., Price, I., Seaborne, M., and Taylor, K. (2001). The 2dF Galaxy Redshift Survey: spectra and redshifts. *Mon. Not. Royal Astron. Soc.*, 328(4):1039–1063.

Condon, J. J. (1992). Radio emission from normal galaxies. *Ann. Rev. Astron. Astrophys.*, 30:575–611.

Copeland, E. J., Sami, M., and Tsujikawa, S. (2006). Dynamics of Dark Energy. *International Journal of Modern Physics D*, 15(11):1753–1935.

Cronenberg, G., Filter, H., Thalhammer, M., Jenke, T., Abele, H., and Gel-

tenbort, P. (2015). A Gravity of Earth Measurement with a qBOUNCE Experiment. *arXiv e-prints*, page arXiv:1512.09134.

Cui, X., Abdukerim, A., Chen, W., Chen, X., Chen, Y., Dong, B., Fang, D., Fu, C., Giboni, K., Giuliani, F., Gu, L., Gu, Y., Guo, X., Guo, Z., Han, K., He, C., Huang, D., He, S., Huang, X., Huang, Z., Ji, X., Ju, Y., Li, S., Li, Y., Lin, H., Liu, H., Liu, J., Ma, Y., Mao, Y., Ni, K., Ning, J., Ren, X., Shi, F., Tan, A., Wang, C., Wang, H., Wang, M., Wang, Q., Wang, S., Wang, X., Wang, X., Wu, Q., Wu, S., Xiao, M., Xie, P., Yan, B., Yang, Y., Yue, J., Zhang, D., Zhang, H., Zhang, T., Zhang, T., Zhao, L., Zhou, J., Zhou, N., Zhou, X., and PandaX-II Collaboration (2017). Dark Matter Results from 54-Ton-Day Exposure of PandaX-II Experiment. *Phys. Rev. Lett.*, 119(18):181302.

Damour, T. and Polyakov, A. M. (1994). The String dilaton and a least coupling principle. *Nucl. Phys. B*, 423:532–558.

Davies, C. T., Harnois-Déraps, J., Li, B., Giblin, B., Hernández-Aguayo, C., and Paillas, E. (2024). Constraining modified gravity with weak-lensing peaks. *Mon. Not. Roy. Astron. Soc.*, 533(3):3546–3569.

Davis, A.-C., Li, B., Mota, D. F., and Winther, H. A. (2012a). Structure Formation in the Symmetron Model. *Astrophys. J.*, 748(1):61.

Davis, A.-C., Lim, E. A., Sakstein, J., and Shaw, D. J. (2012b). Modified gravity makes galaxies brighter. *Phys. Rev. D*, 85(12):123006.

de Blok, W. J. G., McGaugh, S. S., Bosma, A., and Rubin, V. C. (2001a). Mass Density Profiles of Low Surface Brightness Galaxies. *Astrophys. J. Lett.*, 552(1):L23–L26.

de Blok, W. J. G., McGaugh, S. S., and Rubin, V. C. (2001b). High-Resolution Rotation Curves of Low Surface Brightness Galaxies. II. Mass Models. *Astron. J.*, 122(5):2396–2427.

de Jong, R. S. (1996). Near-infrared and optical broadband surface photometry of 86 face-on disk dominated galaxies. III. The statistics of the disk and bulge parameters. *Astron. & Astrophys.*, 313:45–64.

Deason, A. J., Fattahi, A., Frenk, C. S., Grand, R. J. J., Oman, K. A., Garrison-Kimmel, S., Simpson, C. M., and Navarro, J. F. (2020). The edge of the Galaxy. *Mon. Not. Royal Astron. Soc.*, 496(3):3929–3942.

Decca, R. S., López, D., Fischbach, E., Klimchitskaya, G. L., Krause, D. E., and Mostepanenko, V. M. (2007). Tests of new physics from precise measurements of the Casimir pressure between two gold-coated plates. *Phys. Rev. D*, 75(7):077101.

Decca, R. S., López, D., and Osquiguil, E. (2010). New Results for the Casimir Interaction:. Sample Characterization and Low Temperature Measurements. In Milton, K. A. and Bordag, M., editors, *Quantum Field Theory Under the Influence of External Conditions (QFEXT09)*, pages 88–97.

Deffayet, C. (2001). Cosmology on a brane in Minkowski bulk. *Phys. Lett. B*, 502:199–208.

Dehnen, H., Frommert, H., and Ghaboussi, F. (1992). Higgs field and a new scalar - tensor theory of gravity. *Int. J. Theor. Phys.*, 31:109–114.

Dehnen, W. and McLaughlin, D. E. (2005). Dynamical insight into dark matter haloes. *Mon. Not. Royal Astron. Soc.*, 363(4):1057–1068.

DESI Collaboration, Adame, A. G., Aguilar, J., Ahlen, S., Alam, S., Aldering, G., Alexander, D. M., Alfarsy, R., Allende Prieto, C., Alvarez, M., Alves, O., Anand, A., Andrade-Oliveira, F., Armengaud, E., Asorey, J., Avila, S., Aviles, A., Bailey, S., Balaguera-Antolínez, A., Ballester, O., Baltay, C., Bault, A., Bautista, J., Behera, J., Beltran, S. F., BenZvi, S., Beraldo e Silva, L., Bermejo-Climent, J. R., Berti, A., Besuner, R., Beutler, F., Bianchi, D., Blake, C., Blum, R., Bolton, A. S., Brieden, S., Brodzeller, A., Brooks, D., Brown, Z., Buckley-Geer, E.,

Burtin, E., Cabayol-Garcia, L., Cai, Z., Canning, R., Cardiel-Sas, L., Carnero Rosell, A., Castander, F. J., Cervantes-Cota, J. L., Chabanier, S., Chaussidon, E., Chaves-Montero, J., Chen, S., Chuang, C., Claybaugh, T., Cole, S., Cooper, A. P., Cuceu, A., Davis, T. M., Dawson, K., de Belsunce, R., de la Cruz, R., de la Macorra, A., de Mattia, A., Demina, R., Demirbozan, U., DeRose, J., Dey, A., Dey, B., Dhungana, G., Ding, J., Ding, Z., Doel, P., Doshi, R., Douglass, K., Edge, A., Eftekharzadeh, S., Eisenstein, D. J., Elliott, A., Escoffier, S., Fagrelius, P., Fan, X., Fanning, K., Fawcett, V. A., Ferraro, S., Ereza, J., Flaugher, B., Font-Ribera, A., Forero-Sánchez, D., Forero-Romero, J. E., Frenk, C. S., Gänsicke, B. T., García, L. Á., García-Bellido, J., Garcia-Quintero, C., Garrison, L. H., Gil-Marín, H., Golden-Marx, J., Gontcho, S. G. A., Gonzalez-Morales, A. X., Gonzalez-Perez, V., Gordon, C., Graur, O., Green, D., Gruen, D., Guy, J., Hadzhiyska, B., Hahn, C., Han, J. J., Hanif, M. M. S., Herrera-Alcantar, H. K., Honscheid, K., Hou, J., Howlett, C., Huterer, D., Iršič, V., Ishak, M., Jacques, A., Jana, A., Jiang, L., Jimenez, J., Jing, Y. P., Joudaki, S., Jullo, E., Juneau, S., Kizhuprakkat, N., Karaçaylı, N. G., Karim, T., Kehoe, R., Kent, S., Khederlarian, A., Kim, S., Kirkby, D., Kisner, T., Kitaura, F., Kneib, J., Koposov, S. E., Kovács, A., Kremin, A., Krolewski, A., L'Huillier, B., Lambert, A., Lamman, C., Lan, T. W., Landriau, M., Lang, D., Lange, J. U., Lasker, J., Le Guillou, L., Leauthaud, A., Levi, M. E., Li, T. S., Linder, E., Lyons, A., Magneville, C., Manera, M., Manser, C. J., Margala, D., Martini, P., McDonald, P., Medina, G. E., Medina-Varela, L., Meisner, A., Mena-Fernández, J., Meneses-Rizo, J., Mezcua, M., Miquel, R., Montero-Camacho, P., Moon, J., Moore, S., Moustakas, J., Mueller, E., Mundet, J., Muñoz-Gutiérrez, A., Myers, A. D., Nadathur, S., Napolitano, L., Neveux, R., Newman, J. A., Nie, J., Nikutta, R., Niz, G., Norberg, P., Noriega, H. E., Paillas, E., Palanque-Delabrouille, N., Palmese, A., Zhiwei, P., Parkinson, D., Penmetsa, S., Percival, W. J., Pérez-Fernández,

A., Pérez-Ràfols, I., Pieri, M., Poppett, C., Porredon, A., Pothier, S., Prada, F., Pucha, R., Raichoor, A., Ramírez-Pérez, C., Ramirez-Solano, S., Rashkovetskyi, M., Ravoux, C., Rocher, A., Rockosi, C., Ross, A. J., Rossi, G., Ruggeri, R., Ruhlmann-Kleider, V., Sabiu, C. G., Said, K., Saintonge, A., Samushia, L., Sanchez, E., Saulder, C., Schaan, E., Schlafly, E. F., Schlegel, D., Scholte, D., Schubnell, M., Seo, H., Shafieloo, A., Sharples, R., Sheu, W., Silber, J., Sinigaglia, F., Siudek, M., Slepian, Z., Smith, A., Sprayberry, D., Stephey, L., Suárez-Pérez, J., Sun, Z., Tan, T., Tarlé, G., Tojeiro, R., Ureña-López, L. A., Vaisakh, R., Valcin, D., Valdes, F., Valluri, M., Vargas-Magaña, M., Variu, A., Verde, L., Walther, M., Wang, B., Wang, M. S., Weaver, B. A., Weaverdyck, N., Wechsler, R. H., White, M., Xie, Y., Yang, J., Yèche, C., Yu, J., Yuan, S., Zhang, H., Zhang, Z., Zhao, C., Zheng, Z., Zhou, R., Zhou, Z., Zou, H., Zou, S., and Zu, Y. (2023). The Early Data Release of the Dark Energy Spectroscopic Instrument. *arXiv e-prints*, page arXiv:2306.06308.

Desmond, H. and Ferreira, P. G. (2020). Galaxy morphology rules out astrophysically relevant Hu-Sawicki f(R) gravity. *Phys. Rev. D*, 102(10):104060.

Desmond, H., Ferreira, P. G., Lavaux, G., and Jasche, J. (2018a). Fifth force constraints from galaxy warps. *Phys. Rev. D*, 98(8):083010.

Desmond, H., Ferreira, P. G., Lavaux, G., and Jasche, J. (2018b). Fifth force constraints from the separation of galaxy mass components. *Phys. Rev. D*, 98(6):064015.

Desmond, H., Ferreira, P. G., Lavaux, G., and Jasche, J. (2018c). Reconstructing the gravitational field of the local Universe. *Mon. Not. Royal Astron. Soc.*, 474(3):3152–3161.

Desmond, H., Ferreira, P. G., Lavaux, G., and Jasche, J. (2019a). The fifth force in the local cosmic web. *Mon. Not. Royal Astron. Soc.*, 483(1):L64–L68.

Desmond, H., Jain, B., and Sakstein, J. (2019b). Local resolution of the Hubble tension: The impact of screened fifth forces on the cosmic distance ladder. *Phys. Rev. D*, 100(4):043537.

Desmond, H. and Sakstein, J. (2020). Screened fifth forces lower the TRGB-calibrated Hubble constant too. *Phys. Rev. D*, 102(2):023007.

Di Valentino, E., Melchiorri, A., Mena, O., and Vagnozzi, S. (2020). Interacting dark energy in the early 2020s: A promising solution to the H_0 and cosmic shear tensions. *Physics of the Dark Universe*, 30:100666.

Di Valentino, E., Mena, O., Pan, S., Visinelli, L., Yang, W., Melchiorri, A., Mota, D. F., Riess, A. G., and Silk, J. (2021). In the realm of the Hubble tension-a review of solutions. *Classical and Quantum Gravity*, 38(15):153001.

Diemer, B. and Kravtsov, A. V. (2014). Dependence of the Outer Density Profiles of Halos on Their Mass Accretion Rate. *Astrophys. J.*, 789(1):1.

Diemer, B., Mansfield, P., Kravtsov, A. V., and More, S. (2017). The Splashback Radius of Halos from Particle Dynamics. II. Dependence on Mass, Accretion Rate, Redshift, and Cosmology. *Astrophys. J.*, 843(2):140.

Donato, F., Gentile, G., Salucci, P., Frigerio Martins, C., Wilkinson, M. I., Gilmore, G., Grebel, E. K., Koch, A., and Wyse, R. (2009). A constant dark matter halo surface density in galaxies. *Mon. Not. Royal Astron. Soc.*, 397(3):1169–1176.

Dressler, A. (1980). Galaxy morphology in rich clusters: implications for the formation and evolution of galaxies. *Astrophys. J.*, 236:351–365.

Dutton, A. A. and Macciò, A. V. (2014). Cold dark matter haloes in the Planck era: evolution of structural parameters for Einasto and NFW profiles. *Mon. Not. Royal Astron. Soc.*, 441(4):3359–3374.

Dvali, G., Gabadadze, G., and Porrati, M. (2000). 4D gravity on a brane in 5D Minkowski space. *Physics Letters B*, 485(1-3):208–214.

Dyson, F. W., Eddington, A. S., and Davidson, C. (1920). A Determination of the Deflection of Light by the Sun's Gravitational Field, from Observations Made at the Total Eclipse of May 29, 1919. *Philosophical Transactions of the Royal Society of London Series A*, 220:291–333.

Eckart, A. (2018). The early great debate: A comment on ibn al-haytham's work on the location of the milky way with respect to the earth. *Arabic Sciences and Philosophy*, 28(1):1–30.

Eckart, A. and Idriz, M. (2023). Knowledge of the milky way in the arabic cultural region between the 8th and 15th centuries. *Australian Journal of Islamic Studies*, 8(3):1–15.

Eddington, A. S. (1919). The total eclipse of 1919 May 29 and the influence of gravitation on light. *The Observatory*, 42:119–122.

Eddington, A. S. (1923). *The mathematical theory of relativity*. Cambridge University Press.

Einasto, J. (1965). On the Construction of a Composite Model for the Galaxy and on the Determination of the System of Galactic Parameters. *Trudy Astrofizicheskogo Instituta Alma-Ata*, 5:87–100.

Einstein, A. (1905). Zur Elektrodynamik bewegter Körper. *Annalen der Physik*, 322(10):891–921.

Einstein, A. (1916). Die Grundlage der allgemeinen Relativitätstheorie. *Annalen der Physik*, 354(7):769–822.

Einstein, A. (1917). Kosmologische Betrachtungen zur allgemeinen Relativitätstheorie. *Sitzungsberichte der Königlich Preussischen Akademie der Wissenschaften*, pages 142–152.

Eisenstein, D. J., Zehavi, I., Hogg, D. W., Scoccimarro, R., Blanton, M. R., Nichol, R. C., Scranton, R., Seo, H.-J., Tegmark, M., Zheng, Z., Anderson, S. F., Annis, J., Bahcall, N., Brinkmann, J., Burles, S., Castander, F. J., Connolly, A., Csabai, I., Doi, M., Fukugita, M., Frieman, J. A., Glazebrook, K., Gunn, J. E., Hendry, J. S., Hennessy, G., Ivezić, Z., Kent, S., Knapp, G. R., Lin, H., Loh, Y.-S., Lupton, R. H., Margon, B., McKay, T. A., Meiksin, A., Munn, J. A., Pope, A., Richmond, M. W., Schlegel, D., Schneider, D. P., Shimasaku, K., Stoughton, C., Strauss, M. A., SubbaRao, M., Szalay, A. S., Szapudi, I., Tucker, D. L., Yanny, B., and York, D. G. (2005). Detection of the Baryon Acoustic Peak in the Large-Scale Correlation Function of SDSS Luminous Red Galaxies. *Astrophys. J.*, 633(2):560–574.

Elder, B., Khoury, J., Haslinger, P., Jaffe, M., Müller, H., and Hamilton, P. (2016). Chameleon dark energy and atom interferometry. *Phys. Rev. D*, 94(4):044051.

Euclid Collaboration, Mellier, Y., Abdurro'uf, Acevedo Barroso, J. A., Achúcarro, A., Adamek, J., Adam, R., Addison, G. E., Aghanim, N., Aguena, M., Ajani, V., Akrami, Y., Al-Bahlawan, A., Alavi, A., Albuquerque, I. S., Alestas, G., Alguero, G., Allaoui, A., Allen, S. W., Allevato, V., Alonso-Tetilla, A. V., Altieri, B., Alvarez-Candal, A., Alvi, S., Amara, A., Amendola, L., Amiaux, J., Andika, I. T., Andreon, S., Andrews, A., Angora, G., Angulo, R. E., Annibali, F., Anselmi, A., Anselmi, S., Arcari, S., Archidiacono, M., Aricò, G., Arnaud, M., Arnouts, S., Asgari, M., Asorey, J., Atayde, L., Atek, H., Atrio-Barandela, F., Aubert, M., Aubourg, E., Auphan, T., Auricchio, N., Aussel, B., Aussel, H., Avelino, P. P., Avgoustidis, A., Avila, S., Awan, S., Azzollini, R., Baccigalupi, C., Bachelet, E., Bacon, D., Baes, M., Bagley, M. B., Bahr-Kalus, B., Balaguera-Antolinez, A., Balbinot, E., Balcells, M., Baldi, M., Baldry, I., Balestra, A., Ballardini, M., Ballester, O., Balogh, M., Bañados, E., Barbier, R., Bardelli, S., Baron, M., Barreiro, T., Barrena, R., Barriere, J. C., Barros, B. J.,

Barthelemy, A., Bartolo, N., Basset, A., Battaglia, P., Battisti, A. J., Baugh, C. M., Baumont, L., Bazzanini, L., Beaulieu, J. P., Beckmann, V., Belikov, A. N., Bel, J., Bellagamba, F., Bella, M., Bellini, E., Benabed, K., Bender, R., Benevento, G., Bennett, C. L., Benson, K., Bergamini, P., Bermejo-Climent, J. R., Bernardeau, F., Bertacca, D., Berthe, M., Berthier, J., Bethermin, M., Beutler, F., Bevillon, C., Bhargava, S., Bhatawdekar, R., Bianchi, D., Bisigello, L., Biviano, A., Blake, R. P., Blanchard, A., Blazek, J., Blot, L., Bosco, A., Bodendorf, C., Boenke, T., Böhringer, H., Boldrini, P., Bolzonella, M., Bonchi, A., Bonici, M., Bonino, D., Bonino, L., Bonvin, C., Bon, W., Booth, J. T., Borgani, S., Borlaff, A. S., Borsato, E., Bose, B., Botticella, M. T., Boucaud, A., Bouche, F., Boucher, J. S., Boutigny, D., Bouvard, T., Bouwens, R., Bouy, H., Bowler, R. A. A., Bozza, V., Bozzo, E., Branchini, E., Brando, G., Brau-Nogue, S., Brekke, P., Bremer, M. N., Brescia, M., Breton, M. A., Brinchmann, J., Brinckmann, T., Brockley-Blatt, C., Brodwin, M., Brouard, L., Brown, M. L., Bruton, S., Bucko, J., Buddelmeijer, H., Buenadicha, G., Buitrago, F., Burger, P., Burigana, C., Busillo, V., Busonero, D., Cabanac, R., Cabayol-Garcia, L., Cagliari, M. S., Caillat, A., Caillat, L., Calabrese, M., Calabro, A., Calderone, G., Calura, F., Camacho Quevedo, B., Camera, S., Campos, L., Cañas-Herrera, G., Candini, G. P., Cantiello, M., Capobianco, V., Cappellaro, E., Cappelluti, N., Cappi, A., Caputi, K. I., Cara, C., Carbone, C., Cardone, V. F., Carella, E., Carlberg, R. G., Carle, M., Carminati, L., Caro, F., Carrasco, J. M., Carretero, J., Carrilho, P., Carron Duque, J., and Carry, B. (2025). Euclid: I. Overview of the Euclid mission. *Astron. & Astrophys.*, 697:A1.

Everitt, C. W. F., Debra, D. B., Parkinson, B. W., Turneaure, J. P., Conklin, J. W., Heifetz, M. I., Keiser, G. M., Silbergleit, A. S., Holmes, T., Kolodziejczak, J., Al-Meshari, M., Mester, J. C., Muhlfelder, B., Solomonik, V. G., Stahl, K., Worden, Jr., P. W., Bencze, W., Buchman, S., Clarke, B., Al-Jadaan, A., Al-Jibreen, H., Li, J., Lipa, J. A.,

Lockhart, J. M., Al-Suwaidan, B., Taber, M., and Wang, S. (2011). Gravity Probe B: Final Results of a Space Experiment to Test General Relativity. *Phys. Rev. Lett.*, 106(22):221101.

Faber, S. M., Dressler, A., Davies, R. L., Burstein, D., Lynden Bell, D., Terlevich, R., and Wegner, G. (1987). Global Scaling Relations for Elliptical Galaxies and Implications for Formation. In Faber, S. M., editor, *Nearly Normal Galaxies. From the Planck Time to the Present*, page 175.

Faulkner, T., Tegmark, M., Bunn, E. F., and Mao, Y. (2007). Constraining f(R) gravity as a scalar-tensor theory. *Phys. Rev. D*, 76(6):063505.

Fienga, A., Laskar, J., Kuchynka, P., Le Poncin-Lafitte, C., Manche, H., and Gastineau, M. (2010). Gravity tests with INPOP planetary ephemerides. In Klioner, S. A., Seidelmann, P. K., and Soffel, M. H., editors, *Relativity in Fundamental Astronomy: Dynamics, Reference Frames, and Data Analysis*, volume 261 of *IAU Symposium*, pages 159–169.

Fienga, A., Laskar, J., Kuchynka, P., Manche, H., Desvignes, G., Gastineau, M., Cognard, I., and Theureau, G. (2011). The INPOP10a planetary ephemeris and its applications in fundamental physics. *Celestial Mechanics and Dynamical Astronomy*, 111(3):363–385.

Fienga, A. and Minazzoli, O. (2024). Testing theories of gravity with planetary ephemerides. *Living Reviews in Relativity*, 27(1):1.

Foreman-Mackey, D., Hogg, D. W., Lang, D., and Goodman, J. (2013). emcee: The MCMC Hammer. *Publ. Astron. Soc. Pac.*, 125(925):306.

Freeman, K. C. (1970). On the Disks of Spiral and S0 Galaxies. *Astrophys. J.*, 160:811.

Friedmann, A. (1922). Über die Krümmung des Raumes. *Zeitschrift fur Physik*, 10:377–386.

Friedmann, A. (1924). Über die Möglichkeit einer Welt mit konstanter negativer Krümmung des Raumes. *Zeitschrift fur Physik*, 21(1):326–332.

Galilei, G. (1989). *Sidereus Nuncius, or The Sidereal Messenger*. University of Chicago Press, Chicago. Original work published 1610.

Gao, L., Navarro, J. F., Cole, S., Frenk, C. S., White, S. D. M., Springel, V., Jenkins, A., and Neto, A. F. (2008). The redshift dependence of the structure of massive Λ cold dark matter haloes. *Mon. Not. Royal Astron. Soc.*, 387(2):536–544.

Gardner, J. P., Mather, J. C., Clampin, M., Doyon, R., Greenhouse, M. A., Hammel, H. B., Hutchings, J. B., Jakobsen, P., Lilly, S. J., Long, K. S., Lunine, J. I., McCaughrean, M. J., Mountain, M., Nella, J., Rieke, G. H., Rieke, M. J., Rix, H.-W., Smith, E. P., Sonneborn, G., Stiavelli, M., Stockman, H. S., Windhorst, R. A., and Wright, G. S. (2006). The James Webb Space Telescope. *Space Science Reviews*, 123(4):485–606.

Geraci, A. A., Papp, S. B., and Kitching, J. (2010). Short-Range Force Detection Using Optically Cooled Levitated Microspheres. *Phys. Rev. Lett.*, 105(10):101101.

Gessner, E. (1992). A new scalar tensor theory for gravity and the flat rotation curves of spiral galaxies. *Astrophys. Space Sci.*, 196(1):29–43.

Giacconi, R., Gursky, H., Paolini, F. R., and Rossi, B. B. (1962). Evidence for x Rays From Sources Outside the Solar System. *Phys. Rev. Lett.*, 9(11):439–443.

Giannantonio, T., Scranton, R., Crittenden, R. G., Nichol, R. C., Boughn, S. P., Myers, A. D., and Richards, G. T. (2008). Combined analysis of the integrated Sachs-Wolfe effect and cosmological implications. *Phys. Rev. D*, 77(12):123520.

Gilmore, G. and Reid, N. (1983). New light on faint stars - III. Galactic structure towards the South Pole and the Galactic thick disc. *Mon. Not. Royal Astron. Soc.*, 202:1025–1047.

Giocoli, C., Palmucci, L., Lesci, G. F., Moscardini, L., Despali, G., Marulli, F., Maturi, M., Radovich, M., Sereno, M., Bardelli, S., Castignani, G., Covone, G., Ingoglia, L., Romanello, M., Roncarelli, M., and Puddu, E. (2024). AMICO galaxy clusters in KiDS-DR3: Measuring the splashback radius from weak gravitational lensing. *Astron. & Astrophys.*, 687:A79.

Goldhaber, A. S. and Nieto, M. M. (2010). Photon and Graviton Mass Limits. *Rev. Mod. Phys.*, 82:939–979.

Gondhalekar, Y., Bose, S., Li, B., and Cuesta-Lazaro, C. (2025). Emulation of f(R) modified gravity from ΛCDM using conditional GANs. *Mon. Not. Royal Astron. Soc.*, 536(2):1408–1427.

Hamilton, P., Jaffe, M., Haslinger, P., Simmons, Q., Müller, H., and Khoury, J. (2015). Atom-interferometry constraints on dark energy. *Science*, 349(6250):849–851.

Harnois-Déraps, J., Hernandez-Aguayo, C., Cuesta-Lazaro, C., Arnold, C., Li, B., Davies, C. T., and Cai, Y.-C. (2023). mglens: Modified gravity weak lensing simulations for emulation-based cosmological inference. *Mon. Not. Roy. Astron. Soc.*, 525(4):6336–6358.

Harnois-Déraps, J., Munshi, D., Valageas, P., van Waerbeke, L., Brax, P., Coles, P., and Rizzo, L. (2015). Testing Modified Gravity with Cosmic Shear. *Mon. Not. Roy. Astron. Soc.*, 454(3):2722–2735.

Herschel, W. (1785). XII. On the construction of the heavens. *Philosophical Transactions of the Royal Society*, 75:213–266.

Hinterbichler, K. and Khoury, J. (2010). Screening Long-Range Forces through Local Symmetry Restoration. *Phys. Rev. Lett.*, 104(23):231301.

Hinterbichler, K., Khoury, J., Levy, A., and Matas, A. (2011). Symmetron Cosmology. *Phys. Rev. D*, 84:103521.

Hoekstra, H. and Jain, B. (2008). Weak Gravitational Lensing and Its Cosmological Applications. *Annual Review of Nuclear and Particle Science*, 58(1):99–123.

Hofmann, F. and Müller, J. (2018). Relativistic tests with lunar laser ranging. *Classical and Quantum Gravity*, 35(3):035015.

Högås, M. and Mörtsell, E. (2023). Impact of symmetron screening on the Hubble tension: New constraints using cosmic distance ladder data. *Phys. Rev. D*, 108(2):024007.

Hoyland, S., Winther, H. A., Saadeh, D., Koyama, K., and Izard, A. (2025). Fast generation of weak lensing maps in modified gravity with COLA. *Mon. Not. Royal Astron. Soc.*, 541(4):3167–3183.

Hu, W., Barkana, R., and Gruzinov, A. (2000). Fuzzy Cold Dark Matter: The Wave Properties of Ultralight Particles. *Phys. Rev. Lett.*, 85(6):1158–1161.

Hu, W. and Jain, B. (2004). Joint galaxy - lensing observables and the dark energy. *Phys. Rev. D*, 70:043009.

Hu, W. and Sawicki, I. (2007). Models of f(R) cosmic acceleration that evade solar system tests. *Phys. Rev. D*, 76(6):064004.

Hubble, E. (1929). A Relation between Distance and Radial Velocity among Extra-Galactic Nebulae. *Proceedings of the National Academy of Science*, 15(3):168–173.

Hubble, E. P. (1925). Cepheids in Spiral Nebulae. *Popular Astronomy*, 33:252–255.

Hubble, E. P. (1926). Extragalactic nebulae. *Astrophys. J.*, 64:321–369.

Hui, L., Nicolis, A., and Stubbs, C. W. (2009). Equivalence principle implications of modified gravity models. *Phys. Rev. D*, 80(10):104002.

Iorio, L. (2007a). Astronomical Constraints on Some Long-Range Models of Modified Gravity. *Advances in High Energy Physics*, 2007:90731.

Iorio, L. (2007b). Can the Pioneer Anomaly be of Gravitational Origin? A Phenomenological Answer. *Foundations of Physics*, 37(6):897–918.

Iorio, L. (2009). The Recently Determined Anomalous Perihelion Precession of Saturn. *Astron. J.*, 137(3):3615–3618.

Ishak, M. (2019). Testing General Relativity in Cosmology. *Living Rev. Rel.*, 22(1):1.

Ivanov, A. N., Höllwieser, R., Jenke, T., Wellenzohn, M., and Abele, H. (2013). Influence of the chameleon field potential on transition frequencies of gravitationally bound quantum states of ultracold neutrons. *Phys. Rev. D*, 87(10):105013.

Jaeckel, J. and Roy, S. (2010). Spectroscopy as a test of Coulomb's law: A probe of the hidden sector. *Phys. Rev. D*, 82(12):125020.

Jaffe, M., Haslinger, P., Xu, V., Hamilton, P., Upadhye, A., Elder, B., Khoury, J., and Müller, H. (2017). Testing sub-gravitational forces on atoms from a miniature in-vacuum source mass. *Nature Physics*, 13(10):938–942.

Jain, B. and Taylor, A. (2003). Cross-correlation tomography: measuring dark energy evolution with weak lensing. *Phys. Rev. Lett.*, 91:141302.

Jain, B. and VanderPlas, J. (2011). Tests of modified gravity with dwarf galaxies. *JCAP*, 2011(10):032.

Jain, B., Vikram, V., and Sakstein, J. (2013). Astrophysical Tests of Modified Gravity: Constraints from Distance Indicators in the Nearby Universe. *Astrophys. J.*, 779(1):39.

Jain, B. and Zhang, P. (2008). Observational Tests of Modified Gravity. *Phys. Rev. D*, 78:063503.

Jakobsen, P., Ferruit, P., Alves de Oliveira, C., Arribas, S., Bagnasco, G., Barho, R., Beck, T. L., Birkmann, S., Böker, T., Bunker, A. J., Charlot, S., de Jong, P., de Marchi, G., Ehrenwinkler, R., Falcolini, M., Fels, R., Franx, M., Franz, D., Funke, M., Giardino, G., Gnata, X., Holota, W., Honnen, K., Jensen, P. L., Jentsch, M., Johnson, T., Jollet, D., Karl, H., Kling, G., Köhler, J., Kolm, M. G., Kumari, N., Lander, M. E., Lemke, R., López-Caniego, M., Lützgendorf, N., Maiolino, R., Manjavacas, E., Marston, A., Maschmann, M., Maurer, R., Messerschmidt, B., Moseley, S. H., Mosner, P., Mott, D. B., Muzerolle, J., Pirzkal, N., Pittet, J. F., Plitzke, A., Posselt, W., Rapp, B., Rauscher, B. J., Rawle, T., Rix, H. W., Rödel, A., Rumler, P., Sabbi, E., Salvignol, J. C., Schmid, T., Sirianni, M., Smith, C., Strada, P., te Plate, M., Valenti, J., Wettemann, T., Wiehe, T., Wiesmayer, M., Willott, C. J., Wright, R., Zeidler, P., and Zincke, C. (2022). The Near-Infrared Spectrograph (NIRSpec) on the James Webb Space Telescope. I. Overview of the instrument and its capabilities. *Astron. & Astrophys.*, 661:A80.

Joyce, A., Jain, B., Khoury, J., and Trodden, M. (2015). Beyond the Cosmological Standard Model. *Phys. Rept.*, 568:1–98.

Jurić, M., Ivezić, Ž., Brooks, A., Lupton, R. H., Schlegel, D., Finkbeiner, D., Padmanabhan, N., Bond, N., Sesar, B., Rockosi, C. M., Knapp, G. R., Gunn, J. E., Sumi, T., Schneider, D. P., Barentine, J. C., Brewington, H. J., Brinkmann, J., Fukugita, M., Harvanek, M., Kleinman, S. J., Krzesinski, J., Long, D., Neilsen, Jr., E. H., Nitta, A., Snedden, S. A., and York, D. G. (2008). The Milky Way Tomography with SDSS. I. Stellar Number Density Distribution. *Astrophys. J.*, 673(2):864–914.

Käding, C. (2023). Lensing with Generalized Symmetrons. *Astronomy*, 2(2):128–140.

Kapner, D. J., Cook, T. S., Adelberger, E. G., Gundlach, J. H., Heckel, B. R., Hoyle, C. D., and Swanson, H. E. (2007). Tests of the Gravitational Inverse-Square Law below the Dark-Energy Length Scale. *Phys. Rev. Lett.*, 98(2):021101.

Kapteyn, J. C. (1922). First Attempt at a Theory of the Arrangement and Motion of the Sidereal System. *Astrophys. J.*, 55:302.

Keller, B. W. and Wadsley, J. W. (2017). ΛCDM is Consistent with SPARC Radial Acceleration Relation. *Astrophys. J. Lett.*, 835(1):L17.

Kelvin, L. S., Driver, S. P., Robotham, A. S. G., Taylor, E. N., Graham, A. W., Alpaslan, M., Baldry, I., Bamford, S. P., Bauer, A. E., Bland-Hawthorn, J., Brown, M. J. I., Colless, M., Conselice, C. J., Holwerda, B. W., Hopkins, A. M., Lara-López, M. A., Liske, J., López-Sánchez, Á. R., Loveday, J., Norberg, P., Phillipps, S., Popescu, C. C., Prescott, M., Sansom, A. E., and Tuffs, R. J. (2014). Galaxy And Mass Assembly (GAMA): stellar mass functions by Hubble type. *Mon. Not. Royal Astron. Soc.*, 444(2):1647–1659.

Kesden, M. and Kamionkowski, M. (2006a). Galilean Equivalence for Galactic Dark Matter. *Phys. Rev. Lett.*, 97(13):131303.

Kesden, M. and Kamionkowski, M. (2006b). Tidal tails test the equivalence principle in the dark-matter sector. *Phys. Rev. D*, 74(8):083007.

Keselman, J. A., Nusser, A., and Peebles, P. J. E. (2009). Galaxy satellites and the weak equivalence principle. *Phys. Rev. D*, 80(6):063517.

Khoury, J. and Weltman, A. (2004a). Chameleon cosmology. *Phys. Rev. D*, 69(4):044026.

Khoury, J. and Weltman, A. (2004b). Chameleon Fields: Awaiting Surprises for Tests of Gravity in Space. *Phys. Rev. Lett.*, 93(17):171104.

Kilbinger, M. (2015). Cosmology with cosmic shear observations: a review. *Reports on Progress in Physics*, 78(8):086901.

King, I. (1962). The structure of star clusters. I. an empirical density law. *Astron. J.*, 67:471.

Klypin, A., Kravtsov, A. V., Valenzuela, O., and Prada, F. (1999). Where Are the Missing Galactic Satellites? *Astrophys. J.*, 522(1):82–92.

Knox, L., Song, Y.-S., and Tyson, J. A. (2006). Distance-redshift and growth-redshift relations as two windows on acceleration and gravitation: Dark energy or new gravity? *Phys. Rev. D*, 74:023512.

Kormendy, J. and Ho, L. C. (2013). Coevolution (Or Not) of Supermassive Black Holes and Host Galaxies. *Ann. Rev. Astron. Astrophys.*, 51(1):511–653.

Koyama, K. (2016). Cosmological tests of modified gravity. *Reports on Progress in Physics*, 79(4):046902.

Koyama, K. (2016). Cosmological Tests of Modified Gravity. *Rept. Prog. Phys.*, 79(4):046902.

Koyama, K., Maartens, R., and Song, Y.-S. (2009). Velocities as a probe of dark sector interactions. *JCAP*, 10:017.

Kregel, M., van der Kruit, P. C., and de Grijs, R. (2002). Flattening and truncation of stellar discs in edge-on spiral galaxies. *Mon. Not. Royal Astron. Soc.*, 334(3):646–668.

Kumar, S., Nunes, R. C., and Yadav, S. K. (2019). Dark sector interaction: a remedy of the tensions between CMB and LSS data. *European Physical Journal C*, 79(7):576.

Lambrecht, A., Nesvizhevsky, V. V., Onofrio, R., and Reynaud, S. (2005). Development of a high-sensitivity torsional balance for the study of the Casimir force in the 1 10 micrometre range. *Classical and Quantum Gravity*, 22(24):5397–5406.

Lambrecht, A. and Reynaud, S. (2011). Casimir and short-range gravity tests. *arXiv e-prints*, page arXiv:1106.3848.

Lamoreaux, S. K. and Buttler, W. T. (2005). Thermal noise limitations to force measurements with torsion pendulums: Applications to the measurement of the casimir force and its thermal correction. *Phys. Rev. E*, 71:036109.

Landim, R. G., Desmond, H., Koyama, K., and Penny, S. (2024). Testing screened modified gravity with SDSS-IV-MaNGA. *arXiv e-prints*, page arXiv:2407.08825.

Laureijs, R., Amiaux, J., Arduini, S., Augueres, J. L., Brinchmann, J., Cole, R., Cropper, M., Dabin, C., Duvet, L., Ealet, A., Garilli, B., Gondoin, P., Guzzo, L., Hoar, J., Hoekstra, H., Holmes, R., Kitching, T., Maciaszek, T., Mellier, Y., Pasian, F., Percival, W., Rhodes, J., Saavedra Criado, G., Sauvage, M., Scaramella, R., Valenziano, L., Warren, S., Bender, R., Castander, F., Cimatti, A., Le Fèvre, O., Kurki-Suonio, H., Levi, M., Lilje, P., Meylan, G., Nichol, R., Pedersen, K., Popa, V., Rebolo Lopez, R., Rix, H. W., Rottgering, H., Zeilinger, W., Grupp, F., Hudelot, P., Massey, R., Meneghetti, M., Miller, L., Paltani, S., Paulin-Henriksson, S., Pires, S., Saxton, C., Schrabback, T., Seidel, G., Walsh, J., Aghanim, N., Amendola, L., Bartlett, J., Baccigalupi, C., Beaulieu, J. P., Benabed, K., Cuby, J. G., Elbaz, D., Fosalba, P., Gavazzi, G., Helmi, A., Hook, I., Irwin, M., Kneib, J. P., Kunz, M., Mannucci, F., Moscardini, L., Tao, C., Teyssier, R., Weller, J., Zamorani, G., Zapatero Osorio, M. R., Boulade, O., Foumond, J. J., Di Giorgio, A., Guttridge, P., James, A., Kemp, M., Martignac, J., Spencer, A., Walton, D., Blümchen, T., Bonoli, C., Bortoletto, F., Cerna, C., Corcione, L., Fabron, C., Jahnke, K., Ligori, S., Madrid, F., Martin, L., Morgante, G., Pamplona, T., Prieto, E., Riva, M., Toledo, R., Trifoglio, M., Zerbi, F., Abdalla, F., Douspis, M., Grenet, C., Borgani, S., Bouwens, R., Courbin, F., Delouis, J. M., Dubath, P., Fontana, A., Frailis, M., Grazian, A., Koppenhöfer, J., Mansutti, O., Melchior, M., Mignoli, M., Mohr, J., Neissner, C., Noddle, K., Poncet, M., Scodeggio, M., Serrano, S., Shane,

N., Starck, J. L., Surace, C., Taylor, A., Verdoes-Kleijn, G., Vuerli, C., Williams, O. R., Zacchei, A., Altieri, B., Escudero Sanz, I., Kohley, R., Oosterbroek, T., Astier, P., Bacon, D., Bardelli, S., Baugh, C., Bellagamba, F., Benoist, C., Bianchi, D., Biviano, A., Branchini, E., Carbone, C., Cardone, V., Clements, D., Colombi, S., Conselice, C., Cresci, G., Deacon, N., Dunlop, J., Fedeli, C., Fontanot, F., Franzetti, P., Giocoli, C., Garcia-Bellido, J., Gow, J., Heavens, A., Hewett, P., Heymans, C., Holland, A., Huang, Z., Ilbert, O., Joachimi, B., Jennins, E., Kerins, E., Kiessling, A., Kirk, D., Kotak, R., Krause, O., Lahav, O., van Leeuwen, F., Lesgourgues, J., Lombardi, M., Magliocchetti, M., Maguire, K., Majerotto, E., Maoli, R., Marulli, F., Maurogordato, S., McCracken, H., McLure, R., Melchiorri, A., Merson, A., Moresco, M., Nonino, M., Norberg, P., Peacock, J., Pello, R., Penny, M., Pettorino, V., Di Porto, C., Pozzetti, L., Quercellini, C., Radovich, M., Rassat, A., Roche, N., Ronayette, S., and Rossetti, E. (2011). Euclid Definition Study Report. *arXiv e-prints*, page arXiv:1110.3193.

Lavaux, G. and Hudson, M. J. (2011). The 2M++ galaxy redshift catalogue. *Mon. Not. Royal Astron. Soc.*, 416(4):2840–2856.

Lelli, F., McGaugh, S. S., and Schombert, J. M. (2016). SPARC: Mass Models for 175 Disk Galaxies with Spitzer Photometry and Accurate Rotation Curves. *Astron. J.*, 152(6):157.

Lemaître, G. (1931). A homogeneous universe of constant mass and increasing radius accounting for the radial velocity of extra-galactic nebulae. *Mon. Not. Royal Astron. Soc.*, 91:483–490.

Lemaître, G. (1933). L'Univers en expansion. *Annales de la Société Scientifique de Bruxelles*, 53:51.

Liddle, A. R. and Lyth, D. H. (2000). *Cosmological Inflation and Large-Scale Structure*. Cambridge University Press.

Liu, X. et al. (2016). Constraining $f(R)$ Gravity Theory Using Weak Lens-

ing Peak Statistics from the Canada-France-Hawaii-Telescope Lensing Survey. *Phys. Rev. Lett.*, 117(5):051101.

Llinares, C. (2018). Simulation techniques for modified gravity. *International Journal of Modern Physics D*, 27(15):1848003.

Lombriser, L. and Peñarrubia, J. (2015). How chameleons core dwarfs with cusps. *Phys. Rev. D*, 91(8):084022.

Ludlow, A. D., Benítez-Llambay, A., Schaller, M., Theuns, T., Frenk, C. S., Bower, R., Schaye, J., Crain, R. A., Navarro, J. F., Fattahi, A., and Oman, K. A. (2017). Mass-Discrepancy Acceleration Relation: A Natural Outcome of Galaxy Formation in Cold Dark Matter Halos. *Phys. Rev. Lett.*, 118(16):161103.

Ludlow, A. D., Bose, S., Angulo, R. E., Wang, L., Hellwing, W. A., Navarro, J. F., Cole, S., and Frenk, C. S. (2016). The mass-concentration-redshift relation of cold and warm dark matter haloes. *Mon. Not. Royal Astron. Soc.*, 460(2):1214–1232.

Lyth, D. H. and Liddle, A. R. (2009). *The Primordial Density Perturbation*. Cambridge University Press.

Madgwick, D. S., Lahav, O., Baldry, I. K., Baugh, C. M., Bland-Hawthorn, J., Bridges, T., Cannon, R., Cole, S., Colless, M., Collins, C., Couch, W., Dalton, G., De Propris, R., Driver, S. P., Efstathiou, G., Ellis, R. S., Frenk, C. S., Glazebrook, K., Jackson, C., Lewis, I., Lumsden, S., Maddox, S., Norberg, P., Peacock, J. A., Peterson, B. A., Sutherland, W., and Taylor, K. (2002). The 2dF Galaxy Redshift Survey: galaxy luminosity functions per spectral type. *Mon. Not. Royal Astron. Soc.*, 333(1):133–144.

Mandelbaum, R. (2018). Weak Lensing for Precision Cosmology. *Ann. Rev. Astron. Astrophys.*, 56:393–433.

March, B., Burrage, C., and Naik, A. P. (2024). Galactic Compton wavelengths in f(R) screening theories. *JCAP*, 2024(12):027.

Marsh, D. J. E. (2016). Axion cosmology. *Phys. Rep.*, 643:1–79.

Martinet, N., Harnois-Déraps, J., Jullo, E., and Schneider, P. (2021). Probing dark energy with tomographic weak-lensing aperture mass statistics. *Astron. Astrophys.*, 646:A62.

Martínez-Lombilla, C., Brough, S., Montes, M., Baena-Gallé, R., Akhlaghi, M., Infante-Sainz, R., Driver, S. P., Holwerda, B. W., Pimbblet, K. A., and Robotham, A. S. G. (2023). Galaxy And Mass Assembly (GAMA): extended intragroup light in a group at z = 0.2 from deep Hyper Suprime-Cam images. *Mon. Not. Royal Astron. Soc.*, 518(1):1195–1213.

McGaugh, S. S. (2012). The Baryonic Tully-Fisher Relation of Gas-rich Galaxies as a Test of ΛCDM and MOND. *Astron. J.*, 143(2):40.

McGaugh, S. S., Lelli, F., and Schombert, J. M. (2016). Radial Acceleration Relation in Rotationally Supported Galaxies. *Phys. Rev. Lett.*, 117(20):201101.

McGaugh, S. S., Schombert, J. M., Bothun, G. D., and de Blok, W. J. G. (2000). The Baryonic Tully-Fisher Relation. *Astrophys. J. Lett.*, 533(2):L99–L102.

McMillan, P. J. (2017). The mass distribution and gravitational potential of the Milky Way. *Mon. Not. Royal Astron. Soc.*, 465(1):76–94.

McWilliam, A. and Zoccali, M. (2010). Two Red Clumps and the X-shaped Milky Way Bulge. *Astrophys. J.*, 724(2):1491–1502.

Merritt, D., Graham, A. W., Moore, B., Diemand, J., and Terzić, B. (2006). Empirical Models for Dark Matter Halos. I. Nonparametric Construction of Density Profiles and Comparison with Parametric Models. *Astron. J.*, 132(6):2685–2700.

Messier, C. (1781). Catalogue des Nébuleuses et des Amas d'Étoiles (Catalog of Nebulae and Star Clusters). Connoissance des Temps ou des Mouvements Célestes, for 1784, p. 227-267.

Milgrom, M. (2016). MOND impact on and of the recently updated mass-discrepancy-acceleration relation. *arXiv e-prints*, page arXiv:1609.06642.

Milgrom, M. and Sanders, R. H. (2008). Rings and Shells of "Dark Matter" as MOND Artifacts. *Astrophys. J.*, 678(1):131–143.

Minkowski, R. L. and Abell, G. O. (1963). The National Geographic Society-Palomar Observatory Sky Survey. In Strand, K. A., editor, *Basic Astronomical Data: Stars and Stellar Systems*, page 481. University of Chicago Press.

Misner, C. W., Thorne, K. S., and Wheeler, J. A. (1973). *Gravitation*. W. H. Freeman and Company.

Mistele, T., McGaugh, S., Lelli, F., Schombert, J., and Li, P. (2024a). Indefinitely Flat Circular Velocities and the Baryonic Tully–Fisher Relation from Weak Lensing. *Astrophys. J. Lett.*, 969(1):L3.

Mistele, T., McGaugh, S., Lelli, F., Schombert, J., and Li, P. (2024b). Radial acceleration relation of galaxies with joint kinematic and weak-lensing data. *JCAP*, 2024(4):020.

Moffat, J. W. (2016). Acceleration in Modified Gravity (MOG) and the Mass-Discrepancy Baryonic Relation. *arXiv e-prints*, page arXiv:1610.06909.

Mondelin, M., Bournaud, F., Cuillandre, J. C., Codis, S., Stone, C., Bolzonella, M., Sorce, J. G., Kluge, M., Hatch, N. A., Marleau, F. R., Schirmer, M., Bouy, H., Buitrago, F., Tortora, C., Quilley, L., George, K., Baes, M., Saifollahi, T., Sanchez-Alarcon, P. M., Knapen, J. H., Aghanim, N., Amara, A., Andreon, S., Baccigalupi, C., Balestra, A.,

Bardelli, S., Battaglia, P., Biviano, A., Branchini, E., Brescia, M., Brinchmann, J., Capobianco, V., Carbone, C., Castellano, M., Castignani, G., Cavuoti, S., Cimatti, A., Congedo, G., Conselice, C. J., Conversi, L., Copin, Y., Courbin, F., Courtois, H. M., Cropper, M., De Lucia, G., Dupac, X., Fabricius, M., Farina, M., Faustini, F., Ferriol, S., Fotopoulou, S., Gillis, B., Giocoli, C., Grupp, F., Haugan, S. V. H., Holmes, W., Hormuth, F., Hornstrup, A., Jahnke, K., Jhabvala, M., Keihänen, E., Kermiche, S., Kilbinger, M., Kubik, B., Kümmel, M., Kurki-Suonio, H., Le Brun, A. M. C., Ligori, S., Lilje, P. B., Lindholm, V., Lloro, I., Maino, D., Maiorano, E., Mansutti, O., Marcin, S., Marggraf, O., Martinelli, M., Medinaceli, E., Mellier, Y., Merlin, E., Meylan, G., Moscardini, L., Niemi, S. M., Padilla, C., Pasian, F., Pedersen, K., Percival, W. J., Pettorino, V., Pires, S., Poncet, M., Popa, L. A., Pozzetti, L., Renzi, A., Riccio, G., Romelli, E., Saglia, R., Schneider, P., Secroun, A., Serrano, S., Sirignano, C., Steinwagner, J., Tereno, I., Toledo-Moreo, R., Torradeflot, F., Tutusaus, I., Valenziano, L., Vassallo, T., Wang, Y., Weller, J., Zerbi, F. M., Zucca, E., Burigana, C., and Scottez, V. (2025). Euclid: Early Release Observations – The surface brightness and colour profiles of the far outskirts of galaxies in the Perseus cluster. *Astron. & Astrophys.*, 699:A214.

Moore, B., Ghigna, S., Governato, F., Lake, G., Quinn, T., Stadel, J., and Tozzi, P. (1999a). Dark Matter Substructure within Galactic Halos. *Astrophys. J. Lett.*, 524(1):L19–L22.

Moore, B., Quinn, T., Governato, F., Stadel, J., and Lake, G. (1999b). Cold collapse and the core catastrophe. *Mon. Not. Royal Astron. Soc.*, 310(4):1147–1152.

More, S., Diemer, B., and Kravtsov, A. V. (2015). The Splashback Radius as a Physical Halo Boundary and the Growth of Halo Mass. *Astrophys. J.*, 810(1):36.

Moster, B. P., Naab, T., and White, S. D. M. (2013). Galactic star for-

mation and accretion histories from matching galaxies to dark matter haloes. *Mon. Not. Royal Astron. Soc.*, 428(4):3121–3138.

Mota, D. F. and Shaw, D. J. (2007). Evading equivalence principle violations, cosmological, and other experimental constraints in scalar field theories with a strong coupling to matter. *Phys. Rev. D*, 75(6):063501.

Naik, A. P., Evans, N. W., Puchwein, E., Zhao, H., and Davis, A. C. (2020). Stellar streams in chameleon gravity. *Phys. Rev. D*, 102(8):084066.

Naik, A. P., Puchwein, E., Davis, A.-C., and Arnold, C. (2018). Imprints of Chameleon f(R) gravity on Galaxy rotation curves. *Mon. Not. Royal Astron. Soc.*, 480(4):5211–5225.

Naik, A. P., Puchwein, E., Davis, A.-C., Sijacki, D., and Desmond, H. (2019). Constraints on chameleon f(R)-gravity from galaxy rotation curves of the SPARC sample. *Mon. Not. Royal Astron. Soc.*, 489(1):771–787.

Nataf, D. M., Udalski, A., Gould, A., Fouqué, P., and Stanek, K. Z. (2010). The Split Red Clump of the Galactic Bulge from OGLE-III. *Astrophys. J. Lett.*, 721(1):L28–L32.

Navarro, I. and Van Acoleyen, K. (2007). f(R) actions, cosmic acceleration and local tests of gravity. *JCAP*, 2007(2):022.

Navarro, J. F., Frenk, C. S., and White, S. D. M. (1996). The Structure of Cold Dark Matter Halos. *Astrophys. J.*, 462:563.

Ness, M., Freeman, K., Athanassoula, E., Wylie-De-Boer, E., Bland-Hawthorn, J., Lewis, G. F., Yong, D., Asplund, M., Lane, R. R., Kiss, L. L., and Ibata, R. (2012). The Origin of the Split Red Clump in the Galactic Bulge of the Milky Way. *Astrophys. J.*, 756(1):22.

Neugebauer, G., Habing, H. J., van Duinen, R., Aumann, H. H., Baud, B., Beichman, C. A., Beintema, D. A., Boggess, N., Clegg, P. E., de Jong, T., Emerson, J. P., Gautier, T. N., Gillett, F. C., Harris, S., Hauser,

M. G., Houck, J. R., Jennings, R. E., Low, F. J., Marsden, P. L., Miley, G., Olnon, F. M., Pottasch, S. R., Raimond, E., Rowan-Robinson, M., Soifer, B. T., Walker, R. G., Wesselius, P. R., and Young, E. (1984). The Infrared Astronomical Satellite (IRAS) mission. *Astrophys. J. Lett.*, 278:L1–L6.

Nicolis, A., Rattazzi, R., and Trincherini, E. (2009). Galileon as a local modification of gravity. *Phys. Rev. D*, 79(6):064036.

Norberg, P., Baugh, C. M., Hawkins, E., Maddox, S., Madgwick, D., Lahav, O., Cole, S., Frenk, C. S., Baldry, I., Bland-Hawthorn, J., Bridges, T., Cannon, R., Colless, M., Collins, C., Couch, W., Dalton, G., De Propris, R., Driver, S. P., Efstathiou, G., Ellis, R. S., Glazebrook, K., Jackson, C., Lewis, I., Lumsden, S., Peacock, J. A., Peterson, B. A., Sutherland, W., and Taylor, K. (2002). The 2dF Galaxy Redshift Survey: the dependence of galaxy clustering on luminosity and spectral type. *Mon. Not. Royal Astron. Soc.*, 332(4):827–838.

O'Hare, C. A. J. and Burrage, C. (2018). Stellar kinematics from the symmetron fifth force in the Milky Way disk. *Phys. Rev. D*, 98(6):064019.

Olive, K. A. and Pospelov, M. (2008). Environmental dependence of masses and coupling constants. *Phys. Rev. D*, 77:043524.

Oort, J. H. (1932). The force exerted by the stellar system in the direction perpendicular to the galactic plane and some related problems. *Bull. Astron. Inst. Netherlands*, 6:249.

Pedersen, E. M. and Stubbs, C. W. (2023). Using elliptical galaxy kinematics to compare the strength of gravity in cosmological regions of differing gravitational potential - a first look. *Mon. Not. Royal Astron. Soc.*, 524(3):4554–4561.

Peebles, P. J. E. and Ratra, B. (1988). Cosmology with a Time-Variable Cosmological "Constant". *Astrophys. J. Lett.*, 325:L17.

Penzias, A. A. and Wilson, R. W. (1965). A Measurement of Excess Antenna Temperature at 4080 Mc/s. *Astrophys. J.*, 142:419–421.

Percival, W. J., Reid, B. A., Eisenstein, D. J., Bahcall, N. A., Budavari, T., Frieman, J. A., Fukugita, M., Gunn, J. E., Ivezić, Ž., Knapp, G. R., Kron, R. G., Loveday, J., Lupton, R. H., McKay, T. A., Meiksin, A., Nichol, R. C., Pope, A. C., Schlegel, D. J., Schneider, D. P., Spergel, D. N., Stoughton, C., Strauss, M. A., Szalay, A. S., Tegmark, M., Vogeley, M. S., Weinberg, D. H., York, D. G., and Zehavi, I. (2010). Baryon acoustic oscillations in the Sloan Digital Sky Survey Data Release 7 galaxy sample. *Mon. Not. Royal Astron. Soc.*, 401(4):2148–2168.

Pietroni, M. (2005). Dark energy condensation. *Phys. Rev. D*, 72:043535.

Pillepich, A., Springel, V., Nelson, D., Genel, S., Naiman, J., Pakmor, R., Hernquist, L., Torrey, P., Vogelsberger, M., Weinberger, R., and Marinacci, F. (2018). Simulating galaxy formation with the IllustrisTNG model. *Mon. Not. Royal Astron. Soc.*, 473(3):4077–4106.

Pizzuti, L., Sartoris, B., Borgani, S., and Biviano, A. (2020). Calibration of systematics in constraining modified gravity models with galaxy cluster mass profiles. *JCAP*, 2020(4):024.

Planck Collaboration, Aghanim, N., Akrami, Y., Ashdown, M., Aumont, J., Baccigalupi, C., Ballardini, M., Banday, A. J., Barreiro, R. B., Bartolo, N., Basak, S., Battye, R., Benabed, K., Bernard, J. P., Bersanelli, M., Bielewicz, P., Bock, J. J., Bond, J. R., Borrill, J., Bouchet, F. R., Boulanger, F., Bucher, M., Burigana, C., Butler, R. C., Calabrese, E., Cardoso, J. F., Carron, J., Challinor, A., Chiang, H. C., Chluba, J., Colombo, L. P. L., Combet, C., Contreras, D., Crill, B. P., Cuttaia, F., de Bernardis, P., de Zotti, G., Delabrouille, J., Delouis, J. M., Di Valentino, E., Diego, J. M., Doré, O., Douspis, M., Ducout, A., Dupac, X., Dusini, S., Efstathiou, G., Elsner, F., Enßlin, T. A., Eriksen, H. K., Fantaye, Y., Farhang, M., Fergusson, J., Fernandez-Cobos, R.,

Finelli, F., Forastieri, F., Frailis, M., Fraisse, A. A., Franceschi, E., Frolov, A., Galeotta, S., Galli, S., Ganga, K., Génova-Santos, R. T., Gerbino, M., Ghosh, T., González-Nuevo, J., Górski, K. M., Gratton, S., Gruppuso, A., Gudmundsson, J. E., Hamann, J., Handley, W., Hansen, F. K., Herranz, D., Hildebrandt, S. R., Hivon, E., Huang, Z., Jaffe, A. H., Jones, W. C., Karakci, A., Keihänen, E., Keskitalo, R., Kiiveri, K., Kim, J., Kisner, T. S., Knox, L., Krachmalnicoff, N., Kunz, M., Kurki-Suonio, H., Lagache, G., Lamarre, J. M., Lasenby, A., Lattanzi, M., Lawrence, C. R., Le Jeune, M., Lemos, P., Lesgourgues, J., Levrier, F., Lewis, A., Liguori, M., Lilje, P. B., Lilley, M., Lindholm, V., López-Caniego, M., Lubin, P. M., Ma, Y. Z., Macías-Pérez, J. F., Maggio, G., Maino, D., Mandolesi, N., Mangilli, A., Marcos-Caballero, A., Maris, M., Martin, P. G., Martinelli, M., Martínez-González, E., Matarrese, S., Mauri, N., McEwen, J. D., Meinhold, P. R., Melchiorri, A., Mennella, A., Migliaccio, M., Millea, M., Mitra, S., Miville-Deschênes, M. A., Molinari, D., Montier, L., Morgante, G., Moss, A., Natoli, P., Nørgaard-Nielsen, H. U., Pagano, L., Paoletti, D., Partridge, B., Patanchon, G., Peiris, H. V., Perrotta, F., Pettorino, V., Piacentini, F., Polastri, L., Polenta, G., Puget, J. L., Rachen, J. P., Reinecke, M., Remazeilles, M., Renzi, A., Rocha, G., Rosset, C., Roudier, G., Rubiño-Martín, J. A., Ruiz-Granados, B., Salvati, L., Sandri, M., Savelainen, M., Scott, D., Shellard, E. P. S., Sirignano, C., Sirri, G., Spencer, L. D., Sunyaev, R., Suur-Uski, A. S., Tauber, J. A., Tavagnacco, D., Tenti, M., Toffolatti, L., Tomasi, M., Trombetti, T., Valenziano, L., Valiviita, J., Van Tent, B., Vibert, L., Vielva, P., Villa, F., Vittorio, N., Wandelt, B. D., Wehus, I. K., White, M., White, S. D. M., Zacchei, A., and Zonca, A. (2020). Planck 2018 results. VI. Cosmological parameters. *Astron. & Astrophys.*, 641:A6.

Plummer, H. C. (1911). On the problem of distribution in globular star clusters. *Mon. Not. Royal Astron. Soc.*, 71:460–470.

Pontzen, A. and Governato, F. (2012). How supernova feedback turns dark

matter cusps into cores. *Mon. Not. Royal Astron. Soc.*, 421(4):3464–3471.

Poulin, V., Smith, T. L., Karwal, T., and Kamionkowski, M. (2019). Early Dark Energy can Resolve the Hubble Tension. *Phys. Rev. Lett.*, 122(22):221301.

Puchwein, E., Baldi, M., and Springel, V. (2013). Modified-Gravity-GADGET: a new code for cosmological hydrodynamical simulations of modified gravity models. *Mon. Not. Royal Astron. Soc.*, 436(1):348–360.

Ramachandra, N., Valogiannis, G., Ishak, M., Heitmann, K., and LSST Dark Energy Science Collaboration (2021). Matter power spectrum emulator for f (R) modified gravity cosmologies. *Phys. Rev. D*, 103(12):123525.

Read, J. I. and Gilmore, G. (2005). Mass loss from dwarf spheroidal galaxies: the origins of shallow dark matter cores and exponential surface brightness profiles. *Mon. Not. Royal Astron. Soc.*, 356(1):107–124.

Rider, A. D., Moore, D. C., Blakemore, C. P., Louis, M., Lu, M., and Gratta, G. (2016). Search for Screened Interactions Associated with Dark Energy below the 100 μ m Length Scale. *Phys. Rev. Lett.*, 117(10):101101.

Riess, A. G., Casertano, S., Yuan, W., Bowers, J. B., Macri, L., Zinn, J. C., and Scolnic, D. (2021). Cosmic Distances Calibrated to 1% Precision with Gaia EDR3 Parallaxes and Hubble Space Telescope Photometry of 75 Milky Way Cepheids Confirm Tension with ΛCDM. *Astrophys. J. Lett.*, 908(1):L6.

Riess, A. G., Casertano, S., Yuan, W., Macri, L. M., and Scolnic, D. (2019). Large Magellanic Cloud Cepheid Standards Provide a 1% Foundation for the Determination of the Hubble Constant and Stronger Evidence for Physics beyond ΛCDM. *Astrophys. J.*, 876(1):85.

Robertson, H. P. (1935). Kinematics and World-Structure. *Astrophys. J.*, 82:284.

Robertson, H. P. (1936a). Kinematics and World-Structure II. *Astrophys. J.*, 83:187.

Robertson, H. P. (1936b). Kinematics and World-Structure III. *Astrophys. J.*, 83:257.

Ruan, C.-Z., Hernández-Aguayo, C., Li, B., Arnold, C., Baugh, C. M., Klypin, A., and Prada, F. (2022). Fast full N-body simulations of generic modified gravity: conformal coupling models. *JCAP*, 2022(5):018.

Rubin, V. C. (1983). Dark matter in spiral galaxies. *Scientific American*, 248:96–106.

Ruggiero, M. L. and Iorio, L. (2007). Solar System planetary orbital motions and f(R) theories of gravity. *JCAP*, 2007(1):010.

Sakstein, J. (2013). Stellar oscillations in modified gravity. *Phys. Rev. D*, 88:124013.

Sakstein, J. (2015a). Hydrogen Burning in Low Mass Stars Constrains Scalar-Tensor Theories of Gravity. *Phys. Rev. Lett.*, 115(20):201101.

Sakstein, J. (2015b). Testing gravity using dwarf stars. *Phys. Rev. D*, 92(12):124045.

Sakstein, J. (2020). Astrophysical Tests of Screened Modified Gravity. *arXiv e-prints*, page arXiv:2002.04194.

Sakstein, J., Jain, B., and Vikram, V. (2014). Testing Gravity Theories Using Stars. *arXiv e-prints*, page arXiv:1409.3708.

Saridakis, E. N., Lazkoz, R., Salzano, V., Vargas Moniz, P., Capozziello, S., Beltrán Jiménez, J., De Laurentis, M., Olmo, G. J., Akrami, Y., Bahamonde, S., Blázquez-Salcedo, J. L., Böhmer, C. G., Bonvin, C.,

Bouhmadi-López, M., Brax, P., Calcagni, G., Casadio, R., Cembranos, J. A. R., de la Cruz-Dombriz, Á., Davis, A.-C., Delhom, A., Di Valentino, E., Dialektopoulos, K. F., Elder, B., María Ezquiaga, J., Frusciante, N., Garattini, R., Gergely, L. Á., Giusti, A., Heisenberg, L., Hohmann, M., Iosifidis, D., Kazantzidis, L., Kleihaus, B., Koivisto, T. S., Kunz, J., Lobo, F. S. N., Martinelli, M., Martín-Moruno, P., Mimoso, J. P., Mota, D. F., Peirone, S., Perivolaropoulos, L., Pettorino, V., Pfeifer, C., Pizzuti, L., Rubiera-Garcia, D., Levi Said, J., Sakellariadou, M., Saltas, I. D., Spurio Mancini, A., Voicu, N., and Wojnar, A. (2021a). Modified Gravity and Cosmology: An Update by the CANTATA Network. *arXiv e-prints*, page arXiv:2105.12582.

Saridakis, E. N., Lazkoz, R., Salzano, V., Vargas Moniz, P., Capozziello, S., Beltrán Jiménez, J., De Laurentis, M., Olmo, G. J., Akrami, Y., Bahamonde, S., Blázquez-Salcedo, J. L., Böhmer, C. G., Bonvin, C., Bouhmadi-López, M., Brax, P., Calcagni, G., Casadio, R., Cembranos, J. A. R., de la Cruz-Dombriz, Á., Davis, A.-C., Delhom, A., Di Valentino, E., Dialektopoulos, K. F., Elder, B., María Ezquiaga, J., Frusciante, N., Garattini, R., Gergely, L. Á., Giusti, A., Heisenberg, L., Hohmann, M., Iosifidis, D., Kazantzidis, L., Kleihaus, B., Koivisto, T. S., Kunz, J., Lobo, F. S. N., Martinelli, M., Martín-Moruno, P., Mimoso, J. P., Mota, D. F., Peirone, S., Perivolaropoulos, L., Pettorino, V., Pfeifer, C., Pizzuti, L., Rubiera-Garcia, D., Levi Said, J., Sakellariadou, M., Saltas, I. D., Spurio Mancini, A., Voicu, N., and Wojnar, A. (2021b). Modified Gravity and Cosmology: An Update by the CANTATA Network. *arXiv e-prints*, page arXiv:2105.12582.

Schaye, J., Crain, R. A., Bower, R. G., Furlong, M., Schaller, M., Theuns, T., Dalla Vecchia, C., Frenk, C. S., McCarthy, I. G., Helly, J. C., Jenkins, A., Rosas-Guevara, Y. M., White, S. D. M., Baes, M., Booth, C. M., Camps, P., Navarro, J. F., Qu, Y., Rahmati, A., Sawala, T., Thomas, P. A., and Trayford, J. (2015). The EAGLE project: simu-

lating the evolution and assembly of galaxies and their environments. *Mon. Not. Royal Astron. Soc.*, 446(1):521–554.

Schechter, P. (1976). An analytic expression for the luminosity function for galaxies. *Astrophys. J.*, 203:297–306.

Schmidt, F. (2008). Weak Lensing Probes of Modified Gravity. *Phys. Rev. D*, 78:043002.

Schneider, M. D., Frenk, C. S., and Cole, S. (2012). The shapes and alignments of dark matter halos. *JCAP*, 2012(5):030.

Schneider, P., Ehlers, J., and Falco, E. E. (1992). *Gravitational Lenses*. Springer Berlin, Heidelberg.

Schrabback, T., Hoekstra, H., Van Waerbeke, L., van Uitert, E., Georgiou, C., Asgari, M., Côté, P., Cuillandre, J.-C., Erben, T., Ferrarese, L., Gwyn, S. D. J., Heymans, C., Hildebrandt, H., Kannawadi, A., Kuijken, K., Leauthaud, A., Makler, M., Mei, S., Miller, L., Raichoor, A., Schneider, P., and Wright, A. (2021). Tightening weak lensing constraints on the ellipticity of galaxy-scale dark matter haloes. *Astron. & Astrophys.*, 646:A73.

Schwob, C., Jozefowski, L., de Beauvoir, B., Hilico, L., Nez, F., Julien, L., Biraben, F., Acef, O., Zondy, J.-J., and Clairon, A. (1999). Optical frequency measurement of the $2S - 12D$ transitions in hydrogen and deuterium: Rydberg constant and lamb shift determinations. *Phys. Rev. Lett.*, 82:4960–4963.

Shapiro, S. S., Davis, J. L., Lebach, D. E., and Gregory, J. S. (2004). Measurement of the Solar Gravitational Deflection of Radio Waves using Geodetic Very-Long-Baseline Interferometry Data, 1979 1999. *Phys. Rev. Lett.*, 92(12):121101.

Shen, S., Mo, H. J., White, S. D. M., Blanton, M. R., Kauffmann, G., Voges, W., Brinkmann, J., and Csabai, I. (2003). The size distribution

of galaxies in the Sloan Digital Sky Survey. *Mon. Not. Royal Astron. Soc.*, 343(3):978–994.

Simon, G., Schmitt, C., Borkowski, F., and Walther, V. (1980). Absolute electron-proton cross sections at low momentum transfer measured with a high pressure gas target system. *Nuclear Physics A*, 333(3):381–391.

Skordis, C. (2009). TOPICAL REVIEW: The tensor-vector-scalar theory and its cosmology. *Classical and Quantum Gravity*, 26(14):143001.

Smoot, G. F., Bennett, C. L., Kogut, A., Wright, E. L., Aymon, J., Boggess, N. W., Cheng, E. S., de Amici, G., Gulkis, S., Hauser, M. G., Hinshaw, G., Jackson, P. D., Janssen, M., Kaita, E., Kelsall, T., Keegstra, P., Lineweaver, C., Loewenstein, K., Lubin, P., Mather, J., Meyer, S. S., Moseley, S. H., Murdock, T., Rokke, L., Silverberg, R. F., Tenorio, L., Weiss, R., and Wilkinson, D. T. (1992). Structure in the COBE Differential Microwave Radiometer First-Year Maps. *Astrophys. J. Lett.*, 396:L1.

Song, Y.-S. (2006). A Cosmological Test of Standard Gravity by Weak Lensing. *arXiv e-prints*, pages astro–ph/0602598.

Song, Y.-S. and Koyama, K. (2009). Consistency test of general relativity from large scale structure of the Universe. *JCAP*, 01:048.

Sotiriou, T. P. and Faraoni, V. (2010). f(R) theories of gravity. *Reviews of Modern Physics*, 82(1):451–497.

Spergel, D. N. and Steinhardt, P. J. (2000). Observational Evidence for Self-Interacting Cold Dark Matter. *Phys. Rev. Lett.*, 84(17):3760–3763.

Springel, V., Frenk, C. S., and White, S. D. M. (2006). The large-scale structure of the Universe. *Nature*, 440(7088):1137–1144.

Starobinsky, A. A. (1980). A new type of isotropic cosmological models without singularity. *Physics Letters B*, 91(1):99–102.

Starobinsky, A. A. (2007). Disappearing cosmological constant in f(R) gravity. *Soviet Journal of Experimental and Theoretical Physics Letters*, 86(3):157–163.

Tamosiunas, A., Briddon, C., Burrage, C., Cutforth, A., Moss, A., and Vincent, T. (2022). Chameleon screening in cosmic voids. *JCAP*, 2022(11):056.

Tegmark, M., Blanton, M. R., Strauss, M. A., Hoyle, F., Schlegel, D., Scoccimarro, R., Vogeley, M. S., Weinberg, D. H., Zehavi, I., Berlind, A., Budavari, T., Connolly, A., Eisenstein, D. J., Finkbeiner, D., Frieman, J. A., Gunn, J. E., Hamilton, A. J. S., Hui, L., Jain, B., Johnston, D., Kent, S., Lin, H., Nakajima, R., Nichol, R. C., Ostriker, J. P., Pope, A., Scranton, R., Seljak, U., Sheth, R. K., Stebbins, A., Szalay, A. S., Szapudi, I., Verde, L., Xu, Y., Annis, J., Bahcall, N. A., Brinkmann, J., Burles, S., Castander, F. J., Csabai, I., Loveday, J., Doi, M., Fukugita, M., Gott, III, J. R., Hennessy, G., Hogg, D. W., Ivezić, Ž., Knapp, G. R., Lamb, D. Q., Lee, B. C., Lupton, R. H., McKay, T. A., Kunszt, P., Munn, J. A., O'Connell, L., Peoples, J., Pier, J. R., Richmond, M., Rockosi, C., Schneider, D. P., Stoughton, C., Tucker, D. L., Vanden Berk, D. E., Yanny, B., York, D. G., and SDSS Collaboration (2004). The Three-Dimensional Power Spectrum of Galaxies from the Sloan Digital Sky Survey. *Astrophys. J.*, 606(2):702–740.

Terukina, A., Lombriser, L., Yamamoto, K., Bacon, D., Koyama, K., and Nichol, R. C. (2014). Testing chameleon gravity with the Coma cluster. *JCAP*, 2014(4):013.

Thomas, S. A., Abdalla, F. B., and Weller, J. (2009). Constraining Modified Gravity and Growth with Weak Lensing. *Mon. Not. Roy. Astron. Soc.*, 395:197–209.

Thomas, S. A., Appleby, S. A., and Weller, J. (2011). Modified Gravity: the CMB, Weak Lensing and General Parameterisations. *JCAP*, 03:036.

Touboul, P., Métris, G., Rodrigues, M., André, Y., Baghi, Q., Bergé, J., Boulanger, D., Bremer, S., Carle, P., Chhun, R., Christophe, B., Cipolla, V., Damour, T., Danto, P., Dittus, H., Fayet, P., Foulon, B., Gageant, C., Guidotti, P.-Y., Hagedorn, D., Hardy, E., Huynh, P.-A., Inchauspe, H., Kayser, P., Lala, S., Lämmerzahl, C., Lebat, V., Leseur, P., Liorzou, F., List, M., Löffler, F., Panet, I., Pouilloux, B., Prieur, P., Rebray, A., Reynaud, S., Rievers, B., Robert, A., Selig, H., Serron, L., Sumner, T., Tanguy, N., and Visser, P. (2017). MICROSCOPE Mission: First Results of a Space Test of the Equivalence Principle. *Phys. Rev. Lett.*, 119(23):231101.

Touboul, P., Métris, G., Rodrigues, M., André, Y., Baghi, Q., Bergé, J., Boulanger, D., Bremer, S., Chhun, R., Christophe, B., Cipolla, V., Damour, T., Danto, P., Dittus, H., Fayet, P., Foulon, B., Guidotti, P.-Y., Hardy, E., Huynh, P.-A., Lämmerzahl, C., Lebat, V., Liorzou, F., List, M., Panet, I., Pires, S., Pouilloux, B., Prieur, P., Reynaud, S., Rievers, B., Robert, A., Selig, H., Serron, L., Sumner, T., and Visser, P. (2019). Space test of the equivalence principle: first results of the MICROSCOPE mission. *Classical and Quantum Gravity*, 36(22):225006.

Trotta, R. (2017). Bayesian Methods in Cosmology. *arXiv e-prints*, page arXiv:1701.01467.

Troxel, M. A. and Ishak, M. (2015). The intrinsic alignment of galaxies and its impact on weak gravitational lensing in an era of precision cosmology. *Phys. Rep.*, 558:1–59.

Tsujikawa, S. and Tatekawa, T. (2008). The effect of modified gravity on weak lensing. *Phys. Lett. B*, 665:325–331.

Tu, L.-C., Luo, J., and Gillies, G. T. (2005). The mass of the photon. *Rept. Prog. Phys.*, 68:77–130.

Vainshtein, A. I. (1972). To the problem of nonvanishing gravitation mass. *Physics Letters B*, 39(3):393–394.

Vardanyan, V. and Bartlett, D. J. (2023). Modeling and Testing Screening Mechanisms in the Laboratory and in Space. *Universe*, 9(7):340.

Vattis, K., Koushiappas, S. M., and Loeb, A. (2019). Dark matter decaying in the late Universe can relieve the H_0 tension. *Phys. Rev. D*, 99(12):121302.

Verlinde, E. P. (2017). Emergent Gravity and the Dark Universe. *SciPost Physics*, 2(3):016.

Vikram, V., Cabré, A., Jain, B., and VanderPlas, J. T. (2013). Astrophysical tests of modified gravity: the morphology and kinematics of dwarf galaxies. *JCAP*, 2013(8):020.

Vikram, V., Sakstein, J., Davis, C., and Neil, A. (2014). Astrophysical Tests of Modified Gravity: Stellar and Gaseous Rotation Curves in Dwarf Galaxies. *arXiv e-prints*, page arXiv:1407.6044.

Virtanen, P., Gommers, R., Oliphant, T. E., Haberland, M., Reddy, T., Cournapeau, D., Burovski, E., Peterson, P., Weckesser, W., Bright, J., van der Walt, S. J., Brett, M., Wilson, J., Millman, K. J., Mayorov, N., Nelson, A. R. J., Jones, E., Kern, R., Larson, E., Carey, C. J., Polat, İ., Feng, Y., Moore, E. W., VanderPlas, J., Laxalde, D., Perktold, J., Cimrman, R., Henriksen, I., Quintero, E. A., Harris, C. R., Archibald, A. M., Ribeiro, A. H., Pedregosa, F., van Mulbregt, P., and SciPy 1. 0 Contributors (2020). SciPy 1.0: fundamental algorithms for scientific computing in Python. *Nature Methods*, 17:261–272.

Vogelsberger, M., Genel, S., Springel, V., Torrey, P., Sijacki, D., Xu, D., Snyder, G., Nelson, D., and Hernquist, L. (2014). Introducing the Illustris Project: simulating the coevolution of dark and visible matter in the Universe. *Mon. Not. Royal Astron. Soc.*, 444(2):1518–1547.

Wald, R. M. (1984). *General Relativity*. University of Chicago Press.

Walker, A. G. (1937). On Milne's Theory of World-Structure. *Proceedings of the London Mathematical Society*, 42:90–127.

Wang, B., Wei, J.-J., Wu, X.-F., and López-Corredoira, M. (2023). Revisiting constraints on the photon rest mass with cosmological fast radio bursts. *JCAP*, 09:025.

Weinberg, S. (1989). The cosmological constant problem. *Reviews of Modern Physics*, 61(1):1–23.

Weyl, H. (1919). Eine neue Erweiterung der Relativitätstheorie. *Annalen der Physik*, 364(10):101–133.

Wilcox, H., Nichol, R. C., Zhao, G.-B., Bacon, D., Koyama, K., and Romer, A. K. (2016). Simulation tests of galaxy cluster constraints on chameleon gravity. *Mon. Not. Royal Astron. Soc.*, 462(1):715–725.

Will, C. M. (2014). The Confrontation between General Relativity and Experiment. *Living Reviews in Relativity*, 17(1):4.

Williams, J. G., Turyshev, S. G., and Boggs, D. H. (2004). Progress in Lunar Laser Ranging Tests of Relativistic Gravity. *Phys. Rev. Lett.*, 93(26):261101.

Winther, H. A., Schmidt, F., Barreira, A., Arnold, C., Bose, S., Llinares, C., Baldi, M., Falck, B., Hellwing, W. A., Koyama, K., Li, B., Mota, D. F., Puchwein, E., Smith, R. E., and Zhao, G.-B. (2015). Modified gravity N-body code comparison project. *Mon. Not. Royal Astron. Soc.*, 454(4):4208–4234.

Yan, S., Li, L., and Fan, J. (2024). Constraints on photon mass and dark photon from the Jovian magnetic field. *JHEP*, 06:028.

Yin, P., Li, R., Yin, C., Xu, X., Bian, X., Xie, H., Duan, C.-K., Huang, P., He, J.-h., and Du, J. (2022). Experiments with levitated force sensor challenge theories of dark energy. *Nature Physics*, 18(10):1181–1185.

York, D. G., Adelman, J., Anderson, Jr., J. E., Anderson, S. F., Annis, J., Bahcall, N. A., Bakken, J. A., Barkhouser, R., Bastian, S., Berman, E., Boroski, W. N., Bracker, S., Briegel, C., Briggs, J. W., Brinkmann, J., Brunner, R., Burles, S., Carey, L., Carr, M. A., Castander, F. J., Chen, B., Colestock, P. L., Connolly, A. J., Crocker, J. H., Csabai, I., Czarapata, P. C., Davis, J. E., Doi, M., Dombeck, T., Eisenstein, D., Ellman, N., Elms, B. R., Evans, M. L., Fan, X., Federwitz, G. R., Fiscelli, L., Friedman, S., Frieman, J. A., Fukugita, M., Gillespie, B., Gunn, J. E., Gurbani, V. K., de Haas, E., Haldeman, M., Harris, F. H., Hayes, J., Heckman, T. M., Hennessy, G. S., Hindsley, R. B., Holm, S., Holmgren, D. J., Huang, C.-h., Hull, C., Husby, D., Ichikawa, S.-I., Ichikawa, T., Ivezić, Ž., Kent, S., Kim, R. S. J., Kinney, E., Klaene, M., Kleinman, A. N., Kleinman, S., Knapp, G. R., Korienek, J., Kron, R. G., Kunszt, P. Z., Lamb, D. Q., Lee, B., Leger, R. F., Limmongkol, S., Lindenmeyer, C., Long, D. C., Loomis, C., Loveday, J., Lucinio, R., Lupton, R. H., MacKinnon, B., Mannery, E. J., Mantsch, P. M., Margon, B., McGehee, P., McKay, T. A., Meiksin, A., Merelli, A., Monet, D. G., Munn, J. A., Narayanan, V. K., Nash, T., Neilsen, E., Neswold, R., Newberg, H. J., Nichol, R. C., Nicinski, T., Nonino, M., Okada, N., Okamura, S., Ostriker, J. P., Owen, R., Pauls, A. G., Peoples, J., Peterson, R. L., Petravick, D., Pier, J. R., Pope, A., Pordes, R., Prosapio, A., Rechenmacher, R., Quinn, T. R., Richards, G. T., Richmond, M. W., Rivetta, C. H., Rockosi, C. M., Ruthmansdorfer, K., Sandford, D., Schlegel, D. J., Schneider, D. P., Sekiguchi, M., Sergey, G., Shimasaku, K., Siegmund, W. A., Smee, S., Smith, J. A., Snedden, S., Stone, R., Stoughton, C., Strauss, M. A., Stubbs, C., SubbaRao, M., Szalay, A. S., Szapudi, I., Szokoly, G. P., Thakar, A. R., Tremonti, C., Tucker, D. L., Uomoto, A., Vanden Berk, D., Vogeley, M. S., Waddell, P., Wang, S.-i., Watanabe, M., Weinberg, D. H., Yanny, B., Yasuda, N., and SDSS Collaboration (2000). The Sloan Digital Sky Survey: Technical Summary. *Astron. J.*, 120(3):1579–1587.

Yukawa, H. (1935). On the interaction of elementary particles. i. *Proceedings of the Physico-Mathematical Society of Japan. 3rd Series*, 17:48–57.

Yunes, N. and Pretorius, F. (2009). Dynamical Chern-Simons modified gravity: Spinning black holes in the slow-rotation approximation. *Phys. Rev. D*, 79(8):084043.

Zhao, Y.-L., Tan, Y.-J., Wu, W.-H., Luo, J., and Shao, C.-G. (2021). Constraining the chameleon model with the HUST-2020 torsion pendulum experiment. *Phys. Rev. D*, 103(10):104005.

Appendices

Appendix A

Metric Components for a Spherical Source

The metric is a fundamental object in general relativity, describing the geometry of spacetime around a source mass. In this section, we derive the metric components for a static, spherically symmetric source, which is relevant for modelling dark matter halos in galaxies. We consider two common density profiles: the Singular Isothermal Sphere (SIS) and the Navarro–Frenk–White (NFW) profile.

We start our derivation with a spherical metric ansatz, given by

$$\mathrm{d}s^2 = -\mathrm{e}^{2\xi(r)}\mathrm{d}t^2 + \mathrm{e}^{2\zeta(r)}\mathrm{d}r^2 + r^2\mathrm{d}\Omega^2\,, \tag{A.1}$$

where $\xi(r)$ and $\zeta(r)$ are functions to be determined, and $\mathrm{d}\Omega^2 = \mathrm{d}\vartheta^2 + \sin^2\vartheta\,\mathrm{d}\phi^2$ is the metric on the unit 2-sphere. We restrict motion to the equatorial plane (i.e. $\vartheta = \pi/2$, $\dot{\vartheta} = 0$), without loss of generality. For a static, spherically symmetric perfect fluid, the energy-momentum tensor is given by eq. (1.15),

$$T_{\mu\nu} = (\rho + p)u_\mu u_\nu + p g_{\mu\nu}\,,$$

where u_μ is the four-velocity of the fluid, $\rho(r)$ is the energy density and $p(r)$ is the pressure. For a static fluid, the four-velocity is given by $u^\mu = (1, 0, 0, 0)$. Given we are modelling a pressureless dark matter gas, we set $p(r) = 0$. With these simplifications, the components of the energy–

momentum tensor are given by

$$T_{tt} = \rho(r), \quad T_{rr} = T_{\theta\theta} = 0\,. \tag{A.2}$$

Now, we turn to Einstein's field equations, eq. (1.5),

$$G_{\mu\nu} = 8\pi G T_{\mu\nu}\,,$$

which relates the geometry of spacetime to the energy–momentum content. Looking first at the G_{tt} component, we arrive at the gravitational mass equation

$$\frac{\mathrm{d}}{\mathrm{d}r}\left(r\left(1 - \mathrm{e}^{-2\zeta(r)}\right)\right) = 8\pi G r^2 \rho(r)\,, \tag{A.3}$$

which can be integrated to give the rr metric component formula

$$\mathrm{e}^{2\zeta(r)} = \left(1 - \frac{2Gm(r)}{r}\right)^{-1}\,, \tag{A.4}$$

where

$$m(r) = \int_0^r 4\pi x^2 \rho(x)\,\mathrm{d}x \tag{A.5}$$

is the enclosed mass. Next, we look at the G_{rr} component, which gives us

$$\frac{\mathrm{d}\xi}{\mathrm{d}r} = \frac{Gm(r)}{r^2\left(1 - 2Gm(r)/r\right)}\,. \tag{A.6}$$

This equation can be solved for certain forms of $m(r)$, as we will see in the next subsections. Upon solving, one must impose boundary conditions to ensure $\xi(r)$ is well behaved and matches the exterior Schwarzschild metric component at the outermost surface of the source, R, i.e., $\mathrm{e}^{2\xi(R)} = 1 - \frac{2GM}{R}$.

A.1 SIS Metric Components

The first source model we will consider is the Singular Isothermal Sphere (SIS) dark matter halo, with a density profile given by eq. (1.54),

$$\rho(r) = \frac{\sigma_v^2}{2\pi G r^2}\,,$$

where σ_v is the velocity dispersion of the dark matter particles. The enclosed mass function for this model is given in eq. (1.55),

$$m(r) = \frac{2\sigma_v^2 r}{G}\,.$$

Uniquely, the SIS model results in a constant gravitational potential throughout the object,

$$\frac{Gm(r)}{r} = \frac{GM}{R} = 2\sigma_v^2\,, \tag{A.7}$$

which we will use interchangeably throughout this derivation. Given this fact, the rr metric component is simply given by

$$\mathrm{e}^{2\zeta(r)} = \left(1 - \frac{2Gm(r)}{r}\right)^{-1} = \left(1 - 4\sigma_v^2\right)^{-1}\,, \tag{A.8}$$

which automatically matches the exterior Schwarzschild metric component at the surface.

Determining the form of the tt metric component is slightly more involved, but still relatively straightforward. We start with the equation

$$\frac{\mathrm{d}\xi}{\mathrm{d}r} = \frac{Gm(r)}{r^2\left(1 - 2Gm(r)/r\right)} = \frac{2\sigma_v^2}{r\left(1 - 4\sigma_v^2\right)}\,, \tag{A.9}$$

resulting in

$$\xi(r) = \frac{2\sigma_v^2}{1 - 4\sigma_v^2}\ln r + C\,. \tag{A.10}$$

We determine the integration constant C by matching to the exterior Schwarzschild metric at the outer surface of the halo, R,

$$\mathrm{e}^{2\xi(R)} = 1 - \frac{2GM}{R} = 1 - 4\sigma_v^2 \quad \Rightarrow \quad \xi(R) = \frac{1}{2}\ln\left(1 - 4\sigma_v^2\right)\,, \tag{A.11}$$

giving us

$$C = \frac{1}{2}\ln\left(\left(1 - 4\sigma_v^2\right)R^{\frac{-4\sigma_v^2}{1-4\sigma_v^2}}\right)\,. \tag{A.12}$$

Combining this with our expression for ξ and rearranging we arrive at the tt metric component

$$\mathrm{e}^{2\xi(r)} = \left(1 - 4\sigma_v^2\right)\left(\frac{r}{R}\right)^{\frac{4\sigma_v^2}{1-4\sigma_v^2}}\,. \tag{A.13}$$

So, the interior region of an SIS dark matter halo is described by the metric

$$\mathrm{d}s^2 = -\left(1 - \frac{2GM}{r}\right)\left(\frac{r}{R}\right)^{\frac{4\sigma_v^2}{1-4\sigma_v^2}}\mathrm{d}t^2 + \left(1 - \frac{2Gm(r)}{r}\right)^{-1}\mathrm{d}r^2 + r^2\mathrm{d}\Omega^2\,. \tag{A.14}$$

It should be noted that for typical galactic parameters, $\sigma_v \ll 1$, so the term $\left(\frac{r}{R}\right)^{\frac{4\sigma_v^2}{1-4\sigma_v^2}} \approx 1$, given that $0 < r \leq R$ necessarily.

A.2 NFW Metric Components

Shifting to a more realistic and commonly used, but also more mathematically complex, density model, the NFW profile, with density given in eq. (1.50)

$$\rho(r) = \frac{\rho_{\mathrm{NFW}}}{\frac{r}{r_{\mathrm{NFW}}}\left(1 + \frac{r}{r_{\mathrm{NFW}}}\right)^2}\,, \tag{A.15}$$

where ρ_{NFW} is the characteristic density and r_{NFW} is the scale radius. The enclosed mass function for this model is given by

$$m(r) = 4\pi\rho_{\mathrm{NFW}}r_{\mathrm{NFW}}^3\left[\ln\left(1 + \frac{r}{r_{\mathrm{NFW}}}\right) - \frac{r/r_{\mathrm{NFW}}}{1 + r/r_{\mathrm{NFW}}}\right]\,. \tag{A.16}$$

We follow the same procedure as in the last section, although we will be required to make some simplifying assumptions to obtain a final metric. Specifically, we will assume that the metric component functions, ζ and ξ, are small quantities, and that Gm/r is small, so that we can expand the metric components in powers of these quantities. This is equivalent to working in the weak-field limit, which is well justified for galactic halos where $Gm/r \ll 1$ and the gravitational potentials are much less than unity.

First, we take the rr metric component, eq. (A.4), and apply the weak-field limit,

$$\mathrm{e}^{2\zeta(r)} = \left(1 - \frac{2Gm(r)}{r}\right)^{-1} \approx 1 + \frac{2Gm(r)}{r}\,. \tag{A.17}$$

For the tt component, we are required to simplify the right-hand side of

eq. (A.6) before integration,

$$\frac{\mathrm{d}\xi}{\mathrm{d}r} = \frac{Gm(r)}{r^2\left(1-2Gm(r)/r\right)} \approx \frac{Gm(r)}{r^2}. \tag{A.18}$$

This simplification enables us to perform the integral required to find $\xi(r)$

$$\xi(r) = 4\pi G\rho_{\mathrm{NFW}} r_{\mathrm{NFW}}^3 \int \left[\frac{1}{r^2}\ln\left(1+\frac{r}{r_{\mathrm{NFW}}}\right) - \frac{1}{r^2}\frac{r/r_{\mathrm{NFW}}}{(1+r/r_{\mathrm{NFW}})}\right]\mathrm{d}r \tag{A.19}$$

$$= 4\pi G\rho_{\mathrm{NFW}} r_{\mathrm{NFW}}^2 \int \left[\frac{\ln(1+x)}{x^2} - \frac{1}{x(1+x)}\right]\mathrm{d}x\,, \tag{A.20}$$

where we have made the substitution $x = r/r_{\mathrm{NFW}}$. Solving the first term in $\xi = 4\pi G\rho_{\mathrm{NFW}} r_{\mathrm{NFW}}^2 (I_1 - I_2)$ using integration by parts,

$$I_1 = \int \frac{\ln(1+x)}{x^2}\,\mathrm{d}x = -\frac{\ln(1+x)}{x} + \int \frac{1}{x(1+x)}\,\mathrm{d}x \tag{A.21}$$

and noticing that the new integral in I_1 exactly cancels I_2, we arrive at

$$\xi = -4\pi G\rho_{\mathrm{NFW}} r_{\mathrm{NFW}}^2 \frac{\ln(1+r/r_{\mathrm{NFW}})}{r/r_{\mathrm{NFW}}} + C\,. \tag{A.22}$$

We determine the integration constant C by matching to the exterior Schwarzschild metric at the outer surface of the halo, R,

$$\begin{aligned} \mathrm{e}^{2\xi(R)} &\approx 1 + 2\xi(R) = 1 - \frac{2GM}{R}\,, \\ \Rightarrow \xi(R) &\approx -\frac{GM}{R} = -4\pi G\rho_{\mathrm{NFW}}\frac{r_{\mathrm{NFW}}^3}{R}\left[\ln\left(1+\frac{R}{r_{\mathrm{NFW}}}\right) - \frac{R/r_{\mathrm{NFW}}}{1+R/r_{\mathrm{NFW}}}\right]. \end{aligned} \tag{A.23}$$

Comparing these equations, we find

$$C = 4\pi G\rho_{\mathrm{NFW}} r_{\mathrm{NFW}}^2 \frac{1}{1+R/r_{\mathrm{NFW}}}\,, \tag{A.24}$$

resulting in the final form of the tt metric component function

$$\xi(r) = -4\pi G\rho_{\mathrm{NFW}} r_{\mathrm{NFW}}^2 \left[\frac{\ln(1+r/r_{\mathrm{NFW}})}{r/r_{\mathrm{NFW}}} - \frac{1}{1+R/r_{\mathrm{NFW}}}\right]. \tag{A.25}$$

We can convert this to the metric component using

$$\mathrm{e}^{2\xi(r)} \approx 1 + 2\xi(r) \approx 1 - 8\pi G\rho_{\mathrm{NFW}} r_{\mathrm{NFW}}^2 \left[\frac{\ln(1+r/r_{\mathrm{NFW}})}{r/r_{\mathrm{NFW}}} - \frac{1}{1+R/r_{\mathrm{NFW}}}\right]. \tag{A.26}$$

Equally, this could be written in the form

$$e^{2\xi(r)} \approx 1 - \frac{2Gm(r)}{r} - 8\pi G\rho_{\rm NFW} r_{\rm NFW}^2 \left[\frac{1}{1 + r/r_{\rm NFW}} - \frac{1}{1 + R/r_{\rm NFW}}\right]. \tag{A.27}$$

Here, the first term $1 - \frac{2Gm(r)}{r}$ represents the standard Schwarzschild-like contribution from the enclosed mass, while the final correction term accounts for the deviation from a point mass due to the extended NFW density profile, ensuring that the metric matches the exterior solution at the truncation radius R.

Combining our results, we find the approximate form of the NFW metric to be

$$ds^2 \approx \left(1 - \frac{2Gm(r)}{r} - f_{\rm NFW}(r)\right) dt^2 + \left(1 + \frac{2Gm(r)}{r}\right) dr^2 + r^2 d\Omega^2 , \tag{A.28}$$

where for brevity we have defined the correction term

$$f_{\rm NFW} = 8\pi G\rho_{\rm NFW} r_{\rm NFW}^2 \left[\frac{1}{1 + r/r_{\rm NFW}} - \frac{1}{1 + R/r_{\rm NFW}}\right]. \tag{A.29}$$

This metric describes the interior region of an NFW dark matter halo and is valid in the weak-field limit, where $Gm(r)/r \ll 1$ and $f_{\rm NFW} \ll 1$.

Appendix B

General Radial Acceleration from Geodesic Equation

In this section, we derive a general formula describing the radial acceleration of a particle for a static, spherically symmetric metric, $\tilde{g}_{\mu\nu}$. Starting with the geodesic equation,

$$\frac{d^2x^\mu}{\mathrm{d}\tau^2} + \tilde{\Gamma}^\mu_{\alpha\beta}\frac{\mathrm{d}x^\alpha}{\mathrm{d}\tau}\frac{\mathrm{d}x^\beta}{\mathrm{d}\tau} = 0\,, \tag{B.1}$$

where $\tilde{\Gamma}^\mu_{\alpha\beta}$ are the Christoffel symbols defined in terms of the Jordan frame metric tensor, $\tilde{g}_{\mu\nu} = A^2(\phi)g_{\mu\nu}$, as

$$\tilde{\Gamma}^\mu_{\alpha\beta} = \frac{1}{2}\tilde{g}^{\mu\nu}\left(\partial_\alpha\tilde{g}_{\nu\beta} + \partial_\beta\tilde{g}_{\nu\alpha} - \partial_\nu\tilde{g}_{\alpha\beta}\right)\,. \tag{B.2}$$

Our objective is to find the radial acceleration, so we focus on the radial component of this geodesic equation, i.e., $\mu = r$. Assuming that the metric is diagonal, static, and spherically symmetric, we can write the Christoffel symbols in terms of the metric components as follows:

$$\tilde{\Gamma}^r_{\alpha\beta} = \frac{1}{2}\tilde{g}^{rr}\left(2\partial_r\tilde{g}_{rr} - \partial_r\tilde{g}_{\alpha\beta}\right) = 0\,, \tag{B.3}$$

as such, the radial component of the geodesic equation simplifies to

$$\frac{\mathrm{d}^2r}{\mathrm{d}\tau^2} + \frac{1}{2}\tilde{g}^{rr}\left(2\partial_r\tilde{g}_{rr}\left(\frac{\mathrm{d}r}{\mathrm{d}\tau}\right)^2 - \partial_r\tilde{g}_{\alpha\beta}\frac{\mathrm{d}x^\alpha}{\mathrm{d}\tau}\frac{\mathrm{d}x^\beta}{\mathrm{d}\tau}\right) = 0 \tag{B.4}$$

$$\frac{\mathrm{d}^2 r}{\mathrm{d}\tau^2} = \frac{1}{2}\tilde{g}^{rr}\left(\partial_r \tilde{g}_{tt}\left(\frac{\mathrm{d}t}{\mathrm{d}\tau}\right)^2 - \partial_r \tilde{g}_{rr}\left(\frac{\mathrm{d}r}{\mathrm{d}\tau}\right)^2 + \partial_r \tilde{g}_{\theta\theta}\left(\frac{\mathrm{d}\theta}{\mathrm{d}\tau}\right)^2\right). \tag{B.5}$$

Given the symmetries imposed earlier (static, spherically symmetric), we have the following conserved quantities

$$\tilde{g}_{tt}\frac{\mathrm{d}t}{\mathrm{d}\tau} = E \quad \text{and} \quad \tilde{g}_{\theta\theta}\frac{\mathrm{d}\theta}{\mathrm{d}\tau} = h\,, \tag{B.6}$$

and for a diagonal metric

$$\tilde{g}^{\alpha\lambda}\tilde{g}_{\lambda\beta} = \delta^{\alpha}_{\beta} \quad \Rightarrow \quad \tilde{g}^{rr} = \frac{1}{\tilde{g}_{rr}}\,. \tag{B.7}$$

With these simplifications, the radial acceleration becomes

$$\frac{\mathrm{d}^2 r}{\mathrm{d}\tau^2} = \frac{1}{2\tilde{g}_{rr}}\left(\frac{E^2}{\tilde{g}_{tt}^2}\partial_r \tilde{g}_{tt} - \partial_r \tilde{g}_{rr}\left(\frac{\mathrm{d}r}{\mathrm{d}\tau}\right)^2 + \frac{h^2}{\tilde{g}_{\theta\theta}^2}\partial_r \tilde{g}_{\theta\theta}\right). \tag{B.8}$$

All that remains unknown is the radial velocity $\frac{\mathrm{d}r}{\mathrm{d}\tau}$. We can relate this to the known quantities via the line element, given by

$$\tilde{g}_{tt}\left(\frac{\mathrm{d}t}{\mathrm{d}\tau}\right)^2 + \tilde{g}_{rr}\left(\frac{\mathrm{d}r}{\mathrm{d}\tau}\right)^2 + \tilde{g}_{\theta\theta}\left(\frac{\mathrm{d}\theta}{\mathrm{d}\tau}\right)^2 = q\,, \tag{B.9}$$

where $q = 0$ for massless particles and $q = -1$ for massive particles. Substituting the conserved quantities and rearranging, we arrive at

$$\left(\frac{\mathrm{d}r}{\mathrm{d}\tau}\right)^2 = \frac{q}{\tilde{g}_{rr}} - \frac{E^2}{\tilde{g}_{tt}\tilde{g}_{rr}} - \frac{h^2}{\tilde{g}_{rr}\tilde{g}_{\theta\theta}}\,. \tag{B.10}$$

Substituting this into the radial acceleration equation, we find

$$\frac{\mathrm{d}^2 r}{\mathrm{d}\tau^2} = \frac{1}{2\tilde{g}_{rr}}\left(\frac{E^2}{\tilde{g}_{tt}^2}\partial_r \tilde{g}_{tt} + \partial_r \tilde{g}_{rr}\left(\frac{E^2}{\tilde{g}_{tt}\tilde{g}_{rr}} + \frac{h^2}{\tilde{g}_{rr}\tilde{g}_{\theta\theta}} - \frac{q}{\tilde{g}_{rr}}\right) + \frac{h^2}{\tilde{g}_{\theta\theta}^2}\partial_r \tilde{g}_{\theta\theta}\right). \tag{B.11}$$

Converting this quantity from proper time τ to coordinate time t via

the chain rule

$$\begin{aligned}\frac{\mathrm{d}^2 r}{\mathrm{d}t^2} &= \frac{\mathrm{d}\tau}{\mathrm{d}t}\frac{\mathrm{d}}{\mathrm{d}\tau}\left(\frac{\mathrm{d}\tau}{\mathrm{d}t}\frac{\mathrm{d}r}{\mathrm{d}\tau}\right) \\ &= \frac{\tilde{g}_{tt}^2}{E^2}\frac{\mathrm{d}^2 r}{\mathrm{d}\tau^2} + \frac{\tilde{g}_{tt}}{E^2}\frac{\mathrm{d}r}{\mathrm{d}\tau}\frac{\mathrm{d}\tilde{g}_{tt}}{\mathrm{d}\tau} \\ &= \frac{\tilde{g}_{tt}^2}{E^2}\frac{\mathrm{d}^2 r}{\mathrm{d}\tau^2} + \frac{\tilde{g}_{tt}}{E^2}\left(\frac{\mathrm{d}r}{\mathrm{d}\tau}\right)^2\frac{\mathrm{d}\tilde{g}_{tt}}{\mathrm{d}r}\,, \end{aligned} \tag{B.12}$$

where we have again used the fact that $\frac{\mathrm{d}t}{\mathrm{d}\tau} = \frac{E}{\tilde{g}_{tt}}$. Now, upon substituting equations (B.10) and (B.11) into (B.12), rewriting $\frac{\mathrm{d}\tilde{g}_{tt}}{\mathrm{d}r}$ as $\partial_r \tilde{g}_{tt}$ and collecting like terms, we arrive at the full expression for the radial acceleration in coordinate time t

$$\begin{aligned}\frac{\mathrm{d}^2 r}{\mathrm{d}t^2} = \frac{1}{2}\Bigg[&\partial_r \tilde{g}_{tt}\left(\frac{2q}{E^2}\frac{\tilde{g}_{tt}}{\tilde{g}_{rr}} - \frac{1}{\tilde{g}_{rr}} - \frac{2h^2}{E^2}\frac{\tilde{g}_{tt}}{\tilde{g}_{rr}\tilde{g}_{\theta\theta}}\right) \\ &+ \partial_r \tilde{g}_{rr}\left(\frac{\tilde{g}_{tt}}{\tilde{g}_{rr}^2} + \frac{h^2}{E^2}\frac{\tilde{g}_{tt}^2}{\tilde{g}_{rr}^2\tilde{g}_{\theta\theta}} - \frac{q}{E^2}\frac{\tilde{g}_{tt}^2}{\tilde{g}_{rr}^2}\right) \\ &+ \partial_r \tilde{g}_{\theta\theta}\left(\frac{h^2}{E^2}\frac{\tilde{g}_{tt}^2}{\tilde{g}_{rr}\tilde{g}_{\theta\theta}^2}\right)\Bigg]\end{aligned} \tag{B.13}$$

If one is interested in the acceleration of a particle with no scalar field coupling, i.e., $A(\phi) = 1$, then it is sufficient to set $\tilde{g}_{\mu\nu} = g_{\mu\nu}$, and the above equation reduces to the standard form of the radial acceleration in general relativity. In our case, we are interested in the acceleration of a particle with a scalar field coupling, so we expand in terms of our conformal coupling factor, $\tilde{g}_{\mu\nu} = A^2(\phi)g_{\mu\nu}$. In such a scenario, the radial acceleration becomes

$$\begin{aligned}\frac{\mathrm{d}^2 r}{\mathrm{d}t^2} = \frac{1}{2}\Bigg[&\partial_r g_{tt}\left(\frac{2qA^2}{E^2}\frac{g_{tt}}{g_{rr}} - \frac{1}{g_{rr}} - \frac{2h^2}{E^2}\frac{g_{tt}}{g_{rr}g_{\theta\theta}}\right) \\ &+ \partial_r g_{rr}\left(\frac{g_{tt}}{g_{rr}^2} + \frac{h^2}{E^2}\frac{g_{tt}^2}{g_{rr}^2 g_{\theta\theta}} - \frac{qA^2}{E^2}\frac{g_{tt}^2}{g_{rr}^2}\right) \\ &+ \partial_r g_{\theta\theta}\left(\frac{h^2}{E^2}\frac{g_{tt}^2}{g_{rr}g_{\theta\theta}^2}\right) + \partial_r A^2\left(\frac{q}{E^2}\frac{g_{tt}^2}{g_{rr}}\right)\Bigg]\,.\end{aligned} \tag{B.14}$$

Here we see that all the scalar-dependent terms, containing either A or $\partial_r A$, come with a prefactor of q, indicating that any scalar contribution to gravity is only relevant for massive particles.

In the proceeding sections, we apply this general formula to the specific metrics of interest: exterior Schwarzschild metric, interior SIS metric, and interior NFW metric. In each case, we consider the non-relativistic, weak-field limit, and show comparisons between all three metrics in section B.4.

B.1 Exterior Schwarzschild Metric

We begin with the exterior Schwarzschild metric, describing the curvature outside of a spherical source with total mass M. The non-zero components of this metric are given by

$$g_{tt} = -\left(1 - \frac{2GM}{r}\right), \quad g_{rr} = \left(1 - \frac{2GM}{r}\right)^{-1} \quad \& \quad g_{\theta\theta} = r^2 \,. \tag{B.15}$$

Substituting these into eq. (B.14) gives us the radial acceleration for a particle in the exterior Schwarzschild metric

$$\begin{aligned} \frac{\mathrm{d}^2 r}{\mathrm{d}t^2} = &\frac{2GM}{r^2}\left(1 - \frac{2GM}{r}\right) + \frac{3qA^2}{E^2}\frac{GM}{r^2}\left(1 - \frac{2GM}{r}\right)^2 \\ &+ \frac{h^2}{E^2}\frac{1}{r^3}\left(1 - \frac{2GM}{r}\right)^2\left(1 - \frac{5GM}{r}\right) + \frac{q}{2E^2}\left(1 - \frac{2GM}{r}\right)^3 \partial_r A^2 \,. \end{aligned} \tag{B.16}$$

This expression can be simplified further by removing terms that are small in the weak-field limit, i.e., $GM/r \ll 1$, assuming that the fifth force is comparable to the usual gravitational force, i.e., $\partial_r A^2 \sim \frac{GM}{r^2} \ll 1$, and working in the non-relativistic limit where h^2 is a small quantity. With these assumptions, we are left with

$$\frac{\mathrm{d}^2 r}{\mathrm{d}t^2} \approx \frac{2GM}{r^2} + \frac{3qA^2}{E^2}\frac{GM}{r^2} + \frac{h^2}{E^2}\frac{1}{r^3} + \frac{q}{2E^2}\partial_r A^2 \,. \tag{B.17}$$

We can simplify this further for a massive particle ($q = -1$) in the Newtonian limit, where $A^2 \approx 1$, $h \ll 1$, and $\tau \to t$, resulting in the conserved quantity $E^2 \approx g_{tt}^2 \approx 1$, leaving us with

$$\frac{\mathrm{d}^2 r}{\mathrm{d}t^2} \approx -\frac{GM}{r^2} + \mathcal{O}\left(h^2\right) - \frac{1}{2}\partial_r A^2 \,. \tag{B.18}$$

This leaves us with the standard Newtonian radial acceleration, plus a

fifth-force contribution. The term containing h^2 is a small correction due to angular momentum, which is negligible compared to the other terms.

B.2 Interior SIS Metric

Moving to an extended mass profile, we consider the interior of a Singular Isothermal Sphere (SIS) dark matter halo, with metric components given by eq. (A.14). Substituting these into eq. (B.14) gives us the radial acceleration for a particle in the interior SIS metric

$$\begin{aligned}\frac{\mathrm{d}^2 r}{\mathrm{d}t^2} = &-\frac{2\sigma_v^2}{r}\left(\frac{r}{R}\right)^{\frac{4\sigma_v^2}{1-4\sigma_v^2}}\left[-(1-4\sigma_v^2)-\frac{2qA^2}{E^2}(1-4\sigma_v^2)^2\left(\frac{r}{R}\right)^{\frac{4\sigma_v^2}{1-4\sigma_v^2}}\right.\\ &\left.-\frac{2h^2}{E^2r^2}(1-4\sigma_v^2)\left(\frac{r}{R}\right)^{\frac{4\sigma_v^2}{1-4\sigma_v^2}}\right]\\ &+\frac{h^2}{E^2r^3}\left(1-4\sigma_v^2\right)^3\left(\frac{r}{R}\right)^{\frac{8\sigma_v^2}{1-4\sigma_v^2}}\\ &+\frac{q}{2E^2}\left(1-4\sigma_v^2\right)^3\left(\frac{r}{R}\right)^{\frac{4\sigma_v^2}{1-4\sigma_v^2}}\partial_r A^2\,.\end{aligned} \tag{B.19}$$

Given $0 < r \leq R$ and $\sigma_v \ll 1$, all factors of $\left(\frac{r}{R}\right)^{\frac{4\sigma_v^2}{1-4\sigma_v^2}}$ can be approximated as $1 + 4\sigma_v^2 \ln(r/R)$.[1] Now, applying the weak-field, non-relativistic limit, i.e., simplifying to first order in σ_v^2, $\partial_r A^2$, and h^2, we find

$$\frac{\mathrm{d}^2 r}{\mathrm{d}t^2} \approx \frac{Gm}{r^2}\left(1+\frac{2qA^2}{E^2}\right)+\frac{h^2}{E^2r^3}+\frac{q}{2E^2}\partial_r A^2\,, \tag{B.20}$$

given that $\sigma_v^2 = \frac{Gm}{2r}$. Again, for a massive particle ($q = -1$) in the Newtonian limit, where $A^2 \approx 1$ and $E^2 \approx 1$, this simplifies into the same standard classical radial acceleration as in eq. (B.18).

[1] Note, this derivation is used to probe the outer regions of galaxies, well outside the baryonic disc ($r \gtrsim 30\,\mathrm{kpc}$). As such the smallest possible radius we will consider is of order $0.05R$.

B.3 Interior NFW Metric

Following the same procedure as the previous section, but with an extended mass profile described by the NFW density model, eq. (1.50), with metric components given in eq. (A.28), we find the radial acceleration for a particle in the interior NFW metric to be

$$\begin{aligned}\frac{\mathrm{d}^2 r}{\mathrm{d}t^2} = &\left(-\frac{Gm}{r^2}+\frac{Gm'}{r}\right)\left[-1-\frac{qA^2}{E^2}+\frac{h^2}{E^2r^2}\right]\\ &\times\left(1-\frac{2Gm}{r}-f_{\mathrm{NFW}}(r)\right)\left(1+\frac{2Gm}{r}\right)^{-2}\\ &-\frac{Gm}{r^2}\Bigg[-\left(1+\frac{2Gm}{r}\right)\\ &\quad-\frac{2qA^2}{E^2}\left(1-\frac{2Gm}{r}-f_{\mathrm{NFW}}(r)\right)\left(1-\frac{2Gm}{r}\right)^{-1}\\ &\quad-\frac{2h^2}{E^2r^2}\left(1-\frac{2Gm}{r}-f_{\mathrm{NFW}}(r)\right)\left(1-\frac{2Gm}{r}\right)^{-1}\Bigg]\\ &+\frac{h^2}{E^2r^3}\left(1-\frac{2Gm}{r}-f_{\mathrm{NFW}}(r)\right)^2\left(1-\frac{2Gm}{r}\right)^{-1}\\ &+\frac{q}{2E^2}\left(1-\frac{2Gm}{r}-f_{\mathrm{NFW}}(r)\right)^2\left(1-\frac{2Gm}{r}\right)^{-1}\partial_r A^2\,, \end{aligned} \tag{B.21}$$

where m' is the radial derivative of the NFW mass profile, and $f_{\mathrm{NFW}}(r)$ is the correction term defined in eq. (A.29).

Simplifying this rather unwieldy equation in the non-relativistic, weak-field limit, i.e., to first order in $\frac{Gm}{r}$, $\frac{Gm'}{r}$, $f_{\mathrm{NFW}}(r)$, $\partial_r A^2$, and h^2, we find

$$\frac{\mathrm{d}^2 r}{\mathrm{d}t^2} \approx \frac{Gm}{r^2}\left(2+\frac{3qA^2}{E^2}\right)-\frac{Gm'}{r}\left(1+\frac{qA^2}{E^2}\right)+\frac{h^2}{E^2r^3}+\frac{q}{2E^2}\partial_r A^2\,. \tag{B.22}$$

Once again, for a massive particle ($q=-1$) in the Newtonian limit, where $A^2 \approx 1$ and $E^2 \approx 1$, this simplifies to the same standard classical radial acceleration as in eq. (B.18).

B.4 Comparison of Radial Accelerations

In the previous sections, we have derived the radial acceleration for three different metrics, namely the exterior Schwarzschild metric, the interior SIS metric, and the interior NFW metric, equations (B.17), (B.20) and (B.22) respectively. In this section, we compare these three accelerations and show that all three can be written in one equivalent form.

First, we restate all three radial accelerations for ease of comparison:

$$\left.\frac{\mathrm{d}^2 r}{\mathrm{d}t^2}\right|_{\text{Ext.Sch.}} \approx \frac{GM}{r^2}\left(1+\frac{2qA^2}{E^2}\right)+\frac{h^2}{E^2 r^3}+\frac{q}{2E^2}\partial_r A^2\,,$$
$$\left.\frac{\mathrm{d}^2 r}{\mathrm{d}t^2}\right|_{\text{SIS}} \approx \frac{Gm}{r^2}\left(1+\frac{2qA^2}{E^2}\right)+\frac{h^2}{E^2 r^3}+\frac{q}{2E^2}\partial_r A^2\,,$$
$$\left.\frac{\mathrm{d}^2 r}{\mathrm{d}t^2}\right|_{\text{NFW}} \approx \frac{Gm}{r^2}\left(2+\frac{3qA^2}{E^2}\right)-\frac{Gm'}{r}\left(1+\frac{qA^2}{E^2}\right)+\frac{h^2}{E^2 r^3}+\frac{q}{2E^2}\partial_r A^2\,.$$

All three share the same terms in h^2 and $\partial_r A^2$, whilst differing in their dependence on the mass m, the mass derivative m', and the correction terms. However, this can be reconciled by noticing that in the Schwarzschild case, the mass is a point mass, and thus the derivative of the mass vanishes. Meanwhile, in the SIS case, the mass profile is proportional to r; therefore, $m'/r = m/r^2$, explaining the difference between the factors in the SIS and NFW accelerations. As a result of this, all three models can be expressed most generally in the same way as the NFW acceleration,

$$\frac{\mathrm{d}^2 r}{\mathrm{d}t^2} \approx \frac{Gm}{r^2}\left(2+\frac{3qA^2}{E^2}\right)-\frac{Gm'}{r}\left(1+\frac{qA^2}{E^2}\right)+\frac{h^2}{E^2 r^3}+\frac{q}{2E^2}\partial_r A^2\,. \quad \text{(B.23)}$$

As discussed at the end of the previous sections, in the classical limit ($q=-1$, $A^2\approx 1$, and $E^2\approx 1$), this equation reduces to the typical radial acceleration equation

$$\frac{\mathrm{d}^2 r}{\mathrm{d}t^2} \approx -\frac{GM}{r^2}+\mathcal{O}\left(h^2\right)-\frac{1}{2}\partial_r A^2\,. \quad \text{(B.24)}$$

Conveniently, this limit removes any contribution from the derivative of the enclosed mass profile, simplifying the comparison between the different

models. Whilst this derivation may seem excessive to confirm a well-known result in scalar modified gravity, it is required for later parts of this work, namely chapter 5. Specifically, to confirm that the acceleration in the form of the mass profile can be directly compared with lensing results, i.e., to compare $\frac{Gm(r)}{r^2}$ between models, and not for instance the derivative of the potential, $\frac{\mathrm{d}}{\mathrm{d}r}\left(\frac{Gm(r)}{r}\right)$, which would complicate the analysis.

It should be noted that in all cases, attempting to determine the behaviour of a massless particle ($q = 0$) results in the unphysical conclusion that photons experience a repulsive gravitational force. This arises because proper time τ is not defined along null geodesics (the worldlines of massless particles), so the conversion between proper time and coordinate time used in the derivation breaks down mathematically. As a result, expressions involving $\frac{\mathrm{d}t}{\mathrm{d}\tau}$ become ill-defined for photons, leading to odd or unphysical results such as apparent repulsive gravitational forces. For a correct treatment of massless particles, the geodesic approach must be replaced by methods that avoid improper time conversions for massless particles. On top of this, we have made the assumption throughout this derivation that we are working in the non-relativistic limit ($h \ll 1$). As a result the equations derived in this appendix are only applicable to massive particles moving at speeds much less than the speed of light.

Appendix C

Lensing in Modified Gravity Theories

In chapter 5, we explore the lensing signatures of modified gravity theories in the outer regions of galaxies. To do this, we derived an novel framework for calculating the lensing of light in modified gravity theories with a conformal coupling to a scalar field. This method is detailed in full in section 5.7.1. We also derived the specific modifications to lensing for an NFW dark matter halo in the same section. In this appendix we also detail the result of this derivation for an exterior Schwarzschild metric and an interior SIS metric. We also comment on the difference between the solutions for different metrics at the end of section 5.7.1.

C.1 Exterior Schwarzschild Metric

Considering the simple case of the exterior Schwarzschild metric, with metric components given by eq. (B.15). Substituting these into the angular acceleration equation, eq. (5.19), and rearranging, we find

$$\begin{aligned}\frac{\mathrm{d}^2u}{\mathrm{d}\theta^2} =& -\frac{1}{r}+\frac{3GM}{r^2} \\ &+\frac{qA^2r^2}{2h^2}\left(1-\frac{2GM}{r}\right)\left[-\frac{2GM}{r^2}\left(1-\frac{2GM}{r}\right)^{-3}-\frac{1}{A^2}\frac{\mathrm{d}A^2}{\mathrm{d}r}\right].\end{aligned} \tag{C.1}$$

Taking the weak-field limit (ignoring terms that are sub-leading order in GM/r, GM/r^2, and $\partial_r A^2$), we arrive at the following expression for the angular acceleration of a light ray in the exterior Schwarzschild metric

$$\frac{\mathrm{d}^2 u}{\mathrm{d}\theta^2} \approx -\frac{1}{r} + \frac{3GM}{r^2} - \frac{qA^2 GM}{h^2} - \frac{qr^2}{2h^2}\frac{\mathrm{d}A^2}{\mathrm{d}r}\,. \tag{C.2}$$

In this equation, the first two terms are the standard GR lensing terms, as found in eq. (5.19), the third term is the modification arising from the massive photon, and the final term is the fifth-force contribution. Note that the modification terms are only present for massive particles (i.e., $q = -1$) and vanish for massless particles (i.e., $q = 0$).

With this expression, consider that $\frac{\mathrm{d}^2 u}{\mathrm{d}\theta^2}$ encodes the observable amount of lensing for a given mass profile. As such, in observations that measure the amount of mass from lensing, there will be noticeable differences between the GR and modified gravity cases. Previous works that have assumed GR to be the underlying theory of gravity may measure more deflection of light, and therefore assume more mass is present, due to the impact of the modification terms. We can quantify this overestimation by comparing the modified gravity lensing equation to the GR lensing equation (with $q = 0$, $A = 1$)

$$\left.\frac{\mathrm{d}^2 u}{\mathrm{d}\theta^2}\right|_{\mathrm{GR}} = \left.\frac{\mathrm{d}^2 u}{\mathrm{d}\theta^2}\right|_{\mathrm{MG}} \tag{C.3}$$

$$\frac{3GM_{\mathrm{GR}}}{r^2} = \frac{3GM_{\mathrm{MG}}}{r^2} - \frac{qA^2 GM_{\mathrm{MG}}}{h^2} - \frac{qr^2}{2h^2}\frac{\mathrm{d}A^2}{\mathrm{d}r}$$

$$\frac{GM_{\mathrm{GR}}}{r^2} = \frac{GM_{\mathrm{MG}}}{r^2}\left(1 - \frac{qA^2 r^2}{3h^2}\right) - \frac{qr^2}{6h^2}\frac{\mathrm{d}A^2}{\mathrm{d}r}\,. \tag{C.4}$$

This equation can be further developed by adopting a parameterisation for the angular conserved quantity, h. In lensing, this parameter is typically related to the other conserved quantity E, via $h \approx bE$, as in eq. (1.126), where b is the impact parameter, defined as the perpendicular distance between the photon trajectory and the centre of the mass distribution. In our case, the impact parameter is equivalent to the radial coordinate r. So

we can express h as a function of r and E, namely $h \approx bE = rE$. With this, the angular acceleration becomes

$$\frac{GM_{\rm GR}}{r^2} = \frac{GM_{\rm MG}}{r^2}\left(1 - \frac{qA^2}{3E^2}\right) - \frac{q}{6E^2}\frac{\mathrm{d}A^2}{\mathrm{d}r}\,. \tag{C.5}$$

Both sides of this equation result in the same observable amount of lensing for their respective theories. In the GR case, contemporary data suggests that a large amount of extra mass is required in the outskirts of a galaxy — more than predicted by standard DM halo models. The additional lensing measured could instead arise from the new terms in the modified theory, allowing for the same amount of lensing to be observed without the need for additional mass, since $m_{\rm MG} < m_{\rm GR}$ for $q = -1$.

C.2 Interior SIS Metric

Moving to an extended mass profile, described by the SIS density model, with metric components given by eq. (A.14), we substitute these into the angular acceleration equation, eq. (5.19), and rearranging, we find

$$\frac{\mathrm{d}^2u}{\mathrm{d}\theta^2} = -\frac{1}{r} + \frac{4\sigma_v^2}{r} + \frac{E^2 r}{2h^2}\frac{4\sigma_v^2}{1-4\sigma_v^2}\left(\frac{r}{R}\right)^{-\frac{4\sigma_v^2}{1-4\sigma_v^2}} - \frac{qr^2}{2h^2}\left(1-4\sigma_v^2\right)\frac{\mathrm{d}A^2}{\mathrm{d}r}\,. \tag{C.6}$$

Taking the weak-field limit (ignoring terms that are sub-leading order in σ_v^2 and $\partial_r A^2$), we arrive at

$$\frac{\mathrm{d}^2u}{\mathrm{d}\theta^2} \approx -\frac{1}{r} + \frac{4\sigma_v^2}{r} + \frac{2E^2\sigma_v^2 r}{h^2} - \frac{qr^2}{2h^2}\frac{\mathrm{d}A^2}{\mathrm{d}r}\,. \tag{C.7}$$

At this point, in order to compare assumed mass/acceleration profiles, we must convert from σ_v^2 back to $\frac{Gm}{2r}$, to find

$$\frac{\mathrm{d}^2u}{\mathrm{d}\theta^2} \approx -\frac{1}{r} + \frac{2Gm}{r^2} + \frac{E^2r^2}{h^2}\frac{Gm}{r^2} - \frac{qr^2}{2h^2}\frac{\mathrm{d}A^2}{\mathrm{d}r}\,. \tag{C.8}$$

It should be noted that the SIS metric derivation freely swapped between $2\sigma_v^2$, Gm/r and GM/R; however, in this calculation we are specifically

interested in comparing mass profiles, not the constant value of the potential at the surface R. Fortunately, a proper treatment, explicit in these quantities, evaluates to the same expression we arrived at after taking the weak-field limit.

Now we compare predicted mass/acceleration profiles between GR and MG, in the same way as the previous section

$$\begin{aligned}
\left.\frac{\mathrm{d}^2u}{\mathrm{d}\theta^2}\right|_{\mathrm{GR}} &= \left.\frac{\mathrm{d}^2u}{\mathrm{d}\theta^2}\right|_{\mathrm{MG}} \\
\frac{2Gm_{\mathrm{GR}}}{r^2} + \frac{E^2r^2}{h^2}\frac{Gm_{\mathrm{GR}}}{r^2} &= \frac{2Gm_{\mathrm{MG}}}{r^2} + \frac{E^2r^2}{h^2}\frac{Gm_{\mathrm{MG}}}{r^2} - \frac{qr^2}{2h^2}\frac{\mathrm{d}A^2}{\mathrm{d}r} \\
\frac{Gm_{\mathrm{GR}}}{r^2} &= \frac{Gm_{\mathrm{MG}}}{r^2} - \frac{qr^2}{4h^2 + 2E^2r^2}\frac{\mathrm{d}A^2}{\mathrm{d}r}\,. \qquad \text{(C.9)}
\end{aligned}$$

And again, we can adopt the parameterisation $h = bE = rE$ to find

$$\frac{Gm_{\mathrm{GR}}}{r^2} = \frac{Gm_{\mathrm{MG}}}{r^2} - \frac{q}{6E^2}\frac{\mathrm{d}A^2}{\mathrm{d}r}\,. \qquad \text{(C.10)}$$